Studying the origin of cosmic-rays : Multi-messenger studies with very-high-energy gamma-ray instruments

Monica Seglar-Arroyo

université PARIS-SACLAY

PennState

UNIVERSITÉ PARIS SUD
Comprendre le monde, construire l'avenir

NNT : 2019SACLS260

Thèse de doctorat

Studying the origin of cosmic-rays : Multi-messenger studies with very-high-energy gamma-ray instruments

Thèse de doctorat de l'Université Paris-Saclay
préparée à Université Paris-Sud
au Commissariat à l'Energie Atomique et aux Energies Alternatives (CEA),
au sein du Département de Physique des Particules (DPhP)
de l'Institut de Recherche sur les lois Fondamentales de l'Univers (IRFU)

Ecole doctorale n°576 Particules, Hadrons, Énergie, Noyau, Instrumentation, Imagerie, Cosmos et Simulation (PHENIICS)
Spécialité de doctorat : Astroparticules et Cosmologie

Thèse présentée et soutenue à Saclay, le 23 Septembre, par

Monica Seglar-Arroyo

Composition du Jury :

Tiina Suomijarvi Professeur, Institut de Physique Nucleaire	Présidente
Catherine Boisson Professeur, Observatoire de Paris	Rapporteur
Karl-Heinz Kampert Professeur, Bergische Universität Wuppertal	Rapporteur
Marica Branchesi Professeur assistant, Gran Sasso Science Institute	Examinatrice
Marcos Santander Professeur assistant, University of Alabama	Examinateur
Miguel Mostafa Professeur, Penn State University	Directeur de thèse
Fabian Schüssler Ingénieur de recherche, IRFU, CEA, Université Paris-Saclay	Directeur de thèse

"*I know nothing with any certainty, but the sight of the stars makes me dream.*"

Vincent Van Gogh

Preamble

Astronomy is one of the oldest science in human history. It is bounded to our curiosity and fascination for Nature, and has evolved by leaving the myths aside and following the scientific method.

Today, thanks to our ever-evolving knowledge of Nature and technological development, we are able to go beyond the traditional astronomical observations in the optical domain. We are now able to observe astrophysical sources in the entire electromagnetic spectrum, from radio to gamma rays wavelengths. New messengers as neutrinos and gravitational waves have been recently discovered, unveiling new realities and opening the door to new types of *astronomy*. Amongst the most violent events, candidates to produce multi-messenger signals are the mergers of the two densest objects in the Universe, neutron stars and black holes; and the most luminous persistent sources of electromagnetic radiation, active galactic nuclei, with important accretion activity onto a supermassive black hole. Observing these extreme events and the associated counterparts enables researchers to answer open questions in astrophysics. Nevertheless, there are challenges associated to time-domain multi-messenger astronomy, which involves simultaneous coordinated efforts across facilities and astronomical disciplines worldwide.

In this dissertation I zoom out to the primary motivation of this research: the origin of cosmic rays, to later move to multi-messenger astronomy from the point of view of gamma-ray observatories. During these last three years of PhD, I mainly concentrated on the quest for electromagnetic gamma-ray signals from explosive events producing gravitational waves, with the aim to broaden the understanding of the connection between these two events and the physics of bursts of gamma rays, in particular at very-high energies. I focused on the improvement of techniques used in both small FoV and large FoV gamma-ray observatories, to overcome the challenges inherent to the search for gravitational-wave counterparts in current and next generation of instruments. Results of these improvements yield to successful follow-up observations in current small FoV experiments and first studies forecasts bright prospects for future facilities. In addition, in the context of time-domain astronomy and as a result of a multi-wavelength coordinated effort, the discovery of an active galactic nucleus at very-high energies undergoing a flaring state will be presented.

Préface

L'astronomie est l'une des plus anciennes sciences de l'histoire de l'humanité. Elle est liée à notre curiosité et à notre fascination pour la nature, et a évolué en laissant de côté les mythes et en suivant la méthode scientifique. En regardant le ciel, l'humanité est confrontée aux questions les plus vastes qui incluent, entre autres, l'origine, la dynamique et le destin de l'Univers.

Actuellement on sait que dans l'Univers, les phénomènes explosifs extremes qui se produisent sont capables d'accélérer des particules jusqu'aux plus hautes énergies. Cependant, la recherche sur l'origine du rayonnement ambiant observé sur Terre, commencé il y a plus d'un siècle, est toujours en cours. Dans un premier temps, des hypothèses aux scientifiques sur son origine, avec comme premier candidat la radioactivité naturelle de la Terre. Plusieurs expériences ont été menées afin de quantifier la dépendance de l'ionisation en fonction de la hauteur au-dessus de la surface, afin de tester l'hypothèse ultérieure, en espérant trouver une ionisation plus élevée plus près de la Terre. Au lieu de cela, en 1912, Victor Hess a démontré qu'après un premier déclin à la sortie de la surface de la Terre, le rayonnement augmentait en fait avec la hauteur. Au cours des années suivantes, des tentatives ont été effectuées afin de mieux comprendre la nature de ce rayonnement *cosmique*. Ce n'est qu'en 1933 que Rossi et Johnson ont confirmé indépendamment que le rayonnement cosmique était composé de particules chargées, car elles étaient courbées par le champ magnétique terrestre en fonction de leur signe de charge. Une autre étape importante a été franchie en 1937, lorsque Pierre Auger a découvert des averses d'air atmosphérique étendues en étudiant les coïncidences de détecteurs placés à plusieurs mètres les uns des autres.

Les observations ont montré que le spectre des rayons cosmiques s'étend sur 12 ordres de grandeur en énergie et 30 ordres de grandeur en flux. Les caractéristiques spectrales observées sont certainement liées aux processus physiques sous-jacents d'accélération des particules dans la source, soit des sources proches ou extragalactiques, et aux effets de propagation. Néanmoins, on ne comprend pas encore parfaitement quelles sont les sources de ce rayonnement ni comment ces rayons cosmiques sont accélérés à la source. Au fil des ans, plusieurs mécanismes d'accélération diffuse des particules ont été invoqués pour expliquer ces hautes énergies, qui seront introduits dans ce travail, ainsi que leur lien avec la production de rayons gamma.

Grâce aux développements technologiques du dernière siècle, nous sommes désormais en mesure d'aller au-delà des observations directes des rayons cosmiques, et étendre l'étude de cette question à d'autres domaines de l'astronomie. Les sources astrophysiques sont observables dans l'ensemble du spectre électromagnétique, des du domaine radio aux rayons gamma. De la même façon, des nouveaux messagers tels que

les neutrinos et les ondes gravitationnelles ont été récemment découverts, dévoilant de nouvelles réalités et ouvrant la porte à de nouveaux types de *astronomie*, ce qui va faciliter la compréhension du comportement des sources. Cette révolution dans les techniques de détection a permis ce que l'on appelle l'astrophysique *multi-messager*, qui a pour but de comprendre les sources en les étudiant à travers les messagers qui ont potentiellement une origine commune.

Parmi les événements les plus violents, les candidats à la production de signaux *multi-messager* sont les fusions des deux objets les plus denses de l'Univers, les étoiles à neutrons et les trous noirs; et les sources persistantes de rayonnement électromagnétique les plus lumineuses, les noyaux galactiques actifs, avec une importante activité d'accrétion sur un trou noir supermassif situé au centre. L'observation de ces événements extrêmes, candidats à être les sources des rayons cosmiques mentionnés auparavant, et de leurs contreparties permet aux chercheurs de répondre à des questions ouvertes en astrophysique. Néanmoins, ces évènements explosifs sont souvent des phénomènes transitoires où une grande quantité d'énergie est émise sur différente forme. C'est pour cela que l'astronomie multi-messagers dans le domaine temporel nécessite des efforts simultanés et coordonnés entre les installations et les disciplines astronomiques du monde entier, ce qui présente des défis importants.

En revenant sur la détection des rayons gamma, bien qu'étant un domaine d'étude relativement nouveau, il a prouvé sa valeur pour étudier la nature du rayon cosmique. L'astronomie gamma a connu une évolution impressionnante qui abouti aux instruments sophistiqués d'aujourd'hui. Les détecteurs de rayons gamma au sol utilisent l'atmosphère comme un *calorimètre*. Différentes techniques ont été développées afin d'obtenir des informations sur le rayon gamma qui a déclenché la douche électromagnétique. Leur conception a été adaptée pour fournir de grandes zones de collecte jusqu'à $\sim$ km^2.

Une première division peut être faite entre deux approches différentes. La technique de détection basée sur la collecte de la lumière de Tcherenkov produite par les particules chargées de la douche d'air est connue sous le nom de technique d'imagination de la douche d'air de Tcherenkov, réalisée par les *Imaging Atmospheric Cherenkov Telescopes* (IACT). Une autre technique de détection possible des rayons gamma de haute énergie est basée sur l'échantillonnage direct des particules chargées de la douche par des détecteurs de particules, réalisés par des matrices de douche d'air étendues (EAS). Alors que les EAS arrays prennent un instantané des particules de la douche lors de leur passage à un moment donné, les IACTs permettent d'obtenir un *image* (empreinte dans la caméra) de la lumière de Tcherenkov émise lors du développement de la douche aérienne.

Les études et les résultats présentés dans cette thèse portent sur certaines des principales expériences en matière de rayons gamma. Actuellement, la couverture complémentaire des deux hémisphères par des IACTs est assurée par les trois observatoires terrestres de rayons gamma de deuxième génération H.E.S.S., MAGIC et

VERITAS. Les observatoires de rayons gamma au sol de deuxième génération utilisant la technique EAS sont représentés par l'expérience HAWC. S'appuyant sur le succès des installations actuelles mentionnées, plusieurs projets de nouvelle génération ont été développés au cours des dernières années. Un effort global a été fait par la communauté IACT, où l'expérience et les forces ont été fusionnées, ce qui a donné naissance au projet connu sous le nom de Cherenkov Telescope Array (CTA). Par rapport aux IACT actuels, il apporte une amélioration de la sensibilité d'un ordre de grandeur ainsi qu'un accès aux deux hémisphères grâce à sa conception à deux sites. Ces expériences ont des caractéristiques très différentes qui sont discutées en détail dans ce manuscrit, les avantages et les inconvénients sont présentés, en se concentrant sur le défi de suivre des sources explosives, montrant une variabilité temporelle.

Dans cette thèse, je me penche sur la motivation première de cette recherche : l'origine des rayons cosmiques pour passer plus tard à l'astronomie multi-messagers du point de vue des observatoires de rayons gamma. Je me suis principalement concentrée sur l'étude de l'Univers par l'emission de rayons gamma de très haute énergie et sur le lien avec l'astrophysique multi-messagers et multi-longueurs d'onde. Mon principal sujet de recherche est l'étude du lien entre les salves de rayons gamma (GRB) et les coalescences binaires compactes (CBC), et l'émission de rayons gamma de très haute énergie provenant de ces événements explosifs. Je me suis plus particulièrement concentré sur la recherche d'homologues électromagnétiques des coalescences binaires compactes produisant des ondes gravitationnelles avec des observatoires de rayons gamma de petit et grand champ de vue, dans les instruments actuels et de la prochaine génération. Ce travail a été présenté pour la première fois aux Rencontres de Moriond et publié dans les Actes de la Science (Seglar-Arroyo and Schüssler, 2017).

Dans les cas des observatoires de petit champ de vue, j'ai développé de nouvelles stratégies d'observation optimisées pour le suivi des GW, capables d'apporter une réponse rapide et compétitive aux alertes, en tenant compte des caractéristiques de l'événement GW et en maximisant les chances de détecter la contrepartie électromagnétique. Les algorithmes que j'ai développés tiennent compte non seulement des contraintes d'observation du site et de l'optimisation sur la sélection des coordonnées d'observation pour atteindre une couverture de faible énergie, mais aussi de la distribution des galaxies qui pourraient potentiellement accueillir l'événement cataclysmique.

Ce travail, qui a débuté au début de l'O2, nous a permis de réaliser un suivi efficace des ondes stationnaires aux rayons gamma de très haute énergie avec l'expérience H.E.S.S., du début de 2017 à aujourd'hui. Aujourd'hui, le planificateur de suivi des observations GW a été mis en place dans le système d'alerte H.E.S.S. et il est capable d'effectuer des suivis de manière automatique, chaque fois que les critères préétablis sont remplis. Néanmoins, l'équipe du CEA-Saclay et moi-même étudions attentivement les caractéristiques de chaque alerte d'onde gravitationnelle détectée par LIGO-Virgo et prenons la décision de déclencher des observations de suivi, dans les cas où l'alerte survient pendant la journée. Le programme de suivi des ondes gravitationnelles de la collaboration H.E.S.S. a été présenté à la 36e conférence internationale

sur les rayons cosmiques et il est décrit dans les Actes de la science correspondants (Seglar-Arroyo et al., 2019).

J'ai utilisé les algorithmes développés pour effectuer l'observation de suivi de GW170817. Cela a conduit à des observations de suivi réussies de la fusion d'étoiles à neutrons par H.E.S.S., qui a été le premier télescope au sol couvrant l'emplacement de l'homologue électromagnétique récemment identifié (Abbott et al., 2017c). L'analyse de ces observations de suivi des ondes gravitationnelles a fixé des contraintes sur l'émission du reste aux rayons gamma de très haute énergie, qui a été publiée dans Abdalla et al., 2017.

Dans le cadre de la collaboration HE.S.S., j'ai été au cours de ces trois dernières années un *expert de garde* pour le suivi de la GW. J'ai également été *expert de garde* du programme de suivi de la GRB ainsi que membre du groupe AGN sur les torchères. J'ai présenté l'état d'avancement du programme "Target-of-Opportunity" du groupe AGN lors de la 35e conférence internationale sur les rayons cosmiques (Seglar-Arroyo et al., 2017). Ce type de suivi et de programmes de cibles d'opportunité est essentiel pour répondre aux défis de l'astronomie multi-messager de forte variation temporelle.

Suite à ces activités, je dirige actuellement l'analyse de la première détection d'émission de VHE de l'AGN OT081. Cette source, classée comme le pic de bas synchrotron BL Lac, présente une émission à large bande qui a été difficile à modéliser avec les modèles plus simples de SSC à une zone d'emission, comme d'autres sources (comme AP Lib) avec un comportement intermédiaire entre deux6FSRQ et BL Lacs. Les observations obtenues sur les LMS, de la radio aux rayons gamma, ont permis de mieux comprendre la source et l'état de torchage. Ces travaux ont conduit à une analyse multi-longueurs d'onde en collaboration croisée, impliquant H.E.S.S., MAGIC et Fermi-LAT, qui sera publiée prochainement.

J'ai travaillé sur la recherche d'homologues électromagnétiques dans les suivis de GW dans un observatoire VHE différent, mais complémentaire, à large champ de vision : l'expérience HAWC. Dans le cadre de l'étude de la connexion GRB-CBC, j'ai rejoint le réseau d'observatoires astrophysiques multi-messagers (AMON) et je suis devenu membre de HAWC et membre associé de la collaboration LIGO. AMON se concentre sur l'exploitation des événements en dessous du seuil en réalisant des études de corrélation qui peuvent potentiellement conduire à l'identification d'événements astrophysiques. J'ai développé une nouvelle analyse multi-messagers qui combine les événements de vagues gravitationnelles avec les données HAWC, en effectuant d'abord une sélection spatiale et temporelle, puis une estimation de la probabilité sur l'origine de l'événement. J'ai utilisé cette technique pour les données LIGO-Virgo et HAWC obtenues pendant la période de la première série d'observation de LIGO-Virgo (O1) bien que, malheureusement, aucun événement GW+γ n'ait été identifié. La discussion de l'état actuel du réseau AMON par mes collègues et moi-même a été récemment publiée (Solares et al., 2020).

J'ai étudié les perspectives du télescope IACT de prochaine génération, le CTA,

sur les observations de suivi des ondes gravitationnelles et la détection potentielle de la contrepartie électromagnétique dans les rayons gamma de très haute énergie. Je me suis concentré sur l'adaptation et le développement ultérieur des algorithmes et de la stratégie de suivi des ondes gravitationnelles au programme d'ondes gravitationnelles du CTA, dans le but de relier les observations à l'analyse en temps réel. Dans ce contexte, je dirige l'effort de simulation complexe pour la préparation du CTA aux déclencheurs des ondes gravitationnelles. Cette étude détaillée part des simulations de fusions NS-NS et de la simulation de l'émission de la contrepartie GRB aux rayons gamma de très haute énergie, qui a été réalisée à l'aide de `Gammapy`. Ensuite, j'ai développé un pipeline d'analyse dédié `Gammapy` pour l'ensemble des données obtenues, où les observations couvrent de larges régions du ciel et où la source peut être située n'importe où dans le FoV. De plus, en raison de la nature du transitoire, les premières études ont été réalisées sur l'optimisation de la programmation des observations ainsi que des fenêtres temporelles en utilisant la simulation GRB basée sur des modèles phénoménologiques. Les connaissances acquises grâce à ces travaux comprennent le lancement des discussions sur les futures stratégies de suivi GW du CTA et la dérivation de taux de détection GW-EM communs. J'ai présenté les grandes lignes et les étapes de ces simulations lors de la 36e conférence internationale sur les rayons cosmiques (Seglar-Arroyo et al., 2019). Un document du consortium CTA comprenant les détails de ces simulations et les perspectives du CTA pour détecter les rayons gamma dans les observations de suivi des GW est en préparation.

Acknowledgements

The sum of the decisions that I took in my life brought me here. For this reason, I want to thank not only the people that accompanied me during these last 3 years, but to all the people that were part of this entire process. It has not been easy but at least it has been fun. I am grateful for all the opportunities in life and especially in the last three years; there have been very special moments where knowledge has been the main protagonist. Seeing the same enthusiasm for this field in the eyes of my collaborators and the desire to continue working to go further has inspired me enormously.

To Fabian Schüssler and Miguel Mostafa, my PhD supervisors, which believed in me to be part of this big project and have given me support during these 3 years. Working with you has been an extraordinarily inspiring process, where you have taught me what science is really like, that there is always things to learn and that there is never a bad time to ask further questions. I truly appreciate your guidance and vision, and hope that we can continue to collaborate for many more years to come.

To my colleagues at CEA Saclay, thank you for sharing your knowledge and experience with others, and of course, for making every meal more enjoyable. To my colleagues at Penn State University, thanks for all the moments; maybe the office cactus died, but I guess even a cactus doesn't survive without being watered. Thank you very much for welcoming me and for your work ethics. You are a reference for me; I wish you the best in your scientific careers. In the same way, I feel very grateful to have been part of the HESS, HAWC and CTA collaborations. These years I have learned from the best in the field, and I have been able to witness scientific discoveries that are memories that I will keep very warmly with me.

On a more personal note, I thank the supporters in my life, my family. If I have come this far, it is undoubtedly thanks to you. I thank my father for always going beyond and teaching me from a young age to question reality, to inspire in my brother and me the taste for science. I thank my mother for her integrity and human strength, for believing in me and for always being present. I thank my sweet brother, for his kindness and for putting up with the heaviest sister.

I also want to thank my childhood friends from my beloved *terreta*, where the best paellas are made, that I always carry in my heart. To my friends from the University, where this adventure in Physics began and with whom I spent the longest nights of study; I love you as siblings. To those who have accompanied me during these three years of my thesis and have been in my ups and downs; thank you. And to Jose, for never letting go and for sharing life as what it is; the best of adventures.

Contents

Part I

Very-high-energy astroparticle physics and the multi-messenger connection

Chapter 1

Astroparticle Physics

1.1 Introduction to Astroparticle Physics

1.1.1 The discovery of cosmic rays

The discovery of *cosmic rays* (CR) as charged nuclei coming from outer space took place a century ago. The beginning of the XX^{th} century was specially marked by the discovery of radioactivity, which initiated a revolution that had implications in many other fields of science. The discovery of this new property of matter and type of interaction lead scientists to observe that ionizing radiation, from an *unknown* source, was surrounding us. The quest for the identification of the origin of this ambient radiation made scientists hypothesize about its origin, with the natural radioactivity of the Earth as first candidate. Several experiments were carried in order to quantify the ionization dependency on the height above the surface, in order to test the later hypothesis, expecting to find higher ionization closer to Earth.

In 1912, Victor Hess used a balloon in order to measure the variation of ionization on his way up through the atmosphere showing that, after a first decline when leaving the Earths surface, the radiation actually increased with height, reaching an enhancement by a factor of 80 at 5000 meters. Through the following years, attempts were performed in order to obtain more insights on the nature of this *cosmic* radiation. It was not until 1933, that Rossi and Johnson independently confirmed that cosmic radiation was composed of charged particles, as they were bent by the Earth's magnetic field depending on their charge sign. A further major step was taken in 1937, when Pierre Auger discovered extensive atmospheric air showers by studying the coincidences of detectors placed several meters apart.

The interested reader on a deeper insight of the history of cosmic rays is invited to read the detailed review by Kampert and Watson, 2012.

1.1.2 Cosmic ray spectrum and mass composition

The spectrum of cosmic rays, in Figure 1.1, expands over 12 orders of magnitude in energy and 30 orders of magnitude in flux. The relationship between energy and flux can be described, in first approximation, as a power law $F \sim E^{\Gamma}$, where Γ varies with the energy range. These different values of Γ are linked to the underlying physical

process of particle acceleration in the source and to propagation effects.

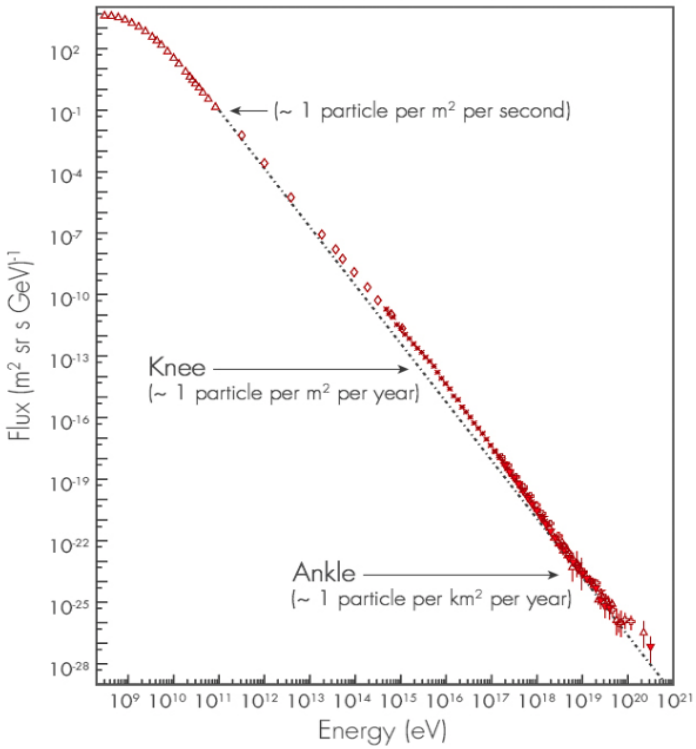

FIGURE 1.1: Differential energy spectrum of cosmic-rays expanding in several orders of magnitude in energy. Figure from S. Swordy, U. Chicago

The main spectral features observed in Figure 1.1 are known as the *knee* and the *ankle*. Recent, high precision observations have enabled the identification of more complex structures. These are known as the *second knee* or *iron knee*, an ankle-like feature between the knee and the second knee and the *cut-off*. These features are visible in Figure 1.2, where the high energy differential energy spectrum of cosmic rays from recent measurements, multiplied by a factor $E^{2.6}$, is shown through six orders of magnitude in energy (Patrignani et al., 2016).

The origin of the low energy part of the cosmic ray spectrum, until $E \sim 10^{10}$ eVs, corresponds to charged particles produced in sources in the nearest environment, as ordinary stars. The main contribution to this low-energy cosmic radiation comes from the closest-to-Earth star: the Sun. These low-energy charged particles interact in the upper atmosphere with the magnetic fields of the heliosphere and with the geomagnetic fields. As a product of the interaction, charged particles spiral into the Earth's magnetic poles, atoms in the atmospheric gas excite and produce impressive glows of various colors and complexities, known as *auroras*.

In the range between $E = 10^{15} - 10^{18.5}$ eVs, three spectral breaks, the *knee*, the *second knee* and the *ankle*, are observed.

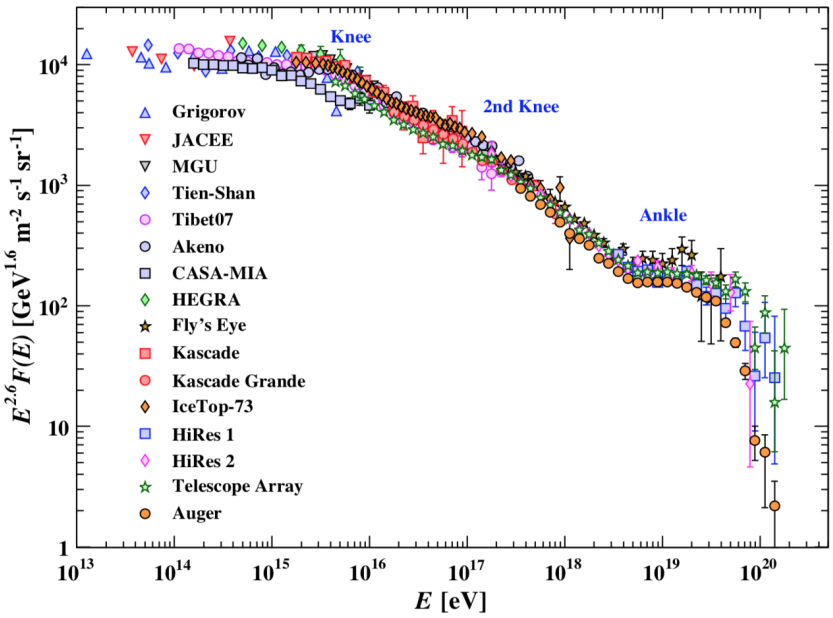

FIGURE 1.2: High energy range of the differential energy spectrum of cosmic-rays, as observed by various experiments, expanding in several orders of magnitude in energy. The differential spectrum has been multiplied by $E^{2.6}$ in order to enhance the main spectral changes. From Patrignani et al., 2016

The spectral break at the knee is due to light elements (Antoni et al., 2002). Two possible origin scenarios have been contemplated to explain the particle reaching the PeV energy scale. These energies can be the results of the inefficient confinement of the magnetic fields in the magnetic turbulent sea within the Galactic disk, mainly driven by supernova remnants (SNR), which gives rise to a steepening of the CR spectrum. Alternatively, they can point out to the maximum energy achieved by their sources in the galaxy, believed to be supernova remnants (SNRs). Observation of shell-type supernova remnants in X-ray and TeV energies provided evidence in favor of galactic cosmic rays being produced in shock acceleration at the outer boundaries of supernova remnants. Other sources, as high-energy stellar winds, pulsars, magnetars, microquasars, could contribute in a small percentage level (Hillas, 2006).

Regardless of the physical origin of the knee, a set of features corresponding to the particles of different rigidities, i.e. different nuclear species, is typically expected to be observed at higher energies compared to the features in the proton spectrum. The second knee, which is observed at $\sim$ 100 PeV could be explained as an *iron* knee-like feature, assuming that the composition of the knee is dominated by protons.

The interpretation of the second knee and its connection to the knee highlights the importance of the mass composition determination of cosmic rays. This is essential to unveil the physical origin of the discussed features and ultimately, the sources of cosmic rays. Observations have shown that the CR composition evolves with energy:

while at knee energies, the CR composition is still debated, at energies approaching the ankle, observations point towards a lighter composition that evolves with energy to a dominance of heavier elements at ultra-high energies (Batista et al., 2019).

Beyond the *second knee*, at $E = 10^{17} - 10^{18}$ eVs, the lack of anisotropy of cosmic rays points to an extragalactic origin, at least for the lighter components. In addition, there have been speculations on an additional *ankle*-like feature from observations made by the KASCADE-Grande experiment (Haungs, 2014).

At even higher energies, beyond $E = 10^{18}$ eVs, the first evidences for the origin of cosmic rays beyond the ankle was given by the large scale anisotropy observed by the Pierre Auger Observatory (Aab et al., 2017b). Further discussion of the possible candidates to be the sources of extragalactic cosmic rays will be presented in Section 1.2.2.

At the highest energies, a cut-off of the cosmic ray spectrum is observed whose origin is still under debate. In a first attempt to explain its origin, this flux suppression has been associated to the theoretical Greisen-Zatsepin-Kuzmin (GZK) limit, based on the interaction between cosmic rays and cosmic microwave background (CMB) radiation. In this scenario, protons lose energy due to photo-pion production via Δ resonance, whereas nuclei undergo photo-disintegration. Other possible explanation of the flux suppression is as a result of the limit on the acceleration, reached in UHECR sources. The most promising way to discriminate between these two hypotheses would be the identification of individual sources of UHECR (Batista et al., 2019).

1.2 Acceleration processes of charged particles

1.2.1 Charged particle acceleration

Observation of cosmic rays with extremely high energies indicates that these particles undergo important acceleration processes. Through the years, several mechanisms in diffusive particle acceleration have been invoked to account for such high energies. Amongst them, the most popular mechanisms are the *first-order* and *second order* Fermi acceleration mechanism, illustrated in Figure 1.3.

Second-order Fermi acceleration

In 1949, E. Fermi proposed the first theory of particle acceleration, which later was designated as the *second-order* Fermi mechanism. In the original version of the *second-order* Fermi acceleration mechanism, charged particles are accelerated stochastically to high energies through reflections by the irregularities of the magnetic fields of clouds, which act as *magnetic mirrors* (Fermi, 1949). An illustration of the mechanisms can be found in Figure 1.3.

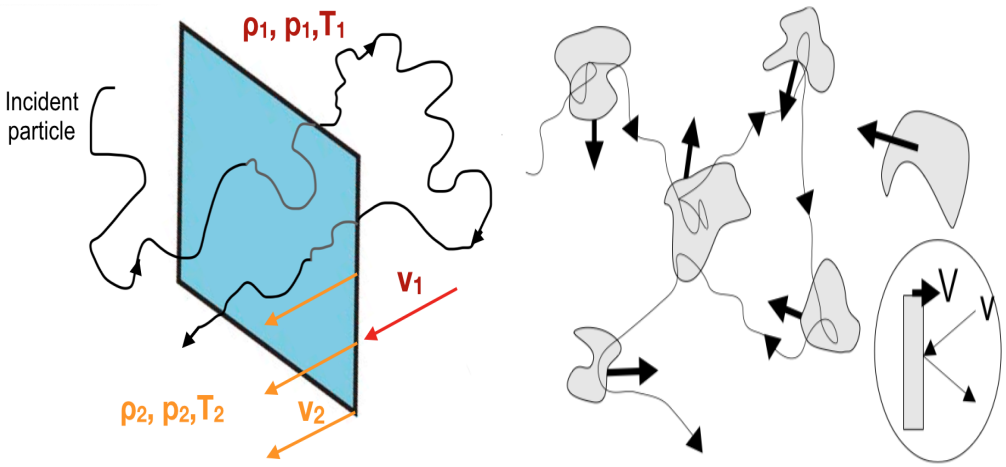

FIGURE 1.3: (Left) First-order Fermi acceleration where the acceleration is achieved in shock waves. (Right) Second-order Fermi acceleration, where the acceleration happens in the environment of moving magnetized gas clouds. Second figure from De Naurois, 2000

The particle undergoes a head-on collision with the cloud moving at velocity V, under angle θ between the particle and the normal of the surface. When the collision happens, the energy of the particle is conserved and the momentum in the x-direction is reversed. The transformation between relativistic frames enables the computation of the gain in energy over a cycle, which averaged out following the prescriptions in Longair, 2011, yields to an average energy gain per collision:

$$\left\langle \frac{\Delta E}{E} \right\rangle = \frac{8}{3} \left(\frac{V}{c} \right)^2 \tag{1.1}$$

which shows that the increase in energy of the particle goes with the *second order* in V/c. This original form of the Fermi mechanism presents low efficiency on accelerating particles due to the low amount of collisions expected in interstellar clouds, leading to a slow particles acceleration mechanism.

First-order Fermi acceleration

The *first-order* Fermi acceleration or *diffusive shock acceleration* was independently proposed in the late 1970s (Axford, Leer, and Skadron, 1977, Krymskii, 1977, Bell, 1978, Blandford and Ostriker, 1978). In this mechanism, illustrated in Figure 1.3, the particle acceleration takes place in strong shock waves and is first order in the shock velocity. Shock wave acceleration consists of a transfer of energy from macroscopic motion to microscopic particles through the interaction of those particles with magnetic inhomogeneities, which are typically present in shock waves.

Let us consider a charged particle crossing the shock front back and forth, changing the reference frame at each shock crossing. In the upstream reference frame, the shock front is approaching at a velocity v_1 and v_2 refers to the shock gas velocity in

the shock-front reference frame. The speed difference between them is $\Delta v = v_1 - v_2$, which is also the velocity of the shock front in the upstream reference frame V. After a cycle of shock-wave crossing, the reference frame changes translate to an increase in the energy of the particle, measured in the same local frame.

The increase in energy of the particle of speed v and initial energy E, after a cycle of shock-wave crossing, considering that the particles are relativistic and have an energy $E = pc$ and momentum in the x-direction $p_x = (E/c)\cos\theta$, can be expressed as:

$$\Delta E = E\frac{v_1 - v_2}{v}\cos\theta = pV\cos\theta \qquad \frac{\Delta E}{E} = \frac{V}{c}\cos\theta \tag{1.2}$$

where θ is the incident angle of the particle onto the shock-wave. The average energy increase gained when the particle crosses the shock wave is obtained by considering the crossing probability which is proportional to $\cos\theta$ and averaging over the incident angles, as:

$$\left\langle \frac{\Delta E}{E} \right\rangle = \frac{V}{c}\int_0^{\pi/2} 2\cos^2\theta \mathrm{d}\cos\theta = \frac{2}{3}\frac{V}{c} \tag{1.3}$$

which shows a dependency of *first order* with V/c. The fractional energy is the average energy increase over a full shock-wave cycle, expressed as:

$$\left\langle \frac{\Delta E}{E} \right\rangle = \frac{4}{3}\frac{V}{c} \tag{1.4}$$

The energy increment of the particle is the same every time it crosses the shock-wave, independently of the direction of the crossing between the downstream and upstream. The shape of the energy spectrum of the accelerated particles can be obtained making some considerations on the escape probability of the particle.

Following Longair, 2011(based on Bell, 1978), the probability that the particle remains within the accelerating region after one collision P can be expressed as $P = 1 - \frac{4}{3}\frac{v_1 - v_2}{v} = 1 - \langle\frac{\Delta E}{E}\rangle$, so after n cycles, the probability is expressed as $P^n = (1 - \langle\frac{\Delta E}{E}\rangle)^n$. The number of particles after n collisions evolves as $N = N_0 P^N$ particles with energies $E = E_0\beta^n$, with β defined as $\beta = 1 - \langle\frac{\Delta E}{E}\rangle$. One can define the ratio between these two quantities as:

$$\frac{ln(N/N_0)}{ln(E/E_0)} = \frac{ln(P)}{ln\beta} \qquad \rightarrow \qquad \frac{N}{N_0} = \left(\frac{E}{E_0}\right)^{lnP/ln\beta} \tag{1.5}$$

In first-order Fermi acceleration, the differential energy spectrum of the high energy particle is naturally described by a power-law spectrum as:

$$N(E)dE \propto E^{-1+(lnP/ln\beta)} \quad \text{where} \quad \frac{lnP}{ln\beta} \simeq -1 \tag{1.6}$$

Hence, the energy distribution of the number of accelerated particles follows a power law spectrum of index -2. This result also implies that such power-law energy

spectra with a particular spectral index can be expected to be valid in multiple astrophysical environments. Such strong shocks can be found in supernova remnants, active galactic nuclei and extended components of extragalactic radio sources, which could be then sources of high energy particles.

The maximum energy achieved mainly depends on the physical conditions of the cosmic accelerator which are the energy losses, age and geometry of the system. The acceleration time needed for a particle to reach a given energy can be computed from the diffusion time in both the downstream and the upstream media, the magnetic fields, the diffusion regime and the velocity of the shock wave (Reynolds, 1998).

1.2.2 Astrophysical acceleration site candidates

In order for particles to accelerate up to the highest energies by non-exotic acceleration processes, they need to be confined, at least partially, in the acceleration region. This confinement requirement implies that the Larmor radius of the particle that is being accelerated should be smaller than the size of the accelerating region. Once the particle reaches a certain energy at which the magnetic field is not able to confine it anymore, the particle escapes the accelerator. Hence, the potential acceleration sites need to fulfill the set of conditions established by Hillas (Hillas, 1984).

The confinement condition of this Hillas criterion establishes the relationship between the maximum energy of a particle of charge Z_e, the size of the acceleration region R, the strength of the magnetic field B of the object, the velocity β of the accelerating shock wave, in speed of light units, and the efficiency of acceleration η.

$$E_{MAX} = \eta \beta Z_e B R \tag{1.7}$$

The maximum achievable acceleration efficiency is expected for diffusive processes occurring at the ideal Bohm limit (Malkov, 1997), for which η=1. In addition to the confinement condition, the maximum energy at which the CR is accelerated depends on further details of the acceleration mechanism and the adiabatic energy losses in the source environment.

The illustration of this condition is shown in the well-known Hillas diagram in Figure 1.4.

The energy reached by an accelerated particle for a given magnetic field B and region R can be at a first approximation, for values $\eta = 1$, estimated as $E_{MAX} \sim BR$ which is represented in Figure 1.4 as red/blue lines for proton/iron nuclei at $E = 10^{20}$ eV, where two different values for the velocity of the shock β have been considered. In this way, although a variety of astrophysical objects are shown in the Hillas diagram, only those lying *above* the diagonal line can accelerate particles to such high energies. Note however that the condition established by Hillas is necessary yet not sufficient for those astrophysical sites to be acceleration sites.

Another condition on the *potential* acceleration sources is given using similar arguments on the energy budget to produce the observed UHECR diffuse flux. Although the energy production rate of UHECR depends on several source parameters as the spectrum and composition, estimates have been recently derived from data obtained at the Pierre Auger Observatory (Aab et al., 2017a). In the right panel of Figure 1.4, these estimates, assuming different relationships between the luminosity of CRs and their radiative luminosity are plotted. In the same figure, different *candidate* source classes are included, whose energy budget is based on observations throughout the electromagnetic (EM) spectrum (Batista et al., 2019).

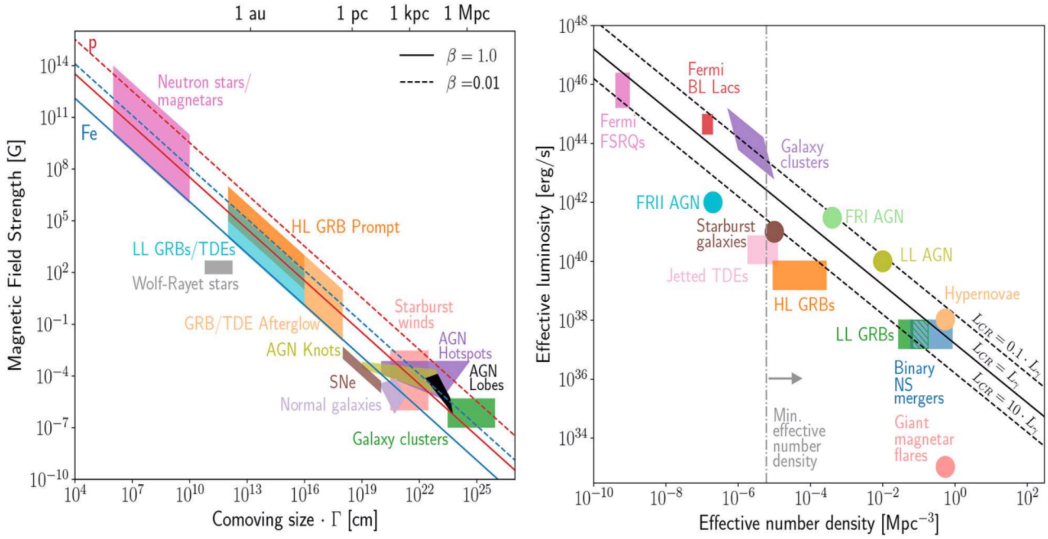

FIGURE 1.4: (Left) Hillas diagram where sources have been plotted as function of their characteristic size, R and their magnetic field strength, B, assuming the most optimistic value for the accelerator efficiency $\eta = 1$. Diagonal lines set the values of the product BR for which the confinement condition is satisfied for two different species: proton (red) and iron (blue). (Right) Potential acceleration sources where steady and transient sources are plotted as a function of their characteristic source luminosity and the source number density. Diagonal values correspond to the energy production rate of UHECR derived in (Aab et al., 2017a). From Batista et al., 2019.

The acceleration site candidates include a large variety of astrophysical objects, as observed in Figure 1.4. Galactic cosmic rays, as previously noted, are thought to be accelerated via first-order Fermi processes in supernova remnant shocks. After the supernova, ejected material expanding from the explosion propagates outwards and interacts with the interstellar medium creating a shock wave. Other galactic accelerators, although the accelerated particle would be less energetic, are pulsars, pulsar nebulae and colliding wind binaries, where the collision of two massive stars results on a persistent shock and acceleration of particles. Pulsars are highly magnetized, rapidly rotating neutron stars formed when the core of a massive star is compressed during a supernova, which continuously emit electromagnetic radiation due to the rotation of the strong B-field. Particles can be accelerated on the surface due to these high magnetic fields, propagate as a particle *wind* and further interact with the

rest of the supernova, the nebulae..

The principal extragalactic candidate sites which may be able to accelerate charged particles range from compact objects as neutron stars, white dwarfs or gamma-ray bursts (GRBs), to large scale structures as merging galaxies, or merging galaxy clusters, processes in Active Galactic Nuclei (AGNs) either in the core or the jets, hot spots of Fanaroff-Riley class II (FR-II) radio galaxies and starbursts galaxies. In the following, I will concentrate on AGNs and GRBs.

Active Galactic Nuclei have been considered to be potential acceleration sites, with acceleration taking place either in the jet, hot spot of AGNs, and/or in AGN cores (Kotera and Olinto, 2011). In particular, in jetted AGNs, the sub-parsec scale extension of the lobes and the magnetic fields of the order of several Gauss, could potentially allow protons to be accelerated to few tens of exa-electron volts (EeVs, 10^{18} eV). For this reason, the AGN subclass whose jets points towards the Earth, known as *blazars*, would be potential candidates to UHECR accelerators. Exploiting the connection between CR acceleration and the associated production of gamma-ray photons, observations of blazars in gamma-rays are thought to bring light in the acceleration of UHECR. This relationship is the underlying motivation of the work developed in Chapter 3. Other popular UHECR acceleration candidates are jetted AGNs whose jet is pointing out of the line of sight, known as radio galaxies, such as Cen A (e.g. Rachen and Biermann, 1993).

Gamma-ray bursts, due to their extreme brightness, do satisfy the minimum energy budget to be sources of UHECR, including several types of GRBs, from high-luminosity GRB to low luminosity GRBs. In GRBs, the acceleration size is smaller than a parsec, and thus, very high magnetic fields are required. In the case of GRBs, magnetic fields are more than 12 orders of magnitude higher than the Earth's magnetic field in its surface, which is of 0.25-0.65 Gauss (Finlay et al., 2010).

The most popular progenitors of *short* GRB are neutron star mergers (Blinnikov et al., 1984). Recently, after the first observation of an electromagnetic counterpart of a neutron star merger (Abbott et al., 2017a), it was proposed that this class of sources could be the accelerators of cosmic rays observed below the ankle (Rodrigues et al., 2019).

1.3 The high-energy Universe through multi-messenger astrophysics

The charged nature of cosmic rays implies a temporal shift with respect to the time when they have been produced, as well as a spatial shift, caused by the magnetic fields that modify the trajectory of the particles in their way to Earth (Waxman, 2004). The uncertainties on the measurements of galactic magnetic fields and extragalactic magnetic fields, together with the fact that recent observations on the UHECR composition point to a composition domination of heavy nuclei (Bellido, 2017), make

UHECR astronomy remarkably challenging even beyond E$\sim 10^{19}$ eV.

In this scenario, and unless light primaries are selected for astronomy, the study of acceleration sites has been partially shifted from cosmic-ray observations to indirect cosmic-ray production-site observations through multi-messenger astrophysics. This includes three fields of research and their intersections: astrophysical neutrino observations, gravitational wave observations and electromagnetic observations. In these three science fields, the issue of the interaction of the messenger in its way to Earth is avoided. Due to the non-charged nature of the messenger, as well as their massless (low mass, for neutrinos) properties, they propagate in straight lines at (nearly) the speed of light.

Multi-messenger astrophysics can be seen as the natural next step forward in astrophysics, where events are not only observed in *isolated* wavelengths. With the experience of multi-wavelength astrophysics in mind, it is clear that studying and interpreting each confined channel does no longer hold. Multi-band approaches to long standing questions have been used in many domains, from high energy accelerator physics where electromagnetic, weak and strong interactions are in place, to the way we explore the world with our five senses.

Multi-messenger observations are able to provide information about particle production processes in the sources, which enable their physical description, the study of the cosmic evolution of source populations and various propagation effects both in Extragalactic and Galactic environments.

1.3.1 The Universe through weakly interacting neutrinos

Neutrinos are very-light, elementary particles which are electrically neutral and known to *weakly* interact with matter. They are produced *naturally* in nuclear reactions like fusion in the core of stars or *artificially* in nuclear reactors and particle accelerators. They are also created through radioactive decays of atomic nuclei and hadrons. In a broad astrophysical context, neutrinos are produced in charged particle acceleration sites, since charged particles can decay to neutrinos of very high energy.

In 1987, the beginning of multi-messenger astrophysics was set with the observation of the supernova SN1987 (Hirata et al., 1987). Not only was the luminosity of the supernova measured in different wavelengths; two to three hours before the visible light reached Earth, a burst of neutrinos was independently identified in three neutrino observatories: INR Baksan (Alexeyev et al., 1988), IMB detector (Haines et al., 1988) and Kamiokande-II (Hirata et al., 1988). For this same event, first attempts were made to search for coincident gravitational waves and neutrinos (Amaldi et al., 1989).

The main production of neutrinos in cosmic accelerators is due to photo-hadronic interaction or $p - p$ interaction, summarized in Equations 1.10, 1.11 and 1.12. After the neutrino is produced, weak interaction of these particles with matter allows them

to escape from dense environments, which would be opaque to photons. For this same reason, they can also travel large distances in the Universe without interacting, which enables the study of broad types of cosmic accelerators at different distances, even though without reach for other messengers. Nevertheless, this exceptional feature is at the same time the main challenge of neutrino detection.

A summary of the cosmic accelerators which are believed to be neutrino sources is found in Figure 1.5.

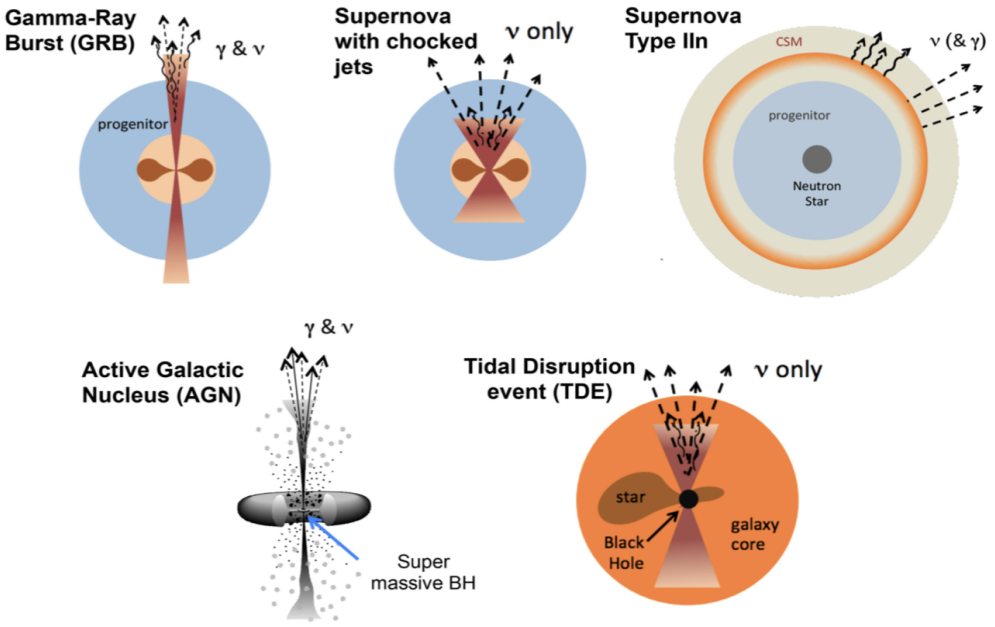

FIGURE 1.5: Illustration of the cosmic events where production of neutrinos is expected. Other messengers such as photons, cosmic rays and gravitational waves are emitted as a result of those events. From Bartos and Kowalski, 2017

1.3.2 The Universe through the ripples of space-time

Einstein's general theory of relativity (Einstein, 1916) states that that massive objects modify the curvature of space-time, creating gravitational fields around them. When a massive object accelerates, it creates a perturbation in the curvature of space–time around it. These *ripples* of space-time which propagate away from the astrophysical source are known as *gravitational* waves.

Gravity is the weakest of the four fundamental forces of physics, and only the most violent cosmic events produce *measurable* gravitational waves: very massive, rapidly accelerating objects.

A primary source of gravitational waves are colliding compact objects, which reach rapid accelerations as they get very close to each other until they merge. In the NS-NS merger scenario, the neutron star material surrounding the newly formed

black hole can accrete onto it, supplying the matter that will be accelerated to high velocities. These compact binary mergers, producing gravitational waves, have been long proposed to be linked to origin of GRBs (Blinnikov et al., 1984) and thus candidate to be cosmic accelerators. In addition to the expected electromagnetic emission up to gamma-ray energies, high-energy neutrino emission is expected too.

A second source of gravitational waves are core collapses of massive stars, where if the fall of matter is neither spherically nor axially symmetric, in-falling matter may emit gravitational waves. Otherwise, symmetric acceleration effectively cancels out any GW emission. This event is associated with GRB emission (Heger et al., 2003) and with neutrino production as well. An illustration of the mentioned processes can be found in Figure 1.6.

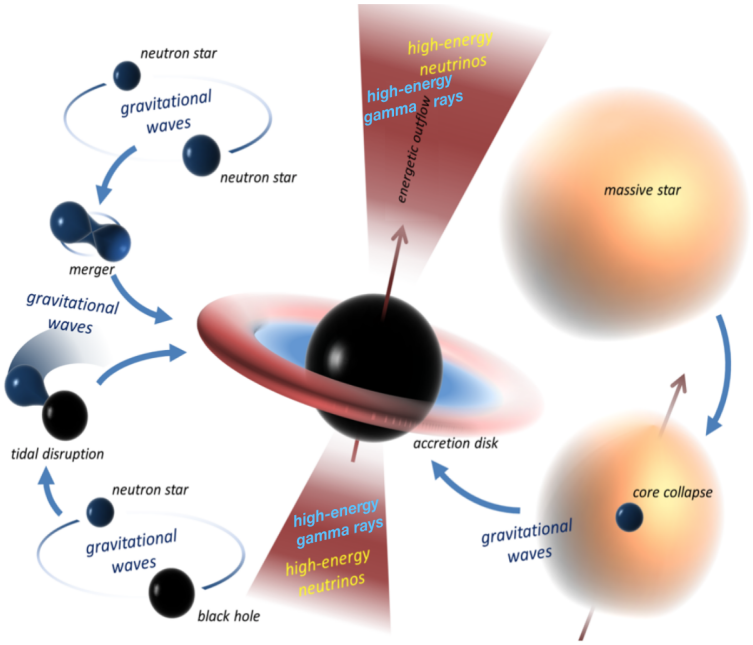

FIGURE 1.6: Illustration of the multi-messenger emission from the merger of compact binary objects and a stellar core collapse. Emission includes: gravitational wave, gamma-rays, neutrinos and cosmic rays. Modified from I. Bartos

In this thesis, a particular focus lays on the intersection between gravitational wave and gamma-ray emission. Further details on compact binary coalescences, expected counterparts and detection methods will be given Chapter 4.

1.3.3 The Universe through multi-wavelength photons

Historically, astronomy has mainly focused on the electromagnetic spectrum, in particular in the visible range. Broad-wavelength coverage of the electromagnetic emission from a source provides deep insights in many astrophysical objects and phenomena as it carries the signatures of the several astrophysical processes at play. As an

example, multi-wavelength observations of the Crab Nebulae from radio to gamma-rays are provided in Figure 1.7, where the wavelength and the energy corresponding to each observation are quoted.

A general division in the emission in the electromagnetic spectrum can be done into thermal radiation and non-thermal radiation. In thermal processes, molecules, atoms and ions are heated up in plasmas, creating photons of increasing energies. Thus, the thermal emission originates from the random movement of particles and it is associated with a certain temperature. In contrast, non-thermal processes, consist on the acceleration of particles though the acceleration processes mentioned in Section 1.2.

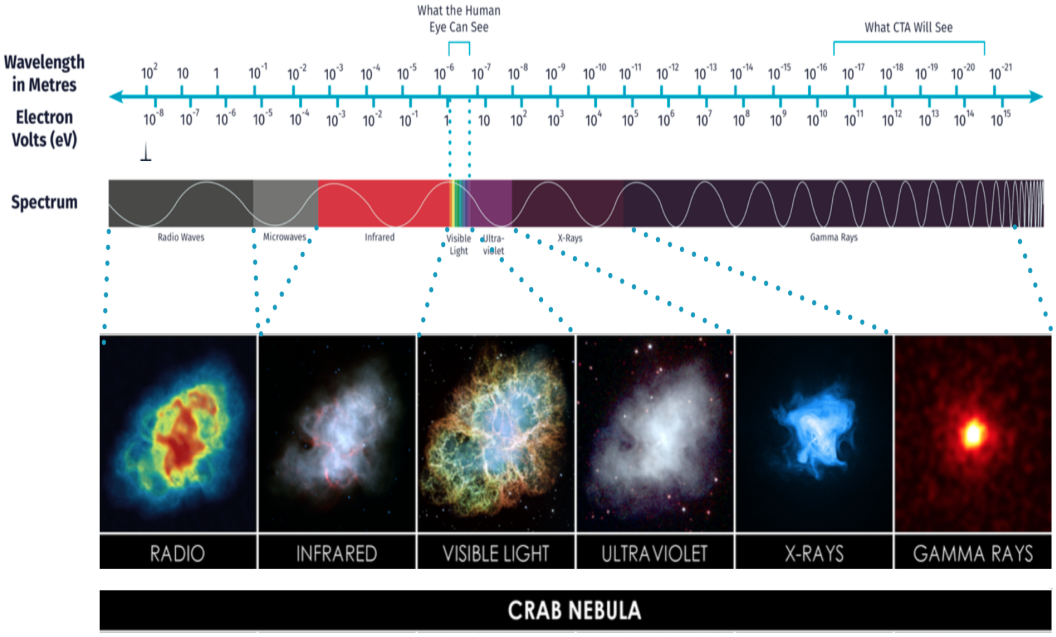

FIGURE 1.7: Multi-wavelength observation of the Crab Nebulae where a label on the energy, wavelength and spectrum has been included for reference. Modified from `https://commons.wikimedia.org` and `www.cta-observatory.org/science/`.

In the case of radio emission, thermal processes do not produce appreciable amounts of emission, so non-thermal processes are dominant. Radio emission is often found as the result of the interaction between a particle outflow and the surrounding gas. This type of processes can be found in AGN jets or in the interaction of outflows of GRBs with the interstellar medium. The resulting radio emission is potentially detectable at long timescales of $\sim$ years after the short initial burst.

Most of the optical emission is produced through thermal processes. Focussing on violent processes, this emission is present for instance in the photosphere of core collapse supernova, in accretion disks around supermassive black holes and also as a product of neutron star mergers, in the *kilonova* emission. In these events, a strong

electromagnetic radiation, mainly in near-infrared bands, is produced due to the decay of the heavy elements formed through the nucleosynthesis of the neutron-rich material ejected.

X-ray emission is expected in astronomical objects containing hot gases at temperatures that range from 10^6-10^9 kelvins, but also in non-thermal processes. For example, as a relativistic jet expands from its source, it interacts with the interstellar gas and creates a shock wave in the gas, which produces X-ray photons. The energies of the produced photons will decrease to optical and eventually to radio energies, as the jet slows down. This process is observed in the afterglow emission of GRBs.

The last window in the electromagnetic spectrum when going to higher energies, starting from $\sim$ 100s of keVs, corresponds to gamma rays. The production of gamma-ray photons is non-thermal and it is directly linked to the acceleration of charged particles. The common thread of this thesis work is the study of very-high-energy gamma-ray emission. In the following we will focus on several aspects related to this wavelength range.

1.4 Gamma-ray production processes

The physical processes taking place in cosmic ray acceleration sites directly link the production of accelerated cosmic rays and the charged particle population to the production of gamma-ray photons. These photons are produced in non-thermal interactions where cosmic rays gain energy by acceleration processes. In this way, gamma rays give accessa to the highest energy phenomena in the Universe.

1.4.1 Leptonic processes

The leptonic processes considered here are those which include electrons, the lightest charged lepton of the standard model. The three possible emission processes can be generalized as $e\gamma \rightarrow e\gamma$ type processes, and are described below.

- Deceleration radiation or *Bremsstrahlung*: Electromagnetic radiation is emitted when a charged particle is deflected and decelerated by the electric field of the atomic nucleus. This is a particular case of Compton scattering of a virtual photon of the Coulomb field of the scattering charge (Blumenthal and Gould, 1970). The energy spectrum of the emitted photons shows the same behavior than the spectrum of the injected charged particles (Longair, 2011). However, in many astrophysical sources, due to the low density of the region, the emitted photon flux is not enough for this interaction to be dominant.

- Synchrotron radiation: The Lorentz force acts on charged particle of mass m, charge q and velocity v when they interact with an external magnetic field B. The charged particle is accelerated radially and photons are emitted as a result,

through the so-called synchrotron process. The energy of the photon emitted by an electron of energy E_e is given by:

$$E_\gamma = 0.67\,\mathrm{eV}\left(\frac{E_e}{1\,\mathrm{TeV}}\right)^2\left(\frac{B}{1\,\mathrm{nT}}\right)\sin\theta \tag{1.8}$$

where θ is the angle formed by the velocity vector and the magnetic field orientation (Longair, 2011). The energy of the photons produced by a synchrotron process depend linearly on the environmental magnetic field. The spectral distribution of the emitted photons through synchrotron radiation depends on the energy spectrum of the electron population: for an electron population following a power law $N(E_e)\,dE_e \propto E_e^{-\alpha_e} dE_e$, the differential spectral distribution of the emitted photons follows a power law $dN/dE_\gamma \propto E_\gamma^{(1+\alpha_e)/2}$.

The energy spectrum of synchrotron radiation for population of electrons with different energies, following a power law distribution, is given by the sum of all the emitted spectra. This effect is shown in Figure 1.8. For a population of electrons with an energy distribution following a power-law of index n, the emitted spectrum obtained from the sum of spectra at different energies follows a power-law $F \sim \nu^\alpha$, with $\alpha = (n-1)/n$ (Longair, 2011).

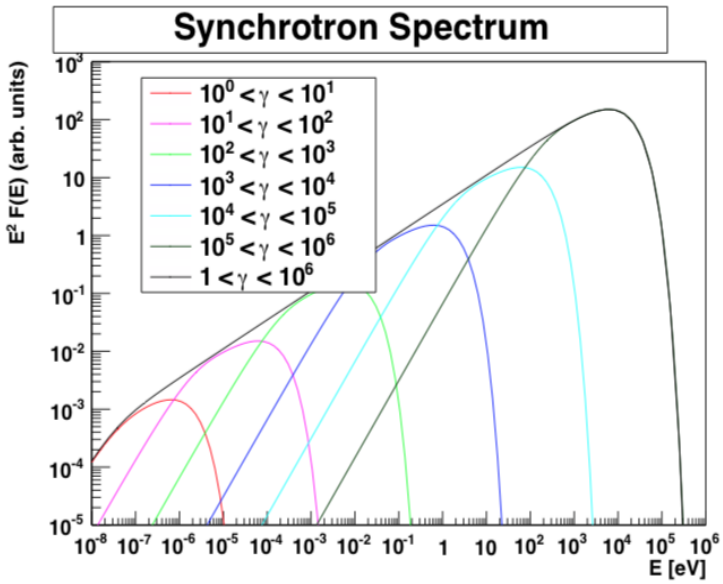

FIGURE 1.8: Energy distribution of synchrotron radiation emitted by a population of electrons at different energies, following a power law from De Naurois, 2012

The synchrotron radiation emission can be observed from radio to high energies, where the limit is set by the maximum energy that the electron population can achieve.

- Inverse Compton radiation: The Inverse Compton process takes place when an ultra-relativistic charged particle scatters a low energy photons to high energies. In this way, the loss of energy in the charged particle is gained by the photon. Two different regimes can be defined, depending of the energy of the incident photon E_γ in its reference frame. At low energies, when the energy of the incident photon is $E_\gamma < 2m_e\,c^2$, the probability of scattering can be described by the Thompson scattering cross section, σ_T=0.66 barns. However, at higher energies of the incident photon, relativistic and quantum mechanical effects should be taken into account in order to compute the cross section of the interaction. This cross-section derived by Klein and Nishina (Klein and Nishina, 1929), decreases with energy and is given in Equation 1.9, where $\alpha = E_\gamma / m_e\,c^2$.

$$\sigma_{KN} = \frac{3}{4}\sigma_T \left[\left(\frac{1+\alpha}{\alpha^2} \right) \left(\frac{2(1+\alpha)}{1+2\alpha} - \frac{\ln(1+2\alpha)}{\alpha} \right) + \frac{\ln(1+2\alpha)}{2\alpha} - \frac{1+3\alpha}{(1+2\alpha)^2} \right] \tag{1.9}$$

The differential spectral distribution of the photons emitted by Inverse Compton scattering by a population of electrons following a power-law distribution $N(E_e)\,\mathrm{d}E_e \propto E_e^{-\alpha_e}\,\mathrm{d}E_e$, takes the form $\mathrm{d}N/\mathrm{d}E_\gamma \propto E_\gamma^{(1+\alpha_e)/2}$.

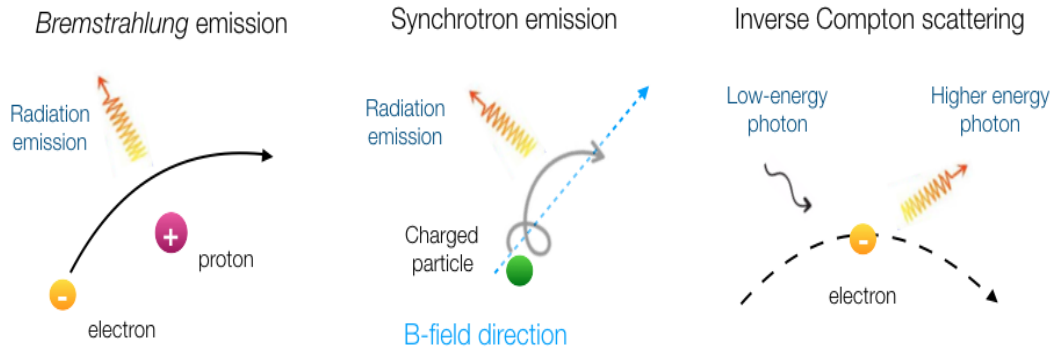

FIGURE 1.9: Illustration of the leptonic process of gamma-ray production, including *bremstrahlung*, synchrotron radiation production and inverse Compton emission.

1.4.2 Hadronic processes

Hadronic processes by definition are those that include an hadron, which is a composite of two or more quarks. In the following, the main interactions of the *proton* which lead to the production of gamma-rays are discussed.

- Pion decay: When hadronic particles are accelerated and collide inelastically with other hadronic particles, pions are produced as result. The simplest case is proton-proton interaction:

$$p + p \rightarrow p + p + (\pi^-, \pi^0, \pi^+) \tag{1.10}$$

where (π^-, π^0, π^+) are produced in similar amounts. Pions are also produced in photon-hadron interaction, as:

$$\begin{aligned} p + \gamma \rightarrow \Delta \rightarrow p + \pi^0 \quad (p = 2/3) \\ p + \gamma \rightarrow \Delta \rightarrow n + \pi^+ \quad (p = 1/3) \end{aligned} \tag{1.11}$$

Regarding pion decay, while charged pions decay into charged leptons and neutrinos, neutral pions create gamma-rays.The neutral pion π^0, lighter than its charged versions, disintegrates rapidly due to its short mean lifetime of $\sim 10^{-17}$ seconds to two photons, each of them with a mass in the center of mass reference system of $E_\gamma = m_{\pi^0}/2 = 135.0$ MeV$/2 \simeq 67.5$ MeV. These neutral and charged pion decays go as:

$$\begin{aligned} &\pi^0 \rightarrow \gamma + \gamma \\ &\pi^+ \rightarrow \mu^+ + \nu_\mu \rightarrow e^+ + \bar{\nu}_\mu + \nu_\mu + \nu_\mu \\ &\pi^- \rightarrow \mu^- + \bar{\nu}_\mu \rightarrow e^- + \nu_\mu + \bar{\nu}_\mu + \bar{\nu}_\mu \end{aligned} \tag{1.12}$$

This production mechanisms open the door to multi-messenger astrophysics of neutrinos and electromagnetic emission, as neutrinos provide a smoking gun for the identification of hadronic interactions. Further gamma-rays can be produced from charged pions, as these are created by radiation mechanisms of charged leptons, as previously explained. The spectrum of the produced γ-rays presents an overall similar shape than the spectrum of the primary protons, with a bump at the previously mentioned E_γ resulting from the π^0 decay.

- Synchrotron emission: Protons can radiate photons through synchrotron emission in the presence of magnetic fields. Nevertheless, the emission of synchrotron radiation shows a quartic dependency on the mass of the accelerated particle, as m^{-4}. Considering the ratio between m_e/m_p to be $\sim 10^3$, this contribution will be less important than the one expected for leptonic synchrotron emission.

1.4.3 Beyond the Standard Model processes

Besides the standard emission processes mentioned above, other *exotic* processes of photon production in the Universe have been proposed in order to alleviate limitations of the Standard Model of particle physics and in cosmology. Weakly interacting massive particles (WIMPs) have been proposed to constitute dark matter. WIMPs are thought to annihilate or/and decay, producing different types of standard model particles, with photons amongst them. The spectrum and intensity of a gamma ray signal is computed using phenomenological models and depends on the annihilation products.

1.4.4 Propagation effects: The gamma-ray horizon

TeV photons produced in extragalactic sources travel through diffuse photon fields which are present in the interstellar and intergalactic medium. They are said to *tell the history of the universe* since they are the results of the evolution of our Universe at different timescales.

The photons observed from the Cosmic Microwave Background (CMB) are a remnant of the processes that took place early after the Big Bang, at the epoch of recombination (z=1100) when light and matter decoupled. They are largely studied in cosmology. Other photon fields of different wavelengths are the results of processes occurring after reionisation (z=10) until the closest galaxies, from the diffuse sources to the resolved sources. The spectrum of the CMB and these additional diffuse photon fields, from radio to gamma energies, is shown in Figure 1.10.

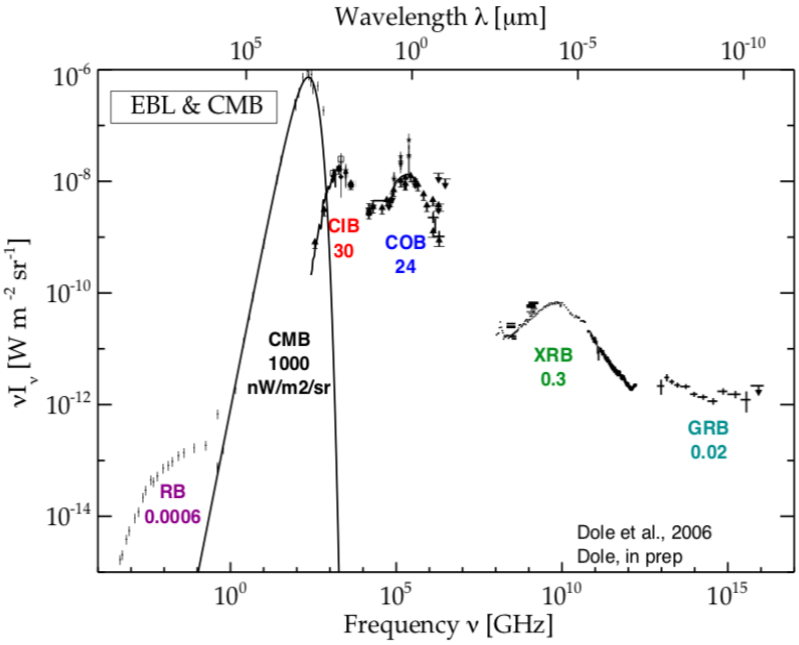

FIGURE 1.10: Intensity representation of the spectral energy distribution of the diffuse extragalactic photon fields from radio to γ frequencies ν. From Dole, 2010

As the Universe is filled with these diffuse photon fields, they are likely to interact with the VHE gamma rays traveling towards Earth. The interaction probability depends on the energy of the particle and the distance to be travelled, i.e the redshift of the gamma-ray source. In the case of TeV photons, the main candidates for interaction are diffuse photons at optical and infrared energies. They are grouped under the same name and known as *Extragalactic Background Light* or EBL. The attenuation effect of the EBL absorption in GeV-TeV gamma-ray energies between the detected flux and the intrinsic flux, is given as:

$$F_{det} = F_{int} \times e^{-\tau(E,z)} = F_{0,int}(E/E_{0,int})^{-\Gamma_{int}} \times e^{-\tau(E,z)} \tag{1.13}$$

where τ represents the optical depth, is shown in Figure 1.11.

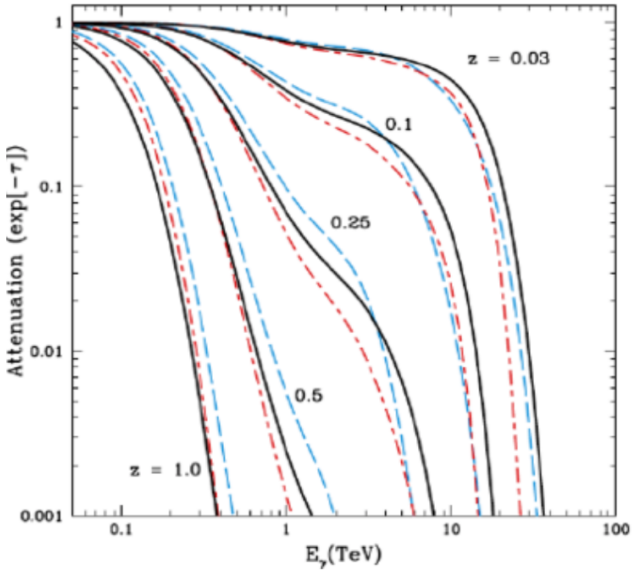

FIGURE 1.11: Attenuation of GeV-TeV gamma-ray flux by EBL absorption for five different redshift values. From Primack et al., 2011

Other possible contributions which could affect the VHE imprint of distant sources are Lorentz Invariance Violation (LIV) processes. These have been proposed in the context of several quantum gravity and effective field theories (e.g. Nambu, 1968, Kostelecký and Samuel, 1989). The strongest limits put so far in LIV processes have been obtained by studying the modification in photon propagation at different energy that LIV fosters, to which the broad-band emission of blazars would be sensitive.

1.5 Gamma-ray detection techniques

Gamma radiation was discovered by P. Villard in 1900 when studying the radiation emitted by radium. This penetrating electromagnetic radiation is issued by the radioactive decay of an atomic nucleus. The name to this strongly penetrating radiation was given by Ernest Rutherford, in the context of the previously discovered decay radiations, e.g. *alpha* radiation and *beta* radiation. Gamma radiation consist of photons with the highest energies, which corresponds to the shortest wavelengths of the electromagnetic spectrum.

Gamma-ray astronomy starts around $\sim$ 100 keVs and covers up to 9 orders of magnitude in energy. Various detection techniques have been developed in order to cover this broad energy range.

At low energies, below $\sim$ 30 MeV, detectors are based on the photo-electrical effect or Compton effect. Then, in the range up to several GeVs, known as *high-energy* (HE)

gamma rays, the detection is based on pair production, a technique typically used in gamma-ray satellites. Above several GeVs, the energy range is known as *very-high energies* (VHE). Typical astrophysical sources have gamma-ray fluxes whose dependency with energy goes as $\mathrm{d}N/\mathrm{d}E \simeq E^{-2}$, as shown above. Thus, as the gamma-ray energy increases, the effective area of the detector needs to increase as well, in order to compensate for the decrease in gamma-ray flux.

Consequently, as gamma-ray satellites effective detection areas for energies above 100 GeV are not large enough, in the order of the $\sim \mathrm{m}^2$, new techniques are needed. The air shower produced by a very-high-energy gamma ray can be observed with ground-based detectors, which use the atmosphere as a *calorimeter*.

1.5.1 Atmospheric Air Showers

Very-high-energy gamma rays are produced at an astrophysical source and then travel all the way to Earth, as described in Section 1.4.4. The atmosphere shields the Earth from gamma rays, a positive aspect for living organisms as these are biologically hazardous due to their ionizing nature.

For a high energy photon (MeV or higher), the dominant interaction process with matter is electron-pair production near the nucleus. The incident photon interacts in the upper atmosphere with the Coulomb field of the nucleus to produce an electron-positron pair, as:

$$\gamma + \gamma \rightarrow \gamma + e^+ + e^- \tag{1.14}$$

These charged particles resulting from the first interaction undergo bremsstrahlung when they interact with the fields of the nucleus of other charged particles. The photons produced through bremsstrahlung initiates the pair creation process over again, which results in the production of an air *shower* of secondary particles, as it is sketched in Figure 1.12.

The electromagnetic shower develops in the atmosphere for several kilometers, creating a footprint with a diameter of $\sim$ hundreds of meters. The radiation length defines the mean distance over which a high-energy particle loses energy through bremsstrahlung until it has decreased to $1/e$ of the initial value. This is equivalent to 7/9 of the mean free path for electron pair production by a high-energy photon. The value for the radiation length of atmospheric dry air is $\mathrm{X}_0 = 36.7\ \mathrm{gcm}^{-2}$. Thus, the atmosphere is a calorimeter of $\sim$ 28 radiation lengths. The evolution of the number of particles in an electromagnetic air shower as function of the radiation length for different energies of the primary gamma-ray can be observed in Figure 1.13.

Atmospheric air showers are also produced by cosmic rays, both protons or atomic nuclei, when they interact with the nuclei of the upper part of the Earth's atmosphere. Indeed, cosmic rays are the main background of gamma-ray observatories. The result of the nucleus-nucleus interaction is a shower of particles which is dominated by

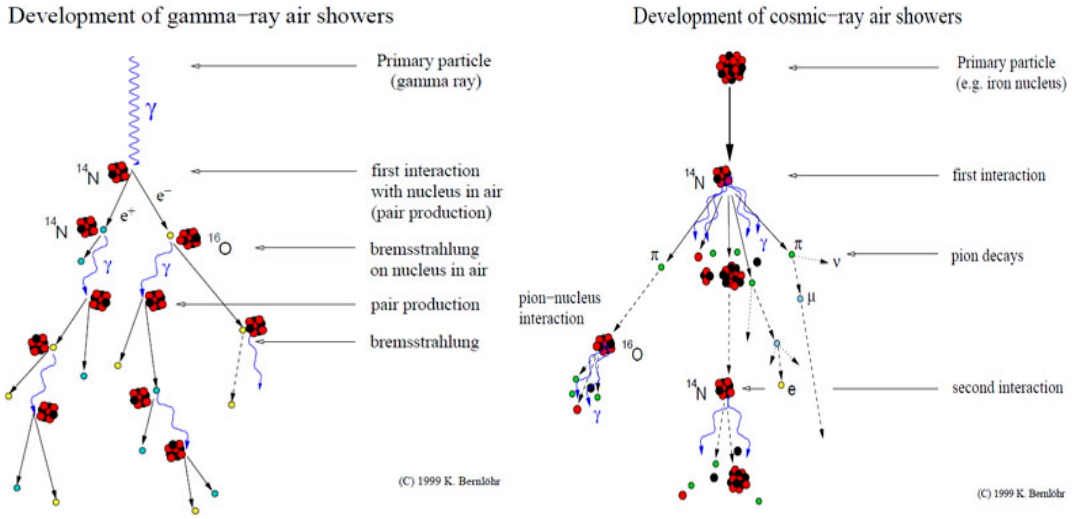

FIGURE 1.12: Schematic drawing of the development of air showers in the atmosphere initiated by a gamma ray and by a cosmic ray. Figure from K. Benlöhr

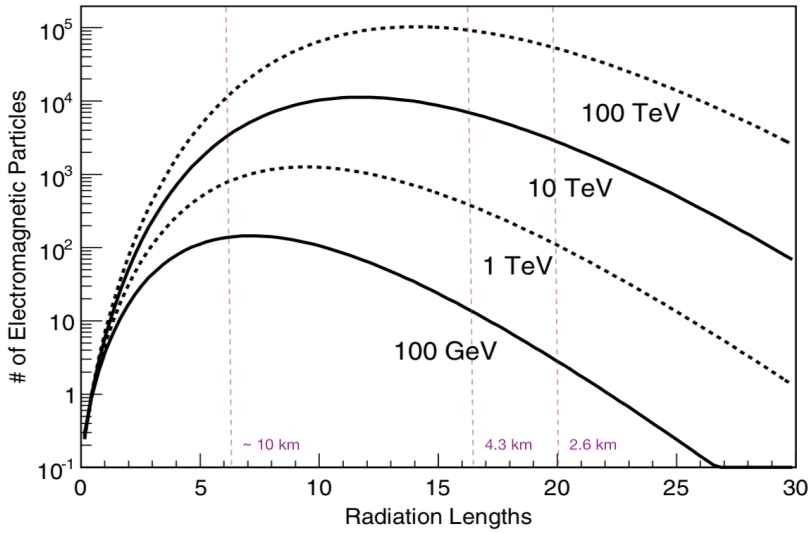

FIGURE 1.13: Evolution of the number of particles in an electromagnetic air shower with the number of radiation lengths, for different primary gamma-ray energies E=100 GeV, 1 TeV, 10 TeV and 100 TeV. Purple dashed lines are quoted which refer to 10 kms, which is usually quoted as the altitude corresponding to the maximum of the shower for gamma-ray energies $\sim$ 100 GeVs, 4.3 km which represents a typical altitude value for EAS arrays and 2.6 km which is related to typical values of IACT facilities. Adapted from Aharonian et al., 2008

pions, both charged (π^-, π^-) and neutral (π^0), heavier particles as nucleons, heavier mesons and bosons, as kaons ($K^{\pm}$), etc. A schematic view of the particles which continue interacting and decaying in the hadronic shower is given in Figure 1.12. The subsequent interactions that occur with different probabilities in the shower include three types of components: electromagnetic, hadronic and muonic. Due to the different components taking place in the evolution of the air shower, hadronic air showers

are topologically different than gamma-ray-induced air showers. The former are specially chaotic and their lateral distribution is typically broader than electromagnetic showers due to deep inelastic interactions with large transverse momentum transfer, as illustrated in Figure 1.14.

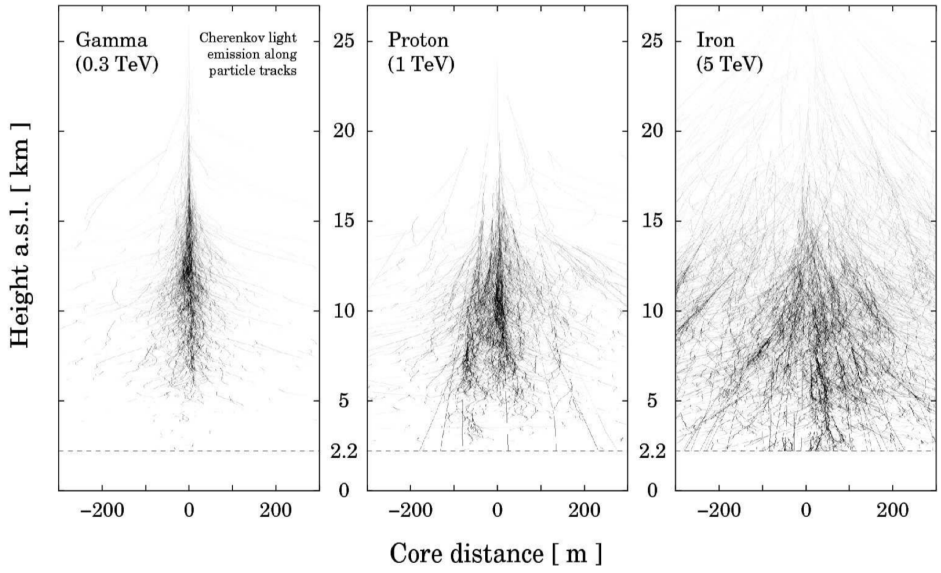

FIGURE 1.14: Simulation of the air shower of particles produced by different primary particle, namely 0.3 TeV gamma-ray, 1 TeV proton and 5 TeV iron nuclei. From Bernlöhr, 2008

Note that for these reasons, cosmic rays detection techniques are not too different from gamma-ray observation techniques. This is the case of the cosmic ray observatory Pierre Auger (Collaboration, 1997), in Malargüe, where extended air showers produced by hadrons are detected using water Cherenkov tanks and the shower development observed using fluorescence techniques.

Lateral shower development and curvature

At ground level, the electromagnetic air-shower is composed of electrons, positrons, and photons which due to the introduced transverse momenta, spread laterally away from the axis defined by the primary particle. A disk is formed which shows a spherical curvature with respect to the position of the primary particle interaction, as the particles travel at approximately the speed of light.

The geometry of the curved shower front centered on the trajectory of the original primary particle is illustrated in Figure 1.15.

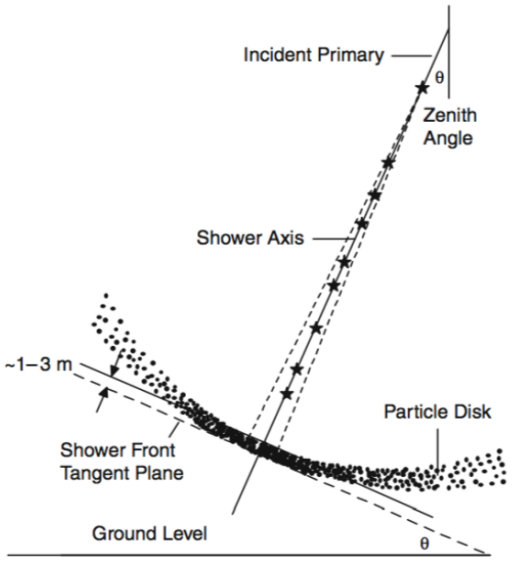

FIGURE 1.15: Illustration of extensive air shower plane showing the width and curvature of the particle distribution with respect to the shower axis. From Grieder, 2010

Cherenkov radiation emission

During the development of the air shower in the atmosphere, the charged particles present in the shower achieve superluminous velocities. They emit a type of electromagnetic radiation emitted by a charged particle when it passes through a medium characterized by a refraction index n, at a velocity v, which is greater than the velocity of light in that medium, c/n (Cherenkov, 1937). This radiation, named after the Nobel-award winner Pavel Cherenkov, is known as Cherenkov radiation.

The condition which leads to the emission of Cherenkov light in the velocity of the particle can be written as $c/n < v_{\text{part}} < c$, which translates to a threshold energy for the charged, relativistic particle energy:

$$v_{thresh} = c/n \rightarrow E_{thresh} = \frac{m_0 c^2}{\sqrt{1 - \frac{1}{n^2}}} \tag{1.15}$$

The electromagnetic wave front emitted when the particle moves through the medium takes the shape of a forward cone. The emission angle is given as $\cos\theta{=}1/\beta n$, where $\beta = v/c$. The number of photons emitted at a given wavelength λ, i.e. the spectral distribution of the Cherenkov light, is given as:

$$\frac{d^2N}{dxd\lambda} = \frac{2\pi\alpha Z^2 e^2}{\lambda^2}\left(1 - \frac{1}{\beta^2 n^2}\right) \tag{1.16}$$

where α is the fine-structure constant and Z_e is the electric charge of the particle.

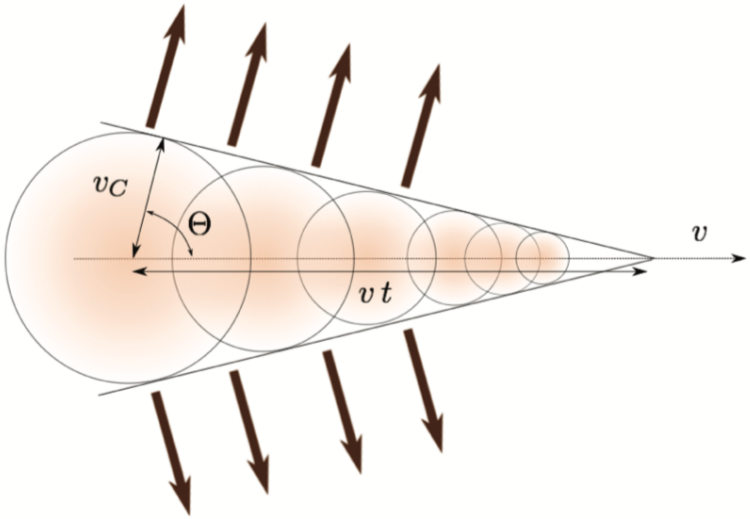

FIGURE 1.16: Cherenkov radiation cone created when a charged particle is moving at superluminous velocities. From Arrieta Lobo, 2017

1.5.2 Ground based detection techniques

Ground-based gamma-ray detectors use the atmosphere as a *calorimeter*. Various techniques have been developed in order to obtain the information about the gamma ray that started the electromagnetic shower. Their design has been adapted to provide large collection areas up to $\sim$ km^2.

A first division can be made between two different approaches. The detection technique based on the collection of the Cherenkov light produced by the charged particles of the air shower is known as imagining air-shower Cherenkov technique, performed by Imaging Air-shower Cherenkov Telescopes (IACTs). Another possible detection technique is based on direct sampling of the charged particles of the shower by particle detectors, performed by Extensive Air Shower arrays (EAS arrays). While EAS arrays take a snapshot on the particles of the shower when they pass through at a given time, IACTs allow to obtain an *image* (imprint in the camera) of the Cherenkov light emitted in the air-shower development.

An illustration of the two gamma-ray ground based techniques is shown in Figure 1.17.

1.5.3 History of gamma-ray astronomy

The first detection of Cherenkov light from an air shower happened 19 years after the discovery of the physical phenomenon by P. Cherenkov. In 1953, W. Galbraith and J. V. Jelley experimentally demonstrated the existence of emission of Cherenkov light by relativistic charged particles as well as the feasibility to detect such faint emission (Galbraith and Jelley, 1953). They performed observations in clear dark nights with

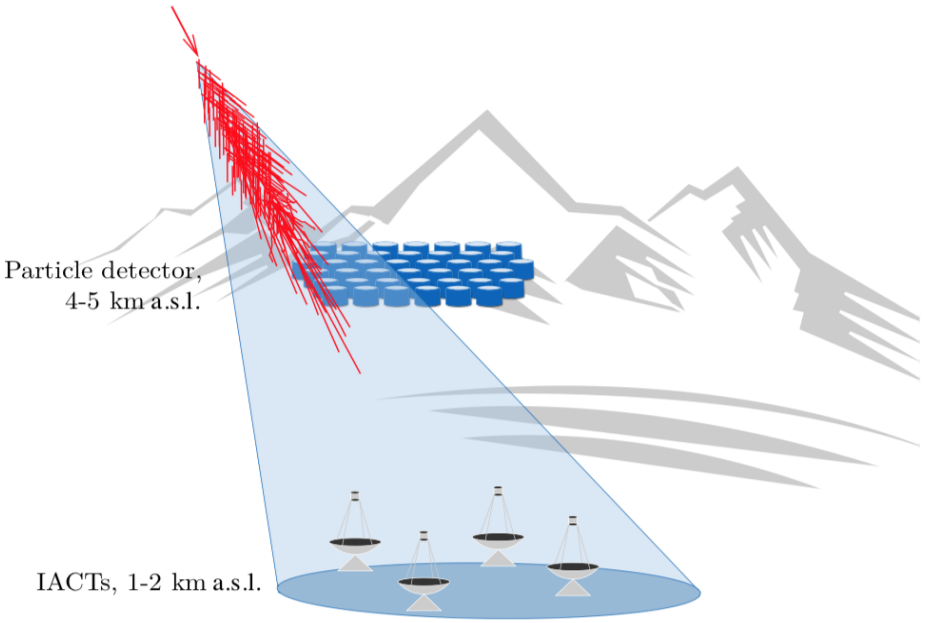

FIGURE 1.17: Illustration of a EM shower started by a gamma ray and the instruments which are able to detect the products of the initial particle through either imaging the Cherenkov light (IACTs) or through a particle sampler technique (particle detectors, EAS). From Albert et al., 2019

a simple set-up consisting of a search-light mirror of 25 cm of diameter and a single photomultiplier tube acting as light detector. They observed signals at a rate of $\sim$ one event per two or three minutes. The threshold on the rate of these observations, given in units of night sky background (NSB) which is the observational background corresponding to the light coming from stars and diffuse light; it was above four times the NSB level.

The experimental set-up was refined through the years by including larger mirrors and adding more PMTs. In parallel, first studies on the separation of electromagnetic and hadronic air showers using computer simulations were performed (Wills and Battrick, 1977). Then, new techniques to observe air showers were advocated by utilizing stereoscopy. Michael Hillas proposed in 1985 the *imaging* technique (Hillas, 1985), which included hardware upgrades consisting on a fast 37-PMT camera placed at the focal plane of a telescope. This ideas translated into important improvements in angular resolution.

In 1968, a group of scientists under the lead of Trevor Weekes started operations of a large 10 m telescope installed at the Fred Lawrence Whipple Observatory on Mount Hopkins in Arizona, USA. It was in 1989 that the Whipple Observatory discovered the first astrophysical gamma-ray emitter at TeV energies: the Crab Nebula (Weekes et al., 1989).

In the 90s, two different instrumental paths in imaging Cherenkov telescopes were followed after the meeting organized by Patrick Fleury and Giuseppe Vacanti (Fleury and Vacanti, 1992). These two approaches resulted in the construction of two major facilities: the Cherenkov Array at Thémis (CAT) and HEGRA. In addition, the CANGAROO collaboration constructed in Australia a Whipple-like telescope. The projects that came after, at the beginning of the XXth century strongly benefited from these first experiences. These are known as the second-generation ground-based gamma-ray observatories using Imaging Air-shower Cherenkov Techniques, and are: the H.E.S.S. (Hofmann and Collaboration, 2000) experiment in Africa, the MAGIC (Baixeras and Collaboration, 2003) experiment in Europe and the VERITAS (Holder et al., 2006) experiment, in America.

The first extensive air shower (EAS) arrays where composed of small plastic scintillators of $\sim$ 1 m^2 each, distributed over large areas of thousands of square meters. The largest experiments of this type CYGNUS (Alexandreas et al., 1992) and CASA, were unsuccessful to do astrophysics due to their high energy threshold of $\sim$ 200 TeVs. The first successful EAS array was the water Cherenkov-tecnique based, the Milagro detector (Atkins et al., 2004) in Los Alamos, which operated from the 1999 until 2008. From the data collected between July 2000 and January 2007, Milagro was able to detect several sources along the Galactic Plane.

The breakthrough in extensive air shower arrays has come with the HAWC experiment (DeYoung and Collaboration, 2012), by the combination of high fill-factors ($>$50%) and high altitudes above 4 kilometers, to allow detection at $\sim$1 TeV energies and provide background rejection power through the measurement of shower substructure at the ground and/or identification of muons.

The interested reader is referred to the review on ground-based detectors in very-high-energy gamma-ray astronomy by Naurois and Mazin, 2015.

The sky in very-high-energy gamma-rays

Over the years, many VHE sources have been detected by the mentioned facilities, assessing the physics potential of gamma-rays to study the very-high-energy Universe. These are plotted in 1.18, showing the catalog of TeV sources by the time this manuscript is written.

The galactic sources that can be observed are extended TeV halo Pulsar Wind Nebulae, pulsar gamma-ray binaries and supernova remnant shells. Note that all the grey points refer to objects whose nature is not clear, as they are placed in crowded regions of the Galactic Plane.

The subset of extragalactic source showing emission in the TeV range is dominated by high synchrotron peaked BL Lac objects, which are a specific type of AGN. The extragalactic sources detected so far by VHE energy facilities includes blazars, starburst galaxies, radio galaxies and since recently, transient sources as GRBs. Note that

in Chapter 3, the discovery of a new extragalactic VHE emitter, the AGN OT081, is presented.

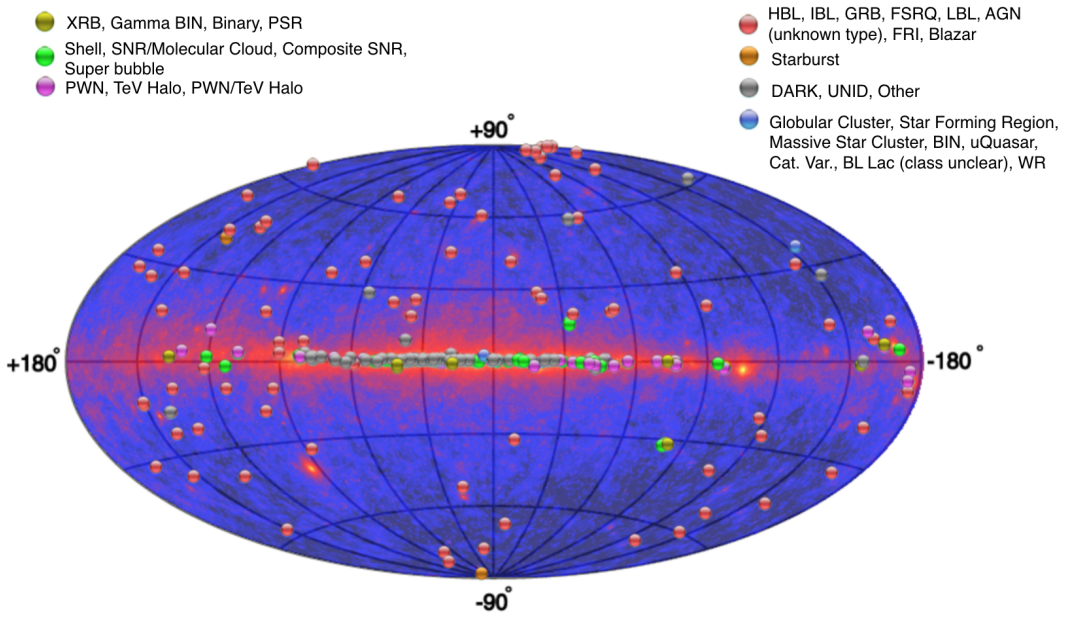

FIGURE 1.18: Catalog of TeV sources in 2019 from `http://tevcat.uchicago.edu/`

1.5.4 Imaging Atmospheric Cherenkov Telescopes

The detection technique of IACTs is based on the observation and study of the Cherenkov light which is radiated from the charged particles of the shower started by a high energy photon. As previously discussed, the number of the particles in the shower reaches its maximum at a height of at approximately 10 km (Figure 1.13). Thus, IACTs need to be placed at moderate altitudes, looking for a good compromise between atmospheric transparency to gamma rays and successful development of the showers.

An extra parameter to consider in IACTs is the effective area of the facility. The Cherenkov radiation emitted by the charged particles of the air shower is beamed around the direction of the incident primary photon. The Cherenkov light arriving to the ground, known as Cherenkov light pool, is about 200 meters in diameter. In order to observe such light pools, the telescopes need to be located within, so several telescopes will be able to observe the cone and better reconstruct the photon parameters. This means that the effective detection area of the telescope, for a telescope like H.E.S.S. of 120 m of side length, is about 50000 m^2. In high energy detection with instruments on-board of satellites, the effective detection area is 1 m^2 (*Fermi*-LAT), which shows the power of IACTs.

The characteristics of the Cherenkov radiation are responsible of some of the inherent difficulties of this technique. Although the emission achieves large lateral extension, the time interval for the arrival time of the light coming from the air shower is of the order of $\sim$ nanoseconds. Moreover, the emitted Cherenkov radiation is extremely faint compared to other sources of light, so big efforts need to be done in order to isolate these signals. The detector capabilities to distinguish a Cherenkov signal S from a night sky background B_{NSB} of a flux ϕ_B can be quantified as the ratio:

$$\frac{S}{\sqrt{B}} \propto \sqrt{\frac{A}{\Delta t \phi_B \Omega}} \tag{1.17}$$

where A is the collection area of the detector, Δt is the temporal resolution of the detector and Ω is the solid angle of the photo-detectors. The energy threshold of the instrument is proportional to:

$$E_{th} \propto \sqrt{\frac{\Delta t \phi_B \Omega}{A \epsilon}} \tag{1.18}$$

where A is the collection area of the telescope, and ϵ refers to the global efficiency of the system. Equations 1.17 and 1.18 set the conditions to built an IACTs which has powerful background discrimination capabilities and low energy threshold. The optimal scenario for imaging Cherenkov air showers is a telescope which has a large collection area, which can be achieved by an extended distribution of the array, a fast response camera and electronics with low dead time, and a large field of view (FoV), which can collect extremely faint signals.

1.5.5 Extensive Air Shower Arrays

Extensive air shower arrays are particle detectors. Therefore, in order to collect the maximum number of particles from the shower, the facility needs to be built at high altitudes to get closer to the shower maximum. The constraints on the availability and accessibility of high altitude sites and reasonable working conditions for the installation and running of the experiments, translates to altitudes around several thousands of meters.

The sensitivity of these facilities depends on the capability to detect the particles of the air-shower when they arrive to the detector. Hence, the sensitivity depends on the effective area of the array, which will give access to air-showers of different energies, the fill-factor of the array, which quantifies how dense the array is, and the energy resolution of the primary particle which depends on how well a shower can be reconstructed. The capabilities of the detector to reject hadronic background plays an important role as well.

The strength of these facilities is the ability to continuously observe large regions and the high duty cycle. Examples of particle detector designs that can be used in large FoV observatories are scintillator arrays, resistive plate chamber carpets or water Cherenkov tanks. Due to the detection technique, the energy threshold is

	IACTs	EAS Arrays
Field of view	3-10°	90 °
Duty cycle	10-30%	$>$ 95%
Energy range	10s of GeV →100 TeV	100s of GeV → 100 TeV
Angular resolution	0.05°-0.02°	0.4°-0.1°
Energy resolution	7%	60%-20%
Background rejection	$>$95%	90-99.8%

TABLE 1.1: Characteristic parameters quantifying the performance of the two types of ground-based instruments observing the very high-energy gamma-ray sky: IACTs and EAS array. From Albert et al., 2019

usually higher than in IACTs, and presents as well a dependency on the zenith angle at which the shower initiates.

1.5.6 Complementarity of VHE gamma-ray facilities

The different gamma-ray detection techniques present inherent challenges, which sometimes can not be easily overcome. A summary of the characteristic parameters of the two types of facilities linked to the very-high-energy gamma-ray detection techniques is found in Table 1.1.

In order to have a better insight into astrophysical phenomena, a complementary approach is worth to be taken. Together, the two type of facilities give access to a large range of physical phenomena producing very-high-energy gamma rays in the Universe.

On one hand, IACT facilities are currently limited to fields of view less than several degrees due to the telescope optics and the size of the camera. IACTs have low duty cycle 15%. Nevertheless, the precision and instantaneous sensitivity achievable with IACTs is much greater than ground-level particle detectors. IACTs provide a view of the whole shower in the atmosphere, enabling a calorimetric shower energy estimate and extremely effective background rejection through image parameters and image template fitting. This translates to a better sensitivity to the observation of faint sources and in a better energy resolution of the gamma-ray flux on the order of $\sim$ 7%, which is important in the study of energy spectrum of sources.

On the other hand, ground level particle detectors have duty cycles that approach 100% and present a wide field, with shower directions established through nanosecond-level accuracy measurements of particle arrival times. This features give access to the study of extended regions as TeV halos, which are challenging for IACTs due to the background computation methods.

Regarding time-domain astronomy, any follow-up of transients requires fast procedures and suitable observing conditions. This translates in limitation on the observation of transient sources due to the location of the instrument. For this reason, in

transient science, the complementarity between facilities at different locations, and also with different FoVs, is particularly beneficial. While facilities with wide FoV and continuous operations have the advantage of being able to monitor sources through their transit in the sky, IACTs need to point the telescopes and suffer of low duty cycles. Nevertheless, small FoV facilities are able to reach lower energies in their observations.

Currently, complementary coverage of both hemispheres is provided by the three second-generation ground-based gamma-ray observatories H.E.S.S., MAGIC and VERITAS. The second-generation ground-based gamma-ray observatories using EAS technique is represented by the HAWC experiment.

Building on the success of the mentioned current facilities, several next-generation projects have been developed over the last years. A global effort has been done by the IACT community, where experience and forces have been merged, resulting in the project known as the Cherenkov Telescope Array (CTA). Compared to current IACTs, it brings an order of magnitude sensitivity improvement as well as access to both hemispheres thanks to its two-site design. Future projects of large FoV instruments include what will be the largest facility for cosmic ray studies and gamma-ray astronomy, now under construction in the Sichuan province of China, LHAASO (Di Sciascio and Collaboration, 2016), as well as the SGSO (Albert et al., 2019), in South America. While LHAASO is a facility designed as a hybrid of different techniques, EAS, scintillation and IACT, the idea of SGSO is to build a water-Cherenkov based instrument which has access to the southern sky, larger fill factors and larger extension compared to HAWC.

A summary of current ground based gamma-ray observatories, as well as some future projects can be found in Figure 1.19.

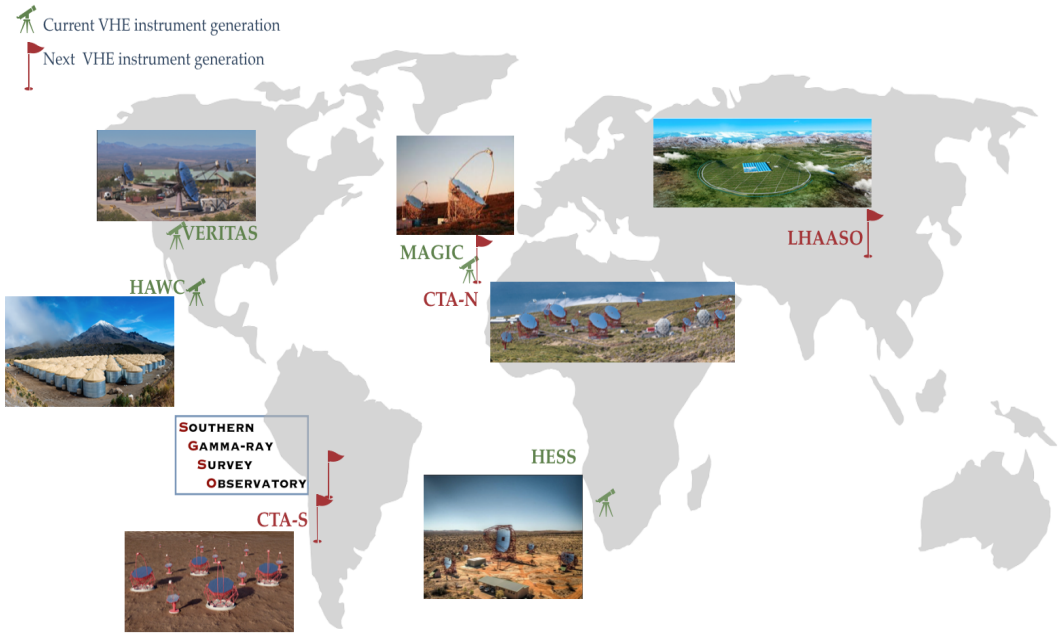

FIGURE 1.19: Illustration of the different IACTs and EAS instruments currently observing the VHE sky (green) and the future projects (red), which includes facilities in phase of construction and facilities which were recently proposed.

Chapter 2

Very-high-energy gamma-ray experiments

2.1 The H.E.S.S. experiment

The High Energy Stereoscopic System (H.E.S.S), named after the discoverer of cosmic rays in 1912, Victor Hess, is a network of telescopes designed to study the Universe in very-high-energy gamma-rays through the Cherenkov light emitted by secondary particles. The observatory is operated by a international consortium of 14 countries and more than 260 scientists [1].

It is located at 1800 meters above see level, near the Gamsberg mountain, in the Khomas Highland in Namibia. The site location was chosen due to the good compromise between several key requirements of imaging techniques using atmospheric Cherenkov light. The clear skies of the area are known to amateur astronomers due to the low cloud coverage, the low light contamination, which is due to the isolation of the region, and low humidity conditions in the hot desert climate. The altitude of 1800 m presents a good compromise between the necessary air shower development and Cherenkov light emission versus the light absorption in the atmosphere. Last but not least, the observability of the southern sky and the optimal observations conditions of the inner regions of the Galactic Plane at low zenith angles, played a key role on the selection of the site.

2.1.1 Telescopes and camera

The first phase of the experiment, called H.E.S.S. I, started operations in 2001 when the first telescope was deployed. The installation of the first phase was fully completed in 2003. It was composed by four small telescopes of 12 meters in diameter known as CT1-4, each of them with a mirror area of 108 deg^2. From its first design, the array of telescopes has been conceived to operate stereoscopically, in order to overcome the difficulties to accurately reconstruct the shower properties with a single telescope. The telescopes are placed at the corners of a 120 m of side length square, each of the telescopes has an effective area of 108 m^2 and the energy threshold of the

[1] `https://www.mpi-hd.mpg.de/hfm/HESS/pages/about/`

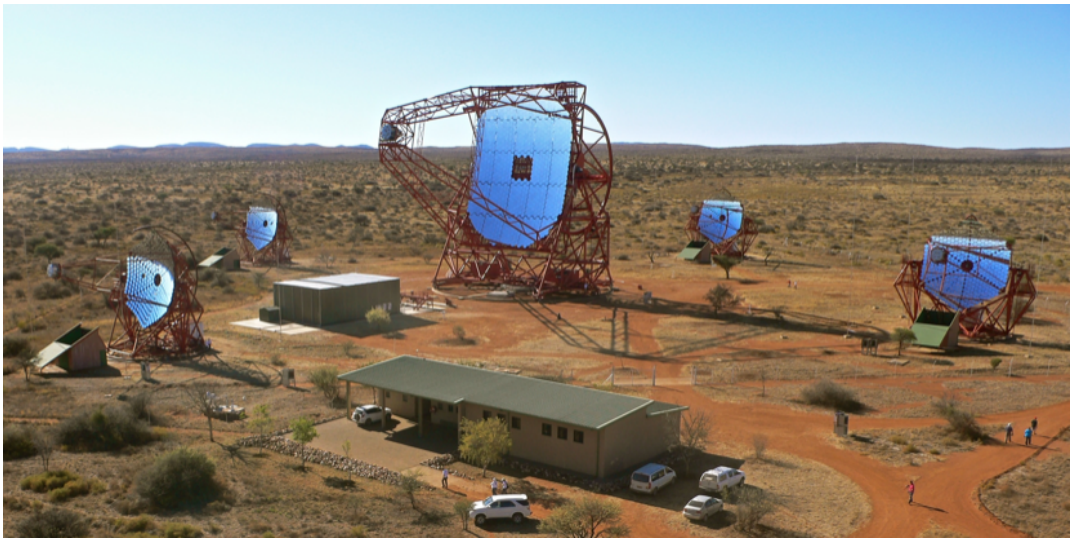

FIGURE 2.1: Photo of the H.E.S.S. experiment in phase H.E.S.S. II. The four telescopes, CT1-4, can be observed at the corners of the square array. The 28m telescope, CT5, is located in the center of the observatory. In the foreground of the picture one can see the control room.

array is $\sim$ 100 GeV.

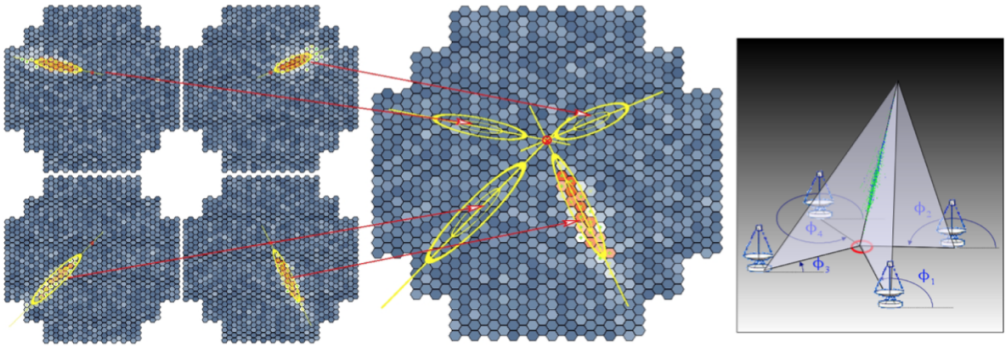

FIGURE 2.2: Illustration of the stereoscopic reconstruction of an air shower by four Cherenkov telescopes. Modified from K. Bernlöhr

In Figure 2.3, the structure of a H.E.S.S telescope as CT1-4 is presented. In IACTs, the telescope design is conceived for the Cherenkov light of an air shower to arrive on a reflector and focalized in the focal plane, where a camera, composed by photo-multiplier tubes (PMTs), is located. The dish with the camera arms is mounted in altitude-azimuth in a rotating base frame, supported by two towers (Bernlöhr et al., 2003).

The reflector of CT1-4 is composed of 382 round mirrors supported by a steel space frame, each of them with a diameter of 60 cm. They are arranged on a Davis-Cotton mount, where the focal length, in this case 15 m, is twice the focal length of

the spherical surface, of 7.5 m. The Davis-Cotton design has been chosen due to its minimization of geometrical aberrations, at expenses of gradual asynchronism at the level of the photon reception between the edges and the center of the spherical surface.

Each camera is mounted in its corresponding telescope and collects the Cherenkov light emitted by the atmospheric air shower. The cameras in CT1-4, with a weight of 900 kg, consist of 960 PMTs which are distributed following a hexagonal pattern. The PMTs convert the incident Cherenkov photons into photo-electrons, which are afterwards multiplied in number within a chain of dynodes, finally producing a measurable electric signal. The ratio between the incident photon and the number of electrons produced in the photocathode is called *gain* and quantifies the efficiency of the process. The nominal gain for a H.E.S.S. PMT is $\sim 2{\cdot}10^5$. Also, in front of the PMT, a Winston cone has been placed in order to reduce the albedo noise from the environment and to guide the light onto the photo-cathode, which reduces the dead-space effect between PMTs.

With a total camera FoV of 5°, extended sources over a few degrees can be observed. The individual pixel size is 0.16°, which be small enough to be able to reconstruct the morphology of the air shower, as it is connected to the properties of the initial gamma-ray and allows to improve the separation of the hadron induced background showers. The camera signal is digitized by fast electronics, which are needed to obtain a good angular resolution and a good background rejection.

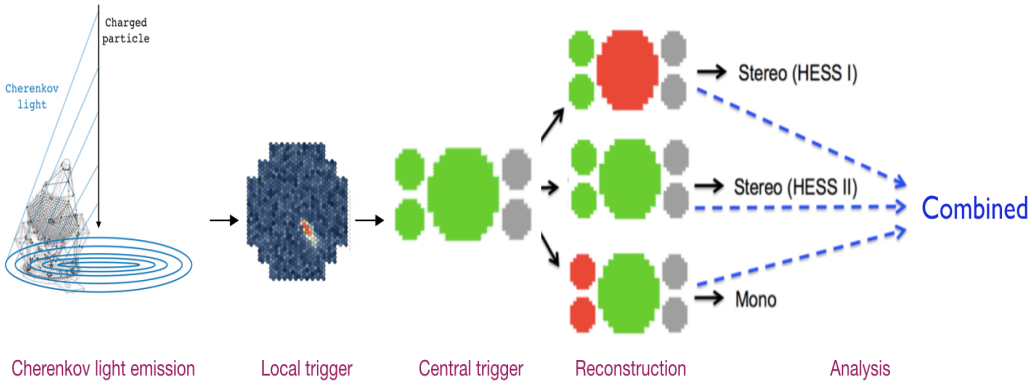

FIGURE 2.3: Simplified scheme of the H.E.S.S. data acquisition chain where the structure of the H.E.S.S. telescope, the collection of Cherenkov light, the dual trigger scheme, the different reconstruction modes and the various possible analyses are outlined.

The second phase of the instrument, known as H.E.S.S II, was fully deployed in 2012. It incorporates a fifth telescope, CT5, the largest Cherenkov telescope up to date, in the center of the square defined by CT1-4. With a diameter of 28 meters, it has a 614 m^2 of mirror area. It was designed to be a *transient hunting* machine, so despite a total weight of 580 tonnes, it can reach any coordinate of the sky in less than a minute. The improvements of CT5 telescope with respect to the H.E.S.S. I

includes better sensitivity, angular resolution and due to the better background rejection capabilities, lower energy γ photons can be observed.

The asynchronism effect associated to the David-Cotton design for a telescope of the size of CT5 is too high, so a different design for the reflector was adapted. Instead, a parabolic design of 32.6×24.3 square meters was chosen in order to minimize dispersion, as the focal length of the mirror facets varies with the distance from the optical axis. A total number of 875 hexagonally-shaped reflectors of 90 cm diameter are mounted in the dish, with a focal distance of CT5 is 36 meters. For all the telescopes CT1-5, the support of the each mirrors has a motor which is used to aligned remotely the mirror reflectors. The mirror alignment is performed using star images viewed when the camera lid is closed and is done by comparing the image obtained by a CCD camera at the center of the dish and the photomultiplier camera (Bernlöhr et al., 2003).

The camera of CT5 consists on 2048 PMT grouped into 128 drawers, which also contain the readout electronics. Although the pixels in the photomultipliers have the same *physical* size, a finer pixilation of 0.067° and better resolution is achieved due to the larger focal length. The total camera FoV is 3.2° radius.

The emission of Cherenkov light by the particles in the air shower happens in an extremely short period of time of the order of ∼10 ns, slightly depending on the inclination angle. Simulated images recorded by the camera for different integration times, can be found in Figure 2.5, where we observe that large integration windows are background-dominated. In order to successfully observe the γ-photons, the cameras have fast, efficient electronics which enables to record the event, where the readout window for an event is $\sim$ 273 μs, the transfer of the event takes $\sim$ 144 μs, and the deadtime of the camera is of $\sim$ 446 μs.

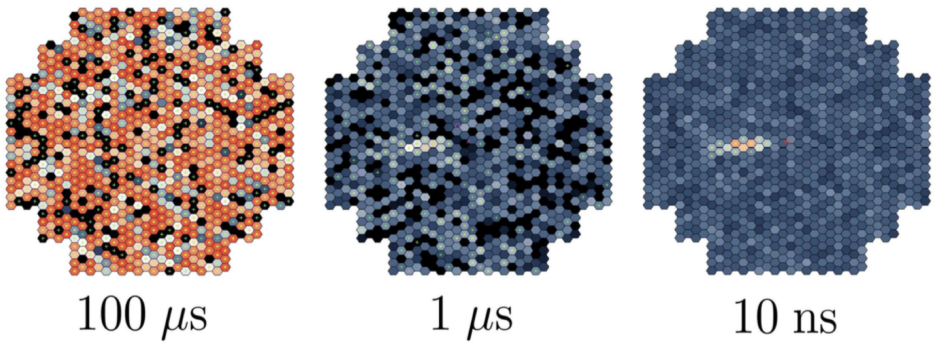

FIGURE 2.4: Simulated images in the camera of a γ-photon observation in a camera H.E.S.S. I-like for different signal integration times of 100 μs, 1μs and 10 ns, where the color scale refers to the intensity per pixel (K. Bernöhr)

Trigger system

The H.E.S.S. experiment incorporates a trigger system which enables background rejection of the NSB contribution from stars and diffuse light, and the rejection of isolated triggers from muons. The H.E.S.S. trigger system presents a dual trigger structure consisting on a *local* and the *central* level.

The first trigger level is *local* as it is internal to the individual cameras. A correlation is performed between a pixel and its neighbors in a short time window in order to decrease the background caused by isolated pixels. The local coincidence window for a typical PMT pulse shape is $\sim$ 1.3 ns. For CT1-4, each camera is divided into 38 overlapping regions of 64 pixels which are effectively triggered only if a number of N_p pixels inside the same region of the camera reaches a given threshold in number of photoelectrons N_{pe}. In the case of *standard* operations, these parameters are set to N_p =3 pixels with N_{pe}=4 photoelectrons. This first trigger criterium has an important effect in reducing the NSB and yields to a camera trigger rate $\sim$ 1.4 kHz.

In the second level, a *central* trigger performs a correlation between the telescopes, in order to not only ensure the stereoscopic reconstruction of the air shower but also to reduce the rate of isolated muons. In Figure 2.5 the effect of stereoscopic observations on the discrimination of muons can be observed. Provided that at least two telescopes are triggered, a confirmation is sent to the telescopes to process the signal that has been stored in an analog ring sampler.

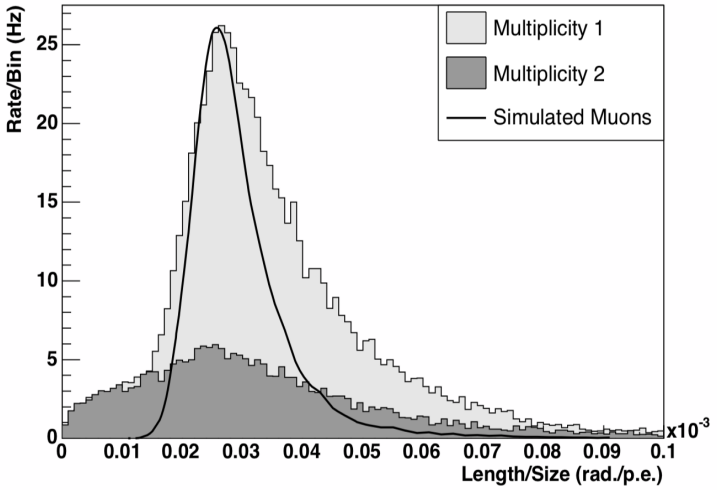

FIGURE 2.5: Distribution of the parameter length/size, where the multiplicity 1 refers to data from a single telescope and multiplicity 2 to a stereoscopic observations with two telescopes involved. The parameters *image* length and *image* size refer to the Hillas parameters introduced later in the chapter. From Funk et al., 2004

Data acquisition

The *standard* data acquisition is performed under *sufficiently* good weather and *darkness* conditions, minimizing the amount of background light, in order to guarantee a performant detection of the atmospheric air showers. The requirements for a *darkness* condition include the altitude of the Sun being below astronomical twilight at $\theta_{ALT}^{Sun} < -18°$ and the altitude of the Moon being below $\theta_{ALT}^{Moon} < -0.5°$.

Nevertheless, in the spirit of increasing data acquisition time, several observation types have been established although being less optimum both hardware-wise and the reconstruction-wise. The acquisition mode of the cameras, e.g. the voltage of the PMTs and the data calibration is adjusted to such observation conditions. This is the case for observation under *moderate* Moon brightness and separation, known as *moonlight* observations. The main requirements to schedule these observations are the Moon-to-Source separation, the Moon phase and the altitude of the Moon. A further type of observations under study are *twilight* observations. These are defined as the period between nautical twilight and astronomical twilight and correspond to the period where the altitude of the Sun goes from -12° to -18°.

Other types of data acquisition modes which are not directly observing physical sources but are needed to monitor the instrument, the observation conditions, and to correctly calibrate the instrument. This is the case of pointing runs, which are taken regularly by looking to a number of stars in order to check whether their positions are correctly obtained. From these observations, the H.E.S.S.pointing corrections are derived, based on the assumption that telescope deformations, and hence pointing deviations, are reproducible, and depend only on the alt-az pointing position (Gillessen, 2004). Standard pointing corrections, by default applied to all H.E.S.S. data, provide a localisation of point-like γ-ray sources with a systematic pointing error of 20" per axis.

Additional data acquisition types related to the calibration are single photoelectron runs, dedicated to control the PMT response by measuring their response to the light emitted by a LED placed in front; flat-field runs, where a LED mounted in the dish lights homogeneously the telescopes and pedestal runs, performed with the lid of the camera closed in order to obtained the electronic output when no Cherenkov light is recorded.

Calibration

The PMT signals are recorded by the cameras in analogue memories and then converted into ADC counts. The data acquisition conditions in IACTs, as the H.E.S.S. experiment, are peculiar due to the use of the atmosphere as a calorimeter and the environment. The calibration, which strongly impacts the final performance of the instrument, has the role to give a physical meaning, in terms of density of Cherenkov photons, to these electronic signals. The calibration of the instrument is performed by relying on the Cherenkov signal emitted by atmospheric muons, which provides

the optical efficiency of the entire system. The Cherenkov light emitted by muons is recorded in the camera as a *muon ring*, as can be observed in Figure 2.6.

The conditions of the data acquisition, from the atmospheric conditions, to the electronics of the camera, passing by the characteristics of the mirrors and the PMT response, needs to be understood and monitored. Simulations of these features for a given set of parameters, describing the instrument response function (IRF), are produced. In the case of the H.E.S.S. experiment, two different calibration chains are in place. More detailed information about those, and on the calibration procedure can be found in De Naurois, 2012.

Other instruments in the H.E.S.S. site

Several instruments are installed in the H.E.S.S. site in Namibia with the motivation of monitoring the atmospheric condition in real-time and using this information in the air shower reconstruction.

A LIght Detection And Ranging (LIDAR) is responsible to measure the aerosol composition of the atmosphere as a function of the altitude by using pulser laser light and measuring the reflected pulses (Brown, 2005).

An *atmospheric monitoring system* is also present on site, which is crucial to monitor in real time the variation of the weather and the appearance of clouds which would introduce fast variability on the data acquisition rates and problems at the level of the reconstruction. The monitoring system is composed by a weather station, where the temperature, pressure, humidity as well as the wind speed and direction are measured. A scanning radiometer obtains real time images of the full sky cloud coverage. Additional radiometers are mounted on each of the telescopes, enabling the monitoring of the cloud coverage in the telescope FoV and the sky temperature.

In addition, the Automatic Telescope for Optical Monitoring (ATOM)(Hauser et al., 2004), a 75-cm alt-azimuth optical telescope, is deployed on site. Observing in the visible (B, V, R and I filters) domain, it has been placed next to the H.E.S.S. array in order to enable simultaneous Multi-Wave Length (MWL) observations and monitor a pre-selected number of sources, mainly AGNs. It works in a fully automatic way, including scheduling and data analysis. Observations obtained by ATOM will be discussed in Chapter 3 in the context of the multi-wavelength observations of the blazar OT 081.

2.1.2 Shower Reconstruction

Once the data is calibrated and the density of Cherenkov photons has been obtained, the next step is the reconstruction of the air shower parameters associated to the primary particle like the direction and energy. Unfortunately, the recorded data not only include gamma-rays but also hadronic showers and muons, which leave different imprints in the camera due to their nature, as seen in Figure 2.6. These have to be

identified and removed as best as possible from the dataset.

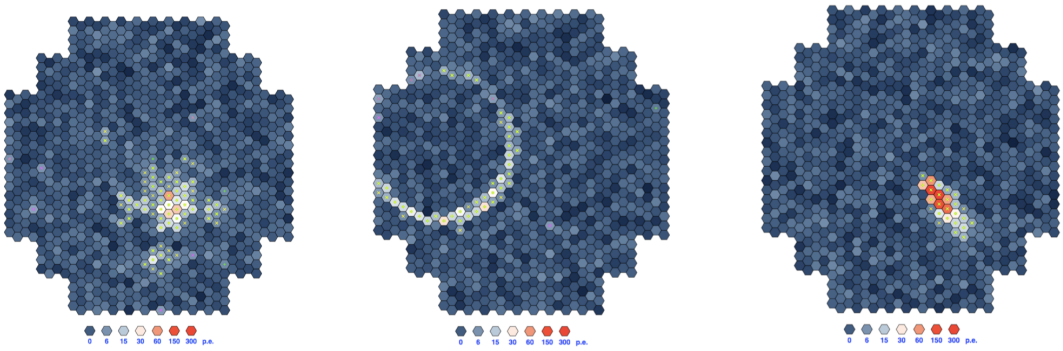

FIGURE 2.6: Simulation of the camera imprint of the H.E.S.S. observations of an air-shower started by a proton, a muon and a γ photon. The color scale refers to the number of photoelectrons collected per pixel. From K. Bernlöhr.

Hillas image parametrization

The historic method for image parametrization in IACTS, developed by Michael Hillas in 1985 (Hillas, 1985), consists in the parametrization of the image left in the camera as an ellipse. The ellipse is described by a two-dimensional gaussian distribution along the longitudinal and transverse axis. In order to avoid background biases, a procedure of image cleaning is applied beforehand. The resulting image can be ajusted by the Hillas parameters describing the ellipse, enumerated in Table 2.1. These are represented in Figure 2.7. A description of the method can be found in De Naurois, 2012, where the relationship between the Hillas parameters and the reconstructed direction and energy of the primary particle are illustrated.

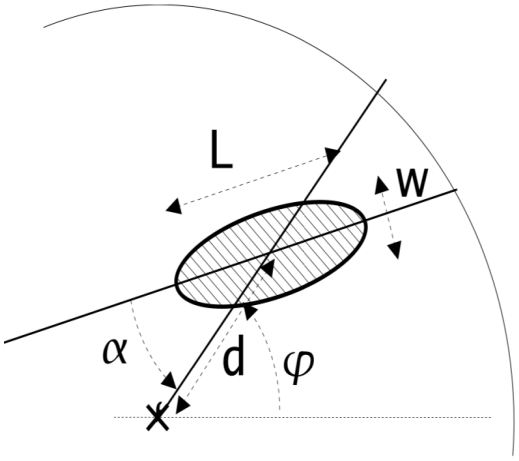

FIGURE 2.7: Geometrical parametrization of an elliptical image coming from an electromagnetic air shower using Hillas parameters

Lenght	L	Measure of the longitudinal development of the cascade.
Width	W	Measure of the lateral development of the cascade
Total Charge	T_{ch}	Total charge inside the ellipse
Distance	D	Distance between the camera center and the barycenter of the ellipse
Azimuthal angle	ϕ	Angle between the center of the camera and the barycenter of the ellipse
Orientation angle	α	Angle between the major axis of the ellipse and the axis defined by the center of the camera and the barycenter of the ellipse

TABLE 2.1: Hillas parameters used for the geometrical parametrization of an elliptical image coming from an electromagnetic air shower.

Semi-analytical image parametrization: *Model Analysis*

In the 90s, a sophisticated gamma-ray likelihood reconstruction technique for IACTs was initiated in the context of the CAT experiment (Le Bohec et al., 1998) and has been further developed through the years (De Naurois and Rolland, 2009). The reconstruction technique is based on the comparison of the raw camera images of an air-shower initiated with the predictions of a Monte Carlo based model. This technique presents important improvements on the reconstruction of the direction and energy of the primary photon, the treatment of night sky background noise and the use of stereoscopy compared to other reconstruction techniques. A factor ~ 2 of improvement in sensitivity is reached if compared to the Hillas parametric technique (De Naurois and Rolland, 2009).

The semi-analytical images of photon-iniciated airshowers are obtained using Monte Carlo (MC) simulations. In the simulation an analytic description of the shower model is obtained by considering the Cherenkov light distribution of charged particles in EM airshowers taking into account collection efficiency, atmospheric absorption conditions, depth of first interaction, night sky background. The analytic models of the light shower observed in the camera is computed from an eight-dimensional integral (De Naurois and Rolland, 2009), so for a set of primary particle parameters, a output bank of four dimensional images in the frame of the camera are produced, which include energy, impact distance, primary interaction depth and zenith angle.

A minimization procedure is the used to compare the *shower model* images to the actual images obtained in the camera, in order to obtain the most likely parameters of the primary γ-ray particle. For this, the optimization of a likelihood function, which depends on the energy, primary interaction depth, direction and impact parameter, which makes a total of 6 parameters, is considered. The log-likelihood of the telescope, assuming the independency of the camera pixels, can be obtained as the sum over all the *log-likelihood* pixels i as:

$$\ln L_{tel} = \sum_i \ln L_i = \sum_i -2 \cdot \ln P(s|\mu, \sigma_p, \sigma_\gamma) \tag{2.1}$$

where the probability to observe a signal s in photo-electron units, in a pixel for an expectation value μ is given by the convolution of the Poisson distribution of the photo-electron number n with the photo-multiplier resolution. This Poisson distribution can be written as:

$$P(s|\mu, \sigma_p, \sigma_\gamma) = \sum_n \frac{\mu^n e^{-\mu}}{n!\sqrt{2\pi(\sigma_p^2 + n\sigma_\gamma^2)}} \exp\left(-\frac{(s-n)^2}{2(\sigma_p^2 + n\sigma_\gamma^2)}\right) \tag{2.2}$$

where σ_p is the width of the charge distribution under pure noise, including NSB, known as the *pedestal* and σ_γ is the width of the single photo-electron peak, which is the PMT resolution.

In IACTs, the performance of an analysis is quantified by the reconstruction accuracies of the parameters of the primary particle, and the capability to discriminate hadronic showers, which are the dominant type of background for gamma-analyses. In the Model Analysis, the *goodness-of-fit* G variable is used to compare the shower model prediction and the actual shower image, quantifying its γ-likeliness. The variable G is defined as the normalized sum over all the pixels of the difference between the actual pixel log-likelihood $\ln L(s_i|\mu_i)$ and the expectation value $\langle \ln L \rangle$, as:

$$G = \frac{\sum_i \left[\ln L(s_i|\mu_i) - \langle \ln L \rangle|_{\mu_i}\right]}{\sqrt{2 \cdot N_{DoF}}} \tag{2.3}$$

where $N_{DoF} = N_{pix} - 6$ is the number of degrees of freedom of the fitting, which is given by the number of N_{pix}. The *Shower Goodness* distribution for the analysis of the blazar PKS 2155-304 obtained from Monte Carlo simulations, the real distribution of the excess events, and the background is included in Figure 2.8.

These are not the only cuts applied in the analysis. Indeed, depending on the analysis configuration, different cuts may be applied to the *Model* analysis in the H.E.S.S. collaboration. The analysis configuration depends on the characteristics of the observed source, environment of the source and observation conditions. Whereas for good observation conditions with low NSB, observing an isolated, strong source, a `Loose` set of cuts can be applied, a faint source in an environment where lot of contamination is possible, `Standard` cuts will be preferred. Details on the definition for each set of cuts can be found in De Naurois and Rolland, 2009.

In addition, a selection on the data included in the analysis, with different telescope configurations, can be perfomed at the analysis level. As there are two types of telescopes, CT1-4 and CT5, three possible telescope configuration data can be analysed: H.E.S.S. II `Mono` (only CT5), H.E.S.S. II `Stereo` (>1 CT1-4 and CT5) and H.E.S.S. I `Stereo` (> 2 CT1-4 telescopes data).

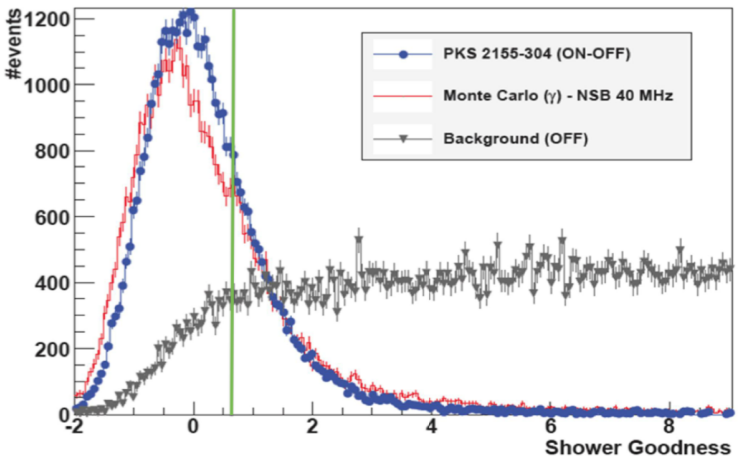

FIGURE 2.8: *Shower Goodness* distribution for real data obtained from blazar PKS 2155-304 in a flaring state in 2006, where the excess events (blue), the background events (grey) and the MC simulations (red) have been included. Green vertical line stands for the cut associated with the discrimination of 90% of the background events. From De Naurois and Rolland, 2009

The *Model* analysis is used to analyze the H.E.S.S. observation presented in this thesis in Chapter 3 and Chapter 6.

Image Pixel-wise fit for Atmospheric Telescopes: *ImPACT*

Slightly different from the Model Analysis described above, the ImPACT technique is based on the comparison per pixel between the signal observed and Monte-Carlo simulations of the expected signal (Parsons and Hinton, 2014a). A further classification based on a multivariate discrimination is performed using decision tree techniques.

This reconstruction methods and the *Model* analysis, are used as a cross-check of each other, which allows to probe the robustness of the obtained results. Apart from these, other reconstruction methods used to analyze H.E.S.S. data have been developed. These are the *Model 3D* (Lemoine-Goumard, Degrange, and Tluczykont, 2006) and the *multivariated* analysis (Dubois, Lamanna, and Jacholkowska, 2009).

2.1.3 Analysis

After the reconstruction of gamma-ray air-shower events, the next step is to collect the events and analyze the data to extract the excess in counts. To this aim, several background characterization techniques have been derived, which are essential in order to correctly identify the gamma-ray signal.

Background characterization

The characterization of the background in the H.E.S.S. telescopes is typically done through the definition of ON and OFF-regions, which are also known as *control zones*. In the OFF region, only background events are expected (N_{OFF}) while in the ON region, a *signal* hypothesis is made and both background *and* signal events are expected (N_{ON}).

Several methods have been proposed to define the control regions in an observation.

The *ON-OFF* observations consist on the acquisition of two consecutive observation runs, with the camera in the same position but a shift in the right ascension of the observation position. Disadvantages of this technique include the variations of the observation conditions, and to double the number of observation run per source. For this reason, *wobble* observations are used in the majority of cases. In this approach, the coordinates of the observation are shifted with respect to the coordinates of the observation target, as shown in Figure 2.9. The main advantages include not only that the acceptance in the *control* and *test* regions is similar but also that several *control* regions can be defined.

Indeed, the control region and the background estimation can be defined in several ways, depending on the dedicated analysis performed (Berge, Funk, and Hinton, 2007a).

The `Ring Background` method is used to estimate the background when computing the gamma excess from the gamma-like events. This method consists in defining a *ring* region around the ON region, where the source is located. This is performed for all the pixels in the skymap, for a given oversampling, resulting in a 2D counts skymap in (RA, Dec). An illustration of this background estimation can be found in Figure 2.9.

The energy distribution of the events is derived by using either the `Multiple OFF/ Reflected regions` method or athe `Ring Background` method (which should be mistaken with the previously mentioned method). The later consider several control regions for each of the observation runs, symmetrically around the source at a radius equal to the distance from the center of the camera to the source. These two background estimations used to compute the spectral distribution of counts are shown in Figure 2.10.

A crucial step in the background characterization technique is the consideration of regions in the sky where significant emission of γ-ray has been previously detected as *excluded regions*. These regions are masked in order to obtain a good, non-biased estimation of the background contribution. This procedure becomes specially challenging in regions with high number of sources, as the Galactic Center.

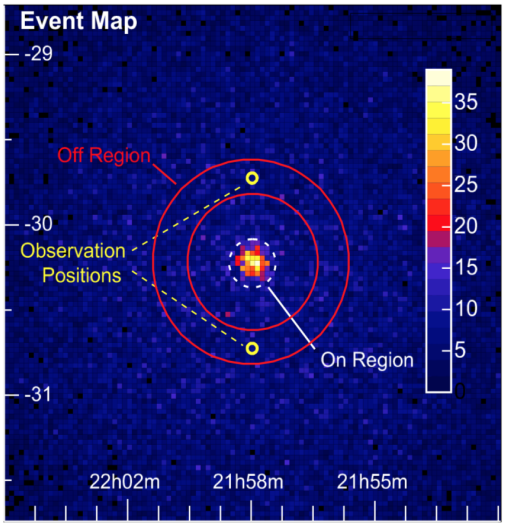

FIGURE 2.9: Illustration of the `Ring background` background estimation on the counts map of γ-like events (colorbar) which results from the analysis of 5 hours of H.E.S.S. observations on PKS 2155-304. The observation positions are shown in yellow, the ON region is noted in white and the OFF region in red as a *ring* surrounding the ON region. From Berge, Funk, and Hinton, 2007b

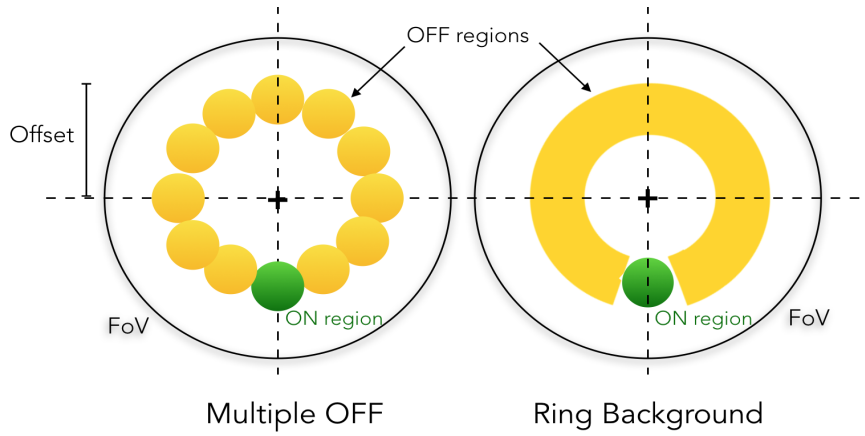

FIGURE 2.10: Illustration of the `Multiple OFF` and `Ring background` background estimation methods targeted to obtain a energy distribution of the γ events

Signal extraction

Following Li and Ma, 1983, the computation of the signal is done by comparing the number of events coming from N_{ON} and N_{OFF} regions selected as described above. In order to compare these two regions, a coefficient which takes into account differences in size, zenith angle or instrumental systematics, between both regions types, is considered. The number of background photons in the ON region is then estimated as $N_B{=}\alpha\ N_{OFF}$. In this way, the number of signal photons from the source is estimated as:

$$N_{excess} = N_{ON} - N_B = N_{ON} - \alpha N_{OFF} \tag{2.4}$$

Following Li & Ma statistics, an excess defined by the number of events observed in the ON-OFF regions, $N_{\rm ON}$ $N_{\rm OFF}$, can be used to obtain the statistic significance of a source, given by the formula:

$$S = \sqrt{-2\ln\lambda} \tag{2.5}$$

where λ refers to the likelihood ratio between the *null* hypothesis. The statistical significance of the observation can be expressed in terms of $N_{\rm ON}$ and $N_{\rm OFF}$ as:

$$\begin{aligned} S &= \left[2\ln\frac{P_0(N_{\rm ON}, N_{\rm OFF}|B)}{P_S(N_{\rm ON}, N_{\rm OFF}|S,B)}\right]^{1/2} \\ &= \sqrt{2}\left[N_{\rm ON}\cdot\ln\frac{1+\alpha}{\alpha}\left(\frac{N_{\rm ON}}{N_{\rm ON}+N_{\rm OFF}}\right) + N_{\rm OFF}\cdot\ln(1+\alpha)\left(\frac{N_{\rm OFF}}{N_{\rm ON}+N_{\rm OFF}}\right)\right]^{1/2} \end{aligned} \tag{2.6}$$

A significance greater than 5 σ units is required to establish a detection.

Once the signal is established, the subsequent steps focus on the characterization of the source through the spatial, energy and temporal distribution of the observed events. This leads to the computation of the morphology, the spectrum and the lightcurve of the source. This *high level* analysis allows to study the morphology, the underlying acceleration mechanisms and the temporal evolution of the source, and the connections between them.

Acceptance effects in the FoV

The γ-ray acceptance in the FoV shows a radial dependency, which decreases as one goes away from the center of the camera. Depending on the zenith angle of the observations, the decrease in acceptance shows a slight variation. The decrease to a 50% of the peak value of the acceptance is observed at $\psi^2 \sim 2.5^\circ$ for moderate zenith angles to $\psi^2 \sim 4^\circ$ to large zenith angles. This effect is illustrated in Figure 2.11 for H.E.S.S.-I.

This dependency on the radial acceptance motivates some of the choices made on the R_{FoV} in the follow-up observation schedule for gravitational waves, described in Chapter 6. In the case of the H.E.S.S. telescopes, CT5 is preferred to perform extragalactic observations. Thus, when the scheduling is obtained for an observation set-up including CT5, a $R_{FoV} = 1.5^\circ$ is considered. If the observation scheduler is obtained for only CT1-4, a $R_{FoV} = 2.5^\circ$ would be chosen.

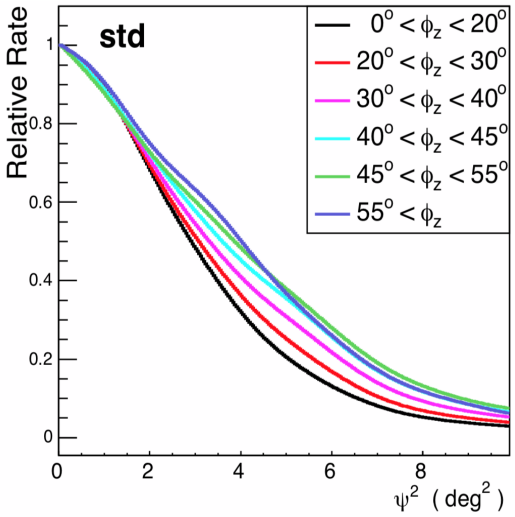

FIGURE 2.11: Dependency of the squared angular distance with zenith angle for standard cuts describing the radial acceptance of the system generated from OFF-source data, for H.E.S.S. I-like telescope. They are arbitrarily normalized to 1. From Berge, Funk, and Hinton, 2007b

Spectra, Upper limits and Lightcurves

In the H.E.S.S. analysis, the energy spectrum is typically obtained by using a *forward-folding* technique. The instrument response functions and an hypothesis on the spectral shape of the source made *a priori* are used in the convolution with the observed data. The most common spectral shapes which are often used in the *forward-folding* technique are:

- Power-law spectrum:

$$\phi = \phi_0 \left(\frac{E}{E_0}\right)^{-\Gamma} \tag{2.7}$$

- Broken power-law spectrum:

$$\phi = \begin{cases} \phi_0 \left(\frac{E}{E_0}\right)^{-\Gamma_1} & \text{if } E \leq E_{cut} \\ \phi_0 \left(\frac{E_{cut}}{E_0}\right)^{\Gamma_2-\Gamma_1} \left(\frac{E}{E_0}\right)^{-\Gamma_2} & \text{if } E \geq E_{cut} \end{cases} \tag{2.8}$$

- Curved power-law spectrum:

$$\phi = \phi_0 \left(\frac{E}{E_0}\right)^{-\Gamma-\beta\log(E/E_0)} \tag{2.9}$$

- Power-law with exponential cut-off power law spectrum:

$$\phi = \phi_0 \left(\frac{E}{E_0}\right)^{-\Gamma} \cdot e^{-E/E_{cut}} \tag{2.10}$$

where ϕ_0 is the flux normalization, E_0 the reference energy of the spectrum, E_{cut} is the cut-off energy, Γ is the photon index and β is the curvature index.

When the significance of the excess in the data is not enough to claim a detection, *upper limits* can be derived on the gamma-ray flux of the source. The upper limits are derived following Feldman and Cousins, 1998, for a given confidence level, assuming usually a power-law spectrum with a given index value. The upper limits on the gamma-ray flux can either be differential, i.e. as function of energy, or integral, where the limit is set *above* a certain energy threshold.

The time evolution of the flux of an astrophysical source is detailed in its *lightcurve*. The lightcurve of the source is obtained by determining the number of ON and OFF gamma-photons in various time intervals and comparing it to the expected number of gamma-photons given the spectral shape, which has been previously obtained and fixed, the acceptance and the angular resolution.

2.2 Cherenkov Telescope Array

The Cherenkov Telescope Array is a next generation project which aims to transform the VHE gamma-ray domain thanks to its cutting-edge technology and design. Moreover, CTA will be the first open ground based γ-ray experiment accessible to the entire scientific community. In contrast to collaboration-based experiments, like the second generation γ-ray experiments, which share private data through MoU agreements, CTA is planed to work under an *observatory* logic. The CTA dataflow and the connection with other observatories is presented in Figure 2.12

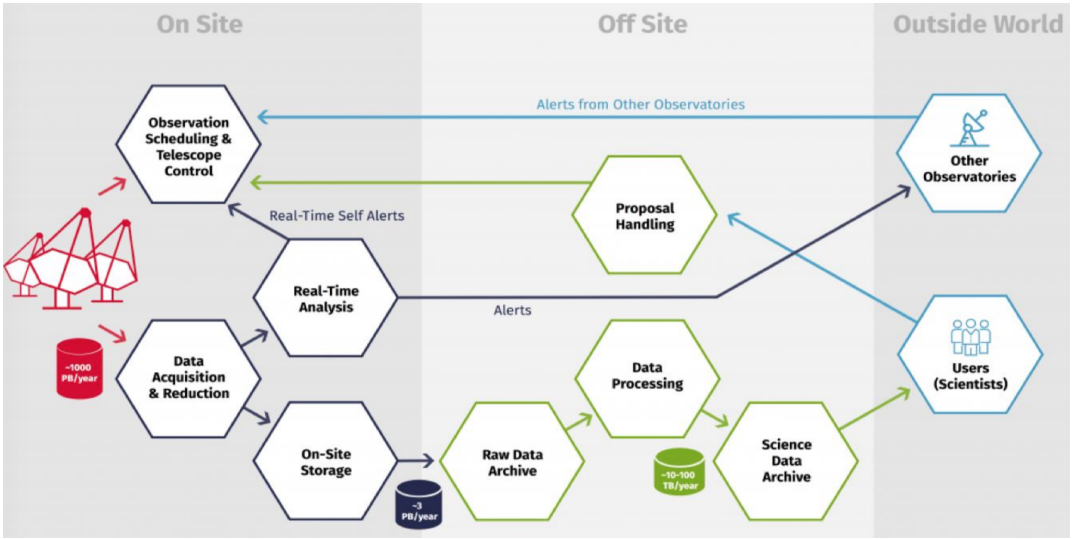

FIGURE 2.12: CTA dataflow and software systems subdivided in *on site*, *off site* and *outside word*. From `www.cta-observatory.org`

The key capabilities of CTA include improvements over current instruments on several aspects (CTA Consortium et al., 2017). Here, we specially focus on the four features which are crucial to be competitive in time-domain astrophysics, which make of CTA a performant observatory to follow up transient events:

The sensitivity of CTA is expected to improve the current instruments sensitivity by an order of magnitude at 1 TeV, as shown in Figure 2.13. Transient studies, as well as variability determination in astrophysical sources as AGNs, will have unprecedented sensitivity to emission in short scales, as it is noticeable if we compare to the performance of satellite based instruments (Figure 2.14). In particular, CTA has $\sim$ 4 orders of magnitude better sensitivity to minute timescales at 25 GeVs. Even at variability timescales of $\sim$ 1 month, CTA will be a factor 100 more sensitive than Fermi-LAT.

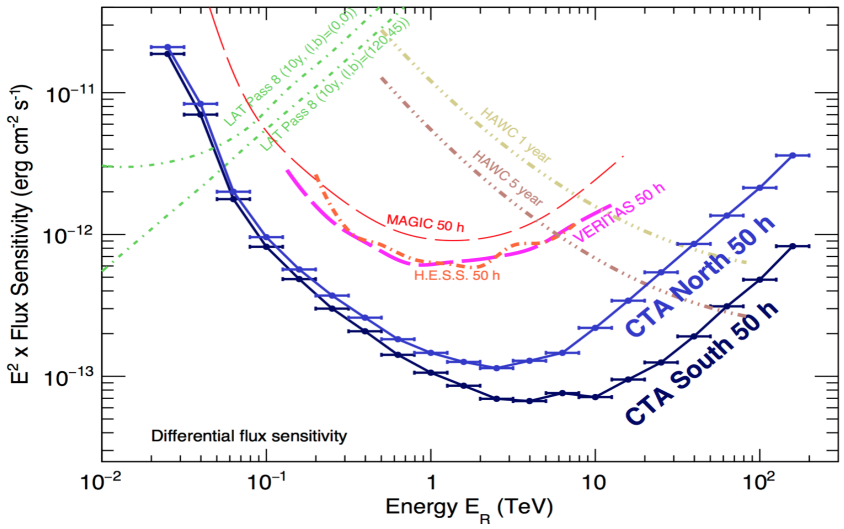

FIGURE 2.13: Differential sensitivity of several VHE instruments compared to the one expected for CTA. From `www.cta-observatory.org/science/cta-performance`.

In the same Figure, we observe that the sensitive energy range of IACTs instrument is limited at low energies and high energies due to two different types of phenomena. While at low energies the limitation comes from the systematic errors in background subtraction due to the high night sky and the cosmic-ray backgrounds, at high energies it is given by the limited instrumented area and the decrease in the photon flux from physical sources.

With CTA, a broad energy coverage for photons from 20 GeV to at least 300 TeV, will be provided by the different telescope design. In particular, the energy coverage down to low energies is assured by the high-statistic measurements performed by the LST. This will shed light on the connection between satellite measurements by *Fermi*-LAT and current IACTS, and the spectral behavior of source at those energies. The low energy coverage is essential in extragalactic physics, cosmology and transient

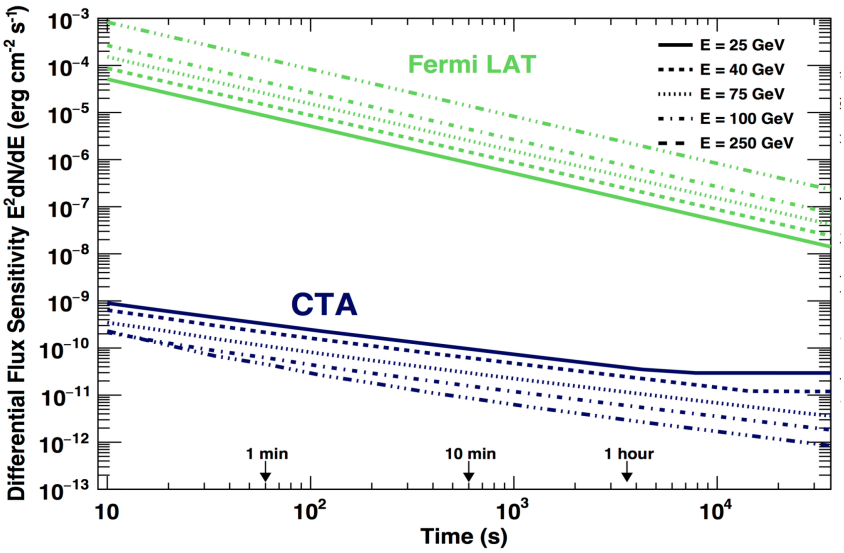

FIGURE 2.14: Differential flux sensitivity of CTA as function of observing time compared to the *Fermi*-LAT instrument sensitivity (`Pass 8` analysis, extragalactic background, standard survey observing mode)

studies. See Figure 2.17 for reference.

The strong increase of the detection area, which impacts the photon rate will improve the instrument capabilities to access transient physics (Figure 2.15, left), without leaving aside improvements in angular resolution and FoV. The invididual FoVs of the Cherenkov cameras are large, which has a double impact since they provide contained shower images up to large primary particle impact distance, which improves resolution and collection area (improving reconstruction), and increases the gamma-ray field of view of the system as a whole. This feature is essential to do morphology studies, extended sources with high resolution but also for following-up alerts with large uncertainty regions, which should be scanned in order to localize the counterpart as it is the case in multi-messenger triggers from neutrinos, GRBs with large uncertainty regions, e.g. *Fermi*-LAT or gravitational waves.

Finally, the last key feature is the flexibility in operations, allowing for simultaneous observations of objects in multiple fields. Rapid slewing of the telescope can be crucial to catch source undergoing flaring states and transient signals. Estimates on the slewing time of the LST telescope to reach any position in the sky are of $\sim$ 30 seconds, while $\sim$ 90 seconds for MSTs and SSTs, although efforts are in place to reach shorter slewing times.

Not only the Cherenkov Telescope Array will benefit from the experience and the updated technology compared to second generations IACTs, but also it will profit from the two CTA sites. As LST are planned to be part of both sites design, this will assure the coverage of the northern and southern sky by telescopes observing at low energies, establishing the link with observations performed by gamma-ray satellites.

Even though lot of improvements are planned, generally speaking the concept of the different trigger levels, the calibration procedure, the air shower reconstruction and analysis of the data will remain similar to the concepts explained for H.E.S.S. For this reason, I focus in the following mainly on the challenges it will face.

2.2.1 Telescopes

The two CTA sites have been chosen following the requirements for IACTs, and to optimize the coverage of the northern and the southern sky. The CTA-North array has been decided to be placed near the MAGIC telescopes at the Roque de los Muchachos in Canary Islands. In this site, the main focus is the low and mid-energies, ranging from 20 GeV to 20 TeV. On the other side, the CTA-South array, whose science present a special focus on galactic phenomena, is planned to be deployed near the Paranal Observatory in the Atacama Desert in Chile, within the European Southern Observatory's site. Schematic layouts of North and South CTA sites are shown in Figure 2.15.

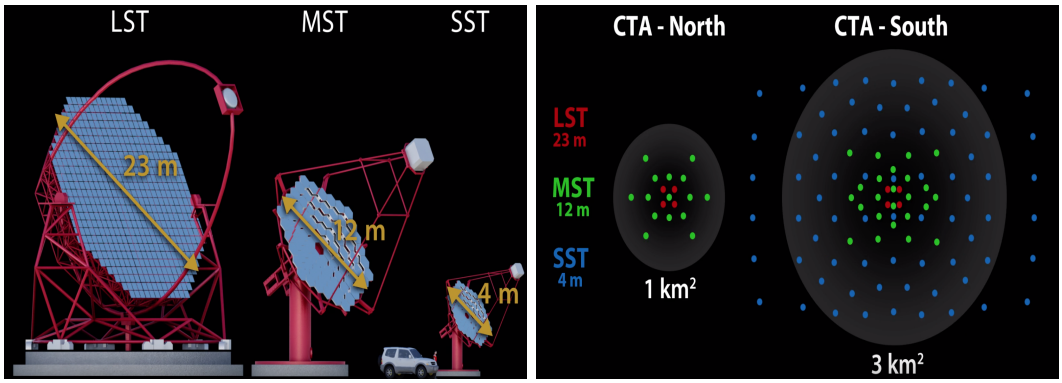

FIGURE 2.15: (Left) LST, MST and SST: the three designs of Cherenkov telescopes which are chosen to be part of CTA. (Right) Proposed layout for CTA North and CTA South sites. From `www.cta-observatory.org`

CTA has been designed to be a complementary two-site observatory with focus on different science topics, which translates to slightly different combination of telescopes per site. Whereas in CTA-N, the number of telescopes is smaller, in CTA-S, much larger in extension, the design has been chosen so that it will include three classes of telescopes, 4 Large Size Telescopes (LST), 25 Medium Size Telescope (MST) and 70 Small Size Telescope (SST), covering in total an energy range from 20 GeVs to 300 TeVs.

2.2.2 Analysis

The analysis of CTA data are inspired and are conceptually similar to the analysis explained in the section dedicated to the H.E.S.S experiment. However, one of the unprecedented challenges in IACTs that CTA is facing, due to the two sites, the number of telescopes and the expected rates, is the huge amount of data and thus,

ID	N_{tel} North/South	D (m)	FoV (°)	E_{range}	Slew time (s)
LST	4/4	23	∼5	20-200 GeV	< 20
MST	15/25	12	∼8	0.1-10 TeV	< 90
SST	-/70	4	∼10	5-300 TeV	< 60

TABLE 2.2: Summary of some of the principal features of the LST, MST and SST, including diameter, FoV, E_{range} and slewing time, and number of telescopes of each type expected to be placed in each site.

the data handling. In Figure 2.16, the definition of the several *data levels* of the CTA analysis pipeline and the expected reduction factor is given.

Data Level	Short Name	Description	Data reduction factor
Level 0 (DL0)	DAQ-RAW	Data from the Data Acquisiton hardware/software	
Level 1 (DL1)	CALIBRATED	Physical quantities measured in each separate camera, i.e. photons, arrival times, etc, and parameters derived from those quantities, per telescope	1-0.2
Level 2 (DL2)	RECONSTRUCTED	Reconstructed shower parameters per event, such as energy, direction, particle ID, as well as related signal discrimination parameters	10^{-1}
Level 3 (DL3)	REDUCED	Set of selected events (e.g. gamma-ray candidates), along with associated instrumental response characterization and other technical data needed to perform science analysis	10^{-2}
Level 4 (DL4)	SCIENCE	High level binned data products like sky maps, spectra, and light curves	10^{-3}
Level 5 (DL5)	OBSERVATORY	Legacy observatory data	10^{-5}-10^{-3}

FIGURE 2.16: Preliminary, ever-evolving definition of the CTA data levels and the reduction factor expected for each step of the chain of reconstruction and analysis.

Instrument Response Functions

The baseline performance expected for CTA is quoted in the Instrument Response Functions (IRFs), which have been obtain from Monte Carlo simulations of the telescopes (Hassan et al., 2017) based on the CORSIKA air shower code (Heck et al., 1998) and telescope simulation tools (Bernlöhr, 2008). The background cosmic-ray spectra of proton and electron/positron particles are modeled using recent measurements of cosmic-ray instruments.

These IRFs are essential in current studies as they describe the expected instrument capabilities and contain all the dependency of performance parameters, as energy or angular resolution with the energy and direction of observation [2].

They have been produced for the CTA Northern Site and the CTA Southern Site, for different zenith angles (20°, 40° and 60 °) and 3 different observation times (0.5h, 5h, 50h). The analysis cuts are tuned to be optimal and maximize the flux sensitivity. The off-axis differential sensitivity curves, of special interest in the case of transient searches, are shown in Figure 2.17, for the North and South facilities.

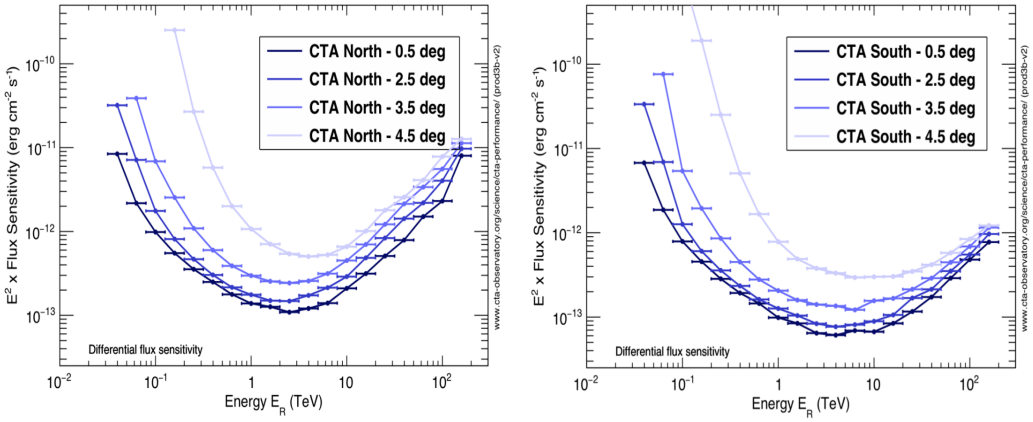

FIGURE 2.17: Differential sensitivity curves for point-like source at different angular distances from the center of the FoV of the observation. From `cta-observatory.org`

Real-Time Analysis

The Real Time Analysis (RTA) science alert system is a product of the CTA On-Site Analysis (Bulgarelli et al., 2015), which is being prepared for fast identification of flaring events. The RTA system presents different analysis products which are associated to different latencies and sophistication. In the On-Site Analysis (OSA)/Level A analysis pipeline, while observations are ongoing, the collected data is calibrated and reconstructed using air-shower imaging techniques. A variability analysis is performed on different timescales, from second to hours. The CTA design goals for the latency of the RTA pipeline is set to 30 seconds for a scenario where the flux of the observed VHE emission is three times the nominal sensitivity of CTA. Then, once the data acquisition finished for a given night, the OSA/Level B analysis is designed to perform a refined analysis of the observations. In this case, the expected latency for the results reaches 10 hours.

First results on the performance of the RTA computed using CTA MC simulations are shown in Figure 2.18. These have been derived for the CTA-Southern array, a Crab-Like index power law spectrum at the center of the FoV at zenith angle of 20° (Fioretti et al., 2015). The differential sensitivities in Figure 2.18 illustrate the

[2] `https://www.cta-observatory.org/science/cta-performance/`

improvements of the sensitivity of CTA, as few hours of observation will obtain similar sensitivities than 50 hours of observations with current generation IACTs as MAGIC and VERITAS.

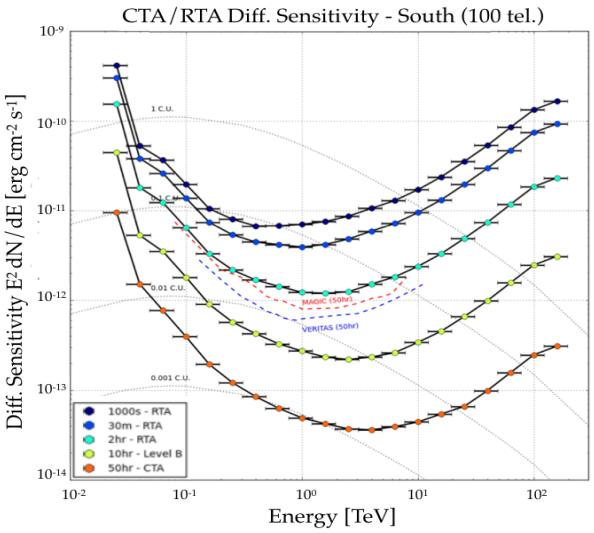

FIGURE 2.18: Differential sensitivity of the OSA/RT and OSA-Level B analysis pipelines computed for five observation times. Dashed lines correspond to the MAGIC and VERITAS sensitivity for an observing time of 50 hours. From Fioretti et al., 2015

Open Source Analysis frameworks

In the context of an evolution towards an Open Source Software and Tools domain, the software development to be used in the new generation of VHE observatories has been done in the spirit of *for anyone and for any purpose*. The main characteristics of the CTA analysis frameworks involve modular design, as a constant evolution of the software is expected, accuracy and reproducibility. From this basis, two analysis software prototypes are been developed: the Python based `gammapy` and C++ based `CTools`. Although these are software prototypes for CTA analysis, both support classical IACT analysis, using data from H.E.S.S., MAGIC or VERITAS.

`Gammapy` is an open-source `Python` package developed for gamma-ray astronomy purposes by the community (Donath et al., 2015) and built on `Numpy` and `Astropy` packages. The scope of the software is to incorporate code for data handling, background modeling and source detection, statistical methods and simulation of point sources, etc.

`Ctools`, whose development has been strongly inspired by the *Fermi*-LAT science tools, is a software package to analyze CTA data based on GammaLib, a toolbox for the high-level analysis of astronomical gamma-ray data (Knödlseder et al., 2016).

2.3 HAWC experiment

The High-Altitude Water-Cherenkov (HAWC) observatory is a ground-based air-shower particle detector observing the Universe at high energies, sensitive to cosmic-ray primaries of energies between 50 GeV and 100 TeV. The array, composed of Water Cherenkov Detectors (WCDs) of two different sizes, is operated by an international consortium of 4 countries and 34 institutions. It is located at 4100 meters above sea level, at 97.3° West longitude and 19° North latitude in Sierra Negra, Mexico. The HAWC experiment is presented in Figure 2.19.

FIGURE 2.19: The HAWC observatory, where the smaller water tanks known as outriggers can be seen surrounding the main water Cherenkov tanks in a denser configuration in the center.

Its large FoV, covering ∼2 sr of overhead sky at any given moment and its large duty cycle, taking data more than 95% of the time, makes HAWC an ideal instrument for VHE transients searches. In Figure 2.20 the HAWC differential sensitivity to 1 s bursts is given, defined as the mean flux in a given half-decade that would result in *at least* a 5 σ detection half of the time.

2.3.1 Instrument and site

Water Cherenkov Detectors

The HAWC detector is an array of 300 large WCD which corresponds to a total collection area of 22000 m^2. The design of each large WCD is based on cylindrical steel tanks of 7.3 m in diameter and 5 m height, which contains a light-tight plastic lining, filled with 188.000 L of purified water. The tank height is chosen to provide enough large volume for the particles of the air shower to range out before they reach the bottom of the tank. In this way, as all the energy of the particle is deposited in the tank, the light recorded in the tank can be directly related to the total electromagnetic energy in the shower at the location of the WCD. Moreover, an additional motivation to the tank height is to veto muon showers, which are present

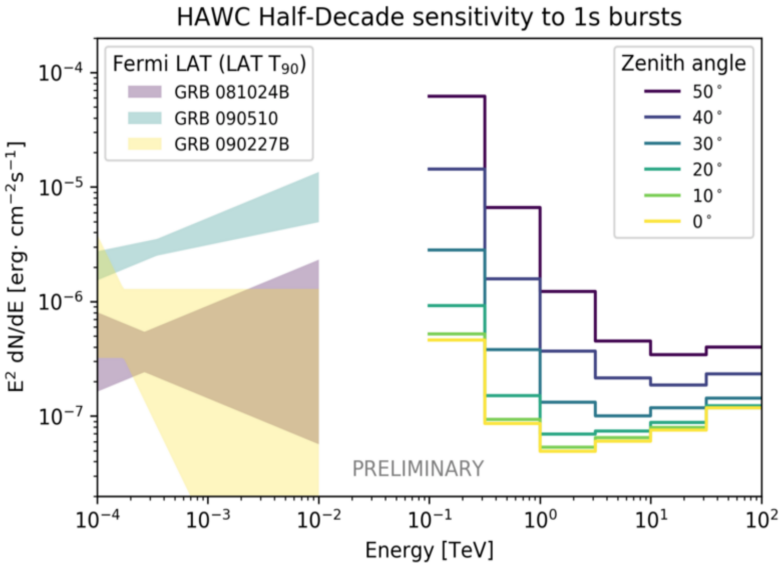

FIGURE 2.20: HAWC differential sensitivity to 1 s bursts, for different zenith angle bands, which has been defined as the mean flux in a given half-decade that would result in *at least* a 5 σ detection half of the time. Several sGRBs detected by Fermi LAT, as measured in in the GBM window, have been included in the figured for reference (From Ackermann, et al. 2013). From Martinez-Castellanos for the HAWC collaboration

in air showers initiated by hadrons. The water overburden of 4 m is *short enough* to allow muons with the median muon energy produced in air shower to travel the entire water height. Hadronic showers are irregular and chaotic, and present a large transverse momentum, as seen in Figure 1.14. Hence, observing particles far from the shower axis which sometimes only triggering one of the PMTs of the tanks, is strong indication of the hadronic nature of the shower.

The selection of water as main detector material is due to its *relative* large index of refraction which favors the Cherenkov light emission process, the transparency of the medium to the propagation of the Cherenkov light towards the PMTs and its comparable cheap price. The water, which has been purified in order to remove contaminants, results in an attenuation length of $\sim$ 10 meters for the wavelengths to which PMTs are sensible.

In addition, a total of 315 smaller WCD, in the following referred as the *outriggers* are distributed sparsely around the large WCDs. These are cylindrical, steel tanks of 1.5 meters in diameter and 1.65 m height. The *outriggers* have been deployed to increase the instrument area by a factor $\sim$ 4, with the motivation of better resolving the core location for large air-showers, which fall off the main array. This improvement in reconstruction translates into an improvement of the sensitivity of the array to high energy events (Joshi and Jardin-Blicq, 2017). The outriggers, surrounding the main array, are shown in Figure 2.19.

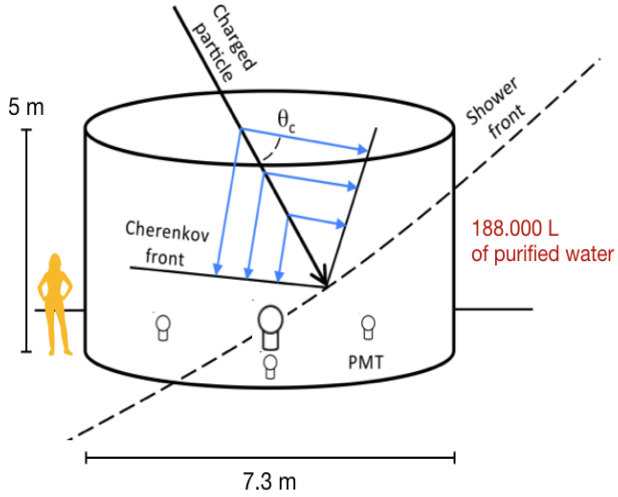

FIGURE 2.21: Secondary particle of the air shower entering the WCD and producing Cherenkov Light. Modified from Abeysekara et al., 2012.

Photomultiplier Tubes and Signal processing

There are 4 PMTs on the bottom of the large WCD, facing upward to observe the Cherenkov light produced by the air showers, as shown in Figure 2.21. In the case of the outriggers, only one 8" PMT has been anchored to the top of the tank. For the large WCDs, the central high-quantum efficiency Hamamatsu 10" R7081 PMT is placed at the barycenter of the equilateral triangle formed by other three Hamamatsu 8" R5912 PMTs located at a distance of 1.85 meter of the central PMT. The 10" PMTs has been selected in order to provide additional sensitivity at low-energies, and they present a factor $\sim$ 2 of improvement on the total collection efficiency for photons, including the quantum efficiencies. They are sensitive enough to detect single photons and their fast response speeds is of $\sim$10s of nanoseconds. An illustration of the PMTs used in the HAWC observatory is given in Figure 2.22.

The PMT signals are sent to the data acquisition system (DAQ) which consist on a set of analog front-end electronic boards (FEBs). The signal is processed and a single digital waveform is output. Afterwards, this waveform is recorded by CAEN time-to-digital converters (TDCs) and the result is transmitted to the computing cluster on-site to proceed with the reconstruction and analysis. A summary of this process is given in Figure 2.22. Further detail on the signal processing by the HAWC DAQ can be found in Wood, 2018.

2.3.2 Reconstruction and Analysis

The on-site computing cluster of the HAWC observatory is able to perform the air-shower triggering and the reconstruction of the shower parameters in real time, at latencies of $\sim$ 4 seconds. The real-time response is a key feature to enable fast reaction to transient events. The obtained data is stored and transfer for off-line analysis,

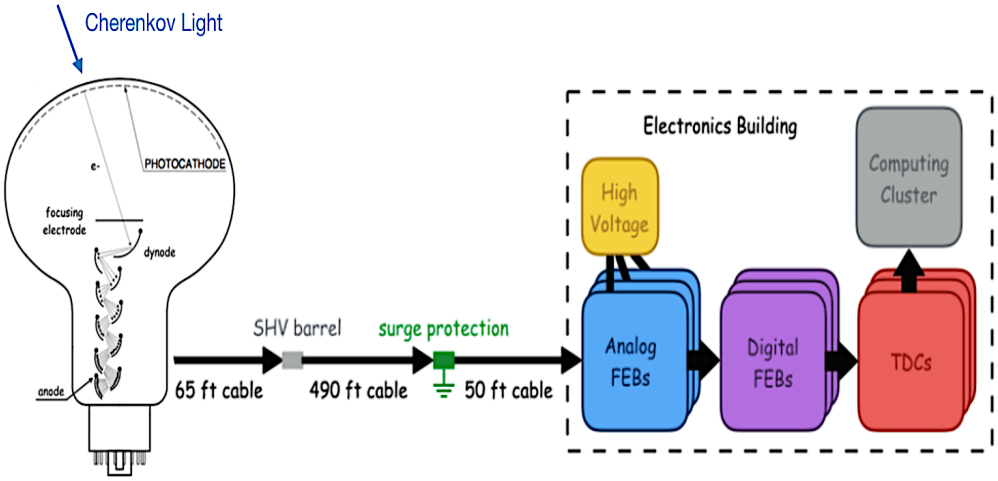

FIGURE 2.22: Diagram of the signal processing from the PMT recording the Cherenkov light emission to the computer cluster. Adapted from Wood, 2018

to be reconstructed with dedicated calibration and reconstruction algorithms.

The localization of the shower core fit is an essential step to reconstruct the air-showers, since is a main ingredient to determine the shower curvature, which impacts the angular resolution of an observed source. Within the HAWC reconstruction, the shower core is defined as the location of maximal energy deposition at ground level.

When an air-shower triggers the HAWC experiment, the mean lateral distribution, which is described by the profiles derived by Nishimura-Kamata-Greisen (NKG)(Greisen, 1960), is recorded as photoelectron charges in the PMTs. The likelihood of observing N charge measurements Z_i, with respect to the mean expected charges $Q(\vec{x})$ fixed by the shower direction and the core location is given as:

$$-2\log\mathcal{L} = \sum_{i=1}^{N} \frac{(Z_i - Q(\vec{x})_i))}{Q(\vec{x})_i + \sigma_i^2} \tag{2.11}$$

In order to obtain the location of the shower core, Equation 2.11 is maximized for all the PMTs of the array, following several approximations which are applied to reduce the computation time. Examples of core fitting are given in Figure 2.23.

The next step after the determination of the shower core location is the reconstruction of the direction of the incident particle. The time registered by all PMTs is compared to a flat timing plane distribution corrected with effects of shower curvature, as a function of the measured charge and the distance to the shower core. Although this timing correction is less than 0.15 nanoseconds per meter of distance to the core, it play a crucial role on the angular resolution of the air shower (Wood, 2018).

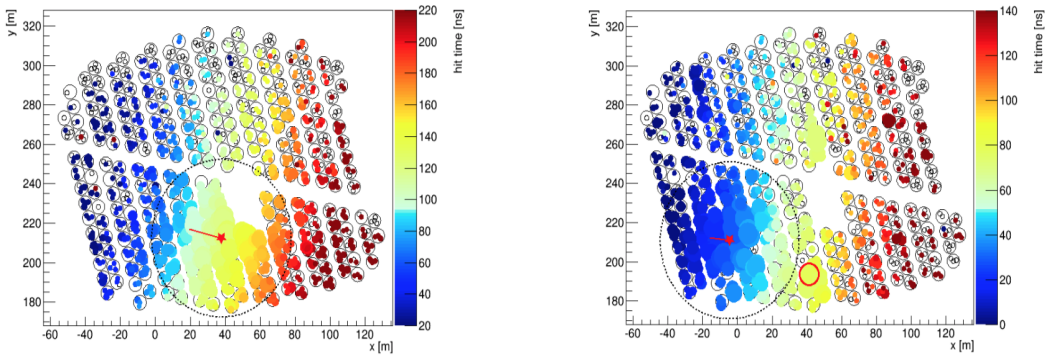

FIGURE 2.23: (Left) PMT measurements and core fitting for a simulated gamma-ray of 47 TeVs and (right) for a proton shower of 7 TeVs. Size of circles refers to the total number of measured photoelectrons at the PMT. Green star stands for the simulated core location, and red star stands for the reconstructed core location. From Wood, 2018.

The following step in the reconstruction of an air shower is the identification of its hadronic or electromagnetic nature. To this aim, the variables of `compactness` and `PINCness` are considered (Abeysekara et al., 2017a).

- `Compactness`: This gamma-hadron separation variable is defined as the largest local deposition of energy far from the shower, at R >40 m, relative to the overall shower size, which is quantified by the number of PMT signals measured within 20 ns of reconstructed shower front:

$$\mathcal{C} = \frac{N_{20}}{Q_{max}(R > 40\text{m})} \tag{2.12}$$

  This variable takes high values for electromagnetic showers since they are *compact* in nature. In contrast, hadronic showers and off-axis cascades are characterized by low values of compactness, due to the lateral extension they present.

- `PINCness`: This gamma-hadron separation variable has been defined to quantify the smoothness of the lateral distribution function (LDF). $\mathcal{P}$ is computed using the χ^2 formula, and obtained using in the total number of PMTs N, in N_R annuli bins of 5 m which include N_i PMTs, and added up as:

$$\mathcal{P} = \frac{1}{N}\sum_{i=0}^{N_R}\left(\sum_{n=0}^{N_i}\frac{(Q_n - Q_i)^2}{\sigma_i^2}\right) \tag{2.13}$$

  where Q_i is the average charge, measured with an uncertainty σ_i. As previously mentioned, gamma-ray showers have smoother LDFs than hadronic air showers.

Skymaps and Energy spectrum

Next step after the reconstruction is to generate event maps, with the histogram of arrival directions of reconstructed events and background maps, computed using direct integration method (Atkins et al., 2003). The analysis is typically separated in nine bins which have been defined by the % of the array which has been triggered, f_{hit} (Abeysekara et al., 2017b).

The sky maps are obtained using the maximum likelihood analysis framework described in Younk et al., 2015. The likelihood $\mathcal{L}$ of a model is given by the comparison of the observed event counts with the expected counts, computed for all pixels in the region of interest and the nine analysis bins. The test statistic is defined as the likelihood ratio obtained by comparing the signal hypothesis model to the null hypothesis as:

$$TS = 2\ln\frac{\mathcal{L}^{MAX}(\text{Source model})}{\mathcal{L}(\text{Null model})} \tag{2.14}$$

where in the null model the expected number of counts are given by background-only maps and in the source hypothesis the expected counts, a signal contribution obtained from simulations is added to the background of the null model. A source model defined by a spectral model and a spatial model and the instrument response functions are considered to compute the signal contribution. Following Wilks' Theorem and considering that the source and null model are nested; the TS is distributed as a χ^2 with one degree of freedom if the statistics are sufficiently large. Hence, the pre-trial significance is given by the square root of the test statistic, $\sqrt{\text{TS}}$. Further detail on the computation of sky maps in the HAWC analysis framework can be found in (Abeysekara et al., 2017b).

The energy of the events is estimated using the *energy estimators*. To this aim, two independent methods, the *ground parameter* algorithm and *neural network* algorithm, which use air shower variables as the core position, shower angle or shower lateral distribution, have been developed. More details can be found in Abeysekara et al., 2019. Then, the energy spectrum of a source in the HAWC analysis framework is obtained using a *forward folding* technique.

Part II

Variable extragalactic gamma-ray emitters

Chapter 3

Studying the blazar sequence with OT081

Contents

3.1 Active Galaxy Nuclei

Active Galactic Nuclei (AGNs) are among the most interesting astrophysical sources, known for being the most luminous objects and efficient energy converters in the Universe. The study of AGNs is linked to the understanding of energy sources, the study of galaxy evolution and morphology of galaxies, as well as their interactions. These extragalactic objects, present in $\sim$ 1% of all galaxies in the Universe, are powerful sources emitting at a sustained rate.

AGNs are compact regions at the center of galaxies, whose luminosity is larger than the contribution from the stars of the host galaxy. This amount of energy can not be explained by thermonuclear reactions, but is produced by gravitational forces in extreme environments. The origin of the high luminosities of an AGN is the gravitational force generated by the accretion onto a supermassive black hole (SMBH), of $M_{SMBH} \sim 10^6 - 10^9_{M\odot}$, at the center of the galaxy (Urry and Padovani, 1995). The gravitational energy of the matter spinning around the SMBH is transformed through viscous and turbulent processes into thermal energy, which forms a disk of material, known as *accretion* disk (Rees, 1978). The accreting material rotates around the central engine and an outward transfer of angular momentum is achieved through viscosity. Infalling matter loses angular momentum and it is heated, increasing the emitted radiation until the event horizon of the SMBH is reached and matter falls into it. This process is responsible for the increase on the brightness of the electromagnetic flares at different timescales.

Examples of the observational signatures of the accretion process in AGNs are the strong radio emission, strong emission lines in the optical range, broad-band continuum spectra and fast temporal variability.

3.1.1 Unification models

A first classification of AGNs was introduced by Kellermann et al., 1989 in the context of the Palomar Bright Quasar Survey observations with the Very Large Array (VLA) in radio frequencies. The sources were classified as either *radio-loud* or *radio-quiet* based on the ratio between the radio luminosity at 5 GHz and the luminosity in the optical B-band:

$$R = \frac{F_\nu(5\mathrm{GHz})}{F_\nu(\mathrm{B})} \tag{3.1}$$

For R values larger than 10, the source is classified as *radio-loud*, which corresponds to $\sim$ 10% of the AGNs and *radio-quiet* for sources with R <10. It was later realized that radio-loud objects produce large scale radio jets where the kinetic power of the jet represents a significant fraction of the total bolometric luminosity and lobes due to the interaction with the interstellar medium (Baum and Heckman, 1989). Furthermore, the radio-loudness of an AGNs is linked to the gamma-ray emission.

The distinction between radio-loud and radio-quiet AGNs gave rise to the first unification ideas, which aim to established a link between the different AGNs types. This revolutionary reinterpretation of the data connected the observational effects of relativistic beaming to the source orientation (Barthel, 1989).

A review of the different attempts to classify the inhomogeneous emission observed from AGNs can be found in Mickaelian, 2015.

In the mid-1990s, the reinterpretation of the AGN types and their spectral characteristics were formally established by Urry and Padovani, 1995. They proposed that the different features seen in the spectra of the objects is the result a geometrical effect, caused by the orientation of the compact object with respect to the observer. Hence, the various AGN classes, in a first approximation, could be differentiated by the viewing angle and the presence and strength of a radio jet. The compact object in the center of the galaxies, seen from different viewing angles, was described as a SMBH accreting matter and ejecting some portion of it through collimated jets of particles accelerated to ultra-relativistic energies, perpendicular to the accretion disk. A schematic view of the unification model for AGNs, from radio-loud to radio-quiet AGNs, can be found in Figure 3.1.

The SMBH is placed at the center of the galaxy in a very compact region, around less than few tens of light days. Then, a luminous accretion disk surrounds the SMBH and an optically thick, obscuring dusty torus (Jaffe et al., 1993). The inner part of the torus structure interacts with the optical and UV photons present in the accretion disk, producing infrared emission through thermal processes as blackbody absorption. The obscuring toroidal structure around the SMBH plays a fundamental role in the observational effects tackled in unification models. It typically expands from tens to hundreds of parsecs away of the SMBH.

In the clouds orbiting the central engine, two regions are differentiated. The closest region to the central engine at a distance around hundred of light-days, where broad emission lines are produced is known as the *broad-line* region (BLR). The BLR is thought to be formed by individual high-density gas clouds of electron densities $n_e \geq 10^9$ cm^{-3}, moving around the SMBH in Keplerian orbits.

The spectra of some AGNs include narrow emission lines, which are thought to be produced by low density, ionized gas with typical densities between $n_e \sim 10^3 - 10^6$ cm^{-3}. This region is located farther from the compact object, at hundreds of parsecs, and it is known as the *narrow-line* region (NLR).

Relativistic jets are highly collimated plasma outflows accelerated at relativistic energies, which are thought to be formed by the coupling of the accretion disk and the magnetic field of the SMBH. Nevertheless, connecting with Chapter 1, the acceleration process of the particles in the jet is still under debate, although in first approximation they are thought to be accelerated through the first order Fermi acceleration mechanism in internal shock waves.

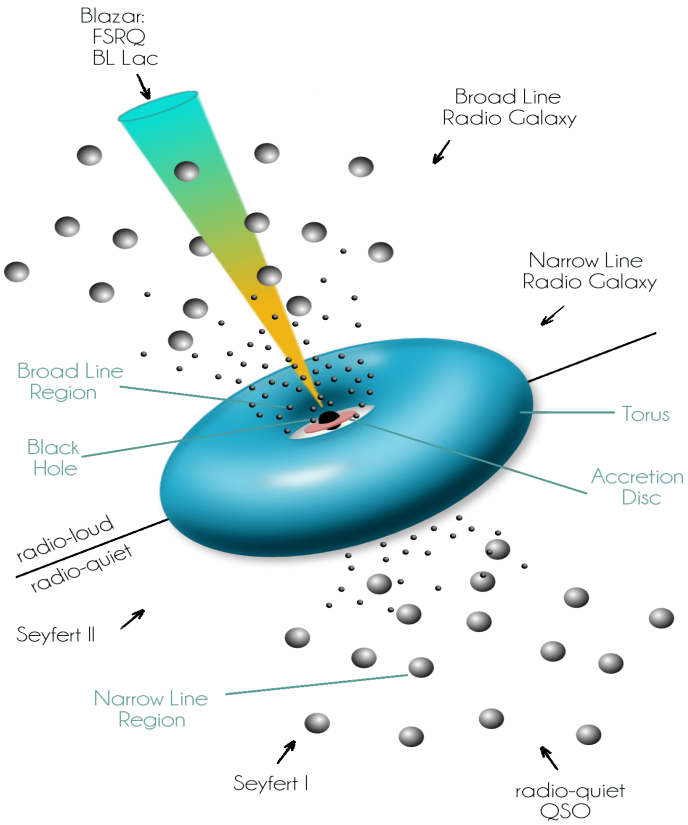

FIGURE 3.1: Unification scheme of AGNs. From F. Krauß, based on Urry and Padovani, 1995

The study of AGN jets started in 1917 with M87 (Curtis, 1917), at radio frequencies. Through the years, developments on radio astronomy have played a key role in a better understanding of AGN jet physics. Nowadays, they are observed at different wavelengths, up to very high energy gamma-rays as shown recently by the H.E.S.S. preliminary results on Cen A (H.E.S.S. collaboration, 2018). Different jet morphologies have been observed: from long and smooth to short and chubby and presenting either straight or curved shapes. In some cases, knots are also present in the jets, which can be static or move in the jet at either sub-luminal or superluminal velocities.

3.2 Blazars

Amongst the different AGNs subclasses, the *blazing quasi-stellar radio sources* commonly referred as blazars are the jetted AGNs whose relativistic jet is oriented closely to the line of sight. Due to the closely aligned jet axis with the viewing angle of the observer, these radio-loud objects present a featureless optical spectra (Blandford and Rees, 1978). They show non-thermal emission with rapid variability, down to

timescales of $\sim$ sub-minutes, as observed for PKS 2155-304 by H.E.S.S (Aharonian et al., 2007). Other characteristics of blazars include highly variable optical polarization, superluminal motion and strong γ-ray emission (Strittmatter et al., 1972).

Relativistic beaming

Observed quantities in jetted AGNs, as it is the case for blazars, suffer from relativistic effects. The effect is known as *relativistic beaming*. The relativistic beaming is described by the *relativistic* Doppler factor δ, which connects the observables on the jet reference frame as:

$$\delta = \frac{1}{\Gamma(1 - \beta \cos\theta)} \tag{3.2}$$

with $\Gamma = 1/\sqrt{1-\beta^2}$ known as the Lorentz factor. Note the difference from the *usual* Doppler factor which is given as $1/(1 - \beta\cos\theta)$.

The apparent speed of blazar emission regions can reach superluminal values due to this relativistic effects, as it has been observed in Very-Long-Baseline Interferometry (VLBI) kinematic studies of propagating jets, whose apparent speed distribution peaks around 10 c, with values up to 50 c (Homan, 2012).

The apparent luminosity L_{obs} observed from jetted AGNs aligned with the line of sight relates to the intrinsic luminosity L_{int} in the jet reference frame as:

$$L_{obs} = \delta^n L_{int} \tag{3.3}$$

where the exponent n is given as $n = p + \alpha$, with p is the the Doopler boost exponent and α the spectral index of the radiation, which in the case of flat spectra, $\alpha = 0$ (Cohen et al., 2007). Another important quantity in AGN studies is the brightness temperature, which relates the non-thermal emission to a thermal temperature, as if the non-thermal radiation was produced as a blackbody emission. For further details on these, the basic relationships between *jet properties* and observed quantities from blazars, as observed by radio/VLBI, can be found in (Ros, 2008).

3.2.1 Radiative processes

Blazars emit across the electromagnetic spectrum, from radio to gamma energies. In order to represent the broad-band emission efficiently at different energies (or frequencies), Spectral Energy Distributions (SEDs) are used. In some cases, the consideration of the broad multi-wavelength spectrum may be the only clue to true classification, as it is the case in some AGNs whose emission in optical wavelengths is obscured or there is an absence of radio and/or X-ray emission.

Their non-thermal SED $E^2 \frac{dN}{dE}$ produced by its jet presents a peculiar overall structure with two broad humps, which typically peak in the IR/soft X-ray band and in the MeV-TeV band. An example of a SED of a BL Lac is presented in Figure 3.2.

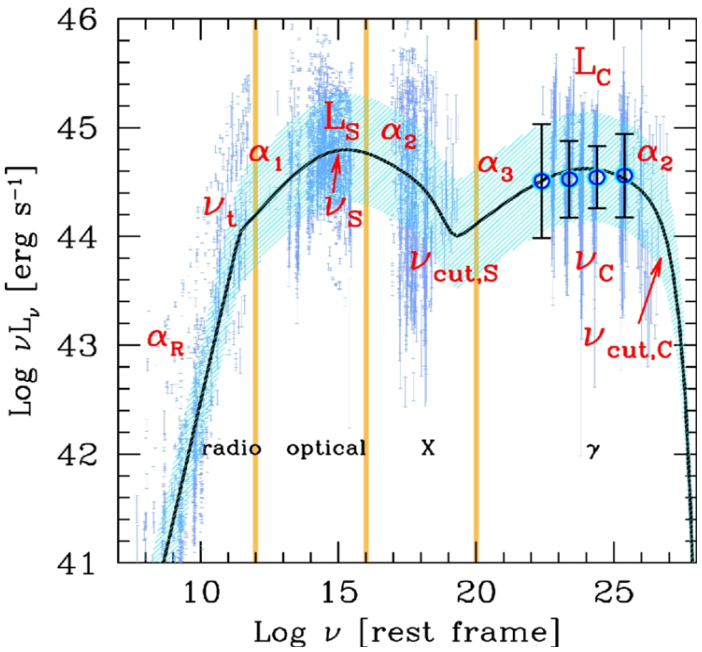

FIGURE 3.2: Illustration of a Spectral Energy Distribution over the entire electromagnetic spectrum from a model describing a high synchrotron peak blazar, where the two humps from synchrotron radiation emission and Inverse Compton radiation emission are observed. The main parameters of the model, which allow to characterize the shape, as the luminosities in the two bumps and the different indices, are indicated. From Tavecchio et al., 2017

Low energy emission in AGNs

Regarding the origin of the emission of the non-thermal SED, there is a consensus on the physical mechanism underlying the first bump. It is explained by the synchrotron radiation that it is emitted when charged particles, usually electrons and positrons, interact with magnetic fields and spiral along the jet. This synchrotron component peaks between the IR and the UV/soft X-ray band, depending on the source.

The energy losses by synchrotron radiation of a population of electron in a environment characterized by a magnetic energy $U_B{=}B^2/2\mu_0$ is proportional to the relativistic Doppler factor as γ^2 and to the magnetic field as B^2:

$$-\left.\frac{dE_e}{dt}\right|_S = 2\sigma_T\beta_e^2\gamma_e^2\sin^2\theta U_B \xrightarrow{\text{averaged over angles}} -\left.\frac{dE_e^{iso}}{dt}\right|_S = \frac{4}{3}\sigma_T\beta_e^2\gamma_e^2 U_B \quad (3.4)$$

with σ_T being the Thompson cross section.

High energy emission in AGNs

The second bump of the SED of blazars typically peaks between MeV and TeV energies. The models trying to account for the high-energy bump are divided into two classes: *leptonic* models and the *hadronic* models. The interactions giving name to these two models have been discussed in Chapter 1.

In leptonic models, the high-energy emission is explained by an IC mechanism, with a low-energy photon field as a seed. In the case where the seed photons are the ones produced by synchrotron emission in the jet, they interact with the *original* electron population, the radiation process is referred as *Synchrotron Self-Compton* (SSC) (Band and Grindlay, 1986). In the case of the simplest SSC model, the *one-zone SSC model*, the relationship between the ratio of the total luminosity of the synchrotron peak L_S and the total luminosity of the IC component L_{IC}, and the radiation energy density U_S and the magnetic field energy density U_B in the source, is expressed as:

$$\frac{L_{IC}}{L_S} = \frac{U_S}{U_B} \tag{3.5}$$

The mean energy loss from the electrons in the IC process can be written as:

$$-\left.\frac{dE_e}{dt}\right|_{IC} = \frac{4}{3}\sigma_T \beta_e^2 \gamma_e^2 U_S \tag{3.6}$$

where we observe the linear dependency of the mean energy loss of electrons with the radiation energy density from the seed photons. If we consider that the radiation energy density from the seed photons is related linearly to the synchrotron luminosity following $U_S = L_S/S$, where the S is the surface of the emitting region, we obtain that the luminosity of the two components of the SED for a One-Zone SSC model are quadratically related as $L_{IC} \propto L_S^2$.

Another possible origin of the seed photons producing the second bump of the spectra energy distribution is at the exterior of the jet. The seed photons at different wavelengths can come from the accretion disk, in the case of optical/UV photons, the hot corona for X-ray photons or the thick, dusty torus, in case of infrared photons. In those cases, the process is then known as *External inverse-Compton* (EIC) process (Finke, 2016).

In hadronic models, the responsible process of the high-energy emission is the photo-hadronic interaction of protons ($p\gamma$) or a proton-proton (pp) interactions which results in the production of π^0, which subsequently disintegrates into VHE gamma rays. Nevertheless, hadronic interactions have difficulties to explain the observed fast variability in blazars. For further details, the reader is invited to consult Böttcher, 2007.

3.2.2 Fast variability

Blazars emission undergo variability episodes which cover timescales ranging from seconds to weeks. Although the origin of such flux variability is still not clear, the

emission region is thought to be caused by disturbances created near the black hole, in the accretion disk. Thus, variability episodes put constrains on the emission zone radius by causality. The upper limit to the emission region of size R given the observed time variability and the redshift of the source, as:

$$R \leq \delta \frac{t_{var}}{(1+z)} \tag{3.7}$$

However, that view was challenged by the observation of ultra-fast flux variability at TeV energies for both PKS 2155-304 (Aharonian et al., 2007) and Mrk 501 (Albert et al., 2007) on minute timescales. For the inferred black hole masses, flux variability was still to two orders of magnitude faster than the shortest possible timescales. Thus, TeV observations indicated that the variability would involve enhanced emission in a small region within an outflowing jet (Begelman, Fabian, and Rees, 2008).

3.2.3 Blazar Sequence

Blazars are considered as one family of objects, since the physical processes that the sources undergo have been considered similar, allowing to some scaling factors (Fossati et al., 1998). This differentiation give birth to the subdivision of blazars, known as *the blazar sequence*. All blazars have a feature in common: their bolometric luminosity is anti-correlated with the position of the synchrotron peak.

The first subdivision in two different subclasses is defined by looking to the presence of emission lines from the BLR in the optical range, which related to their relative strength with respect to the non-thermal emission (Stickel et al., 1991). The two subclasses are known as *Flat spectrum radio quasars* (FSRQs) and *BL Lacertae* (BL Lacs). These together form a *blazar sequence* of increasing accretion power of similar SMBH, which translates into observable variations of the peak luminosity frequencies in the SED.

Flat spectrum radio quasars show strong emission lines, high bolometric luminosity ($10^{46} - 10^{48}$ erg s^{-1}) and have the synchrotron peak in the sub-mm range and IC peak in MeV bands. These objects have efficient radiatively efficient accretion disks, which are able to ionize the clouds of the Broad Line Region. Then, the dusty torus intercepts part of the disk luminosity, and re-emits the absorbed luminosity in the IR. These photons, which are produced externally to the jet, can be used as seed for the Inverse Compton process, thus reaching very powerful high-energy luminosities. Due to this process, the second hump dominates over the lower frequency hump, which gives them the denomination of blazars showing *Compton dominance*.

BL Lacertae objects show lower bolometric luminosities ($10^{45} - 10^{46}$erg s^{-1}) and weak or null emission lines, which sometimes makes it difficult to know their redshifts. They have an inefficient disk which does not ionize the BLR clouds, which then results on a lower number of seed photons to be scattered at high energies. The radiative cooling is weaker, which makes the emitting electrons reach higher energies,

and thus, making this sources be relatively strong TeV emitters. BL Lacs can be further classified depending on the synchrotron peak position: the low frequency-peaked BL Lacs (LBL), the intermediate frequency-peaked BL Lacs (IBL) when they peak in the visible/UV wavelengths, the high frequency-peaked objects when their peak is in UV/X-rays and lastly, the extreme-high frequency-peaked BL Lacs, at high-energies (EBL).

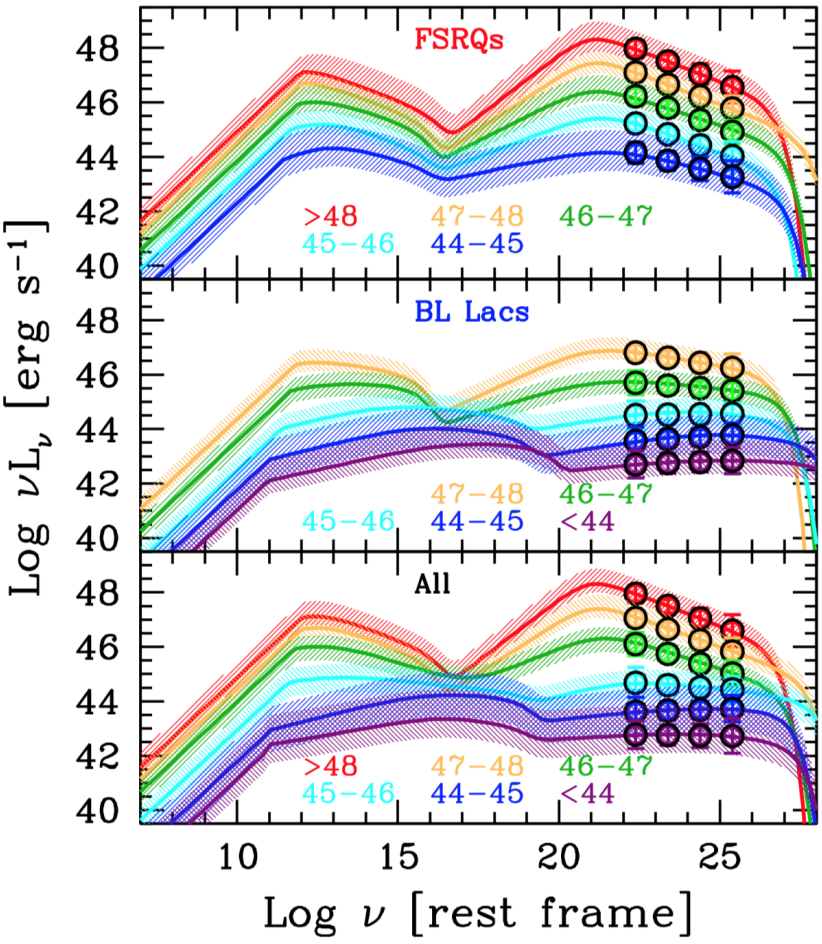

FIGURE 3.3: Revisited *Fermi* blazar sequence. From Tavecchio et al., 2017

In Figure 3.3, it can be observed that the synchrotron peak presents a shift in energy for different blazar types. This translates into a overall shift of the two bumps, which means that the X-ray component of the SED is produced by different mechanisms depending on the blazars class.

In its original form, the sample was subdivided according to their bolometric luminosity, which correlates with the 5 GHz radio luminosities in five bins (Fossati et al., 1998). The recent results on the revisited blazar sequence compared the averaged SEDs from a *total blazar sample* binned according to γ-luminosities using *Fermi*-LAT data. This fact gives the name to the (revisited) *Fermi* blazar sequence, presented in

Figure 3.3.

Other results of the recent studies regarding the blazar sequence showed the observational bias of observing in γ-rays at that time with EGRET, since it was less sensible than the other instruments providing data for the SED (Ghisellini et al., 2017). In Figure 3.4, the γ-rays luminosity of the sample of *Fermi* blazars is represented against their redshift. The diagonal lines represent approximate flux limit of EGRET and *Fermi* and horizontal lines indicate the *gamma*-ray luminosities, which are considered in the paper. This defines a new blazar sequence which is now γ-ray motivated instead of 5-GHz motivated. The BL Lacs objects are represented by blue points, whereas red points correspond to FSRQs.

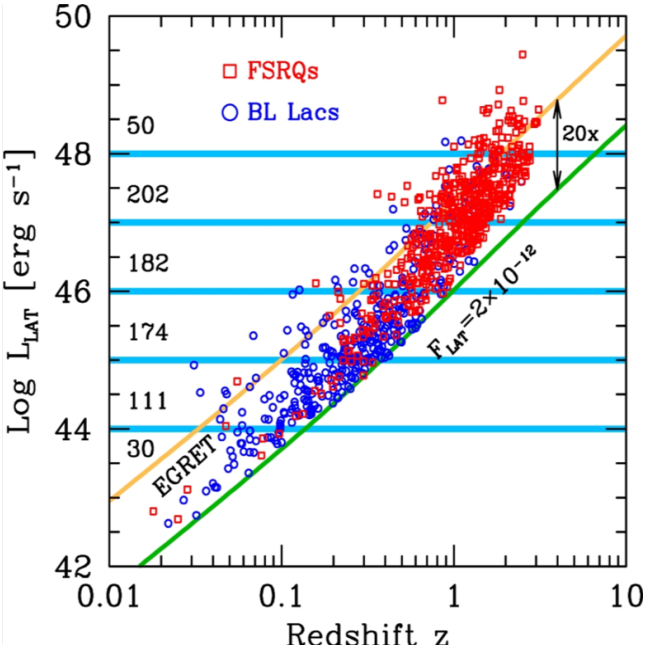

FIGURE 3.4: K-corrected gamma-ray luminosity (in the rest frame 0.1–100 GeV band) of the 3LAC catalog blazars with known redshift as a function of their redshift. The sensitivity of Fermi-LAT for the 3LAC catalog, as well as the EGRET approximated sensitivity, are plotted in diagonal, showing that the almost a factor 20 of improvement yield to the discovery of less γ-luminous blazars. The objects are classified as either FSRQs or BL Lacs (as in the 3LAC catalog), with an important overlap at mid-redshifts. Horizontal lines refer to the recently proposed bins in γ-ray luminosity defining the Fermi blazar sequence, corresponding to Figure 3.3. From Tavecchio et al., 2017

The consequence of observational biased shown in Figure 3.4 is also translated on the original blazar characterization presenting a bias to the less standard, most luminous objects, which translated in an over-representation of the Compton dominance on powerful blazars.

Let us note before moving to next section that the blazar sequence is still a very

controversial scheme, due to the inherent fact that it is biased by observational effects, as poor flux limits on the blazar samples. In the next section, the discovery in very-high energies of the blazar source OT 081, which has been proven challenging to classify following current schemes, will be presented.

3.3 OT 081: A low synchrotron peak blazar

OT 081, also referred in literature as PKS 1749+096 and 4C 09.57, is a luminous LBL object with coordinates (RA = 17:51:32.81855, Dec = +09:39:00.7288 J2000) located at a redshift of z=0.32 (Stickel, Fried, and Kuehr, 1988). It shows a weak extended jet emission to the north-east of the compact VLBI core on parsec scales (Lu et al., 2012). It is well known for its remarkable variability in several energy bands, in particular in the high radio wavelengths, as observed by UMRAO, but also in radio (Reuter et al., 1997), optical (Clements et al., 1995) and X-ray (Urry et al., 1996). High optical polarisation is a common feature of BL Lacs and in the case of OT 081, polarization variability has been detected up to 32% (Brindle et al., 1986).

The source was initially classified as high-frequency peaked (HBL) blazar by Kovalev et al., 1999, due to its radio spectrum peaked above 10 GHz. Few years later it was re-classified as a flat spectrum radio source presenting an inverted spectrum during flares (Torniainen et al., 2005). More recently, in the *Fermi*-LAT 3rd catalog of Active Galactic Nuclei (Ajello et al., 2017), which gathers 1556 sources detected by *Fermi*-LAT above 10 GeV and characterized in the 10 GeV to 2 TeV energy range, it is finally classified as a LBL. *Fermi*-LAT observations discussed in this catalog report emission of OT 081 in the HE γ-ray range (HE, 0.1 GeV $> E >$100 GeV) and a spectral index of 2.98.

In Potter and Cotter, 2013b, properties of a sample of BL Lacs were studied and compared by fitting their spectra. The model accounts for a homogeneous jet with an accelerating, magnetically dominated and a parabolic base whose transitions to a slowly decelerating conical jet which geometry is based on observations on M87. For this study, they find that the inverse-Compton emission of neither OT081 nor Mrk421 are well fitted by SSC while the rest of blazars of the sample are. This is due to the low magnetic field strength value found required to produce the low peak synchrotron frequency. They find that the BLR and dusty torus photons are not able to simultaneously reproduce the observed high energy emission and the archival synchrotron data, as seen in Figure 3.5, left. In contrast, they find that if the jet has a large bulk Lorentz factor, the source is well fitted by scattering of CMB photons, which is in principle surprising for the low redshift of the source (Figure 3.5, right). According to predictions in Potter and Cotter, 2013a, in Compton-dominant blazars, the inverse-Compton emission is best fitted by scattering of Doppler-boosted high redshift CMB photons, but at lower redshift, the energy density of CMB photon decreases as $\rho_{CMB} \propto (1+z)^4$, so we should see blazars with same physical parameters but less Compton-dominance.

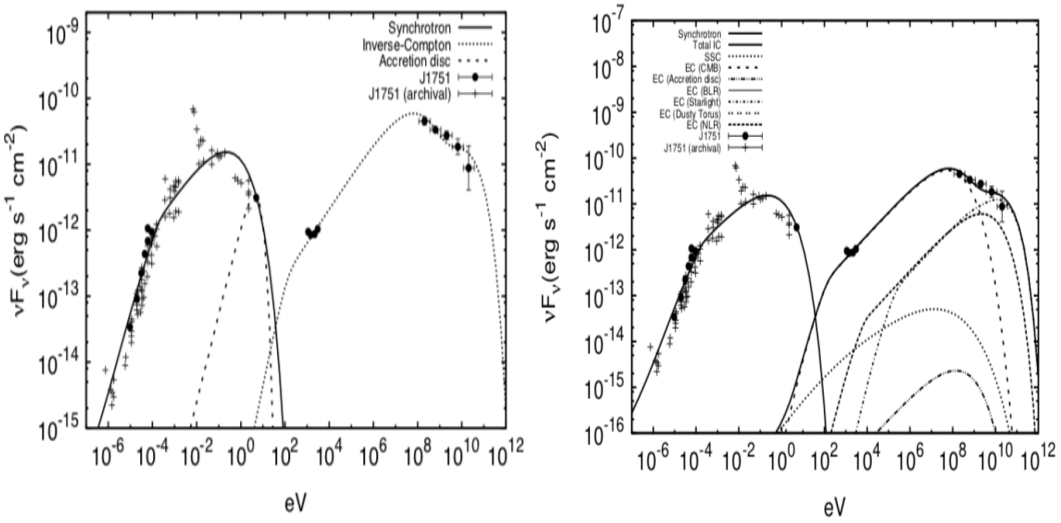

FIGURE 3.5: OT 081 observations fitted to the SSC model described in Potter and Cotter, 2013b, where the Inverse Compton does not follow the proposed model. The authors consider that the low frequency of the IC peak implies that it is a powerful Compton-dominant blazar at low redshift (left) OT081 observations fitted with SSC emission and extra external IC-emission (EIC) components including photons from the CMB, accretion disk, BLR, starlight, dusty torus and NLR (right). From Potter and Cotter, 2013b

They conclude that even though OT 081 is characterized as a BL Lac, it has larger power, larger bulk Lorentz factor and larger transition region radius than the other known BL Lac objects. It shows features of Compton-dominant BL Lacs but it is located at a redshift with lower CMB energy density. In order to reproduce the low frequency peak, a larger transition region is required which will affect the inferred black hole mass if one sticks to the transition region geometry found for M87, as did the authors.

In summary, OT 081 is a peculiar source that escapes modelling attempts and seems to break the boundaries between the different classes of AGNs.

While many observations in the radio, optical and X-ray band have provided a complete description of the synchrotron peak, the Inverse Compton bump of the SED has never been investigated before due to the lack of data in the VHE γ-ray band.

First detection of very high energy emission has been performed by two IACT, MAGIC and H.E.S.S, in July 2016. Observations and analysis results of the H.E.S.S. observations are presents in the following sections. The observations of OT 081 stand as the second low frequency peaked blazar detected by H.E.S.S. after the detection of AP Librae (Abramowski et al., 2015).

3.4 Target of Opportunity program in the H.E.S.S. collaboration

Data presented here were collected in the context of a Target of Opportunity (ToO) program developed in the H.E.S.S. collaboration (Seglar-Arroyo et al., 2017). The main motivation of the program is to study the intrinsic variability of blazars.

To this aim, a continuous monitoring is required to allow for rapid reactions to potential triggers from either other multi-wavelength facilities or auto-triggers. In practice, the H.E.S.S. observation periods, which depend on the moon cycle have a total length of 28 days, are split into two ToO monitoring shifts and in each of them, a triggering monitor person and a contact person are on duty. The trigger monitoring person has the responsibility to analyse on the previous night observations of several experiments in different wavelengths to spot interesting features or flaring states. If an interesting phenomena or an enhanced activity from a source is identified, and fulfill the pre-establish triggering criteria of the ToO observations proposal, the shifters in Namibia are informed and observations are scheduled by the contact person.

The large variety of information that H.E.S.S. ToO program gathers in order to trigger VHE observations is summarized in the following:

- Public MWL alerts. The distribution of those is made via Gamma-ray burst Coordinates Network (GCN) (Barthelmy et al., 1998) or Astronomer's Telegram (ATel)(Rutledge, 1998).
- Public data. To trigger VHE observations, we mainly focus on data from the Swift-XRT, First G-APD Cherenkov Telescope (FACT) and *Fermi*-LAT data. The latter is automatically analysed every day by the tool FLaapLUC (Lenain, 2018), using aperture photometry and a full likelihood analysis.
- Private alerts from MWL partners. Instruments performing VHE observations, i.e. MAGIC, VERITAS, FACT, HAWC, share compelling alerts in the context of Memoranda of Understanding (MoU).
- Optical telescope on-site. At the H.E.S.S. site, the optical telescope ATOM is located that allows to continuously monitor predefined sources (Hauser et al., 2004).

The total amount of time dedicated by the H.E.S.S. experiment to flaring blazars in a ToO context during the 2016 campaign (when observations on OT 081 presented here were performed) reached $\sim$ 60 hours of observation. This corresponds to a $\sim$ 11% of the total allocated time into extragalactic science with H.E.S.S. during the year 2016.

3.5 Discovery of OT 081 at very high energies

On July 9th 2016, *Fermi*-LAT issued an alert on OT 081 stating that the source was undergoing a bright flaring state in the MeV-GeV energy range (Becerra Gonzalez

and Thompson, ATeL 9231). The source reached a daily average gamma-ray flux of $F_E > 100\text{MeV} = (1.0 \pm 0.2) \cdot 10^{-6}$ ph/cm^2 s, which corresponds to ~ 20 times the average fluxed quoted in the 3FGL catalog (Acero et al., 2015).

The high-flux activity in gamma-rays was followed by an enhancement in optical frequencies, observed from July 16 to July 20, which peaked at $R \sim 14.9$ mag (Balonek et al., 2016). In the following days, from the July 17 to the July 20, X-ray and UV ToO follow-up observations by Swift were obtained, showing the correlated activity in the source in gamma-ray/X-ray/UV/optical wavelengths (Ciprini et al., July 2016).

Due to moon constraints, H.E.S.S could only start ToO observations on the source on July 22, 2016 (MJD 57591). The source was observed for the next 6 consecutive nights, until July 27 (MJD 57596) and the details on the analysis of these observations are the topic of the following section. In addition, the source was observed by the MAGIC telescope, reporting the detection of the source in VHE during the night of the July 24 (Mirzoyan, 2016). The joint observation by MAGIC and H.E.S.S. stands as the first detection of this blazar at very-high energy gamma-ray.

In addition, these data were obtained in the context of a simultaneous multi-wavelength campaign, where data from radio to gamma-rays, as well as optical polarization were collected. The spectral energy distribution, considering the entire set of MWL data, is crucial for the interpretation of the flaring state.

3.6 H.E.S.S. analysis of OT 081 observations

Data presented here have been analyzed using the semi-analytical *Model* Analysis (De Naurois and Rolland, 2009), introduced in Chapter 2. A total of 26 observation runs between July 22 to July 27. Each of the observation runs includes 28 minutes of data, which were obtained in the zenith angle range from 33° to 47°, with a mean zenith angle of 38°. The entire dataset passes standard data-quality selection criteria (Aharonian et al., 2006). This translates to a total of 11.7 h of observations, 10.1 h after acceptance correction due to the wobble offsets around the nominal source position are available for analysis.

In order to achieve a lower energy threshold, as it is particularly beneficial for the study of distant objects, we focus on the analysis using the 28-m telescope data. For this analysis, *Standard cuts* from *Model* Analysis are applied to the data. With a minimum requirement of 60 photoelectrons per image used in the analysis, an energy threshold of 20 GeV is achieved for these zenith angles and assuming a spectral index of $\Gamma = 4$ (H.E.S.S Collaboration, in preparation).

Using the Li &Ma (Li and Ma, 1983) formalism, the source is clearly detected, reaching a significance of 6.5 σ for the full obtained dataset, as shown in Figure 3.6, left. In the right part of Figure 3.6, the distribution of the θ^2 of the γ-like events, where θ is the angular distance from the position of the source to the rest of the

coordinates in the FoV. In green we observe the γ-like events, above the computed background which is represented by crosses. A total number of $N_{ON} = 2246$ and $N_{OFF} = 17544$ is obtained, which corresponds to $\alpha = 9.06$ (see Chapter 2 for details on how this values are obtained). The selected background computation method is the `Multiple OFF` method, as it is the standard method used to analyze point sources, as it is the case for OT 081.

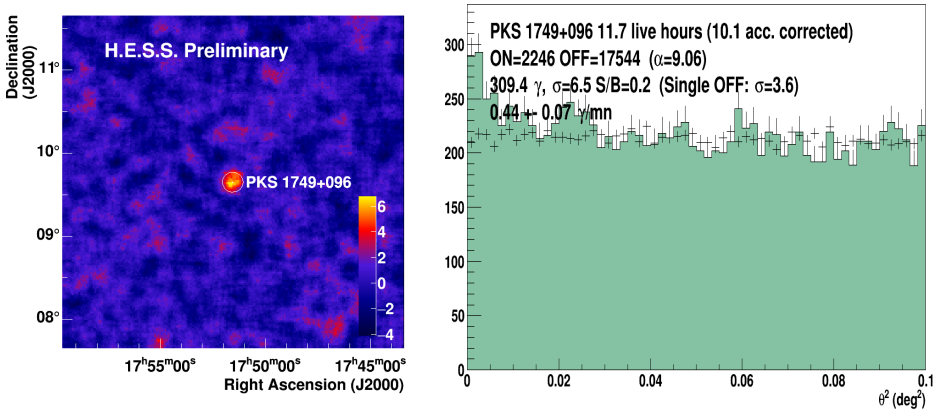

FIGURE 3.6: (Left)Significance map and (Right) theta squared distribution of OT 081 observed by H.E.S.S. from July 22-27 2016

As explained in Chapter 2, in the H.E.S.S. collaboration, results are cross-checked with an independent analysis calibration chain and procedure, using the *ImPACT* reconstruction method (Parsons and Hinton, 2014b). Although not presented in this manuscript, these independent analysis give results that are consistent with the presented analysis, both for this result and the rest of the presented results in the following sections, and prove the robustness of the conclusions.

The analysis has thus been approved by the H.E.S.S. Collaboration. A joint publication with the MAGIC and Fermi-LAT collaborations is in preparation.

3.6.1 Source variability characterisation

The Bayesian Block analysis (Scargle, 1998) adresses the task of detecting and characterizing variability of a source through a period of time, with the goal of identifying significant variations and differentiate them quantitatively against random fluctuations. In contrast with other methods that seek for general features in the data, as wavelets or Fourier transformations, this methods is sensitive to *local* variability, understood as features that are present in subranges of the overall lightcurve. For further explanation, see Scargle et al., 2013

We applied the Bayesian Block method to the arrival times of individual γ-like events detected by H.E.S.S. from the OT 081 blazars. To do so, the arrival times of the events has been corrected by the acceptance in different intervals representing

stable observation conditions. Then, the bayesian block technique was applied to the *acceptance-corrected* times of dataset on the source OT 081 to asses time variability of the gamma-ray emission.

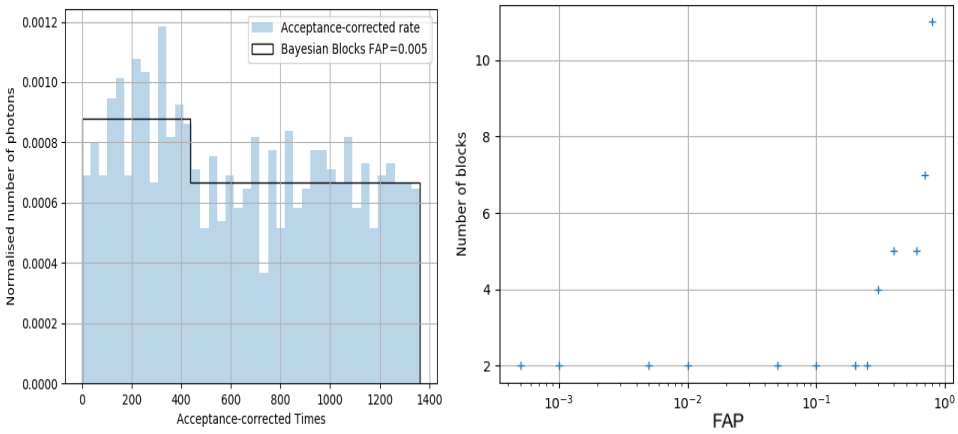

FIGURE 3.7: (Left) Acceptance-corrected rate and time for the H.E.S.S. observations from July 22-27th 2016 for OT 081. (Right) Number of blocks found by a Bayesian Blocks analysis depending on the False Alarm Rate.

This analysis identifies two different flux states of the source as it is shown in the left panel of Figure 3.7. These are referred in the following as *high* flux state and *low* flux state. The bayesian block analysis was repeated for different false-alarm probability (FAP) values, which yield to a number of blocks that stabilizes in a total number of 2 blocks below FAP$\simeq$0.25, as can be observed in the right panel of Figure 3.7.

To further assess this result, in Figure 3.8 we show the cumulative significance obtained from the analysis of the entire set of observations in the OT 081 source through 6 nights, where these two trends can be appreciated. During the first three nights, which are represented by the first 8 observations, we observed an increase of significance, which reaches a total value of $\sim 9\sigma$. In the evolution of the significance, this can be seen as a turning point, as the extra data obtained in the 3 last nights, which consist on 18 observations of 28 minutes, do not increase the source detection significance.

3.6.2 Analysis of the time evolution of OT 081 at VHE

The first bayesian block defines a *high* flux state of the source in gamma rays during the period between the nights of July 22 to July 24, 2016. This *high*-flux subset of data has been analyzed using M++ *Model Analysis* in a *Mono* configuration, using only data from the 28-m telescope, CT5. Limiting the analysis to the high flux state, 3.6 live hours (3.1 acceptance corrected) were obtained during the three first night, between 57591.76 MJD and 57593.86 MJD. These observations result in a 8.8 σ detection of OT 081 in very-high-energy gamma rays. The best fitted position of the VHE γ-ray excess is found at $\alpha_{J2000} = 17^h51^m31.9^s \pm 0.6^s(\text{stat}) \pm 20^s(\text{sys})$

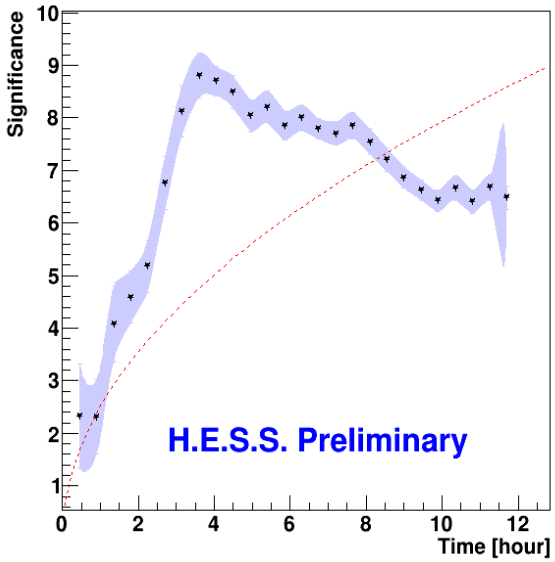

FIGURE 3.8: Cumulative significance evolution through time when the OT 081 source has been observed with the H.E.S.S. telescope during the July 2016 flare.

$\delta_{J2000} = 9°39'00'' \pm 7''(\text{stat}) \pm 20^s(\text{sys})$, consistent with the nominal position of the optical source OT 081 $\alpha_{J2000} = 17^h51^m32.82^s$ $\delta_{J2000} = 9°39'00.73''$ (Lanyi et al., 2010).

The significance map of the source and θ^2 distribution of the γ-like events, which result from the *Model Mono* analysis, are shown in Figure 3.9. In the right part of the figure, we observed that a total of 235 γ-like events in the direction of the source, have been recorded.

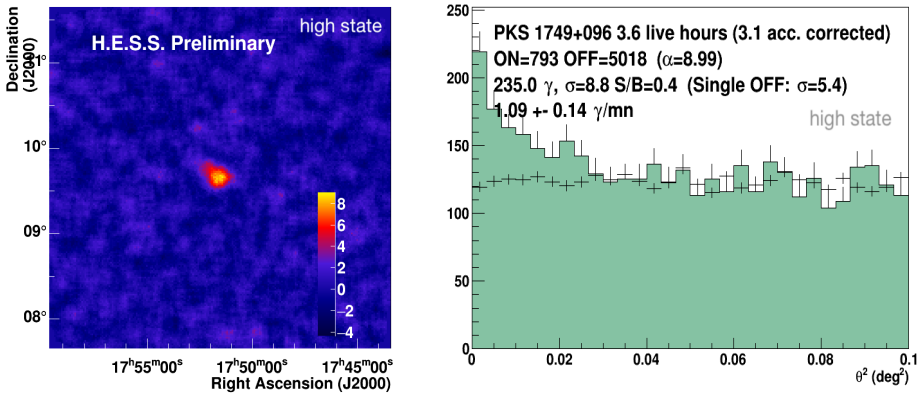

FIGURE 3.9: (Left) Significance map and (Right) θ^2 distribution of OT 081 observed by H.E.S.S. during the flaring state from July 22-24th 2016

The second bayesian block defines a *quiescence* state of the OT 081 source. The

flux of the source is too low and it is not detected anymore. Data for this state has also been analyzed using M++ *Model Analysis* in *Mono* configuration. The source is marginally detected at 1.9 σ for a total lifetime of 8.1, corresponding to 18 observations of 28-minutes between the nights of July 25 to July 27, 2016. The resulting significance map of the quiescence state observations and the θ^2 distribution are shown in Figure 3.10. From the θ^2 distribution, it can be observed that the source is not significantly detected above the background signal.

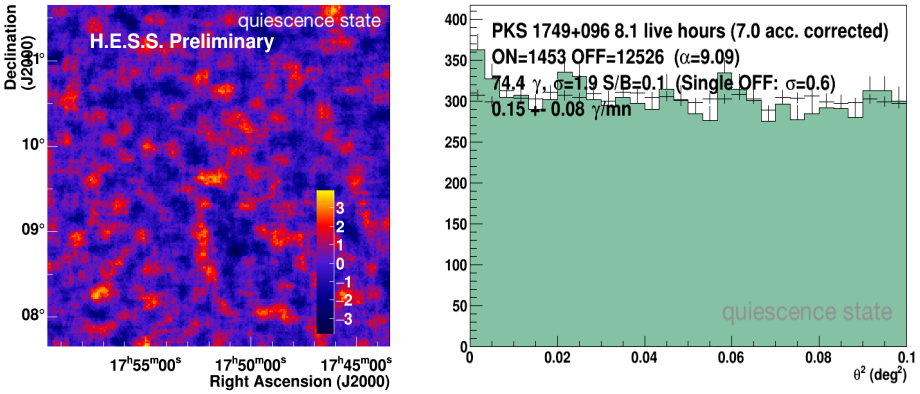

FIGURE 3.10: (Left) Significance map and (Right) θ^2 distribution of OT 081 observed by H.E.S.S. from July 25-27th 2016

A further insight on the significance distribution of the pixels of the skymap presented in previous figures, for each of two states of the OT 081 source, is given in Figure 3.11. The red distribution in the histogram corresponds to the significance of the events in the N_{OFF} region and the black distribution corresponds to the values of the significance obtained in the N_{ON} region. We observe that while in the left plot we observe an excess in standard deviations with respect to the background distribution, in the quiescence state, the two distributions are coincident.

Energy spectrum and light curve of OT 081 at VHE

A forward folding maximum likelihood optimisation (Piron et al., 2001) is used to extract the average power-law spectrum over the high state observation period. The VHE spectrum of the high state can be described by a power-law with photon index of $\Gamma = 4.4 \pm 0.4$ between 118 GeV and 2.8 TeV, and a flux normalisation at 1 TeV of $\phi_{1\ \mathrm{TeV}} = (1.17 \pm 1.16) \cdot 10^{-13} \mathrm{cm}^{-2}\mathrm{s}^{-1}\mathrm{TeV}^{-1}$ (Figure 3.12). The equivalent χ^2 of the fit is 18.4 over 25 degrees of freedom, which translates into a chance probability of 0.82. No indication of curvature or spectral break is present in the observed spectrum.

No significant emission has been observed during the second period of observations of 8.1 hours (7.0 acceptance corrected) from times 57593.86-57596.88 MJD. For this reason, 99% C.L. differential upper limits have been derived for the low flux period following Feldman and Cousins, 1998. We obtain differential upper limits in

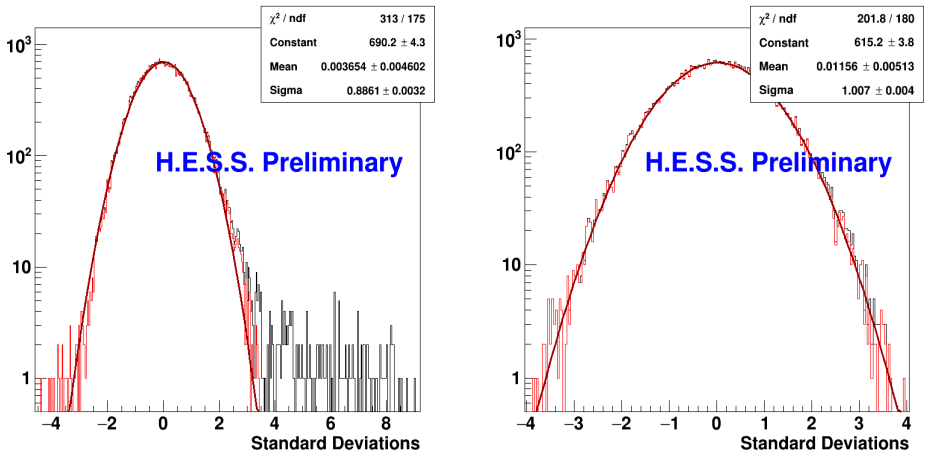

FIGURE 3.11: (Left) Significance distribution of the skymap pixels from the observation of the high state. (Right) *Quiescence* state in very-high-energy γ-rays of the OT 081 blazars observed by H.E.S.S. in July 2016

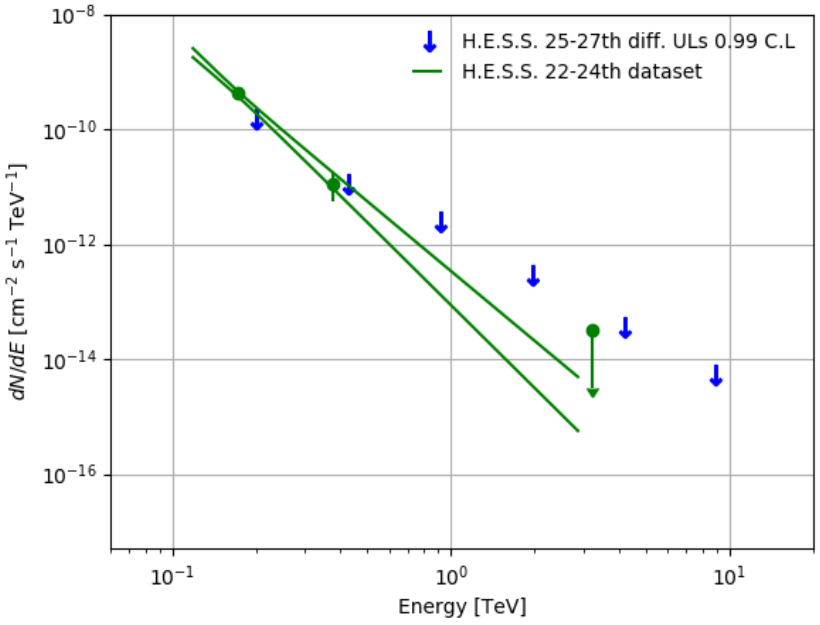

FIGURE 3.12: Differential energy spectra of the observations taken by the H.E.S.S. telescope on OT 081 July 2016 flare, where the data set has been derived into two data subset following the results of bayesian blocks.

the 210 GeV to 5.2 TeV energy range which are shown in Figure 3.12.

The blazar OT 081 has a redshift z=0.32, which make the high energy photons sensible to undergo Extragalactic Background Light absorption. In the case of the high

flux spectrum, we have obtained the absorbed spectrum including the EBL absorption at the level of the *forward folding* technique. The intrinsic spectrum is obtained by fitting the measured spectrum to the spectral power-law (PL) shape described in Equation 1.13, which includes the EBL attenuation in the exponential factor. The index for the power law obtained for the *intrinsic* emission of the source is found to be $\Gamma_{int} = 3.39 \pm 0.58$, again between 118 GeV and 2.8 TeV. The obtained observed spectra considering a power-law shape and a power law with EBL attenuation using the EBL model from Dominguez et al., 2011, together with the obtained intrinsic spectrum of the blazar OT 081 from the H.E.S.S. observations from the 22-24th of July, 2016, are shown in Figure 3.13.

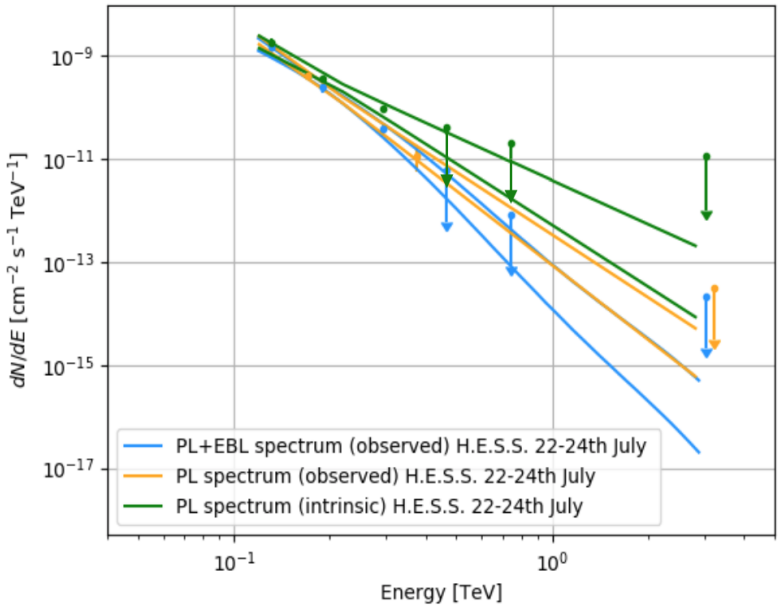

FIGURE 3.13: Observed PL spectrum (orange), observed PL+EBL spectrum (blue) and intrinsic PL spectrum (green), where the EBL attenuation has been corrected following Dominguez et al., 2011, corresponding to the *high* state of OT 081 during the 22-24th July, 2016 as observed by H.E.S.S.

The 99% C.L. differential upper limits have been corrected considering again the EBL model from Dominguez et al., 2011. The observed and the intrinsic 99% C.L. differential upper limits, obtained from the quiescence state of OT 081 observed by H.E.S.S. from the 25-27th of July, 2016, are shown in Figure 3.14.

The lightcurve at very high energies of OT 081 during the H.E.S.S. observations from the 22th to the 27th of July is presented in Figure 3.15. While we derive nightly data points for the period when the source is active in very-high-energy gamma rays, an upper limit is set for the three last nights where no significant signal is detected from the source. To asses this condition, a minimum significance of the period set to 2 σ per night is not reached in the three last nights of H.E.S.S. observations. A combined, integral UL has therefore been computed for the three last nights of the

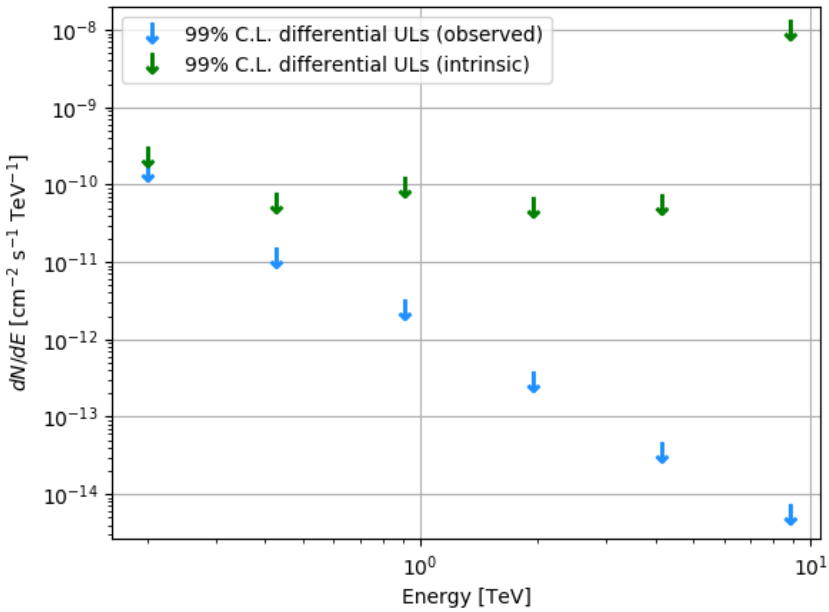

FIGURE 3.14: Observed (blue) and intrinsic (green) 99% C.L. differential upper limits, where the EBL attenuation has been corrected following Dominguez et al., 2011, corresponding to the *quiescence* state of OT 081 during the 25-27th July, 2016 as observed by H.E.S.S.

observations.

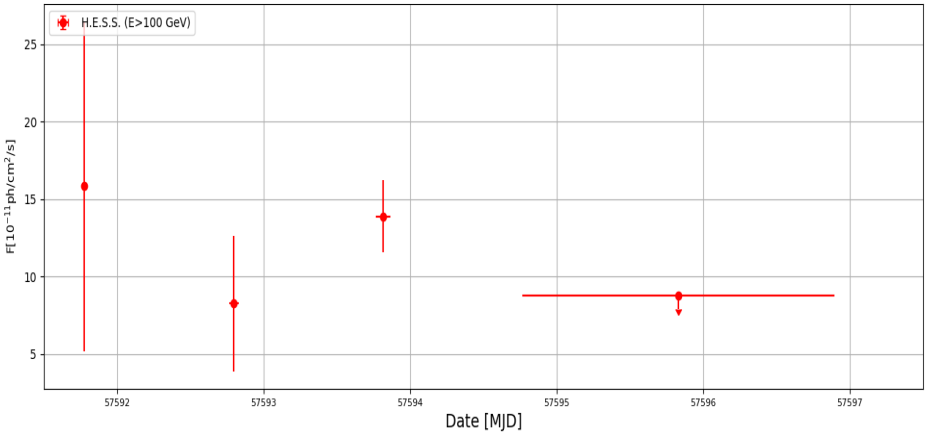

FIGURE 3.15: Lightcurve of the source OT 081 above 100 GeV observed by H.E.S.S from July 22 to July 27, 2016

3.7 Multi-wavelength lightcurve and source modelling

A broad multi-wavelenght coverage is key to model and interpret the processes that the source underwent during July 2016. For this purpose, data has been shared under MoU between the collaborations leading the multi-wavelength effort, namely H.E.S.S., MAGIC and Fermi-LAT. Collaborators of these leading collaborations provided additional MWL data. The final MWL lightcurve includes data at VHE from H.E.S.S. and MAGIC, HE from Fermi-Lat, X-ray data from Swift-XRT, ultra-violet data from UVOT, optical data from RINGO, ATOM and KVA, and radio data from ALMA, OVRO and Metsahovi.

The multi-wavelength lightcurve illustrating the extensive coverage of OT 081 during the July 2016 flare is shown in Figure 3.16. There is an evidence of a certain number of features and shared trends among the emission at different wavelengths which are observed.

The first feature is that in *Fermi*-LAT data from Figure 3.16, two high flux data points in the total lightcurve can be observed. They define two further states of the source, referred as P1 and P2 in the following, for which the SED with respective contemporaneous data has been obtained. The spectral energy distribution of the source for the four states considered in this study is discussed in the next section, and shown in Figure 3.17.

A common trend which is observed in the MWL lightcurve is that Swift-UVOT, Swift-XRT and *Fermi*-LAT observed an enhanced activity state (MJD 57587 - 57590) which peaks in the point P2 of the Figure 3.15, which point to the similar underlaying mechanism. Unfortunately, there is no contemporaneous data available for P1 in basically any wavelength. Nevertheless, it is worth pointing out that the fluxes achieved in these two periods are approximatively at the same level.

No VHE observations contemporaneous to P1 and P2 were performed, so there is a lack of information on the emission during that period. At GeV-TeV energies, we have identified thanks to the analysis of H.E.S.S. data the existence of two states of the blazar source where the source is first detected, and in a latter times is not detected anymore. We refer to these two states as P3 and P4.

3.7.1 Modelling the spectral energy distribution

The MWL coverage observed in the OT 081 lightcurve show in Figure 3.16 enabled the separation of the datasets in four periods: P1,P2, P3, P4, defining the evolution of the source during the enhancement of the MWL activity. The definition of these states allows to model the source state simultaneously through the entire electromagnetic spectrum. The four SED of the source OT 081 during the 2016 flare are shown in Figure 3.17.

The SED of OT 081 in Figure 3.17 shows the Compton dominance present in this blazar and discussed in Section 3.3. From a first comparison of this dataset to the data shown in Figure 3.5 from Potter and Cotter, 2013b, some features can be observed. Considering the factor introduced by the different units of $E^2\mathrm{d}N/\mathrm{d}E$ to be ~ 1.60, we observe an overall increase of $E^2\mathrm{d}N/\mathrm{d}E$ at high energies in the dataset obtained in July 2016, reaching particularly large values during the P1 and P2, an order of magnitude larger in $E^2\mathrm{d}N/\mathrm{d}E$.

With the aim to constrain the nature of the emission and the physical mechanisms in place, several attempts have been made in order to model the emission of the source.

A similar approach to the one taken for AP Librae by Sanchez et al., 2015 has been considered, due to similarities between both sources of intermediate nature between BL Lac objects and FSRQ. An empirical characterization of the two radiative components, used to estimate the synchrotron peak energy $E_{s,peak}$ and IC peak energies $E_{ic,peak}$, can be obtained though the fit of a third-degree polynomial function to each bump in the $\nu F\nu$ representation, following Abdo et al., 2010. The third degree polynomial can be also used to estimate the curvatures of each peak κ_s and κ_{IC}, which considering Paggi et al., 2009 would translate to a relationship $\kappa_s = 2\times\kappa_{IC}$ in a pure Thompson scattering regime and $\kappa_s = 0.2\times\kappa_{IC}$ in Klein-Nishina regime. In the case of OT 081, the factor relating the two curvatures is however estimated to $\sim$0.9.

Concerning radiative scenarios, a single-zone SSC framework has been considered, as a first, most simple attempt to model the source. In the SSC, as mentioned in Section 3.2.1, synchrotron photons are produced by the same electrons which are afterwards the target of the Inverse Compton process of those produced photons. Following Tavecchio, Maraschi, and Ghisellini, 1998, for a single-zone SSC model in the case of the scattering taking place in the Thomson regime, constraints can be applied to the product of the magnetic field B and the Doppler factor δ following:

$$B\delta = (1+z)\frac{8.6\cdot 10^7 E_{s,peak}^2}{E_{ic,peak}} \tag{3.8}$$

In the case of OT 081, considering the values for the peak energies estimated using the third polynomial fit, this product takes very low values, which, assuming typical values for δ, yields to non-physical values for the magnetic field.

The one-zone SSC model is unable to describe the SED of OT 081, similarly to the case of AP Lib (Sanchez et al., 2015), due to the broad high-energy hump observed from X-rays to TeV γ-rays. A spine-layer model (Tavecchio and Ghisellini, 2014) for the jet morphology has been considered. In this case, the jet is has a more complex two-layer structure, where the inner part has larger velocity than the outer part. However, the larger radiation energy density U_S with respect to SSC would require a larger magnetic field U_B (because of the fixed L_{IC}/L_S term and Equation 3.5) and thus, a larger synchrotron peak frequency. This model could also not properly reproduced the obtained data due again to the broad high-energy hump.

Further attempts have been performed to explain the broadband spectrum of OT 081 by adding complexity to the models. Motivated by recent work on a hadronic reinterpretation of Ap Lib, more complex hadronic models have been contemplated in order to model the source emission. In this case, different emission components related to photo-hadronic interactions are superimposed, which were able to explain the emission of AP Lib without evoking external fields (Petropoulou, Vasilopoulos, and Giannios, 2016). Unfortunately, the data obtained during July 2016 for OT 081 shows a larger Compton dominance than the one observed for AP Lib, so problems have been found to simultaneously fit the X-ray and the γ-ray data.

Other attempts to model the source have been proposed, following the results on TXS 0506+056 by Cerruti et al., 2018. In this scenario, single-zone models of lepto-hadronic emission (combination of SSC and synchrotron radiation from hadronic cascades) are invoked, where acceleration of electrons and protons in the jet is assumed to be *co-spatial*. In this mixed model, the SSC emission largely dominates the high-energy peak and the hadronic component is responsible for most of the hard X-rays and VHE γ-rays. The capability of this mixed model to fit the OT 081 emission is still work on-going.

In addition, external photon fields are also being considered for both leptonic and hadronic models. The external photon field considered for this sources comes from the BRL region, as emission lines are observed in the optical spectrum of the source (Stickel, Fried, and Kuehr, 1988). From the mentioned optical/UV spectrum, the luminosity of $L_{\rm BRL}$ can be extracted in order to characterize the luminosity of the photons present in the BLR, considered as photon target of the EIC process.

Finally, the source has been observed by the Very Long Baseline Array (VLBA) from April 2016 to June 2017. The parsec-scale jet of OT 081 is strongly core-dominates at 43 GHz. A compact VLBI core and several knots, one quasi-stationary and two superluminal, are identify in these observations. The interaction between these knots and the correlation with the γ-ray activity from P1 to P4 is currently under study.

The different features described above and the challenges found during the modeling of OT 081 are similar to the case of AP Lib as presented in Hervet, Boisson, and Sol, 2015. In the mentioned work, a blob-in-jet model is proposed and the radio and gamma-ray emission have been linked, all in the context of AP Lib. In addition, the question on whether AP Lib-like sources represent a new family of objects, of intermediate nature between pure FSRQs and BL Lacs, seen as a radiatively extremely faint FSRQ, is discussed. In this proposed scenario, the SED of the source is no longer dominated by one-zone VHE blob (as it is typically the case for HBLs) and the contributions from the jet and the disk become important, as it looks likely to be the case for the emission observed from OT 081.

In this direction, three main characteristics have been identified from AP Lib SED: broken radio-mm spectrum around 250 GHz, X-ray positive slope and high-energy

bump with a relatively flat Fermi spectrum at $\nu \geq 10^{15}$GHz, and a peak luminosity close to the peak synchrotron luminosity. Out of these characteristics, OT 081 fulfills the second and the third, although partially (due to the larger Compton-dominance observed in OT 081). No data is available to know if the first characteristic is also fulfilled. For these reasons, the detailed study of the radiative components of the emission of OT 081 may be an step further to establish a new family of sources, which may improve our knowledge and refine the characterization that the blazar sequence provides.

Although the modeling of OT 081 has been proven challenging so far, efforts are on-going to provide answers to the open questions concerning the modeling and the classification of the source raised throughout this section. A detailed discussion on these aspects will be presented soon in a future publication.

3.8 Discussion

The broad multi-wavelength coverage achieved during the flaring episode of the OT 081 source in July 2016 translates to an important amount of simultaneous data, from radio to gamma-ray energies, essential in AGN modeling. This outcome demonstrates the importance of Target-of-Opportunity programs in time-domain astrophysics, and in particular of the H.E.S.S. ToO program on flaring AGNs.

A joint effort is currently on-going between the leading collaborations, i.e. MAGIC, *Fermi*-LAT and H.E.S.S., and AGN modeling experts. Not only the aim is to constrain the emission mechanisms of this particular source and overcome the challenges of modeling the emission, but also to improve our understanding on sources which present similar properties to those of OT 081, present in other LBLs as AP Librae and 4C+41.11 (Righi, Tavecchio, and Pacciani, 2018). The difficulties found to classify these sources following the blazar sequence scheme may translate into further model improvements which may successfully describe the complex phenomenology of blazars.

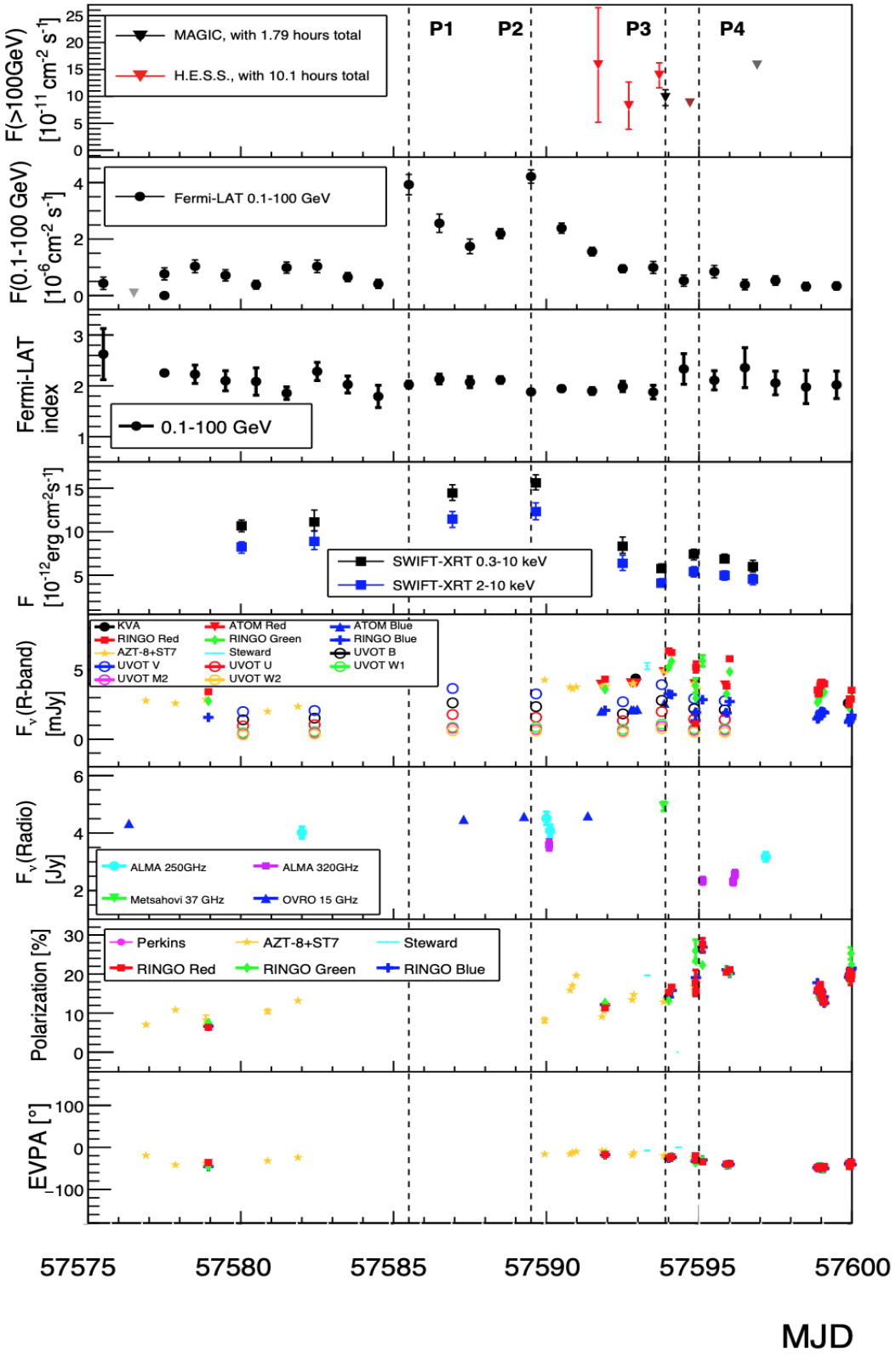

FIGURE 3.16: Multi-wavelength lightcurve covering 25 days of data, from the 57575 to 57600 MJD, which corresponds to July 6 to July 31 2016, showing the evolution of the LBL OT 081

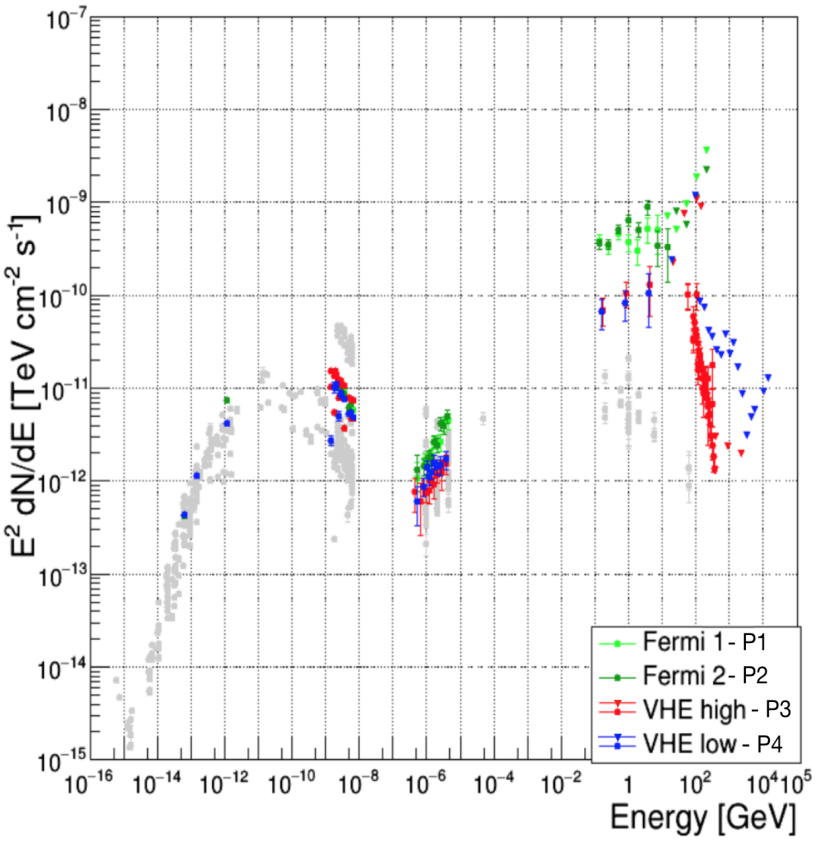

FIGURE 3.17: Spectral Energy Distribution defined by the simultaneous data obtained during to the P1 (Fermi 1), P2 (Fermi 2) , P3 (VHE high) and P4 (VHE low) states of the blazar OT 081 during the July 2016 flare. Grey points correspond to archival MWL data on the source.

Part III

Compact binary coalescences and gamma-ray bursts

Chapter 4

Introduction to compact binary coalescences and gamma-ray burst

Contents

4.1 Gamma-Ray Bursts

4.1.1 Introduction to observations of GRBs

Gamma-Ray Bursts (GRBs) are short, intense flashes of γ-rays, typically at energies in the keV to MeV domain. These events last between tens of milli-seconds to several

thousands of seconds and are observed at a detectable rate of once or twice per day (Nakar, 2007).

Gamma-Ray Bursts were serendipitously discovered in the late 60s by military satellites in the context of the Cold War (Fishman, 1995). In order to verify that all the conditions of the signed nuclear ban treaty were fulfilled, the US Air Force launched a series of satellites to search for possible secret weapon tests. As a result of these observations, signals unlikely to come from such tests were observed: an astrophysical discovery was made. A total of 16 cosmic GRB were identified between July 1969 and July 1972 (Klebesadel, Strong, and Olson, 1973).

After these first observations and focusing on HE emission, first hints of high energy emission from GRBs were seen more than 30 years ago. In 1984, the Solar Maximum Mission detected photons of ~ 0.1 GeV from a very bright GRB (Share et al., 1986).

In the early 90s, the revolutionary time for GRB science arrived with the launch of the Compton Gamma Ray Observatory. Several thousands of GRB were detected by the Burst and Transient Source Experiment (BATSE) instrument, which allowed to infer spectral and temporal properties over a wide range of energies from $\sim$ 20-2000 keV (Band et al., 1993). The position of those GRBs was distributed uniformly over the sky, showing that no direction was privileged, thus ruling out the Galactic origin hypothesis. Measurements of 222 GRBs by BATSE allowed the classification of GRBs according to their duration and spectrum as *short*-burst for short-duration, hard-spectrum objects and as *long*-bursts to long-duration, soft-spectrum GRBs (Kouveliotou et al., 1993). The bimodal distribution of the burst durations showed a minimum around 2 seconds. In addition, a phenomenological description of the GRB spectra was defined from these X-ray observations (Band et al., 1993). The *Band function* was proposed as an empirical function that describes the spectra averaged over the duration of the burst by two smoothly joined power laws which can represent many spectral shapes, i.e. exponential cutoff power-law and single power-law spectra.

Higher energy observations, in the range between 20 MeV-30 GeV were performed by the Energetic Gamma-Ray Experiment Telescope (EGRET), which detected six GRBs with diverse temporal and spectral behavior. While in GRB 930131, the high-energy component was identified as the continuation of the keV-MeV spectrum (Sommer et al., 1994), hints for an additional, long-lasting component at HE were observed in GRB 940217 (Hurley et al., 1994) and in GRB 941017 (González et al., 2003).

Further improvements, in particular on the localization accuracy, were brought by the next generation of satellites. In 1996, BeppoSAX, an Italian-Dutch satellite was launched. With the ability to pinpoint GRBs at the arc-minute level, it enabled the first MWL follow-up observations by other instruments. In 1997, the first proof of the distance reach of GRBs in the Universe was obtained, through the measurement of the spectrum of an optical transient associated with GRB 970508, which contained

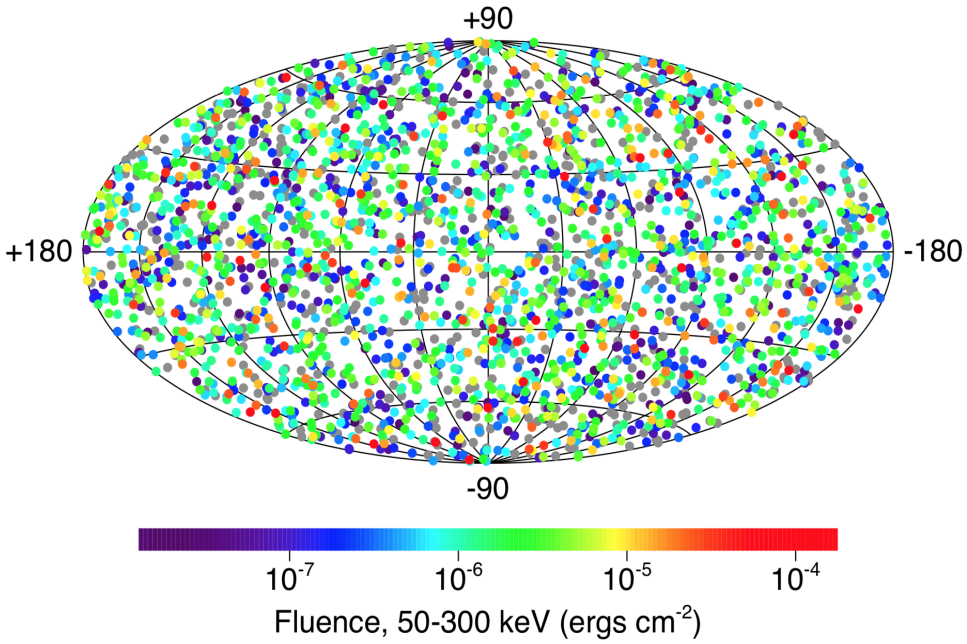

FIGURE 4.1: The location of a total of 2704 GRBs, in galactic coordinates, recorded with the CGRO-BATSE during the nine-year mission (Kaneko et al., 2006)

the absorption spectrum of a galaxy located along the line of sight. This cosmological redshift was found to be z=0.835.

Since the late 90s, the *monitoring* of the evolution of GRB emission has become a standard practice. The different phases of the event that are typically observed start from the detection of the event, passing by the subsequent observation of an associated optical transient to the later detection of the afterglow emission. The Gamma-ray Coordinates Network (GCN) played a key role in the standardization of procedures by supporting the efficient information sharing between observers using satellites and ground-based observatories (Barthelmy et al., 1998).

Next generation of satellites came by the end of the 2000s, with *Astro-Rivelatore Gamma a Immagini Leggero* (AGILE) in 2007 and the *Fermi Gamma-ray Space Telescope* in 2008. Compared to previous satellites like EGRET, AGILE has a larger FoV (∼2.5 sr) and reduced deadtime. Tens of GRBs have been detected by AGILE so far showing emission above tens of MeV (GCNs, 2019).

Concerning the *Fermi* satellite, it is a space observatory with two instruments on board, the full sky monitor Gamma-ray Burst Monitor (GBM) and the large field of view (∼ 2.4 sr at 1 GeV) Large Area Telescope (LAT). While the GBM is sensitive in the range from several keV to tens of MeV, the LAT covers higher energies in the range from ∼20 MeV to ∼ 300 GeV. The GBM GRB detection rate is ∼ 240 per year. The number of GRBs detected by the Fermi-LAT telescope, is about ∼ 14 per year, which represents ∼ 12 % of those detected by GBM. From those, high energy photons above 100 MeV are detected in ∼ 12 GRBs/ year. Another subset of 1% of

them show temporally extended emission (Nava, 2018).

Previous to 2018, various detections of HE photons have been performed by different instrument, with the maximum photon energy detected being at ~ 95 GeV by Fermi-LAT from GRB130427A (Ackermann et al., 2014). The limited statistics provided by the LAT due to its m^2-scale effective area has largely prevented the study of GRBs in the VHE range. Follow-up observation, searching for HE-VHE emission of GRBs detected by LAT, GBM or Swift were unsuccessful for a large period of time, and only upper limits on the emission could be derived by IACTs (Gilmore et al., 2013) and EAS (Alfaro et al., 2017). However, a new milestone in the history of GRB observations has been achieved by the recent detection by the MAGIC and H.E.S.S experiments.

The MAGIC detection of GRB 190114C is the first announcement of a GRB detection at very high energies, with observations starting after 50 seconds after GBM trigger, which corresponds to the early afterglow emission of the GRB. The signal could be observed under moonlight conditions and at high zenith angles at $>20\sigma$ above 300 GeV, even though strong EBL absorption is expected for VHE photons at a redshift $z = 0.425$ (Mirzoyan, Noda, and Moretti, 2019).

Recently reported observations by the H.E.S.S. experiment on late-time emission of the GRB180720B, a particularly bright event at moderate redshift z=0.653, shows the potential of VHE observations of GRB afterglows. Results of the H.E.S.S. observations show a $\sim$5 σ detection of VHE emission in the 100-440 GeV range, 10 hours after the observation of the prompt gamma-ray emission phase. The event was first triggered by *Fermi*-GBM and in follow-up observations, *Fermi*-LAT detected photons from the source with a maximum energy of 5 GeV (H.E.S.S. Collaboration, 2019) at $\sim T_0$+142 seconds, and no further HE emission was detected after T_0+700 seconds.

4.1.2 Current models describing GRB emission and progenitors

The current theoretical model describing gamma-ray emission is know as the *fireball model* (Piran, 1999). The highly energetic emission is modeled as the product of relativistic shocks in the highly relativistic jet which is powered by the central engine, although the energy transfer mechanism and the nature of the central engine are largely unknown. During the *prompt* phase, the emission of the GRB is thought to be dominated by *internal shocks*, which consist in relativistic collisions of highly magnetized plasma shells emitted by the central engine. The *afterglow* emission is thought to be produced in *external shocks*, when the expanding jet of relativistic material collides with the external burst environment. The most popular mechanisms to explain the sub-MeV emission is electron synchrotron emission, which would account for the flux evolution of the *afterglow* emission, showing a characteristic temporal decay, which is thought to correspond to the slowing of the ejecta as it interacts with the external medium. In Figure 4.2, an scheme of this processes is shown.

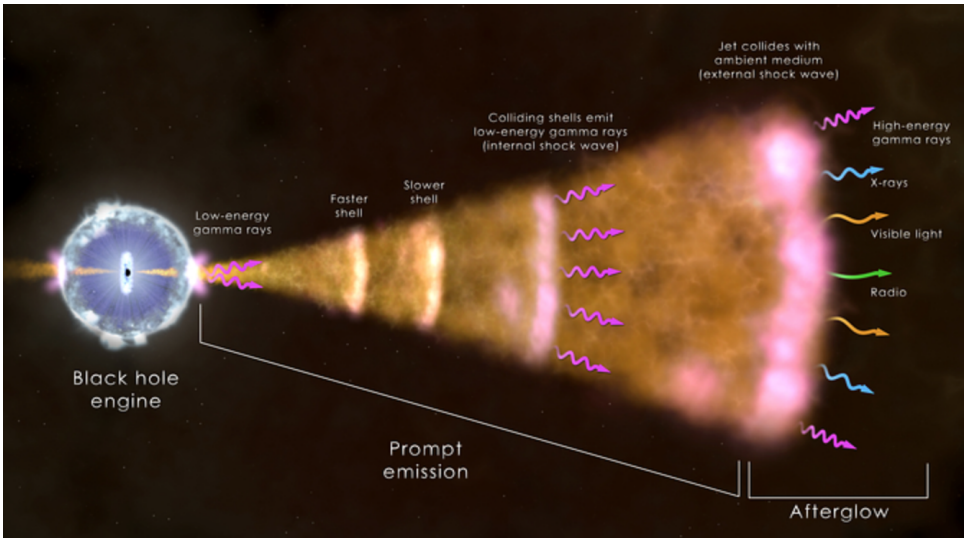

FIGURE 4.2: The several stages explaining the appearance of the burst according to the *fireball* model. From NASA.

The high energy component of GRB emission is still not completely understood. In the case of a synchrotron origin of the emission, this requires an extreme accelerator potentially accelerating the electrons beyond PeV energies (Guilbert, Fabian, and Rees, 1983). Other radiation mechanisms which could account for the GeV emission are leptonic and hadronic non-thermal processes, explained in Chapter 1. Hadronic radiation processes are nevertheless characterized by longer energy-loss timescales than leptonic radiation processes.

The high energy emission observed for GRBs detected by Fermi-LAT seems to show a temporal shift with respect to the trigger time of the keV-MeV component and shows further extension after the prompt emission (Ravasio et al., 2019 and references therein). The early HE emission which is simultaneous to the low energy component in keV-MeV, presents some variability in a first time, but then its long-lasting tail undergoes a smooth decay in time. It has been speculated that there may be a possible transition from an early steep decay which goes as $t^{-1.5}$, followed by a shallower regime as t^{-1} (Ravasio et al., 2019).

The persisting lack of constraints on the radiation mechanisms impacts the constraints on the properties of the emitting region, as well as the composition of the jet and the nature of the progenitor. Due to the high energies reached in the explosion, the duration and the variability of the emission, constraints are placed on the *inner engine*. Thus, the observed emission should be confined in small volumes of tens of kilometers (Piran, 1999). With these constraints in mind, various progenitors and potential production mechanisms have been proposed to produce the observed emissions from GRB. The most promising progenitor of GRBs are the merger of binary neutron stars (BNSs) (Blinnikov et al., 1984, Blinnikov et al., 2018), the merger of a low mass black hole and a neutron star (BH-NS) (Nakar, 2007), both typically connected to *s*GRBs. Other examples of possible progenitors, in this case linked to

*l*GRBs, include the collapse of the core of a massive star (Woosley, 1993) or the global reconfiguration of the magnetic fields in magnetized neutron stars (Duncan and Thompson, 1992), among others (Bartos, Brady, and Marka, 2013).

In order to further increase our understanding of the mechanisms causing GRBs, a complementary, *multi-messenger* approach to study these cataclysmic events can be taken.

4.2 Compact Binary Coalescences and Gamma-Ray Bursts

Einstein's theory of general relativity, presented in 1916 (Einstein, 1916), predicts the propagation of fluctuations in the metric of spacetime as gravitational waves (Einstein, 1918). The existence of gravitational waves was indirectly proven by over three decades of measurements of the orbit of the binary pulsar PSR1912+162 (Hulse and Taylor, 1975), but this fundamental prediction of general relativity had not been directly tested until 2015.

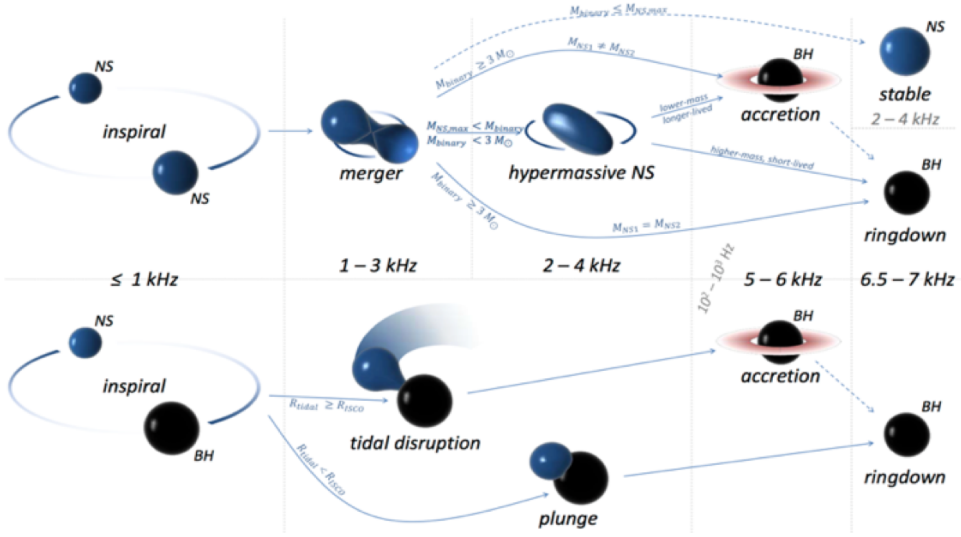

FIGURE 4.3: Schematic diagram of the possible evolution of BNS and BH-NS compact binary coalescences depending on the initial conditions. The frequency of the emitted GW is indicated for the different stages. From Bartos, Brady, and Marka, 2013

Highly compact, accelerated astrophysical objects with non-symmetric mass distributions are expected to be sources of gravitational waves by distorting spacetime (Weinberg, 2008). The orbit of the binary steadily decays as a result of the gravitational wave emission, in the end causing the astrophysical objects to spiral together at a constantly increasing rate as the merger approaches. At the final phase of the process, the compact objects merge and a characteristic burst of gravitational radiation is emitted. The physics that went into the creation of a gravitational wave are encoded in the wave itself. The nature of the resulting object or *remnant*, depends on a variety of parameters like the mass of the compact objects, the ratio of masses, the

nuclear equation of state and the mass losses during the cataclysmic event (Shibata et al., 2006, Shibata and Uryū, 2006,Oechslin, Janka, and Marek, 2007). A summary of the possible evolution of the compact binary is shown in Figure 4.3.

Many of the possible merger scenarios lead to emission of electromagnetic radiation. The most promising EM counterparts of compact object binary merger are discussed in detailed by Metzger and Berger, 2012. A summary of the potential EM counterparts is shown in Figure 4.4. Depending on the angle of the observer with respect to the inclination angle of the merger, the observer is expected to see different emissions from a compact binary coalescence.

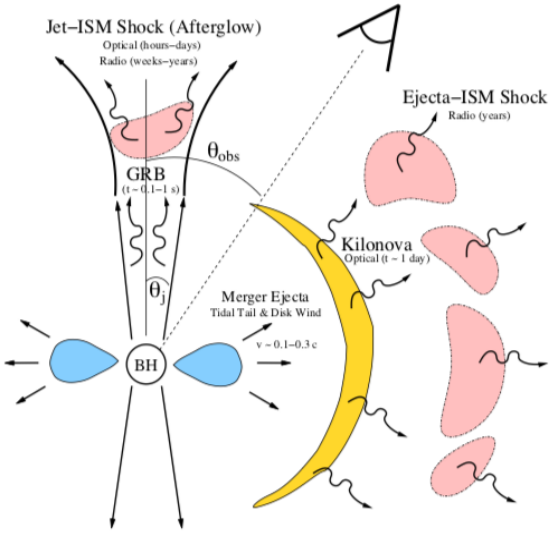

FIGURE 4.4: Schematic summary of the potential electromagnetic counterparts of NS-NS/BH-NS mergers, as a function of the observation angle. From Metzger and Berger, 2012

The merger of the binary system which lead to a formation of the *remnant* compact object and the formation of a centrifugally supported disk around it starts the temporal sequence of radiation emission in different wavelength. In mergers which include at least one neutron star, or core-collapse supernovae with rapidly rotating cores, the outflows are powered by the interaction between the remnant black-hole and accretion disk which are left after the merger. The disk that is formed around the compact object, represented in blue, is accreted and powers a collimated relativistic jet, which produces a gamma ray burst of short duration with an aperture angle θ_j, which will be observable for an observer at $\theta_{obs} \leq \theta_j$. As a result of the interaction of the jet with the interstellar medium, a further non-thermal afterglow emission is produced at larger timescales: from hour to days for optical emission and from weeks to years for radio emission. Regarding the observability of the emission, while the optical emission is observable for viewing angles of $\theta_{obs} \leq 2\theta_j$, the radio emission is isotropic as it is produced in the interaction with the ISM.

The radioactive decay of heavy elements, through the r-process nucleosynthesis in ejecta from the accretion disk, can also be present in the aftermerge scenario (Freiburghaus, Rosswog, and Thielemann, 1999). This is observed through a short-lived optical emission, lasting for few days, isotropic in space called *kilonova* (Tanaka, 2016).

In multi-messenger astrophysics, the goal is to obtain complementary information about the physics of a source and its environment by using at least two different messengers. The study of the connection between CBC and GRBs is performed at the intersection between the gravitational wave and electromagnetic emission. We aim to *monitor* the evolution of the system from the inspiral phase, through the merger, potentially followed by a *meta*stable state of the formed compact object, and ending with the fading of the remnant at various timescales depending on the frequency range of the emitted radiation. From the gravitational wave side, the information that can be extracted includes the mass, spin, eccentricity and orientation of the binary, as well as its luminosity distance and the compact object binary rate, which opens the door to population studies. On the other hand, electromagnetic emission provides information about the localization of the source at the level of arcseconds, and gives thus access to its host galaxy and environment, redshift, acceleration mechanisms at the source and the subsequent emission processes of the remnant. The complementarity of the detections can be summarized as: while the gravitational wave detection describes the fundamental dynamics of the system, the electromagnetic detection hints to the energetics and the environment of the coalescence.

4.3 Interferometric Gravitational Waves Detectors

The energy loss of the binary through gravitational wave emission can be detected on Earth if the wavelength of the propagating wave is in the sensitive range of the instrument. The LIGO Hanford Observatory, in Washington (USA), the LIGO Livingston, in Louisiana (USA) and Virgo, in Cascina (Italy), are the most sensitive second generation detectors of gravitational waves up to date. After observation campaigns between 2002 and 2010, the detectors went through a series of upgrades, noted with *Advanced* before the name of the interferometer. These upgrades were aimed to improve the sensitivity of the interferometers (IFOs) by an order of magnitude to sources in Local Universe (LIGO Scientific Collaboration, 2009).

They are kilometer-scale IFOs, sensitive to frequencies from 20-2000 Hz (Abbott et al., 2018). Each instrument is a modified Michelson interferometer where the differential changes in length between the orthogonal L-shaped arms are measured. The arms of the interferometer, with length L_* are defined by two mirrors which act as test masses. The quantity that measures the modifications caused by the gravitational wave passage is called the *strain*, and it is defined as $h(t) = \frac{L_x(t) - L_y(t)}{L_*}$. The goal of using an interferometric setup is to translate these length variation to a phase difference between the two laser beams when they arrive to a photodetector that detects modifications on the transmitted optical signal, which are proportional to the strain. Further information on the relationship between $h(t)$ and the gravitational

wave polarizations h_+ and h_x can be found in Nishizawa et al., 2009.

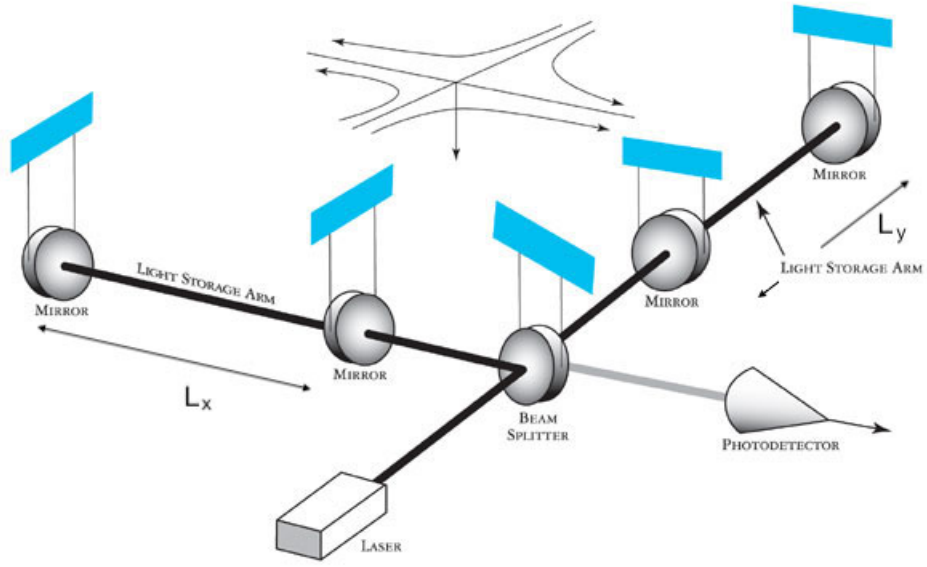

Figure 4.5: Diagram of an interferometer design used to detect gravitational waves. From `ligo.org`.

The most promising astrophysical GW sources in the frequency band of current detectors Advanced LIGO and Advanced Virgo are the inspiral and coalescence of compact binaries with neutron stars and/or solar mass black holes (BH) constituents. The compact binary inspirals enter the LIGO/Virgo sensitive frequency in their last cycles before the merger, when the pair of compact objects reach relativistic values for their orbital velocities and are separated of tens to hundreds of kilometers from each other (Abbott et al., 2018).

4.3.1 Detection and Reconstruction Methods

Compact binary coalescences signals need to be distinguished from the broadband noise of the detectors (Sathyaprakash and Dhurandhar, 1991). The used techniques take advantage of the fact that waveforms of compact binary coalescences can be computed very accurately. Indeed, the most sensitive search is done through the use of accurate physical models based on Einstein's equations, defining a *template* bank, which describe the dynamics of the systems as merger approaches, as well as the gravitational wave emission associated with the event.

In *matched filtering* techniques, the GW detector data is correlated with each waveform in a template bank, defining a parameter space. Then the local maxima of the matched-filter signal-to-noise ratio (SNR) define a list of *potential* candidates,

which have larger SNR than a certain threshold (Allen et al., 2012). Different independent pipelines have been set up in gravitational wave data analysis: `PyCBC` (Dal Canton et al., 2014), `GstLAL` (Cannon et al., 2012) and `MBTA` (Adams et al., 2016).

4.3.2 Gravitational Wave Sky Localization

The all-sky amplitude sensitivity of a gravitational wave interferometer can be quantified by the root mean squared of the antenna pattern, $F^2_{rms}(\theta,\phi) = \frac{1}{2}[F^2_+(\theta,\phi,\psi) + F^2_x(\theta,\phi,\psi)]$. This value is independent of the polarization of the wave form, and in the case of a network of N interferometers, the network RMS antenna pattern takes the form $F^2_{rms,N}(\theta,\phi) = \frac{1}{2}\sum_I F^2_{rms,I}(\theta,\phi)$. Thus, for a given waveform model, the measurements of the polarization ϕ and the inclination angle i allow to reconstruct the on-sky position of an observed source (Abramovici et al., 1992).

The sky localization is based on the posterior probability distributions of the source position, which are constructed following Bayesian methods (see Abbott et al., 2018 and references therein). The main input information is the time of arrival recorded in the interferometers involved and the consistency of phase and amplitude of the gravitational wave across the detectors. Observed time delays at the different sites are used to *triangulate* the localization of the GW source. This means that the timing accuracy is a crucial factor which determines the final localization scale. Timing accuracy is inversely dependent on the Signal-to-Noise ratio and the effective bandwidth of the signal detector, and also depends on other parameters which are common between similar detectors.

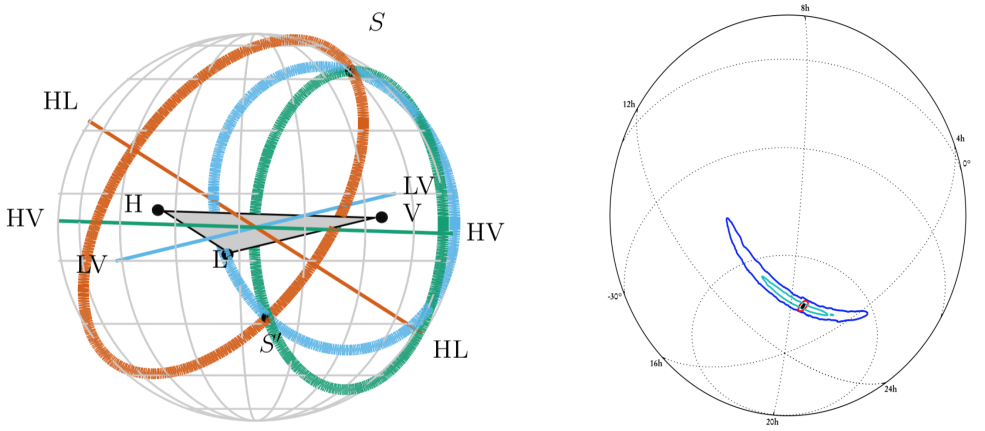

FIGURE 4.6: (Left) Time triangulation method used to locate sources for the advanced gravitational wave detector network. The various rings correspond to the constant time delay direction associated with two of the network detectors. The intersection between three rings shows the location of the source, S, as well as the mirror image, S'. (Right) 90 % credible regions sky localization of a signal with parameters consistent with those for GW150914 for different detector networks. Dark blue is for the O1 LIGO H-L network; light blue is fo LIGO H-L at design sensitivity, red is for LHV network at O2 sensitivity and black is for LHV network at design sensitivity, in orthographic projection. Both figures from Abbott et al., 2018

The result of using timing information of two interferometers, or to say with other words, the intersection between the two instruments sensitive to 4π sr of the sky (without the consideration of the respective interferometer antenna pattern), is an annulus on the sky, as can be observed in Figure 4.6. By including additional information, about the gravitational wave emitted by the source, as the phase and the signal amplitude, or precession effects, the region in the sky is restricted to smaller zones as it is observed in the sky localization in Figure 4.7. When a third interferometer is included, the triangulation method improves the localization to two sky regions which are mirror images, S and S', with respect to the plane defined by the three interferometer's network, HLV plane.

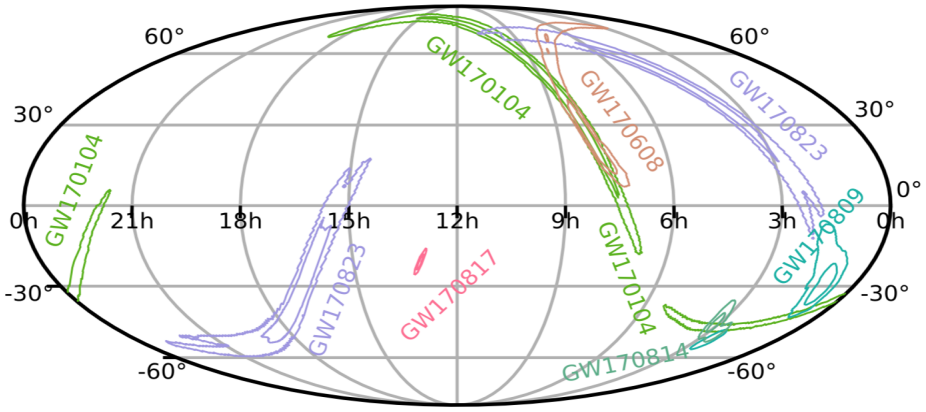

FIGURE 4.7: 50% and 90% confidence region (C.R.) of posterior probability sky localization for the confidently detected GW events during O2, in Mollweide projection and equatorial coordinates, from Abbott et al., 2019.

The localization sky maps of the gravitational wave produced by a compact binary merger coalescence can be reconstructed by two different codes which compromise between sophistication and speed, and sample the full 3 dimensional posterior probability distribution. BAYESTAR which rapidly triangulates matched-filter estimates of the times, amplitudes, and phases on arrival at the GW sites (Singer and Price, 2016) is the algorithm used in LIGO-Virgo to send prompt alerts to follow-up partners. For more sophisticated reconstruction, longer times for computation are needed, as with the LALInference reconstruction algorithm, which stochastically samples from sky location, distance, and component masses and spins (Veitch et al., 2015).

In Figure 4.7, the sky localizations of the gravitational waves observed by LIGO-Virgo during the second observation run, which are part of the Gravitational Wave Transient Catalog (Abbott et al., 2019), are shown. The extension of the localization uncertainty areas are mainly dependent on whether the event has been detected by two or three interferometers. In order to graphically address the improvements in localization to come over the next years, Figure 4.6 illustrates where the updates of a sky localization signal obtain from parameters consistent with those of GW150914. The improvements correspond, from the largest sky localization to the smallest, to

those for the O1 two detector network, LIGO H-L at design sensitivity, LIGO-Virgo HLV at early sensitivity (corresponding to O2) and LIGO-Virgo HLV at design sensitivity.

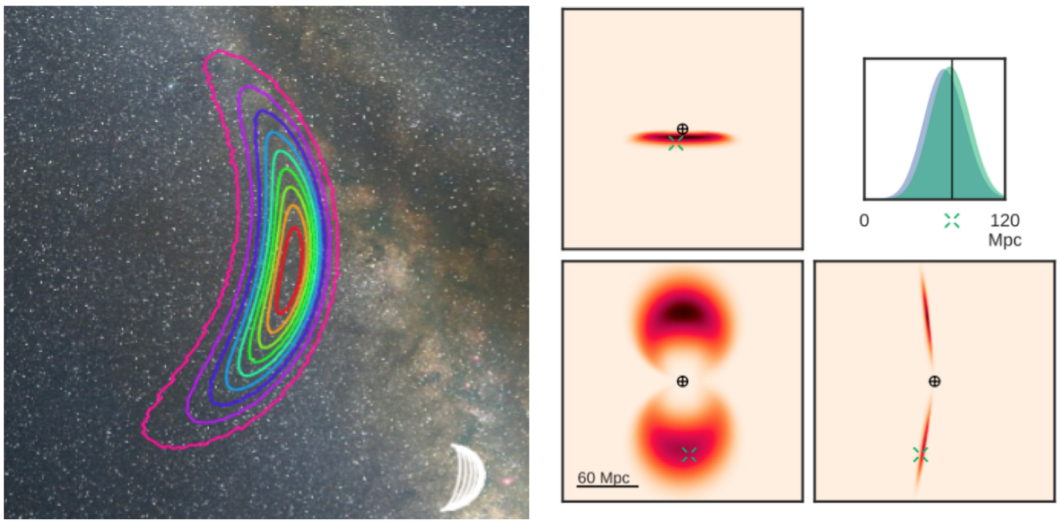

FIGURE 4.8: Contours containing different probability density regions from 90% to 10% of the GW probability map given by the LIGO-Virgo collaboration (left). Marginal posterior probability distribution in the principal planes from Singer et al., 2016a. The inset in the upper right panel shows the marginal distance posterior distribution integrated over the whole sky (blue) and in the true direction of the source (green)

The output of the LIGO–Virgo localization pipelines (e.g. Figure 4.8, left), are HEALPix (Hierarchical Equal Area isoLatitude Pixelization) all-sky images which, in its first layer, contains the posterior probability ρ_i that the source is contained inside pixel i. This represents a 2D probability sky map and this quantity is the first type of probability that can be used to prioritize sky regions to observe during follow-up observations searching for EM counterparts. In the following, we refer to this value as $P_{\rm GW}$

In addition, a posterior probability distribution along the line of sight provides the *conditional distribution of distance* (Singer et al., 2016b). It takes the form of the product of a Gaussian likelihood and a uniform-in-volume prior:

$$p(r|\mathbf{n}) = \frac{\hat{N}(\mathbf{n})}{\sqrt{2\pi}\hat{\sigma}(\mathbf{n})}\exp\left[-\frac{(r-\hat{\mu}(\mathbf{n}))^2}{2\hat{\sigma}(\mathbf{n})^2}\right]r^2 \tag{4.1}$$

This motivates the inclusion of three additional layers in the produced HEALPix file (Figure 4.8, right), also in the form of HEALPix all-sky images, which are location parameter $\hat{\mu}_i$=$\hat{\mu}(n_i)$, the scale $\hat{\sigma}_i$=$\hat{\sigma}(n_i)$ and the normalization $\hat{N}_i$=$\hat{N}(n_i)$.

4.3.3 Rates and Expectations

Advanced LIGO and Advanced Virgo construction projects ended in March 2015 and end of 2016, respectively. After major upgrades of the detector, a period of commissioning is scheduled, where the detectors are further understood and the performance is improved. Commissioning runs are interleaved between *observing* runs, where astrophysical results are produced. Scheduled observation periods which correspond to sequential upgrades of the detectors are noted with numbers, as O1 stands for Observational Run 1, etc. The goal is to step-by-step, achieve design sensitivity performances (Abbott et al., 2018).

Observation periods O1 and O2 were successfully completed, and the O3 year-long observation run started in April 2019. Main improvements included in the Observation Run O3 in the LIGO and Virgo interferometers include higher laser power, inclusion of a squeezed light injection system, improvements related to the suspended test masses and improvements in various control systems, among others. Other gravitational wave interferometers are GEO 600 in Germany, and KAGRA in Japan, which will join the network by the end of O3.

Expectations for each observation run are summed up in Table 3 of Abbott et al., 2018. In the case of O3, which is plan to be a year-long observation run, the estimated BNS detections are for this period lay in the range from 1 to 50, at distances between 120-170 Mpc in LIGO detectors and 65-85 Mpc in Virgo detector. Concerning the 90% C.R. for the localization, between 1-4% of the cases will be within 5 $\deg^2$, while 12-21% within 20 $\deg^2$.

4.4 The beginning of gravitational wave astronomy

In 2015, this first detection of a gravitational wave coming from the coalescence of a compact binary inaugurated a new era in astronomy (Abbott et al., 2016). The groundbreaking detection of gravitational waves stands as a step further in the understanding of the Cosmos. It opens a new window of observation and study, and it benefits from the transparency of the Universe to the propagation of these ripples of space-time.

Before this revolutionary achievement, whose pioneers were laureated with the Nobel Prize in 2017, a lot of effort had been put into it. First interferometric detectors were proposed in the early 60s (Gerstenshtein and Pustovoit, 1963), but it was not until the 2000s that a set of initial detectors were completed. Both LIGO detectors and Virgo, conducted observations for eight years starting in 2002, which set upper limits on various gravitational waves sources, but none was detected. As it was previously mentioned, the detectors underwent upgrades which improved significantly the performance of the network (Abbott et al., 2016).

In 2015, more than 60 years after this new way to study the Universe was proposed, a gravitational wave signal emitted from a compact binary coalescence was independently detected by LIGO Hanford and LIGO Livingston, on September 14 at

9:50:45 UTC. The merger of two black holes, with masses of $m_1 = 36^{+5}_{-4}$ $m_2 = 29^{+4}_{-4}$, happened at redshift $z = 0.09^{+0.03}_{-0.04}$, which corresponds to a luminosity distance of $D_L = 410^{+160}_{-180}$ Mpc.

This event was detected during the first observation run O1, which extended from September 12, 2015 to January 19, 2016. A total of three gravitational-wave events have been reported during O1. During the second observation run O2, which started in November 30, 2016 and ended in August 25, 2017, four events were reported online, namely one BNS and three BBH, and four additional BBH were detected afterwards in off-line searches. Thus, a total of 11 coalescences have been detected with the data taking during the O1 and O2 observing runs. Results have been reported in the first catalog of gravitational wave signals from compact binary coalescence (Abbott et al., 2019), where the localization of the O2 detections are shown Figure 4.7. The masses of these binary black hole (BBH) mergers are plotted together with the black holes detected in X-ray observations of binary systems in Figure 4.9.

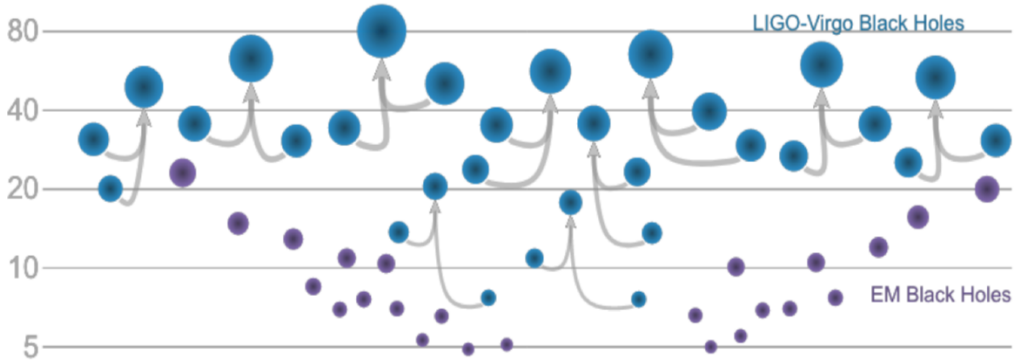

FIGURE 4.9: Masses of black holes detected by the gravitational emission during the coalescense by LIGO/Virgo and the resulted black hole and black holes detected through observations of X-ray binary systems. Image credit: LIGO-Virgo / Frank Elavsky / Northwestern

4.5 First Follow-ups of Gravitational Waves Observations

The discovery of gravitational waves has had a crucial impact in many fields, from cosmology to multi-messenger physics in an astrophysics context, and thus, stands as the basis of many works, as it is the case for this thesis. This is due to the unique view of the Cosmos that gravitational waves provide which, combined with other multi-messenger signals, can shed light on the processes in place when compact binaries merge. Due to the physics of the emission of these multi-messenger counterparts, the multi-messenger signals can be faint and fade rapidly, so a rapid reaction plays an essential role.

In order to efficiently share their detections, the LIGO and Virgo collaborations have put important efforts on real time data analysis of compact binary signals and

their localization reconstruction (Singer and Price, 2016). An alert is issued and sent to the astrophysics community whenever a merger candidate is detected, so that the search of counterparts, i.e. electromagnetic emission or neutrinos, begins.

In the first observation runs O1 and O2, a membership structure based on Memoranda of Understanding (MoU) had been put in place, defining a multi-messenger follow-up network. After O2, a big effort was made by LIGO-Virgo to transition to Open Public Alerts (OPA), where the entire scientific community is invited to join the multi-messenger network, an no MoU requirements are needed to join. This new LIGO-Virgo ElectroMagnetic *Open* (OpenLVEM) forum has been set up in order to encourage and facilitate the free exchange of information and ideas.

The two type of alerts, the human-readable GCN Circulars and the machine-readable GCN Notices are distributed through GCN, set up by NASA. However, several type of GCN Notices are sent at different timescales, which are related to the level of accuracy of the performed analysis. The first notice, which comes within 1 to 10 minutes after the trigger are *Preliminary* notices, where an automatic process is in place and there is no human-vetting. These alerts not always include a sky localization and are thought to be a first *heads-up* for astronomers. Within the next 24 hours, either an *Initial* or *Retraction* notice and circular are issued. These alerts are human-vetted and a sky localization is included if the candidate is confirmed. Subsequent *Update* notices and circulars are sent with refinements on the analysis and localization reconstruction. These steps are summarized in Figure 4.10.

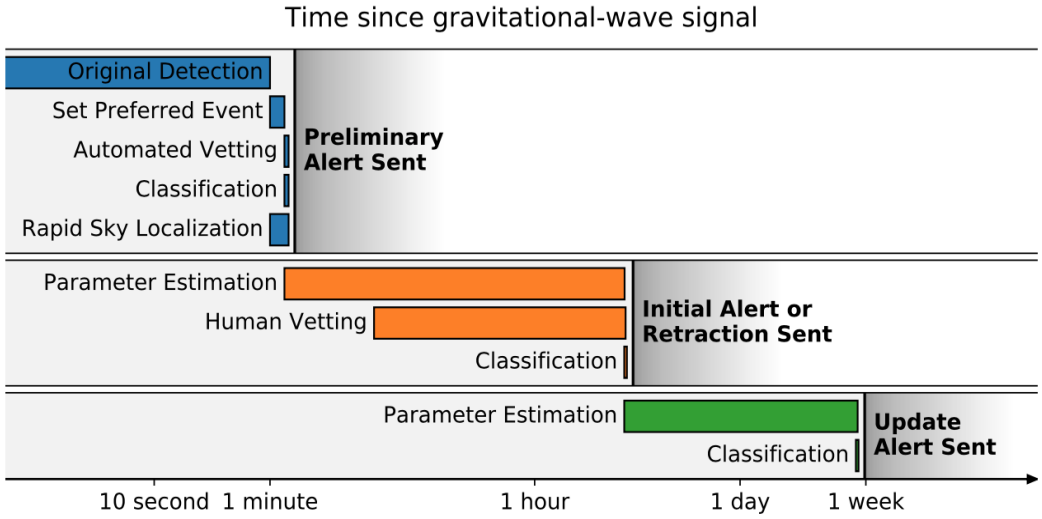

FIGURE 4.10: Sequence of LIGO/Virgo alerts for a single event that will be distributed through the Gamma-ray Coordinates Network (GCN) via notices and circulars. From `https://emfollow.docs.ligo.org`

The information included in all GCN notices, except from the *Retraction* notice, is summarized in the following[1].

- **Name.** A unique identifier is assigned to each event of the GraceDB database, where all the detected GW are stored.
- **Significance.** The significance of the event is given through its associated false alarm rate (FAR). The FAR of an event is defined and computed as the expected rate of events from the pipeline that produced the event with equal or greater significance in the absence of astrophysical signal.
- **Sky localization.** The skymap with the posterior probability distribution as described in Section 4.3.2 is included, embedded in a `URL`.
- **Inference.** This information is only included for events identified as Compact Binary Coalescences (CBCs). The two important parts, which are crucial to schedule follow-ups are the classification and the properties. The classification is given by five probabilities of belonging to specific sources, summing the unity. There are BSN mergers, NSBH merger, BBH merger, *Mass Gap* merger and Terrestrial. These are associated to the mass of the components, and the classification is summarized in Figure 4.11.

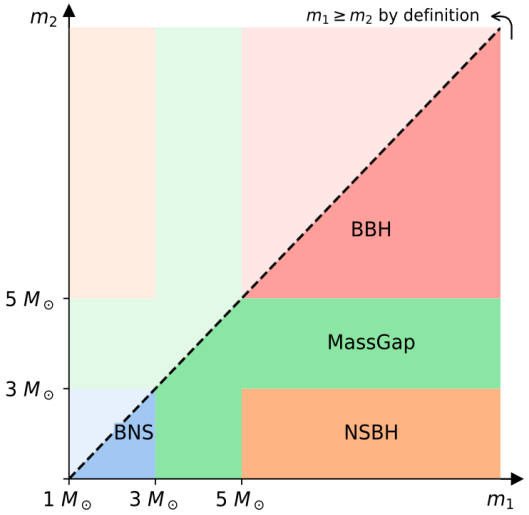

FIGURE 4.11: Classification of observed signals depending ing the compact binary mass parameter space from CBC searches of LIGO-Virgo pipelines. From `https://emfollow.docs.ligo.org`

The *properties* section is aimed to give an estimate of the probability of `HAS_NS` and `HasRemnant` of the CBC to the astrophysicist following gravitational wave events of the CBC. These quantities are based on details of neutron star physics as the maximum NS mass or the equation of state.

[1]More details on the contents of GCN circular and GCN notices can be found in `https://emfollow.docs.ligo.org`

4.5.1 Binary Black Hole Mergers

The first gravitational wave follow-ups were stablished and performed by optical telescopes (Aasi et al., 2014), *Swift* satellite (Evans et al., 2012), LOFAR and the Expanded Very Large Array, during LIGO-Virgo science runs in 2009-2010 (Abadie et al., 2012). A partnership was created between LIGO and Virgo collaborations with a large group of EM observatories in radio, optical and X-rays. Although no convincing transient candidate was observed, these first searches represent a major step: the basis for joint studies between the GW-EM community was stablished. VHE facilities joined the community at later times.

In the following, we focus on the gravitational wave follow-up of binary back holes by very high energy instruments. This type of compact binary coalescences represent the larger amount of detections so far.

First follow-up of gravitational waves in the VHE gamma-ray domain was performed by the MAGIC telescopes in 2015, during O1. The event followed up was GW151226, a binary black hole merger whose 90% C.R. sky localization expanded over $\sim$1400 deg^2 in the sky. The MAGIC collaboration manually selected four regions of the sky localization using information that was shared in the EM follow-up group set by LIGO-Virgo through MoUs. A total of 2.6 h of observation were taken $\sim$ 65.5 h after the GW event, where no significant emission was detected (De Lotto et al., 2016).

The second follow-up observation of a gravitational wave event in the VHE domain was also a binary black hole merger, GW170104, shown in Figure 4.7. VERITAS observed the localization area 21 hours after the GW event. They performed 39 consecutive tiling pointing observations of 5 minutes each, covering 27% of the GW sky localization, on the norther region. With better weather conditions, observation would have been sensitive to sources with a flux greater than 50% of the Crab Nebula above 100 GeV (VERITAS collaboration, 2017).

The HAWC observatory has been following every binary black hole alert from the gravitational wave community, albeit the instantaneous FoV was only covering the localization area in two cases out of five. No significant emission has been observed (Martinez-Castellanos, 2018).

The H.E.S.S. telescopes follow-up the first 3-interferometer detection of a gravitational wave, produced by a binary black hole merger, which happen in August 14 2017, GW170814 (Figure 4.7). The 90% C.R. for the event localization of this BBH expands to 190 deg^2 and it is located in the southern sky. H.E.S.S. observations covered about 80% of the LALInference sky localization uncertainty region with 11 observations in a three night follow-up campaign, which corresponds to a total of $\sim$5h30m of data acquisition time. Although no signal has been observed, constraining upper limits have been derived for the emission of the remnant at energies between 250 GeV $<$ E $<$ 10 TeV. Detailed information about the follow-up strategy implemented and the analysis of the obtained data is given in Section 7.2.2.

However, electromagnetic counterparts are in general not expected from binary black hole coalesces, although some authors have proposed some *exotic* production mechanisms as in Loeb, 2016 or Zhang, 2019, among others. The aforementioned broad MWL signals are on the other hand expected from the merger of binary neutron star systems.

4.5.2 Binary Neutron Star Mergers: the GW170817 campaign

In August 17, 2017, at 12:41:04 UTC, the advanced LIGO-Virgo interferometers observed for the first time the last moments of the in-spiral and the coalescence of a binary system of neutron stars. The signal to noise ratio across the three instruments had a value of SNR = 32.4, which was much louder than other mergers detected previously. The system was composed of two compact objects of masses $m_1 \in (1.36 - 2.26)M_\odot$ and $m_2 \in (0.86 - 1.36)M_\odot$, consistent with two neutron stars. After the observed, long GW signal was observed over a period of $\sim$ 100 seconds, with more than 100 cycles, the pair of neutron stars violently merged, leaving behind a final remnant of mass $m = 2.82^{+0.47}_{-0.09}M_\odot$

The GBM instrument onboard the Fermi satellite detected a sub-luminous, faint short GRB, $\sim$ 1.7 seconds later, GRB170817A, proving for the first time that neutron star mergers can be accompanied by electromagnetic emission (Abbott et al., 2017a).

A large number of facilities followed up this joint detection of a gravitational wave and its EM counterpart, launching a campaign across the electromagnetic spectrum and other messengers. It stands as the largest multi-wavelength campaign up to date 4.12. A bright optical counterpart, SSS17a/AT was pinpointed 11 hours later by the One-Meter, Two-Hemisphere (1M2H) team using the 1 m Swope telescope at Las Campanas Observatory in Chile, which yield to the identification of the location of the source as well as its host, the elliptical galaxy NGC 4993 (Abbott et al., 2017c). Within an hour, other optical telescopes, namely the Dark Energy Camera, the Distance Less Than 40 Mpc survey, Las Cumbres Observatory, the Visible and Infrared Survey Telescope for Astronomy and MASTER, also detected the source. These observations, covering the UV, optical, and IR range, were able to map the emission from the sub-relativistic ejecta.

Regarding other messengers, observations were performed by the neutrino telescopes Antares, IceCube and Pierre Auger. These show that neither directionally coincident neutrinos were observed around the merger time ($\pm$500s) nor MeV neutrino burst was detected coincident with the merger time (Albert et al., 2017). Nonetheless, this non-detection of neutrinos is consistent with model expectations from GRBs seen at large viewing angles.

In GRB afterglows, X-rays are important since they allow to put constrains on the geometry of the outflow, its energy output, and the orientation of the system with respect to the observer. The source was detected in X-rays by *Chandra*-X nine days after merger, but due to the source being too close to the sun, neither Swift nor

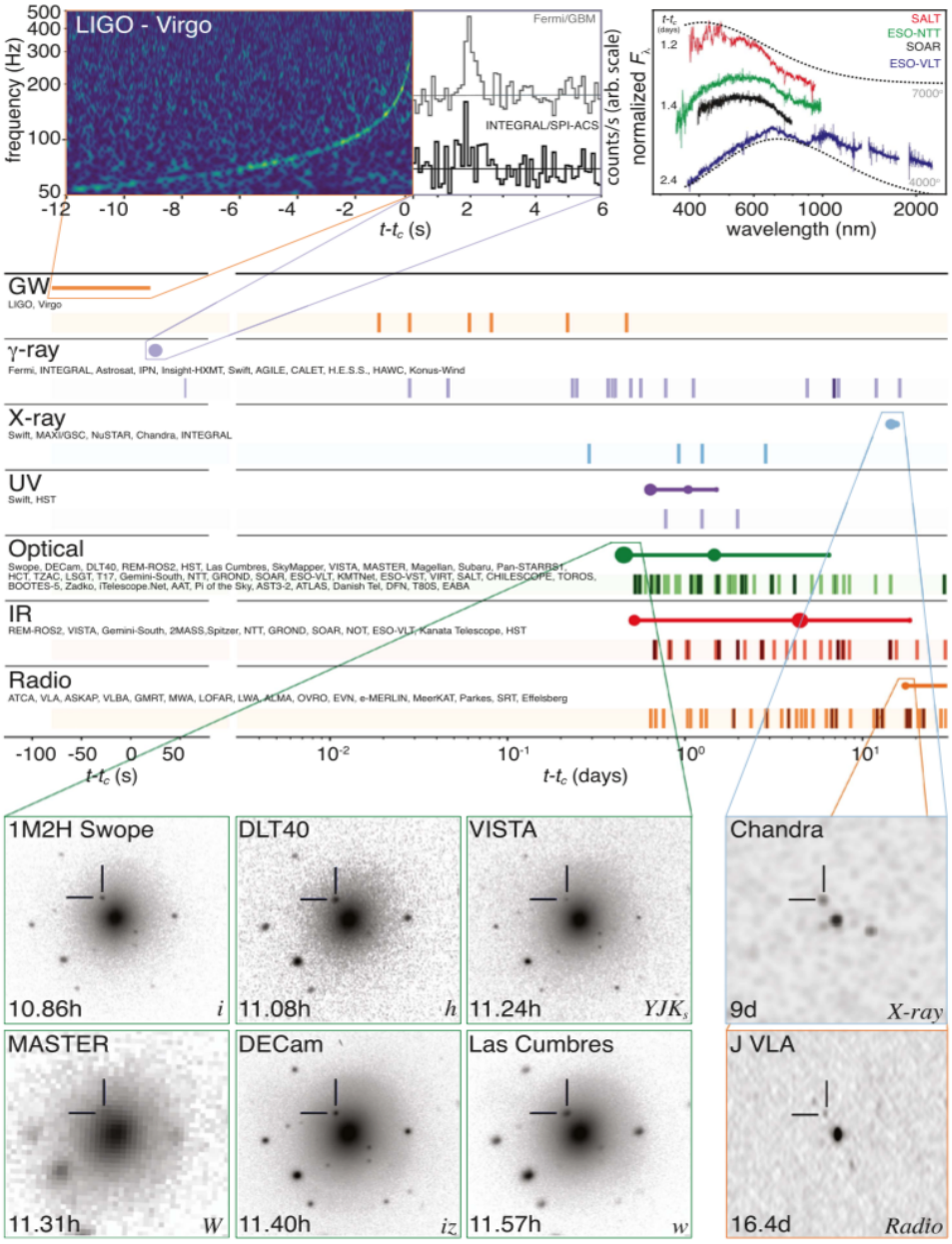

FIGURE 4.12: Timeline of discovery of GW170817, GRB170817A and the optical counterpart SSS17a/AT and the subsequent follow-up campaign shown by messenger and wavelength. Names of the relevant instruments, facilities, or observing teams are quoted at the beginning of each sub-diagram. Shaded dashes refers to the time when observations were reported through GCN Circular, solid circles refer to representative observations where their areas are approximately scaled by brightness and the solid lines indicate that the source was detectable by at least one telescope. From Abbott et al., 2017c

Chandra could carry out more observations until $\sim$ December 2017 (Haggard et al., 2017).

Observations in the radio band can trace the fast moving ejecta after the neutron star merger, which allows to understand the geometry of the ejecta, the energy released in the coalescence and the interactions with its surroundings. First detection happened on September 2 and 3, 2017 by VLA at two different frequencies, ∼3 GHz and ∼6 GHz (Alexander et al., 2017).

While Fermi-LAT was not able to promptly observe the region due to the Southern Hemisphere Anomaly, other satellites as INTEGRAL detected the event in an offline search initiated by the LIGO-Virgo and Fermi-GBM reports, using the Anti-Coincidence Shield of the spectrometer on board (Abbott et al., 2017a). In the very high energy range, H.E.S.S. was able to obtain the first ground based observations after the merger. These results are a fundamental part of my thesis work and are explained in detail in Section 7.2.3.

In the first ∼15 days, the multi-wavelength spectrum of the source consisted of a combination of non-thermal synchrotron emission, dominating in the X-rays and radio energies, and a thermal emission which was powered by the heavy elements synthesized in the merger ejecta undergoing radio active decay, which dominates the UV-optical-NIR bands (Margutti et al., 2018 and references therein). While the thermal component faded rapidly, the non-thermal component brightened over the following ∼ 160 days. The observations performed in radio, optical and X-rays bands with the VLA, Hubble SpaceTelescope and Chandra X-rays Observatory show that the rise of the broadband emission can be described by a power-law $F \propto t^{0.7}$, and that there is no sign of spectral evolution across the EM spectrum, with the spectral index fitted to $F \propto \nu^{0.585}$. From this value, the Lorentz factor of the mildly relativistic material that powers the emission can be estimated to be $\Gamma \sim 3 - 10$ (Margutti et al., 2018), which is far from the values usually found for GRBs (Ghirlanda et al., 2018).

Radio and X-ray observations with the VLA, Chandra X-ray Observatory and Hubble Space Telescope of the remnant at later times, ∼ 220-290 days post merger (Alexander et al., 2018), show the turnover of the radio and X-ray lightcurve (Figure 4.13). The synchrotron emission achieved a peak brightness ∼ 163 days after, and started declining. The spectral index however had not changed, which indicates that the synchrotron cooling break had not been reached yet (Alexander et al., 2017).

These observations were able to rule out some of the most simple models, as the top-hat jets viewed off-axis and uniform spherical outflows, due difficulties to incorporate the temporal evolution. The two models which can reproduce the observations are a either a radially stratified quasi, spherical ejecta traveling at mildly relativistic speeds, which is generally referred to as *choket jet* or *cocoon* or emission from off-axis collimated ejecta characterized by a narrow cone of ultra relativistic material with slower winds extending to large angles, known as the *structured jet* (Troja et al., 2018).

In Chapter 3, it has been pointed out the interest of performing radio observation

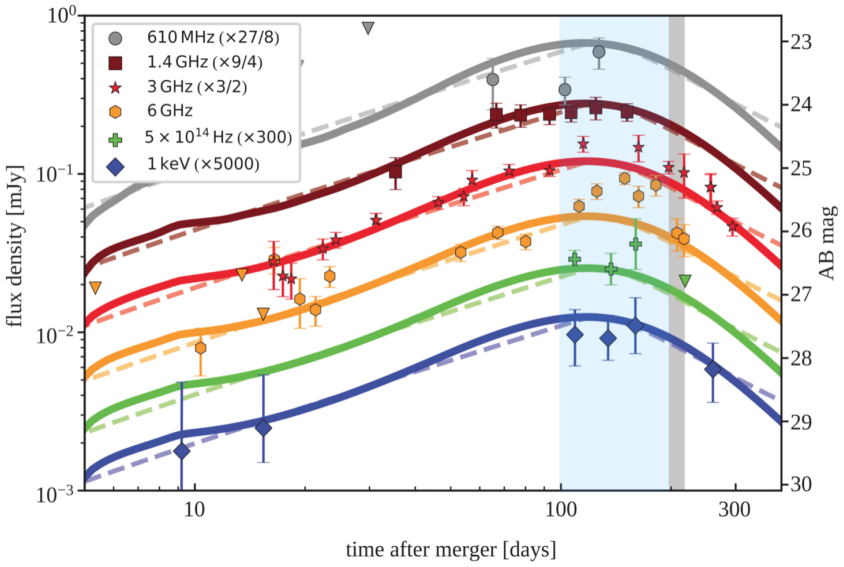

FIGURE 4.13: Multiwavelength light curves of GW170817 in X-rays, optical and radio energies. The proposed models describing the evolution of the remnant are included for the structured jet model (solid lines) and the choked jet cocoon model (dashed lines). The grey region represents the period of VLBI observations mentioned in the text. The light blue region represents H.E.S.S. observations at late times. Modified from Ghirlanda et al., 2019

of jets, in particular VLBI, in the context of AGN jets. In this spirit, high-spatial-resolution measurements using VLBI observations on the source have provided the first clear indication of discrimination between the *cocoon* and the *structured jet* scenario (Ghirlanda et al., 2019). By comparing the image size obtained from VLBI data to the predictions of the spatial distribution of the radio brightness obtained from simulations, cocoon models have been excluded. These observations were performed 207.4 days after the merger using a global network of 32 radio telescopes.

The H.E.S.S. experiment also launched a long-term follow-up campaign between 120 and 270 days after merger. Observations at very-high energies are able to break the ambiguity on the magnetic field of the ejecta and the maximum accelerated particle energy (Rodrigues et al., 2019). Assuming that accelerated electrons undergo SSC on the photons produced by synchrotron radiation at radio and X-rays, the expected peak of this SSC component depends then on the maximum accelerated electron energy. In this context, the radio-to-X-ray emission is able to probe the quantity $u_e \cdot u_B$ and the SSC component at high energies is related to $u_e^2 \cdot u_B$. The results of the H.E.S.S. campaign and the constraints derived by very-high energy emission will be presented in the near future.

To sum up, the broadband monitoring of GW170817 show how multi-messenger observations are able not only to localize the source of the emission but also to jointly set powerful constraints on astrophysical events.

4.6 Discussion

The first detection of a neutron star binary merger has proven successful the multi-messenger approach. This event, probably the first of more to come, has had an important impact in several research fields at different levels. Although in the previous section we focus on the impact in the astroparticle physics domain, with the study of the emission of merging compact object, particle acceleration and geometry of the emission, the event has also had implications in other fields. For example, while in cosmology, this event led to the independent determination of the Hubble constant (LIGO Collaboration et al., 2017), in nuclear physics, it enable to study the r-process in astrophysical source as well as the equation of state of the neutron stars (Evans et al., 2017).

Future observation runs by gravitational wave interferometers, which will be certainly accompanied by multi-wavelength programs set up around the world to cover the evolution of the remnant, will set the stage for future multi-messenger discoveries in astrophysics that started with GW170817 in 2017.

Chapter 5

GW counterparts searches with Water Cherenkov Tanks

Contents

5.1 Introduction

The era of multi-messenger astrophysics is the result of the developments and improvements of novel detection methods of signals from different messengers, improvements on information sharing within the scientific community and the prompt reaction to alerts by very different facilities across the electromagnetic spectrum and novel messengers from the Universe. These yielded not only to unprecedented follow-up campaigns during the last years but also the monitoring of sources, as explained in Chapter 4, as well as archival analyses.

An example is the follow-up campaign on the blazar TXS 0506+056, that was marked by the 3 σ correlation of a high-energy neutrino detected by IceCube with

the gamma-ray flaring episode observed by *Fermi*-LAT and MAGIC (IceCube, 2018). This association lead to an archival search of neutrino events from the same source, which yield to the identification of a neutrino excess from the direction of the blazar TXS 0506+056 at 3.5 σ significance between September 2014 and March 2015 (IceCube Collaboration, 2018)

The TXS 0506+056 example shows how sub-threshold data, in this case the triggering IceCube neutrino had an astrophysical probability of ∼50% (or, 50% probability of atmospheric origin), can trigger observations from other observatories, and lead to valuable astrophysical observations.

It is the case that the majority of the current coincidence analyses performed in the high-energy astrophysics community focus on events which are *well above* the detection threshold stablished for each independent experiment. This leaves out *potential* signal events that are statistically indistinguishable from background due to the sensitivity of the detector, to which we refer in the following as *sub-threshold* events.

The correlation of sub-threshold events in a multi-messenger context could enhance the otherwise marginal independent events, by combining the significance of a joint detection and potentially point to a common astrophysical origin. Hence, this approach could lead to the identification of potential new multi-messenger sources.

5.2 Astrophysical Multi-messenger Observatory Network

The Astrophysical Multi-messenger Observatory Network (AMON) has been established as a general system devised to receive, integrate and distribute above- and sub-threshold data from several observatories in the context of multi-messenger physics (Solares et al., 2020). AMON provides the framework and set up a flexible network and IT infrastructure needed for such aim. AMON relies on publicly available data as well as proprietary data provided by member collaborations that join by Memoranda of Understanding (MoU).

The AMON network focuses on the study of physical processes which occur under the most extreme conditions. The science cases which are of highest interest for the network are the search of cosmic particle accelerators, ultra-high-energy cosmic ray accelerators, gravitational wave sources, supernovae, long gamma-ray bursts, active galactic nuclei, tidal-disruption events (TDEs), fast radio bursts and soft gamma-ray repeaters (SGRs). For further information on the science cases of the AMON network, the reader is invited to consult Solares et al., 2020.

The details of a multi-messenger analysis depend on the characteristics of the facilities involved, where a first distinction can be made into *follow-up* approach, in the case of pointing telescopes, and *coincidence* approach, for observatories which are continuously receiving data and observe large regions of the sky. While the first type

needs to be *triggered*, the latter benefits from the regular provision of data, which can be exploited either in real-time or in archival searches. This type of observatories are the most interesting for a program as AMON, and are the main contributors to the network. The different messengers and the participating experiments are shown in Figure 5.1. These include gravitational wave observatories, facilities observing in the electromagnetic spectrum, neutrino observatories and cosmic ray observatories. In Figure 5.1, monitoring observatories are represented by blue arrows and follow-up observatories by orange arrows [1].

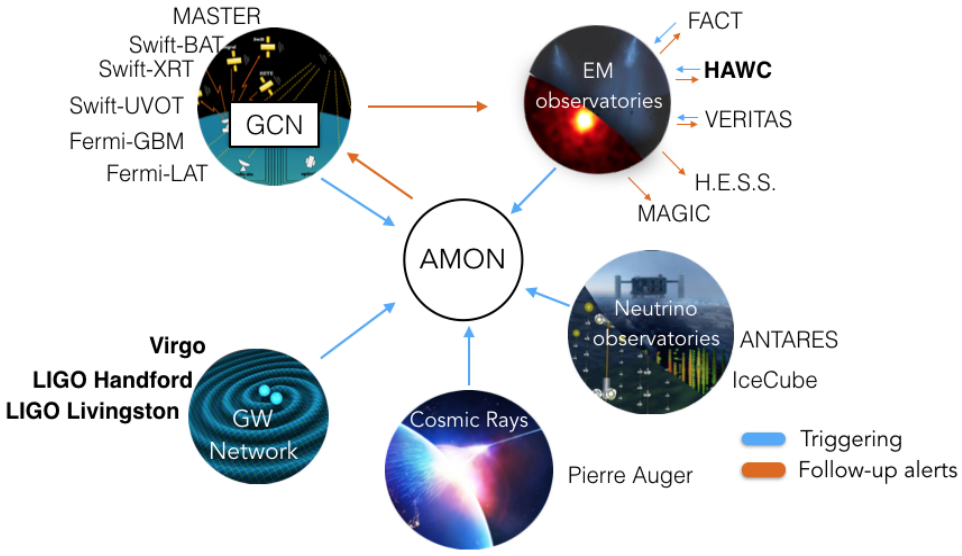

FIGURE 5.1: Diagram showing the AMON role and the workflow of information from different triggering and follow-up observatories

The three main goals of the AMON program can be summarized as:

- Perform coincidence searches of data of different observatories in real-time, with a particular interest on sub-threshold data, and distribute prompt alerts to follow-up observatories. Hence, the goal is the development of real-time pipelines that can handle a variety of inputs and issues an alert if a significant coincidence is found.

- Store events in a database to perform archival searches for significant coincidences. The AMON system is designed to hold a terabyte-scale data.

- Receive events and broadcast them, through the Gamma-Ray Coordinates Network/Transient Astronomy Network (GCN/TAN)[2] (Barthelmy et al., 1995), to the astronomical community for follow-up.

[1] as of July 2019, when this manuscript was written
[2] `https://gcn.gsfc.nasa.gov`

5.2.1 Searching for coincidences: AMON Analysis Channels

Multi-messenger astronomy inherently brings up the question of how to establish a coincidence between two independent observations of the same event. This question has been deeply studied in the literature, when connecting two or more of the four multi-messenger channels, i.e. cosmic rays, neutrinos, gravitational waves and electromagnetic radiation. Some examples can be found for frequentist approaches in Baret et al., 2012 and Urban, 2016 and for bayesian approaches in Vianello et al., 2017 and Ashton et al., 2018.

Concerning the type of coincident analyses, different questions are answered depending on the type of statistical approach: whereas bayesian statistics quantify the *degree of confidence* when comparing two hypothesis through the p-value and where some *prior* assumptions are made, frequentist statistics quantify the consistency of a specific joint observations with respect to a *null* background hypothesis.

The coincidence analyses performed in the AMON network are separated into different channels, depending on the type of messenger of each data stream. The coincidence analyses are constructed mainly on three criteria: temporal selection, spatial selection and construction of a test statistic for ranking the coincident event. Depending on the science case, the requirements on the temporal and spatial coincidence as well as the functional form of the test statistic may vary. In the case of the test statistic, a log-likelihood ratio is used. If further information is provided by the partner observatories on the significance of the events, Fisher's method is used to combine the different p-values which yields to a χ^2 value associated the coincidence (Fisher, 1934).

The latency of the AMON analyses ranges from archival analyses to real-time operations. For searches in real time, the events are transmitted to other AMON partners or to the public through GCN/TAN depending on the agreement with the respective team or collaboration to obtain an extensive and quasi simultenous coverage of the phenomena across the MWL and MMA range.

5.3 HAWC-LIGO/Virgo coincidence analysis

Here I present a likelihood ratio coincidence analysis that has been developed with the goal of studying the gamma-ray burst to neutron star merger connection in the prompt phase of the post-merger evolution. In particular, we search for very-high-energy electromagnetic signatures emitted as a multi-messenger counterpart of a gravitational wave detection emitted by a NS-NS inspiral and coalescence.

For this coincidence-search channel we exploit the large FoV of the HAWC observatory and the LIGO-Virgo interferometers, which, due to their design, can instantaneously monitor large areas of the sky. The HAWC observatory has access to 2 sr of the sky instantaneously and 2/3 of the sky in 24 hours. Regarding Advanced LIGO and Advanced Virgo interferometers, these are interfometers which observe in 4π sr,

with a sensitivity which is dependent of the antenna pattern of the combination of detector during observations (see Chapter 4).

Previously, studies have been performed on the expected rate of GRB detections with HAWC. An expected rate of 1.65 yr^{-1} was derived by an extrapolation of *Fermi*-GBM detection to the HAWC energy range taking into account the expected cutoff due to EBL attenuation (Taboada and Gilmore, 2014). However, there is a difficulty in extrapolating Fermi-LAT GRB spectra to very high energies since it is still unclear if the extra power-law component observed in the spectra of several bright GRBs is a common property at GeV energies. Additional uncertainties are related to the imprecise knowledge of jet Lorentz factor distributions which relate to the intrinsic spectral cutoffs (Piron, 2016). Thus, the expected number of GRB detections at very high energies has large uncertainties. The recent detection of two independent GRBs by IACTs will put constraints on this estimates, as explained in Chapter 4. So far no significant GRB detection has been achieved by the HAWC observatory.

Regarding gravitational wave events, not all the astrophysical events in gravitational waves observatories reach the FAR threshold for open public alerts. For instance, increasing the FAR on the considered events from 1 per 100 years to more than 1000 per year would roughly double the number of detectable astrophysical events, at a low cost on the compact binary distance/area localizations, of less than a factor of 2 and an increase in volume localization by less than a factor of 4 (Lynch et al., 2018). These low-purity events present an outstanding opportunity for coincident analyses and especially for the EM-counterpart searches in very high-energy astrophysics within AMON.

We believe that, given the extraordinary scientific rewards that can be anticipated from every new multi-messenger event discovered, this straightforward argument suffices to demonstrate the substantial scientific value in pursuing joint sub-threshold GW+γ searches. We focus on the development of likelihood ratio technique which, following a frequentist approach, handles the observations performed by experiments searching for correlations between very high-energy photons and gravitational wave emission.

In the following, we firstly describe the statistical framework and then, in Section 5.4.2 the sub-threshold candidates are presented.

5.4 Statistical framework

The preselection of events is based on a hypothesis on the spatial and temporal relationship between the two messengers: the spatial requirements is based on the overlapping of the uncertainty regions and we have made a hypothesis on the possible time shift between the gamma rays and the GWs. These requirements are:

- Temporal coincidence. The window of the coincidence between both messenger is set to an interval [-100, 500] seconds. This value is motivated by the expectations of the prompt emission delays (Fermi-LAT Collaboration, 2013).

- Spatial coincidence. Only photon triggers that lay in the 90% localisation uncertainty region provided by the GW interferometers with the addition of accounting for the HAWC angular resolution at those energies, conservatively taken as 1.5°, are selected.

These two *a priori* spatial and temporal restriction are applied before the statistical analysis starts. These requirements are strong enough to make the successful candidate *interesting* enough due to their low occurrence. The rate of coincidences has been studied, and it is presented in Section 5.6. The workflow of the coincidence analysis for GW+γ events is shown in Figure 5.2.

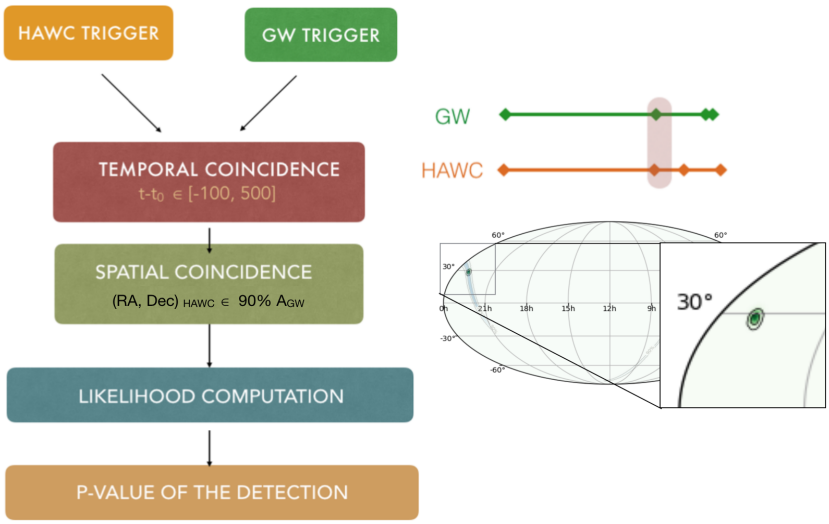

FIGURE 5.2: Workflow of the coincidence analysis presented in the context of AMON, where the join candidates are *a priori* selected, a joint likelihood ratio is computed for each event and a $p_{GW\gamma}$ is finally associated

5.4.1 Joint likelihood ratio construction

The ranking likelihood ratio that is computed follows a frequentist approach, and quantifies how background-likely the joint GW+γ events are. This approach is inspired from previous frequentists approach (Baret et al., 2012) and from the general coincidence studies in the AMON network (Solares et al., 2020).

For each of the messengers considered, we define the *null* hypothesis as the case were the signal originates from a background fluctuation and the *alternative* or *source hypothesis* hypothesis as the signal coming from an astrophysical source.

Several statistical tools are introduced to claim a coincident detection pointing to a common source in order to derive the p-value to associated to the coincident GW+γ event, $p_{GW\gamma}$.

First, the joint likelihood ratio is built taking into account the different messengers involved as:

$$\lambda(\vec{x}_S) = \frac{H_1^{GW}(\vec{x}_S) \cdot H_1^{\gamma}(\vec{x}_S)}{H_0^{GW}(\vec{x}_S) \cdot H_0^{\gamma}(\vec{x}_S)} \tag{5.1}$$

The likelihood represents a 2D likelihood map. However, the localization uncertainty a gravitational wave depends on the detectors involved and their sensitivities, and can extend over 10-1000 deg^2. To be able to compare events with different GW localization uncertainties, a normalization factor needs to be considered at the level of the likelihood.

Then, the p-value is computed as the probability of obtaining the observed value of the test statistic or a greater value than the null hypothesis. The p-value associated with each λ_{max} is computed from the λ_{max} distribution, as:

$$p_{spatial} = \int_{\lambda_{max}}^{\infty} f_{BG}(\lambda'_{max}) d\lambda'_{max} \tag{5.2}$$

The *Fisher's combined probability test*(Fisher, 1934) is used to combine the different information which are part of the same overall hypothesis, as it is the case for different multi-messenger observations, i.e. the independent detections and the spatial association. The result of this combination is the *test statistic* χ^2. In this way, the joint test statistic includes results of the independent observations of the gravitational wave through p_{GW} and the VHE photon cluster, p_γ, and the value obtained in Equation 5.2 for the spatial p-value, $p_{spatial}$, following:

$$\chi^2 = -2 \cdot \ln(p_{spatial} \cdot p_{GW} \cdot p_\gamma) \tag{5.3}$$

The final $p_{GW\gamma}$ results, which quantifies the significance of a joint event is given as:

$$p_{GW\gamma} = \int_{\chi^2}^{\infty} f_{BG}(\chi'^2) d\chi'^2 \tag{5.4}$$

In this way, this analysis of GW+γ coincidences provides a ranking statistic method: the smaller the p-value $p_{GW\gamma}$, the greater the evidence against the null hypothesis. Note, however, that in this *frequentists* approach there is no possibility to translate such result to the probability of an event having an *astrophysical* origin.

5.4.2 Gravitational wave signal

The gravitational event is identified and the localization of the merger is reconstructed as explained in Chapter 4. The alert typically contains information on the FAR, obtained from the study of the background in the interferometers, the 3D-GW localization uncertainty for the event and the time of the detection.

The alternative hypothesis H_1^{GW} is given by the posterior probability on the localization of the source of the gravitational wave, included in the 3D-GW localization.

The null hypothesis H_0^{GW} is considered homogeneous over the whole sky, as all the directions are equally likely to produce a background event.

$$H_0^{GW} = \frac{1}{4\pi} \qquad H_1^{GW} = PSF_{GW} \tag{5.5}$$

Note that the consideration for the H_0^{GW} is an approximation, since different configuration of detection yields to different antenna patterns, being possible 4 types of them when requiring at least two detectors recording the event. However, changes are negligible within the uncertainty region of the HAWC candidates, that although showing a dependency with energy, it does not go beyond the $\sim$ degree level.

The null and the alternative hypothesis are shown in Figure 5.3.

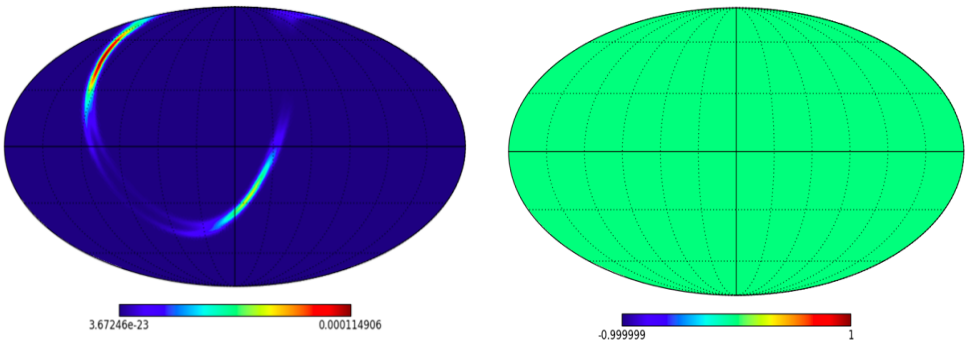

FIGURE 5.3: (Left) Alternative hypothesis H_1^{GW} for GW signal of a simulated event. (Right) Null hypothesis H_0^{GW} for GW signal.

The p-value of the gravitational-wave detection, p_{GW}, is derived by using the individual FAR and the time window of the gravitational-wave search (ΔT_{GW}). Concretely, we assume a Poisson distribution of $k = 0$ outcome with λ average, found by multiplying the coincidence time window by the FAR of the event, as:

$$p_{GW} = 1 - Pois(0, \Delta T_{GW} \cdot \text{FAR}) \tag{5.6}$$

5.4.3 High-energy gamma-ray signal

HAWC has developed an unbiased all-sky search method for short-timescale VHE transients that does not rely on external trigger information (Lennarz et al., 2017). It searches for excesses in four different time windows of 0.2, 1, 10 and 100 seconds, motivated by *short* GRB and *long* GRB distributions. This method is more efficient in short timescales due to the low background regime.

The search of GRB candidates is performed by the detection of a positive excess on the expected number of background counts by using the method described in Wood, 2018. Monte Carlo simulations have been used to optimise the spatial bin size, the time window duration and the post-trials sensitivity, in order to improve the performance of the VHE transient search. The search is done temporally by shifting a fixed-width sliding time window through data in steps of 10% the duration of the

window. The spatial search is based on a rectangular grid in right ascension and declination of 2.1°×2.1° respectively, going through all data from 0 ° to 60° in zenith angle and steps of 0.11°. An example of the described analysis in the recorded data for a 1-second sliding window is presented in Figure 5.4.

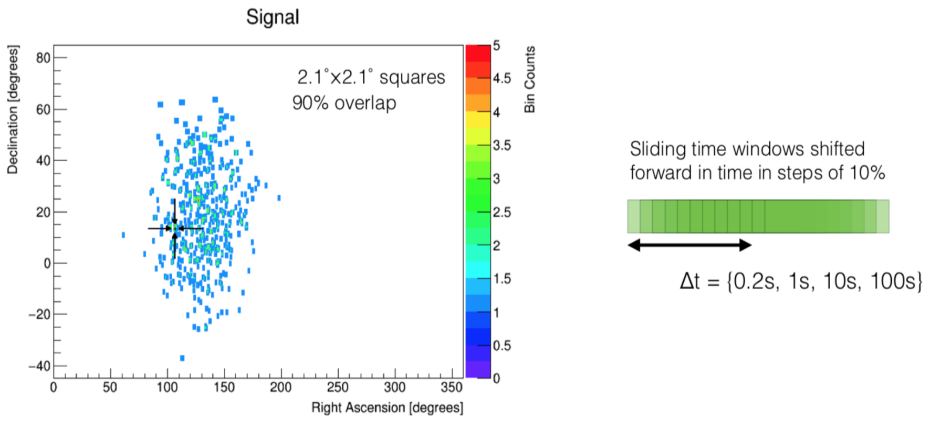

FIGURE 5.4: Observed air-shower counts in the RA-Dec spatial grid, for a 1 second sliding window. The image includes a total of 443 air shower event. The low event rate far from zenith results from the attenuation in the larger atmospheric depth of off-axis showers.The most significant results of the search is marked by the cross defined by arrows. From Wood, 2018

The background distribution of counts, which is expected to follow Poisson statistics, is estimated using the *direct integration* method described in (Lennarz et al., 2017). A background estimation is computed by recording the air showers during a period of 1.5 h at different declination as a function of the hour angle. The expected number of background counts is then obtain from the multiplication of the current total air shower rate, the relative acceptance of a bin and the search duration. An excess is characterised by computing the Poisson probability of finding a larger number of counts in a given bin compared to the expected number of background counts. Then, the subsequent significance of the excess is computed using the inverse of the compliment of the error function. Further description of the *simple-grb* search method can be found in Wood, 2018.

The hypothesis H_1^γ is defined by the *hotspot* candidate found by the *simple-grb* search and described in the GW+γ analysis by a gaussian centered on the coordinates of the candidate, $\vec{x}_S$, with an uncertainty of 1.5° given by a conservative value for the angular resolution of the HAWC experiment.

The null hypothesis H_0^γ is the photon cluster coming from any background fluctuation in any coordinate of the sky, so all directions are in principle equally possible inside the HAWC FoV. However, the response function of the instrument (IRF) is not homogeneous in declination nor in right ascension, with a dependency to the zenith angle and time. The sensitivity distribution across the FoV has been extracted experimentally from events found in the *simple-grb* search. It provides the sensitivity

as function of right ascension and declination IRF(RA, Dec). The distribution of declination has been modeled, and azimuthal axis symmetry has been assumed in order to obtain the 2D distribution of the sensitivity in an instantaneous HAWC FoV. Results are shown in the left side of Figure 5.6. The equations for the null and the alternative hypothesis, which are represented in Figure 5.5, are:

$$H_0^\gamma = \mathrm{IRF}(RA, Dec) = \mathrm{IRF}(RA) \qquad H_1^\gamma = Gauss(\vec{x}_S \mid \vec{x}_i) = \frac{1}{2\pi\sigma} \times e^{-(|\vec{x}_S - \vec{x}_i|^2/2\sigma^2)} \tag{5.7}$$

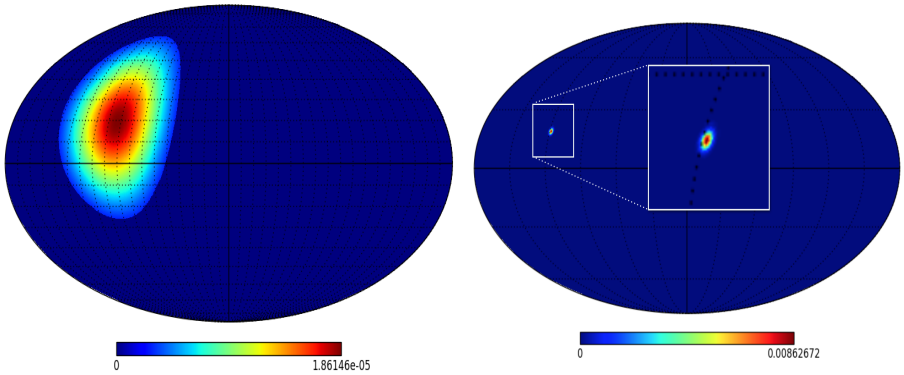

FIGURE 5.5: (Left) Example of the null hypothesis for photon signal for one FoV. (Right) Example of the alternative hypothesis for a photon signal.

The obtained events distribution where entire transits are considered and the declination profile of those candidates can be found in Figure 5.6.

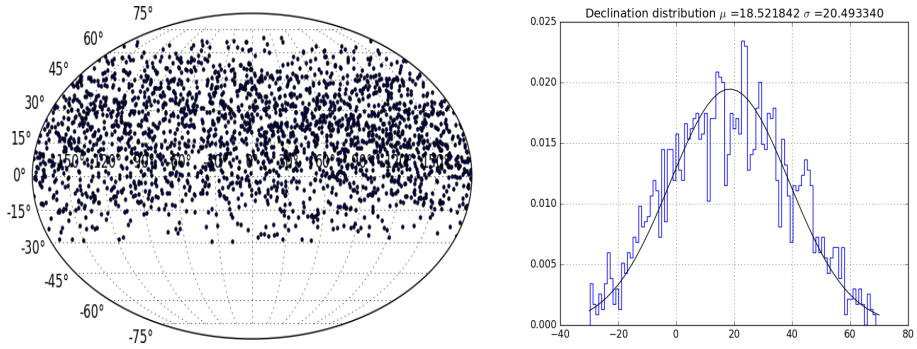

FIGURE 5.6: (Left) Distribution of *hotspot* candidates found by *simple-grb* search in a period of two years. (Right) Declination distribution of hostpot candidates fit to a gaussian distribution.

.

5.4.4 Galaxy catalogs

The use of galaxy catalogs was considered in a first study of the likelihood ratio computation. Nevertheless, it was decided to leave it out of the likelihood computation due to the biases and undesirable effects that it could bring at the level of the scrambling, as event coming from the *avoidance* zone of catalogs which roughly corresponds to the Galactic Plane, would be compared.

Instead, we use the galaxy catalog here for a possible *a posteriori* identification, by comparing the sky coordinates of the potential candidate obtained with the likelihood method with the actual distribution of galaxies.

A detailed discussion on galaxy catalogs and the advantages and the limitations of their use will be provided in Section 6.4.

5.5 Proof-of-concept study of the GW+γ likelihood analysis

The distribution of the variables presented above can be obtained by using *scrambled* data. This allows to compare to values obtained for a potential coincident signal to the distribution of data which includes no astrophysical events.

5.5.1 Candidate selection

Photon background selection: HAWC candidates

First, the *simple-grb* search described in previous sections was ran offline on archival HAWC data of years 2015, 2016 and 2017. The time window is set to ΔT_γ=0.2, 1 and 10 seconds and a threshold significant of the candidates of $p = 10^{-4}$ without accounting for trials. The results from this search are plotted in the left part of Figure 5.6. During the analyzed period 2015-2017, no GRB detection has been establish, which is consistent with the obtained results. The significance distribution after computing trials of the sample of N=2384 candidates is presented in Figure 5.7.

The distribution p_γ is well described by a Gaussian distribution centered at $\mu_\sigma = -0.8$ with a standard deviation of σ_σ=1.3. This result is compatible with a Gaussian distribution with μ_σ= 0 and σ_σ=1 if one considers that the lack of statistics influences the fit of the Gaussian distribution.

Gravitational background selection: LIGO-Virgo candidates

The gravitational wave used here come from the neutron star merger simulations provided before the O2 run by the LIGO-Virgo collaboration in Singer et al., 2016b. These simulations include events with all possible interferometer configurations, thus covering most of the possible real reconstructed events to come in O3.

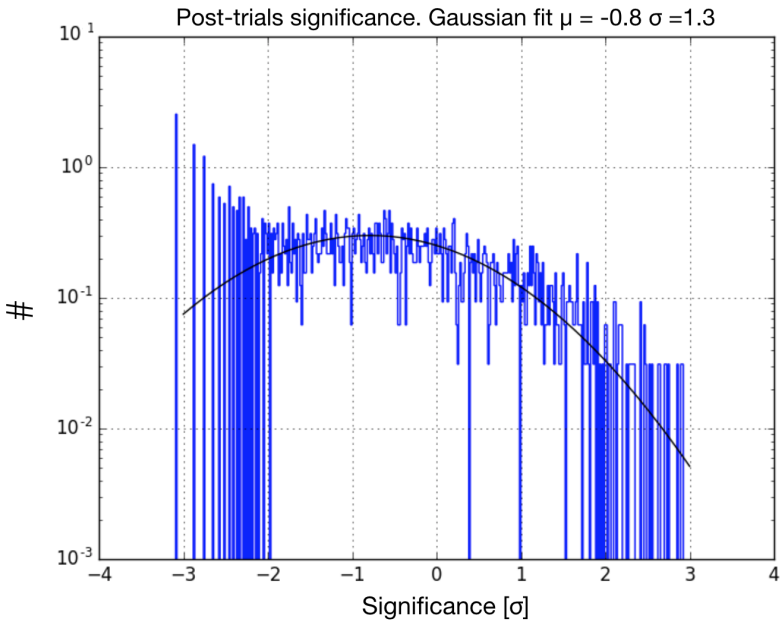

FIGURE 5.7: Normalised significance distribution accounting trials for the *hotspot* candidates found in the *simple-grb* GRB search in HAWC data, for a pretrial p_γ p-value threshold of $p_\gamma < 10^{-4}$ for years 2015 to 2017.

In order to make these *above-threshold* GW simulations look closer to sub-threshold data, we associate a different p-value p_{GW} each time the simulation is considered in the scrambling. The random p-values follow a uniform distribution in the interval typical for sub-threshold observations, from $p_{GW} = 10^{-8}$-10^{-4}.

5.5.2 Background scrambling

The scrambling method is used to recreate the background of our coincidence analysis, where no astrophysical signal is included. For this study we scrambled time (and thus right ascension) of the HAWC values. A time is associated to each of the gamma and GW candidates, which is used at the level of the calculation of the null hypothesis from the the instantaneous HAWC FoV. In this step, we consider the *a priori* restrictions, which only considers events that are included in a total temporal window [-100, 500] seconds and events that are spatially coincident. The decrease from the input scrambled data and the output data which passes this cut is in agreement with Section 5.6.

The maximum likelihood distribution for the injected events and the distribution of the combined likelihood results from the scrambled data are shown in Figure 5.8.

These distributions are used to compute the $p_{spatial}$ distribution. Then, using the Fisher's method presented in Equation 5.3, the p-values of the involved messengers are combined and the *test statistic* χ^2 distribution is computed. Finally, the $p_{GW\gamma}$ is derived for each of the scrambled coincident events. Results are shown in Figure 5.9.

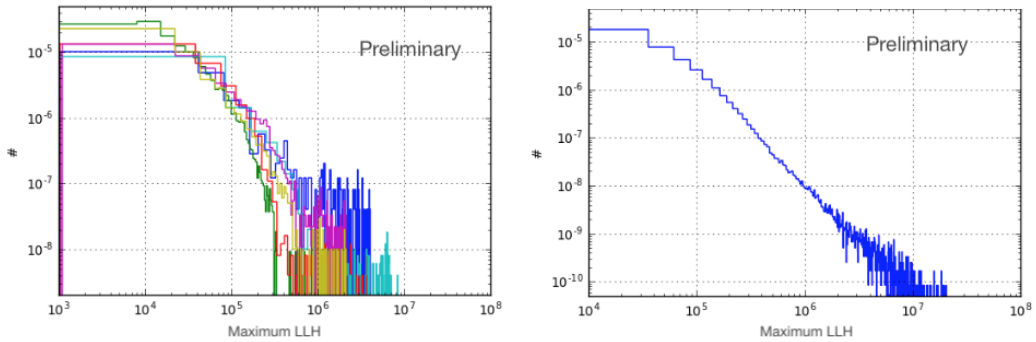

FIGURE 5.8: (Left) Likelihood distribution for a five scrambled datasets and (Right) Likelihood distribution resulting from the combination of the 400 datasets for which the joint likelihood ratio has been computed.

5.5.3 Signal injection

To check the selection process that we just introduced, simulations of astrophysical candidates are injected. We select significance values slightly higher than those found in the distribution of background events for HAWC candidates (Figure 5.7). In the case of gravitational-wave events, we consider three different p-values that are distributed as a Gaussian function with a decadal unit width, centered at $\mu_{p_{GW}}$=10^{-5}, 10^{-7} and 10^{-9}.

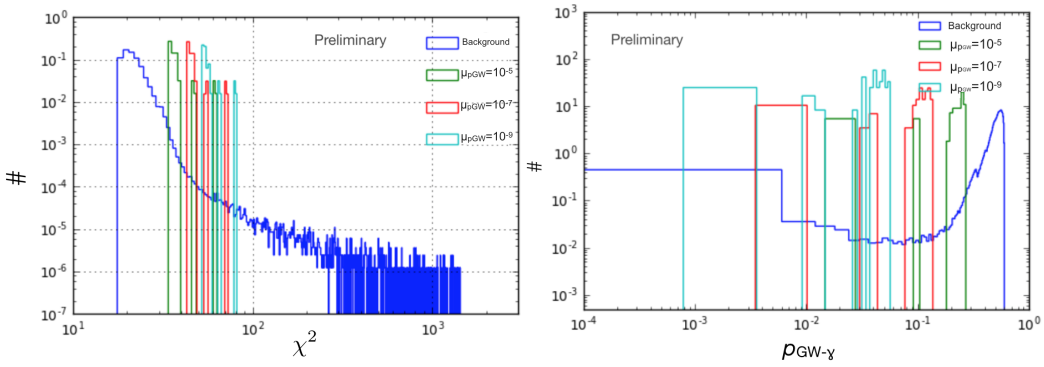

FIGURE 5.9: (Left) χ^2 distribution for background events and *injections* with different p_{GW} values. (Right) $p_{GW-\gamma}$ distribution for background events and *injections* with different p_{GW} values.

The $p_{GW-\gamma}$ distribution shows how the injections are highlighted compared to the scrambled production derived from background.

5.6 Expectations of coincidences

We used simulations to quantify the number of expected background-background coincidences and signal-background coincidences. We have obtained estimations by considering the characteristics and performances of the two experiments that provide

	HAWC	LVC
FAR	100 per day	see Figure 5.10
Search window	1,10,100 seconds	25 seconds

TABLE 5.1: Parameters used to obtained a temporal background coincidence estimation

data to the coincidence pipeline. Expectations are computed independently for spatial and temporal searches.

5.6.1 Temporal coincidence expectations

The temporal coincidence between detections basically depends on the window of both independent searches. If there are n_1 events in detector 1, the total time window for overlapping events in detector 2 is $n_1 \cdot (t_1 + t_2)$. With n_2 being the events observed per unit time in detector 2. We expect to observe $n(1,2)$ overlapping events to be observed per unit of time:

$$n(1,2) = n_1 \cdot n_2 \cdot (t_1 + t_2) \tag{5.8}$$

The total probability for observing $n(1,2)$ coincidences in detectors with averages rates N_1 and N_2:

$$W_{(N_1,N_2)}(1,2) = n_1 n_2 (t_1 + t_2) P_{N_1}(n_1) P_{N_2}(n_2) \tag{5.9}$$

For two independent detectors, the average number of expected coincidences per unit of time:

$$< n(1,2) >= N_1 N_2 (t_1 + t_2) \tag{5.10}$$

with N_i being the average rate of detector i.

The parameters used for the study can be found in Table 5.1. The expected number of background coincidences are plotted in Figure 5.10. In the case of background-background coincidences, we expect from 1 per day to 1 per 10 years, depending on the LIGO-Virgo FAR. In case we consider events where γ hotspot candidate is background-like and GW-event has signal-like FAR, we expect 10^{-14} coincident events per second, what means around 1 per 10^7 years. Note that this result remains conservative since the duty cycle of each experiment has not been considered.

5.6.2 Spatial coincidence expectations

In the case of spatial coincidences, we study how the 90% C.R. of the localization of the reconstructed GW affects the number of background coincidences. Indeed, depending on the number of detectors involved, the 90% C.R. of the reconstructed localization of GW can change from tens of degrees to thousand of degrees. Our main interest is to set an upper limit on the amount of coincident HAWC-LIGO events that

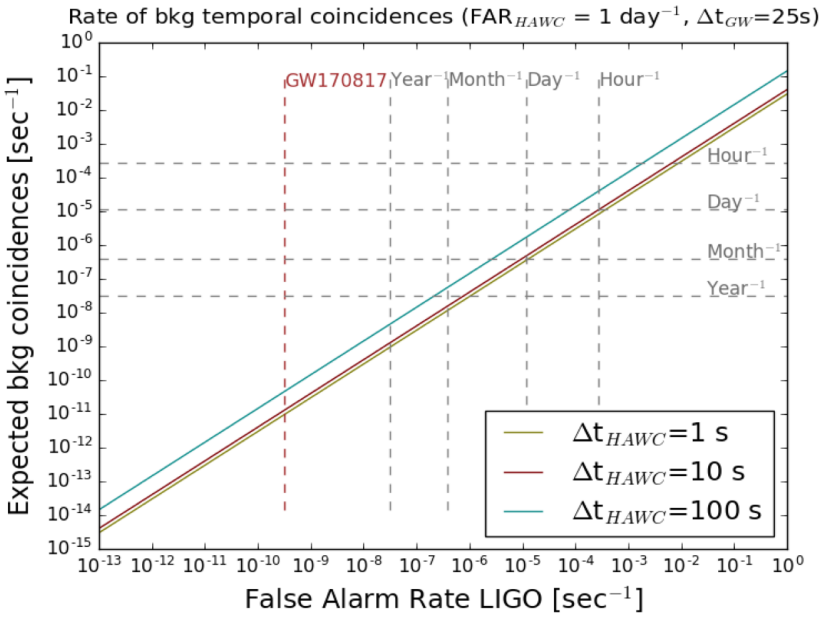

FIGURE 5.10: Expected number of background coincidences in dependance of the FAR from the LVC event, obtained for three different HAWC search windows of Δt_{HAWC} = 1, 10 and 100 s. A Δt_{GW}= 25 s has been assumed and the the FAR of HAWC sub-threshold events has been set to FAR_{HAWC}=10^4. Dashed lines have been included to provide an easier understanding of the results.

one can find depending on the 90% C.R. of the GW localization.

For this purpose, we performed a spatial-coincidence simulation where we combined HAWC hotspots, that implicitly include HAWC sensitivity dependency on zenith angles, and simulated GW skymaps from Singer et al., 2016a. For a coincidence, we require an overlap of the HAWC candidate considering the angular resolution to be $\sim 1.5°$ and the 90% C.R. of the GW event. Results from this study are found in Figure 5.11.

We can now put upper limits on the expected number of spatial coincidences depending on the extension of the GW localization. For the largest values of $A_{90\%GW}$ above 1000 deg^2, a maximum of ∼10% of the HAWC events will be spatially coincident. In the case of intermediate values, between 1000 and 500 deg^2, the spatial coincidence expectations reaches a maximum ∼7%, although the median of the distribution is found below ∼4%. For small values, which we have set to $A_{90\%GW}$ below 500 deg^2, the distribution peaks at ∼0.7%, with values reaching up to 6%.

5.7 O1 sub-threshold data analysis

A search for gravitational waves from double neutron star binaries inspirals in LIGO O1 observation run was recently published (Magee et al., 2019), sensitive to BNS events to an average distance of $\sim$ 85 Mpc over an entire set of ∼93.2 days of data.

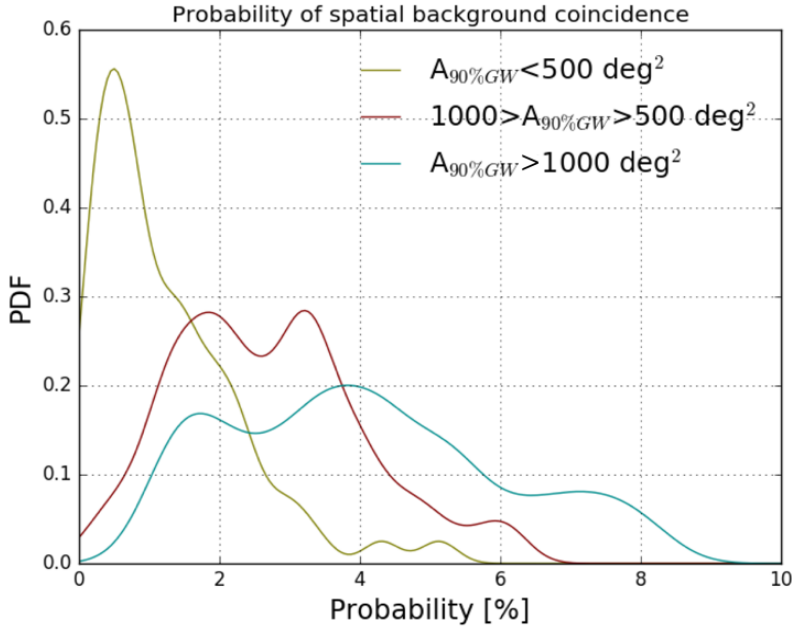

FIGURE 5.11: Percentage of HAWC-LVC background associations depending on the 90% C.R. of the GW localization. These have been divided in three bins in $A_{90\%GW}$, corresponding to *large*,*medium* and *small* size of the GW localization uncertainty regions.

Although no clear gravitational wave signal was observed, they identified 103 sub-threshold candidates with FAR < 1 per day, which corresponds to a contamination fraction of ∼99%. The study argues that if one considers the expected BNS merger rate of 100–4000 $\mathrm{Gpc}^{-3}\mathrm{yr}^{-1}$, due to the duration and the sensitivity of O1 observation run, one or more astrophysical events are expected in the sample. The distribution of the FAR of the GW sub-threshold events in the sample is presented in Figure 5.12.

We have considered the γ candidates obtained by *simple-grb* search of HAWC data from 2015 to 2017, as explained in Section 5.5.1. We have considered three different temporal windows ΔT_{γ}= 1, 0.2, 10 seconds. The *hotspot* candidates corresponding to the period when O1 took place, have been selected to be *signal* events in the coincidence analysis. Events corresponding to an equal period of time but at a different time in the total analyzed period of time are considered as *background* events in the coincident analysis. In order to increase the statistics, these *background* sub-samples have been further scrambled, which yielded to a total of 400 scrambled dataset of the same duration as O1.

We have obtained the temporal separation between GW+γ events for the *signal* sample and the *background* sample. These results are shown in Figure 5.13, where the limits of the x-axis ΔT are chosen to include values which would be likely related to coincident events (∼ seconds) but also values found for this dataset (above 10^4seconds). No clear evidence from a deviation from background expectations is

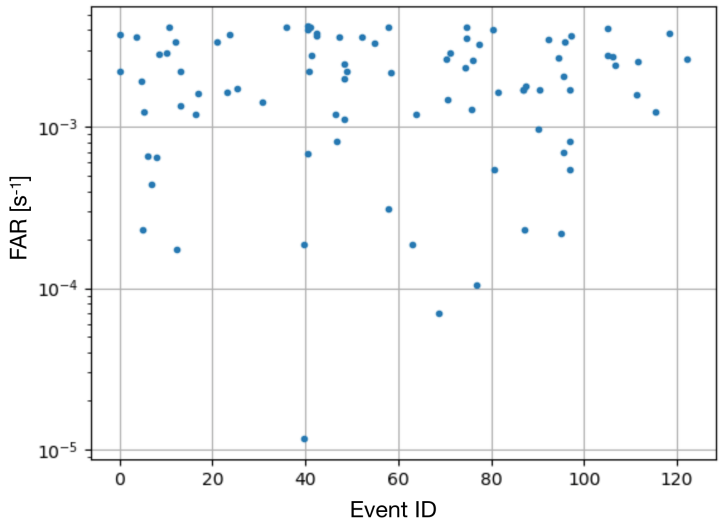

FIGURE 5.12: False alarm rate of the O1 sample of sub-threshold events presented in Magee et al., 2019

observed.

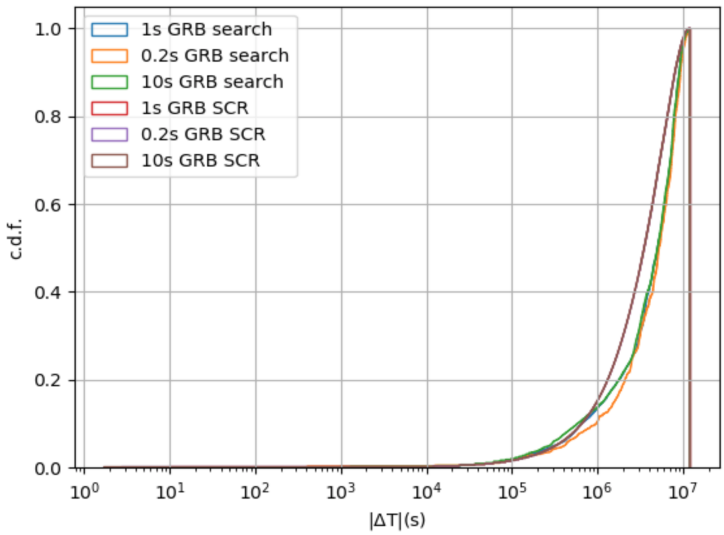

FIGURE 5.13: Temporal shift in absolute units between the GW injections and the γ injections for the *background* scrambled (SCR) and the *signal* dataset, for the three searched windows ΔT_γ= 0.2, 1, 10 seconds.

Temporal GW+γ coincidences in O1 sub-threshold data

We consider the set of GW+γ events, the *signal* sample observed during the O1 observation run period in Advanced LIGO and HAWC, and we search for coincident

T_{GW}	T_γ	RA_γ	Dec_γ	p_γ (s^{-1})	$\mathrm{FAR}_{\mathrm{GW}}$ (yr^{-1})
57300.937	57300.942	292.12	28.91	3.28e-11	140
57379.51	57379.516	179.52	28.26	1.69e-10	60

TABLE 5.3: Candidates obtained in the temporal selection of coincident events for $\Delta T_\gamma = 1$ second. Time in MJD units.

T_{GW}	T_γ	RA_γ	Dec_γ	p_γ (s^{-1})	$\mathrm{FAR}_{\mathrm{GW}}$ (yr^{-1})
57332.421	57332.422	93.66	-19.27	1.98e-12	173
57332.462	57332.461	121.78	42.66	8.52e-10	211
57379.676	57379.681	244.4	-5.91	8.79e-10	290

TABLE 5.4: Candidates obtained in the temporal selection of coincident events for $\Delta T_\gamma = 10$ seconds. Time in MJD units.

events. The temporal-coincidence selection of GW+γ events in the three searched windows ΔT_γ, yield to the resulting events presented in Table 5.3, 5.2 and 5.4.

T_{GW}	T_γ	RA_γ	Dec_γ	p_γ (s^{-1})	$\mathrm{FAR}_{\mathrm{GW}}$ (yr^{-1})
57287.4811	57287.4811	31.14	46.31	4.22e-10	313
57287.4811	57287.4817	76.43	45.7	2.26e-10	313
57374.039	57374.041	19.51	22.53	1.62e-10	84
57379.516	57379.518	158.29	5.36	6.91e-10	60

TABLE 5.2: Candidates obtained in the temporal selection of coincident events for $\Delta T_\gamma = 0.2$ seconds. Time in MJD units.

Temporal and spatial GW+γ coincidences in O1 sub-threshold data

The spatial coincidence requirement for the GW+γ joint subthreshold analysis has been applied to the sub-threshold sample of events obtained during O1 in the LIGO interferometer and HAWC observatory. None of the joint GW+γ that passed the temporal requirement do pass the spatial cut. This fact can be observed in Figures 5.14, 5.15 and 5.16.

5.8 Discussion

In this chapter, the AMON network and the goals of such ambitious multi-messenger have been presented. The analysis pipeline described in this work focuses on compact binary coalescences which presented very-high energy gamma-ray emission, where both events leave a sub-threshold signal in the respective detectors. The *proof-of-concept* study shows the capabilities of coincidence analysis of sub-threshold data when several data streams are combined.

No coincident GW+γ events have been found in the analyzed data from LIGO/Virgo (from Magee et al., 2019) and HAWC during O1 period. Nevertheless, sub-threshold

coincident analysis in the multi-messenger era may lead in the future to the identification of likely-astrophysical events which would improve our understanding of the process that astrophysical sources undergo.

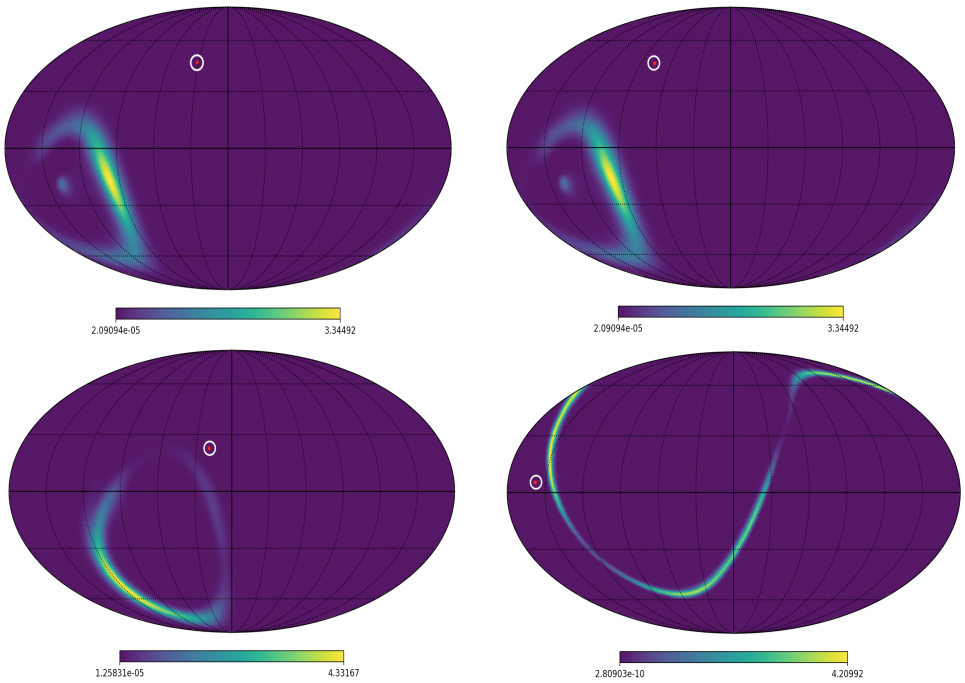

FIGURE 5.14: Candidates obtained from the temporal selection of coincident events for T_{burst}=0.2 seconds

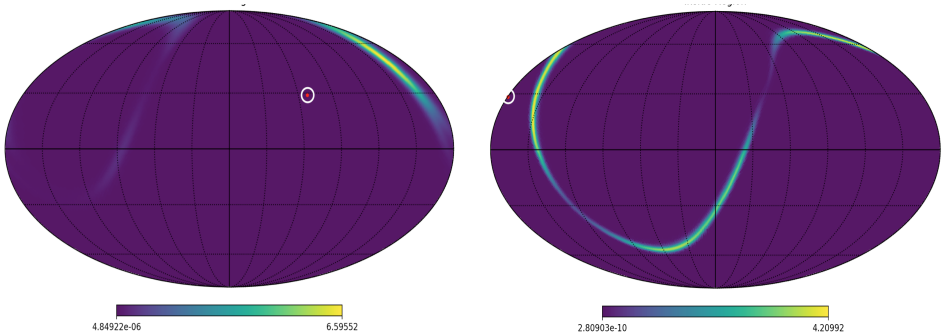

FIGURE 5.15: Candidates obtained from the temporal selection of coincident events for T_{burst}=1 second

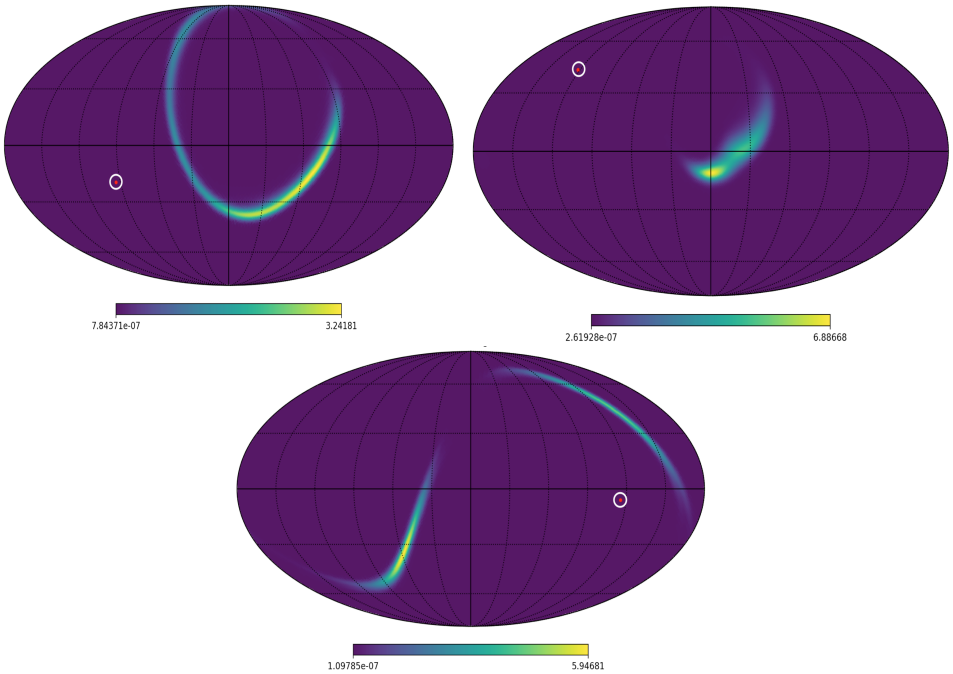

FIGURE 5.16: Candidates obtained from the temporal selection of coincident events for T_{burst}=10 second

Chapter 6

GW counterparts searches with Cherenkov Telescopes

Contents

6.1 Introduction

The complementary approach of multi-messenger astrophysics gives new insights into the most energetic cosmic events by studying the different astrophysical processes that led to the emission of those messengers.

Nevertheless, besides the doubtless potential of multi-messenger observations, the identification of those joint source may be challenging. Several technical challenges are associated to gravitational wave follow-ups. Amongst those, the most relevant issues are the poor source localization of compact binary coalescences by gravitational wave detectors, as well as the low latency of the alert emission by the gravitational wave observatories and the subsequent rapid follow-ups necessary to catch the potentially rapidly fading transient emission.

The localization of compact binary coalescences detected by interferometers on Earth can be as coarse as hundred or thousands of square degrees, depending on the

number of interferometers involved in the detection (see Section 4.3.2). Events detected by 2 interferometers typically expands over 100-1000 deg^2, whereas in events observed by 3 interferometers, the localization uncertainty cover *only* about 10-100 deg^2.

Hence, the search of an electromagnetic counterpart is non trivial, as the localization of the source of gravitational waves is, in many cases, greater than what a EM telescope can cover in a single pointing. Even though being significantly larger than typical optical telescope, the radius of the circular field-of-view (FoV) of second generation IACTs is of the order of several degrees. For the example of H.E.S.S. telescopes, the FoV of the large 28-m H.E.S.S. telescope, is defined by a radius of $\sim$1.5° and if we include the four 12-m telescopes, the FoV radius increases to $\sim$2.5° (values corresponding to the 50% of the radial acceptance in the FoV). The regions in the sky covered per single observation are therefore ~ 7 deg^2 and ~ 20 deg^2, respectively. For this reason, several observations are typically necessary to cover the localization region and a prioritization of the observation coordinates is essential.

Another major challenge for IACTs is related to the latency of the follow-up, which is limited by the duty-cycle of the instrument. IACTs operating only in astronomical darkness, during low moon brightness or even during moonless nights. Furthermore, the accessible range of zenith angles is constrained to sources observable at $\theta_{\mathrm{ZENITH}} < 60°$). These two visibility constraints, which impact the latency of the response in IACTs, should be taken into account to optimize the use of the available observation time.

Due to these challenges, dedicated strategies to follow-up gravitational wave events have been set up by the collaborations operating the current IACTs. In this chapter I focus on outlining the features and design of the software developed within the H.E.S.S. collaboration to identify sky locations which most likely include the source and, therefore, the potential electromagnetic counterpart of the gravitational wave event. The developed algorithms take into account the information provided by the gravitational wave detection as well as the observation constraints of the H.E.S.S. instrument, in order to provide a rapid and optimal schedule of the GW follow-up observation.

6.2 Scheduling gravitational waves follow-up observations

An observation scheduler to perform gravitational wave follow-ups with IACTs, which has been, in particular, developed for the H.E.S.S. experiment, is presented in the following. Since H.E.S.S. joined the EM follow-up group of the LIGO-Virgo collaboration, several algorithms have been developed to optimize the follow-up of GW events while taking into account its particular observational constrains. These algorithms are adapted to the type of event and science case and yet, the same underlying iterative logic is followed in all of the different variants. Here I focus on the general,

iterative technique. The detailed algorithms are discussed in Section 6.4.

Firstly, as it has been explained in Chapter 4, the gravitational wave event triggers LIGO-Virgo detectors, the signal is analyzed, and the localization is reconstructed. An alert is issued for the event and shared with the astronomical community. Upon reception of the alert by the IACT alert system (see Section 7.1.1 for the description of the H.E.S.S. alert system), the configuration of the GW follow-up scheduling algorithm is selected by taking into account the characteristics of the GW event. The compact object coalescence parameters guiding the algorithm selection are the event type, the luminosity distance and the localization uncertainty. Once the event is classified, the observation scheduler algorithm can be summarized in the following steps:

1. A search for an observation time window taking into account several visibility constrains. A set of potential observation windows is defined.
2. The pointing direction with the highest probability to contain the merger location is obtained. The definition of *probability* is explained in detail in Section 6.4, as it can refer to different quantities.
3. The selected region is observed by the instrument.
4. Taking into account the already covered regions of the sky, a new attempt to schedule an observation is performed. To this aim, an iterative process is in place where the algorithm goes back to Step 2.
5. The loop is over when the night finishes or when a maximum number of observations is reached.

In the following sections, the main features of the developed scheduling algorithms are introduced and discuss in detail.

6.3 General considerations to schedule observations with IACTs

6.3.1 Visibility constraints

The detection technique in IACTs, as explained in Section 1.5.1, is only successful when the instruments are operated in appropriate darkness conditions during data acquisition. The related requirements include minimal light level, like reduced values of light pollution caused by human activities and no direct natural light. The H.E.S.S. telescopes have, until recently, only operated after astronomical twilight and with the Moon being below the horizon. In the case of the Moon, the horizon for scheduling observations is defined as the position of the center of the Moon at θ_{ALT} =-0.5° degrees below the horizon. In the case of the Sun, there are three different types of twilight, namely civil, nautical and astronomical, which occur when the Sun is less than 6, 12, and 18 degrees below the horizon, respectively. Once the astronomical

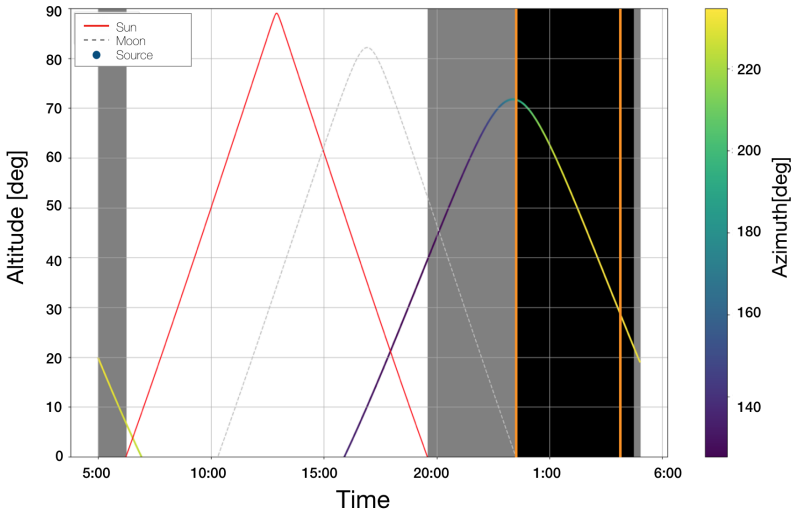

FIGURE 6.1: Altitude evolution with respect to time for the Sun, the Moon and a given point source. The colors for the source correspond to the evolution in azimuth. The black region corresponds to the darkness time when observations take place. Grey regions correspond to the period when the Sun is below the horizon but not the Moon. The region delimited by two orange bars refers to the time interval when the source can be successfully observed by an IACT as both darkness and altitude conditions are fulfilled.

twilight is over, the astronomical night effectively starts.

These conditions, included in the scheduling algorithm, define the available windows of observation. In Figure 6.1, the altitude of the Sun, the Moon and a simulated point source, are shown as function of time over 24 h. Dark time, where H.E.S.S. observation are possible, is given as a black region. The grey region corresponds to the window were the Sun is below the horizon, but not the Moon, where moonlight observations could be taken.

Moonlight Observations

Starting from July 2019, a new mode of observation under *moderate* Moon condition has been adopted in the H.E.S.S. collaboration. The motivation underlying moonlight observations is to extend observation time for regular source, monitoring campaigns as well as transient source. Due to the uniqueness of some transient events, increasing the observation time window boosts the probability to observe events which are triggered by external facilities. These type of observations have an important effect in the transients science case as we increase the availability for prompt follow-ups and the coverage in the case of long-term follow-ups, where more simultaneous data can be potentially taken.

Although moonlight observations have a higher energy threshold and are less sensitive than *standard* observation, these are indeed moderate effects compared to the science motivated discovery potential. The moonlight observation criteria for the

H.E.S.S. experiment are quoted in Table 6.1. The gain on observation time thanks to these type of observations is of the order of $\sim$ 30% of the *standard* observation time, even though it depends on the specific parameters. These condition have been included in the scheduling algorithms as follows.

The altitude and moon phase percentage are check at the level of the visibility window search, broadening the observation windows. In Figure 6.1, the grey region could correspond to observation windows under moonlight conditions, although moon phase percentage should be still checked.

Max Moon Phase	Min Moon Separation	Max Moon Altitude	Min Moon Altitude
60 %	30°	50°	0°

TABLE 6.1: Preliminary choice of values of the parameters defining Moonlight Observations.

The Moon separation condition is included at the level of the selection of the pointing coordinates. The minimum separation region is defined as a circle of radius of 30° centered at the position of the Moon, with respect to any other coordinate in the sky. An illustration of the process is included in Figure 6.2.

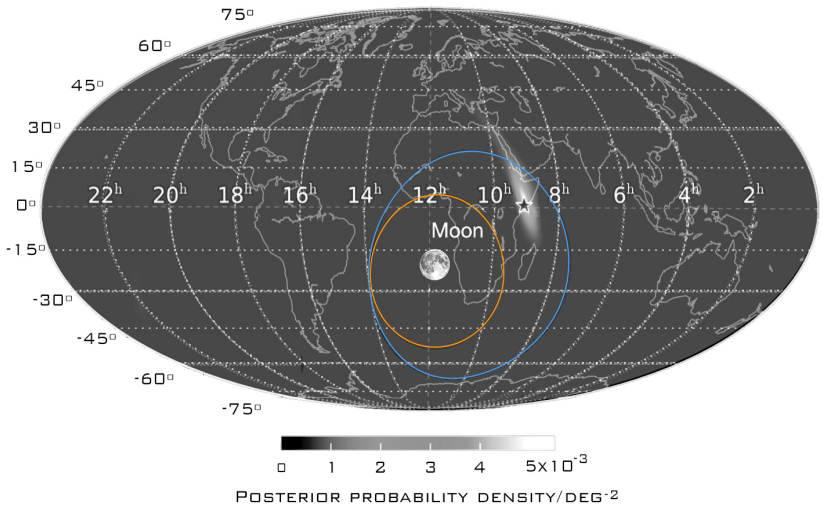

FIGURE 6.2: Illustration of the angular separation between the Moon and the gravitational wave uncertainty region, in white, where the NS-NS merger *true* location is represented by a star. The orange line defines the condition of 30°angular separation between the Moon and any coordinate in the sky. The blue line defines the observable sky by the H.E.S.S. experiment under a zenith angle of θ_{zen}<45°.

The search for observation windows and scheduling coordinates under `greyness` conditions has been included in the scheduling algorithms in a way that it includes previously considered `darkness` conditions. To this aim, the Moon phase percentage

condition is only used whenever the altitude Moon is above the horizon, at $\theta_{ALT} > 0.5°$.

6.3.2 Zenith angle optimization

In IACTs, the energy threshold of an observation depends on the zenith angle under which the source is observed. This is due to the absorption of shower light during its passage through the atmosphere, which is larger for larger zenith angles. In Figure 6.3, this dependency is shown for the H.E.S.S. experiment for different cuts used in the data analysis. Going to lower values of the zenith angle (higher altitudes) translates in lowering the energy threshold of the observations. It can be seen that from $\theta_{\text{ZENITH}} = 0°$ to $\theta_{\text{ZENITH}} = 60°$, there is an order of magnitude of difference in the low energy threshold. The effect increases exponentially and gets critical at very large zenith angles. In Figure 6.1, the orange bars define the visibility window of the source, where altitude requirements and darkness condition are fulfilled. Each observation window is chosen so that it is large enough to properly estimate the background while keeping the homogeneous observation conditions. In H.E.S.S., this requirements translated to a total of $\sim$ 30 minutes per observing run.

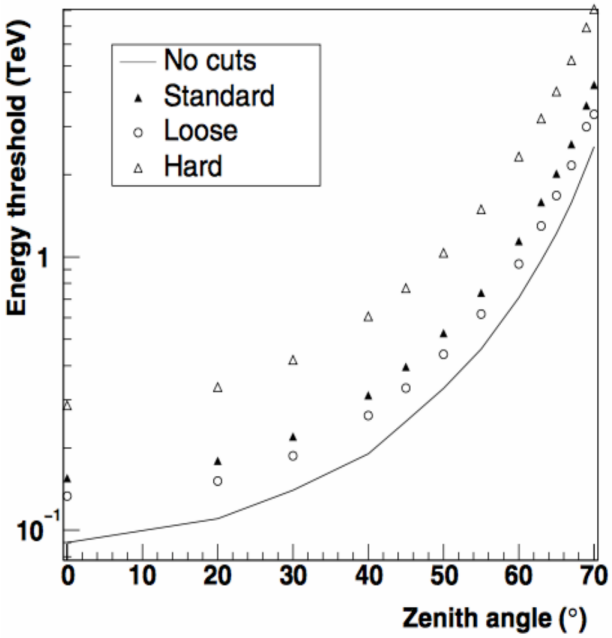

FIGURE 6.3: Zenith angle dependency of the energy threshold of H.E.S.S. II observations applying different data selection cuts.

Based on the soft spectrum of sGRBs observed by *Fermi*-LAT (Fermi-LAT Collaboration, 2013), we prioritize the low-energy domain. To this aim, the scheduling algorithms include a module in which low zenith angle observations are favored. A scan on decreasing values of zenith angle, in steps of 5°, is performed. For each further step in zenith angle, the potentially covered probability is compared to the potential covered probability of in the previous zenith angle bin. A *weight* is considered in the comparison in order to find a good compromise between the prioritization of

small zenith angles observations and probability coverage.This condition is specified in Equation 6.1.

$$p^{FoV_i}_{\theta_{\text{zenith}}} \leq \text{weight} \cdot p^{FoV_j}_{\theta_{\text{zenith}+5^\circ}} \tag{6.1}$$

The selection of the *weight* is based on the maximum photon energy of the sGRBs observed by *Fermi*-LAT (Fermi-LAT Collaboration, 2013) (energies which an IACT could only observe under the lowest zenith angles) but leaving room for new discoveries. The *weight* has been set to 0.75, although tuning would be needed as we improve our knowledge on the very-high-energy emission of GRBs. In Figure 6.4, the decreasing 5 degree-steps in zenith angle are plotted for a fixed observation time, a given gravitational wave localization region and a selected pointing where the optimization in zenith angles has been efficiently performed.

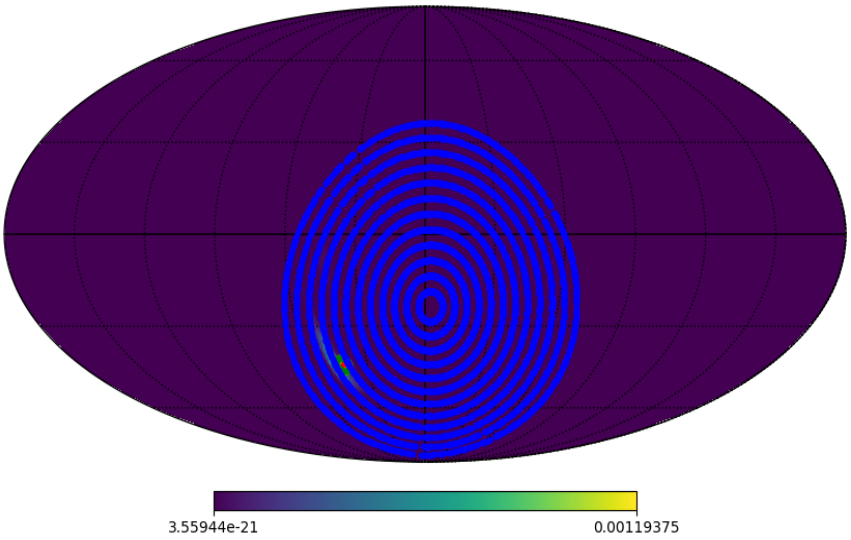

FIGURE 6.4: Gravitational wave sky localization where decreasing 5 degree-steps in zenith angle for a given time are overlaid. The simulated observed region is shown in green, where the red point indicates the center of the FoV.

The altitude evolution of selected observation regions presents a particular behavior which is a consequence of the non-trivial extension of the gravitational wave uncertainty regions, and an example is presented in Figure 6.5. The observation of the region is only possible when the altitude is above 30°, which happens at different time intervals for each coordinate. This time evolution is taken into account in the pointing schedule derived for the H.E.S.S. follow-up.

6.3.3 Second round

A possible situation in observation scheduling is to schedule observations where the covered uncertainty regions happen to pass minimum cuts but are marginal. Furthermore, as time goes by in the observations, there are regions in the sky which can be observed with more favorable zenith angle conditions than they could earlier on

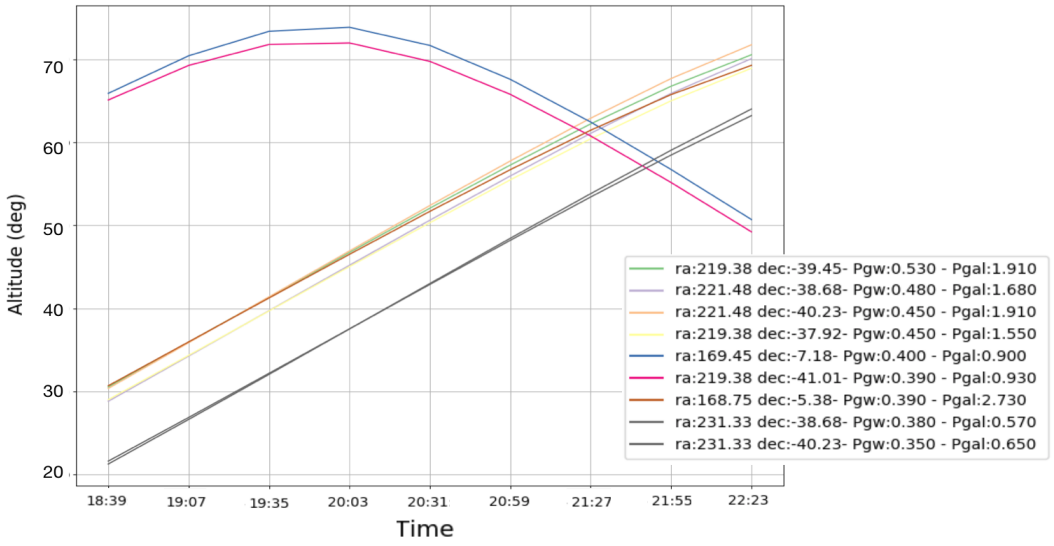

FIGURE 6.5: Evolution of the altitude of the coordinates scheduled for observation, for a given input time and gravitational wave localization skymap. The legend box includes the coordinates of the pointing and the probabilities that are covered in each pointing in %.

the context of a prompt response. These observations, although at later times with respect to the merger, will benefit from lower energy thresholds. In order to illustrate this feature of the algorithm, an example case in given in Figure 6.6.

This situation motivated the development of an additional feature in the algorithms: a *second round* of observations. The implementation of this option has been done so that the algorithm compares two possible observations: the observations of non-covered regions of the sky, and the re-observations of the most probable localization region. Technically, this is done by comparing a masked sky map with an unmasked sky map, and selecting the option which optimizes the probability coverage at a given time.

Several criteria are set to enable a second round of observation. In order to cover a reasonably large region in first observations, the probability coverage of the regions already observed should be at least of $\sim 40\%$. Then, a further filter criteria is applied in cases where the potential observation is a first round of observation fulfills minimum scheduling probability cuts but are *marginal* compared to a potential observation in a second round of observation. The definition of a marginal pointing in this case is quantified as twice the value set as minimum probability to schedule an observation.

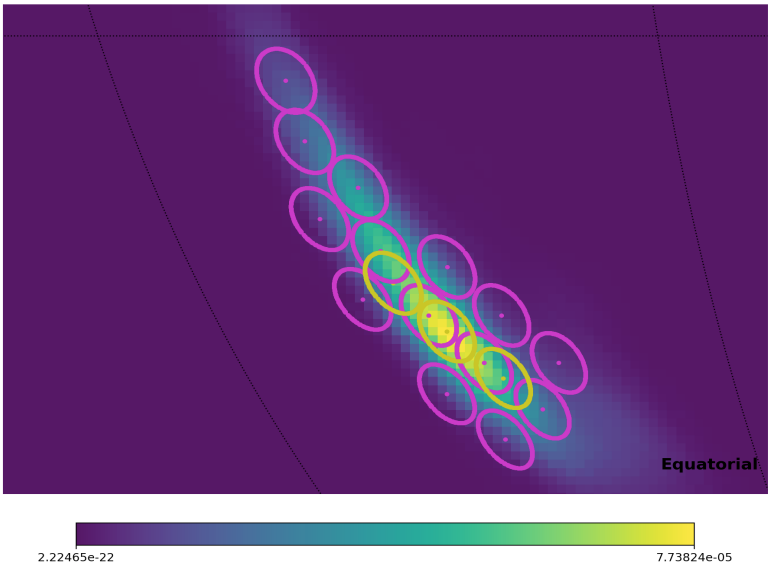

FIGURE 6.6: Example of scheduled observations for a given time and a given gravitational wave localization sky map where a second round of observations is allowed, following the definition given in the text. Pink stands for first round of observations and yellow for the second round. For the simulated case, a total campaign of three nights of observations with a FoV=2.5° is assumed.

6.4 Probability selection algorithms

Several techniques have been developed to guide the follow-up of gravitational wave events in a smart, efficient way, covering the most probable regions as fast as possible (Abadie et al., 2012). A sequential order of the observations based on the covered probabilities in the GW localization maps, from the highest to the lowest, enhances the likelihood of covering the EM counterpart in a shorter period of time. Indeed, in most energy bands, a low latency response is crucial to detected the emission of the remnant, as it is thought to be the case at VHEs.

The approach developed in the following is different from *tiling strategies*, which follow a grid-like scheme. Instead, the novel algorithms presented here are, following an unbinned approach, driven by the maximization of the covered probability.

6.4.1 2D Scheduling Algorithms

The most straightforward approach to the scheduling problem is to use the two-dimensional localization probability provided with the GW alerts, ρ_i, which represents the posterior probability that the source is contained inside pixel i for N_i (see Section 4.3.2) and in the following we will refer to as P_{GW}. The scheduling algorithms determine the pointing pattern of the telescopes by trying to cover most of the GW localization region.

`Pix-in-FoV` algorithm

This strategy is based on pointing observations according to the selection of individual high probability pixels $P^i_{GW} = \rho_i$ in the HealPix skymap provided by the GW instruments, which correspond to coordinates (RA_i,Dec_i) and the observation of the region defined by a circle of radius r=FoV_{IACT}. The largest probability pixel guides the observations, and the surrounding area within the FoV of H.E.S.S. is covered as well.

Nevertheless, this results on a grid-like scheme of the pointing pattern. In the following, a more sophisticated algorithm is introduced.

`PGW-in-FoV` algorithm

In order to obtain a more sophisticated algorithm, instead of looking for the most probable pixel, we can as well look into the most probable region. The pointing is chosen for the coordinates were $P^{\rm FoV}_{\rm GW}$, defined as

$$P^{\rm FoV}_{\rm GW} = \int_0^{FoV_{\rm H.E.S.S.}} \rho_i d\rho_i \tag{6.2}$$

reaches its maximum. The method is based on the use of an auxiliary probability skymap which is re-binned in a way that the bins areas are close the FoV_{IACT}. To this aim, we profit of the various possible pixelizations of the HEALPix maps. HEALPix is the acronym for Hierarchical Equal Area isoLatitude Pixelization of a sphere, so the pixelization scheme subdivides the spherical surface in equal area pixels. The resolution of the map is defined by the N_{side} parameter and the total number of pixels is $N_{pix} = 12 \times N^2_{side}$. In Figure 6.7, two different resolutions, which corresponds to two different N_{side}, are represented.

The algorithm considers in parallel both skymaps: a high resolution one, in order to obtain a good computation of $P^{\rm FoV}_{\rm GW}$, and a low resolution which is used as a grid of coordinates. An example of the grid of coordinates, N_{side}=64, and the actual $FoV_{\rm H.E.S.S.}$, where N_{side}=512 is used, is shown in Figure 6.7. In this way, the method is faster but at a negligible cost on the performance.

In Figure 6.8, a gravitational wave follow-up observation of the event S190512at (LIGO Collaboration and Virgo Collaboration, 2019) has been simulated using `Pix-in-FoV` (left) and `PGW-in-FoV` (right). It can be observed that there is an important difference in the overlapping of the observations, as the second algorithm is able to select pointings which are further apart and maximise integrated probability.

6.4.2 3D Scheduling Algorithms

The horizon of the current gravitational wave interferometers is limited to the local Universe, so one of the possible approach is to search for known astrophysical objects which can be associated with the BNS merger. Following this reasoning, the

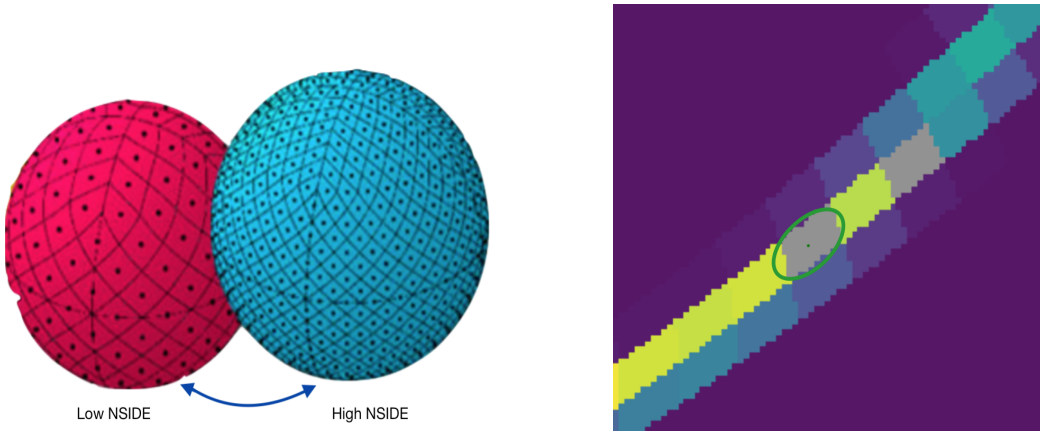

FIGURE 6.7: (Left) Orthographic view of HEALPix partition of the sphere for two different N_{side} resolutions. (Right) HEALPix gravitational wave sky map at $N_{side} = 64$ where the H.E.S.S. FoV at 1.5 deg radius is overlaid. The coordinates have been chosen by using the low N_{side} resolution sky map as a grid, and the covered probability is computed using a high resolution skymap at $N_{side} = 512$.

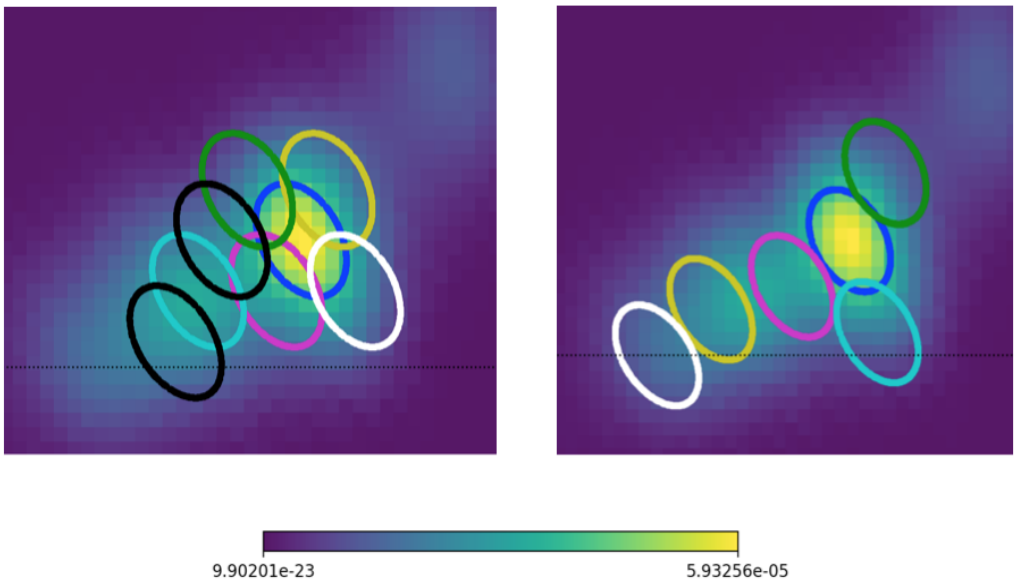

FIGURE 6.8: (Left) Simulated follow-up observation using `Pix-in-FoV` algorithm and (Right) `PGW-in-FoV` algorithm, overlaid to the injected gravitational wave sky map. The algorithms have been run under the same visibility conditions and injected at the same observation time.

searched region can be reduced, and the chances of detecting the EM counterpart can be increased, by convolving the localization region with the galaxies which could plausibly host such cataclysmic events. The restriction of a follow-up based on the galaxy distribution can potentially decrease the number of observations needed to cover most plausible source locations as well as limit the number of false positives.

Some of the characteristics that can be used to obtain a convolution of the probability by the distribution of matter are the mass, the luminosity, the distance or the star formation rate in those nearby galaxies (Abadie et al., 2012).

Although the link between the BNS merger rate and the mentioned galaxy properties are not yet clearly established, the use of the volume reconstruction of the event localization plays an unambiguous role in decreasing the uncertainty regions (Singer et al., 2016a). The reconstructed uncertainty volumes, shown in Figure 4.8, provided by the LIGO-Virgo collaboration, include estimates on the luminosity distance which can be combined by the position and the redshifts of known galaxies. In this way, one can define two different types of probabilities which are used in our algorithms to guide the scheduling algorithms. Using Equation 4.1 introduced in Chapter 4, a posterior probability *volume* can be defined, which represents the probability that a source is within a pixel i, which corresponds to the coordinates (RA_i, Dec_i) at a distance [r,r+dr] as:

$$P(r, \mathbf{n}_i) = \rho_i \frac{\hat{N}(\mathbf{n})}{\sqrt{2\pi}\hat{\sigma}(\mathbf{n})} \exp\left[- \frac{(r - \hat{\mu}(\mathbf{n}))^2}{2\hat{\sigma}(\mathbf{n})^2} \right] r^2 dr \tag{6.3}$$

where ρ_i, $\hat{\mu}_i$=$\hat{\mu}(n_i)$, $\hat{\sigma}_i$=$\hat{\sigma}(n_i)$, $\hat{N}_i$=$\hat{N}(n_i)$ refer to the location parameter, the scale, and the normalization, respectively as defined in Section 4.3.2 of Chapter 4 and P(r,$\mathbf{n}_i$) is normalized to unity. However, Equation 6.3 is defined as a probability distribution in spherical coordinates. As our calculations are going to be performed in Cartesian coordinates, we obtain the conversion of the expression by using the volume element which relates the two coordinate systems as $\mathrm{d}V$=$r^2\mathrm{d}r\delta\Omega$= $\frac{4\pi}{N_{pix}} r^2\mathrm{d}r$. Then, the probability density per unit volume is given as:

$$\frac{dP}{dV} = \rho_i \frac{N_{pix}}{4\pi} \frac{\hat{N}_i}{\sqrt{2\pi}\hat{\sigma}_i} \exp\left[- \frac{(r - \hat{\mu}_i)^2}{2\hat{\sigma}_i^2} \right] \tag{6.4}$$

The convolution of the 3D posterior probability distribution of the localization of a gravitational wave and a three dimensional distribution of potential hosts in the Universe, define a new normalized probability which in the following is referred as P_{GWxGAL} (or P_{GG}), which is defined as

$$P^i_{\mathrm{GWxGAL}} = \frac{dP^i/dV}{\sum_j dP^j/dV} \tag{6.5}$$

where $\sum P^i_{\mathrm{GWxGAL}}$=1. Using the derived equation, in addition to already discussed 2D-algorithms, we developed optimized strategies for events occurring at distances for which *reasonably* complete galaxy catalogs are available.

`One-galaxy` algorithm

The coordinates of the pointing observations are selected according to the selection of individual high probability galaxies and the observation of those one-by-one. The largest probability galaxy, P^{i}_{GWxGAL} guides the observations, and the galaxies included in the region defined by the FoV of the experiment are indirectly observed. The motivation of such algorithm is the trade-off between the speed of computation, which is a key point for transient searches and the astrophysical motivation. However, the observation schedule resulting from this technique can present important overlappings of covered regions, which are usually undesired. Furthermore, although such targeted searches can be very performant for small FoV instruments, like optical and X-ray telescopes (Gehrels et al., 2016), the relatively large FoVs of IACTs motivate a further step on the selection of observation coordinates.

`Galaxies-in-FoV` algorithm

Although the `One-galaxy` algorithm stands as a good first approach to covering large areas in the sky, an improvement from which medium-FoV experiments benefit is the integration of probability regions in the sky following Equation 6.6.

$$P^{\mathrm{FoV}}_{\mathrm{GWxGAL}} = \int_{0}^{FoV_{\mathrm{H.E.S.S.}}} P^{i}_{\mathrm{GWxGAL}} dP_{\mathrm{GWxGAL}} \tag{6.6}$$

The total probability of all individual galaxies contained by the FoV is computed for a fiducial number of galaxies, and the highest probability sky field, which fulfills $P^{\mathrm{FoV},i}_{\mathrm{GWxGAL}} = P^{\mathrm{FoV},MAX}_{\mathrm{GWxGAL}}$ is chosen.

Nevertheless, the motivation of this technique is not only to cover the maximum probability region but also the underlying physics motivation is to target galaxy clusters.

6.4.3 Galaxy catalogs

In order to use the cross-correlation introduced in the previous section, two catalogs are discussed in the following.

- The Census of the Local Universe (CLU) catalog (Cook et al., 2017): This catalog is built as a combination of all known galaxies compiled from other existing catalogs (CLU-compiled; 234,500 galaxies) and a largest area ($\simeq 3\pi$) narrowband imaging survey that deploys 4 filters to search for galaxies with Hα emission out to 200 Mpc. In addition, the CLU-Hα survey has imaged 26,470 square degrees of the northern sky above -20° declination, so it includes objects only from the northern half of the H.E.S.S. sky. Preliminary results on the analysis of 14 fields out of the 3626 fields identifies 151 new objects at 7.1% contamination. Assuming an isotropic distribution, this translated in an approximative mean value of 39087 in the 3626 fields that has been scanned, for the same level of contamination. This means that the CLU catalog includes

a 39087/234,500×100=16% more objects than the CLU-compiled catalog only, which is indeed a non negligible improvement. However, no further update has been presented since 2017, preventing the open-access to the CLU catalog for EM-GW follow-up searches.

- The Galaxy List for the Advanced Detector Era (GLADE) catalog (Dálya et al., 2018 and references therein): This catalog has been built by cross-matching five, non-independent astronomical catalogs, including galaxies and quasars. These are the GWGC, the HyperLEDA catalog, the 2MASS Photometric Redshift Catalog5 (2MPZ), the Sloan Digital Sky Survey quasar catalogue from the 12th data release (SDSS-DR12Q), and the 2 Micron All-Sky Survey Extended Source Catalog (2MASS XSC). This results on a full-sky galaxy catalog which is highly complete and specifically built in order to support EM follow-up of GW signals. The GLADE catalog includes 3,262,881 entries, from which 2,965,718 are galaxies, 297,014 are quasars and 149 are globular clusters. Concerning completeness, in terms of cumulative blue luminosity outside the Galactic plane, the catalog is complete up to $d_L = 37^{+3}_{-4}$ Mpc, and contains all the bright galaxies achieving half of the total B luminosity out to $d_L = 91$ Mpc. This effect can be observed in Figure 6.9.

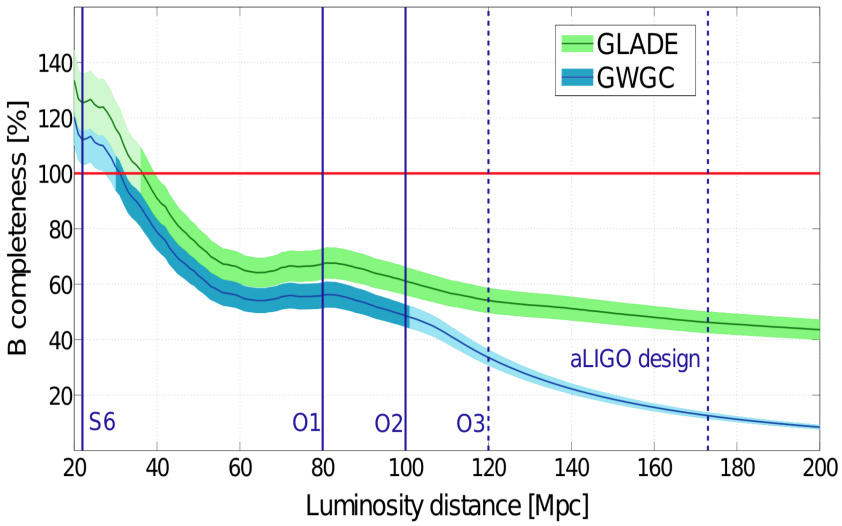

FIGURE 6.9: Normalized integrated B-band luminosity of galaxies in GLADE (green) and in GWGC (blue) with respect to luminosity distances. Extracted form Dálya et al., 2018

Galaxy catalog limitations

In galaxy catalogs, the region which corresponds to the galactic plane has a lower number density of objects, due to the experimental difficulties to perform galaxy targeting observations with the Galactic Plane in the line-of-sight, as can be seen in

Figure 6.10. The gas and dust content of the Milky Way disk reduces significantly the observability of galaxies in the background in optical and infrared wavelengths. To take this effect into account, I introduced a parametrized *avoidance zone* to be used in the GW-Galaxies cross-correlation.

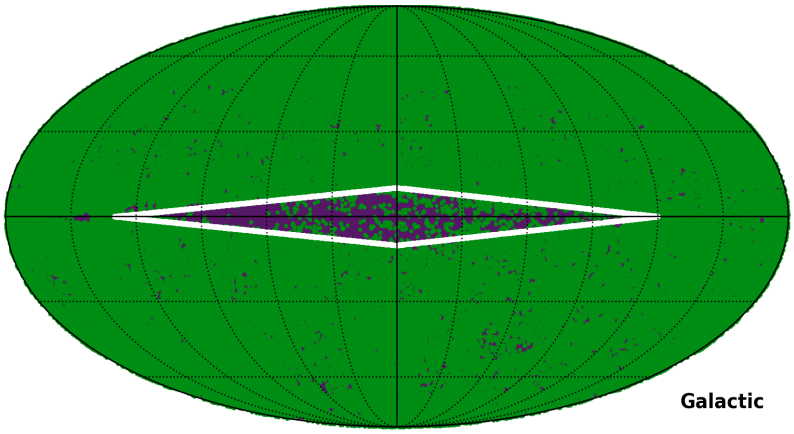

FIGURE 6.10: Spatial distribution in galactic coordinates of the GLADE catalog of quasars and galaxies, where a cut on the distance to 200 Mpc has been applied. Each green point corresponds to an object of the catalog. The parametrization for the proposed galactic avoidance zone is included in white, overlaid to the Galactic Plane that can be differentiated by eye.

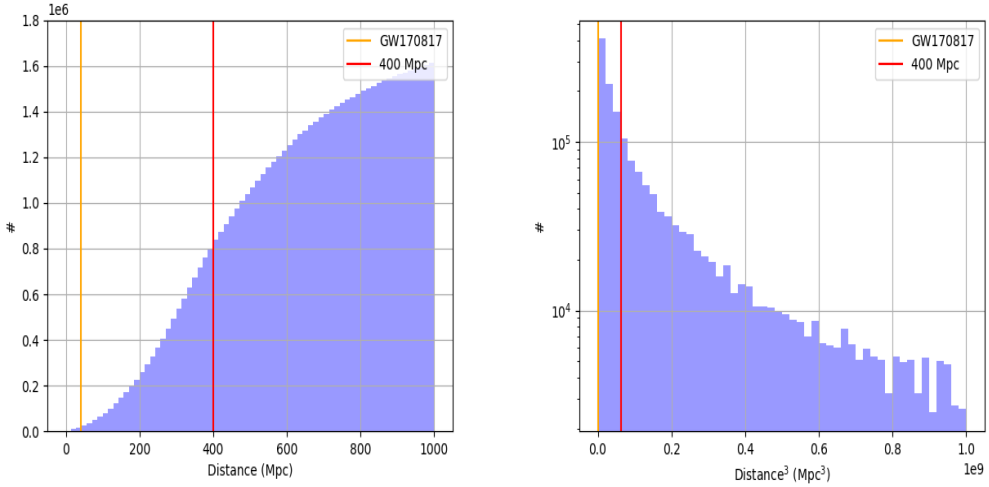

FIGURE 6.11: (Left) Distance distribution and (Right) volume distribution of the objects in the GLADE catalog, with a cut at a luminosity distance of 1000 Mpc, normalized to the unity. For reference, two typical distances have been included, as well as the GW170817 luminosity distance.

These observational biases which affect the galaxy catalogs completeness need to

be taken into account when selecting large number of galaxies to perform a convolution, expanding in large areas of the sky. A parametrization of the avoidance zone in the GLADE catalog has been obtained by studying the distribution of the galaxies at different galactic latitudes and longitudes for luminosity distances, focusing on objects with < 200 Mpc (Figure 6.10).

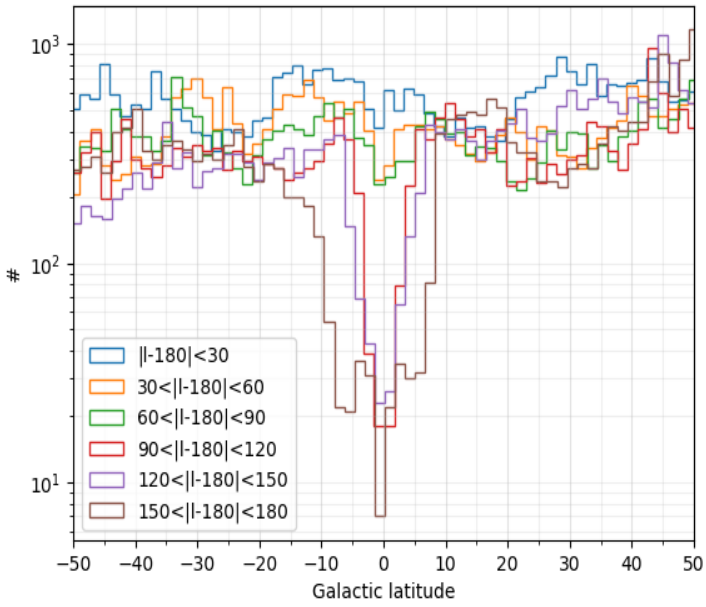

FIGURE 6.12: Number of objects in the GLADE catalog with a 200 Mpc cut with respect to the Galactic Plane latitude profile from -50° $< b <$ 50°, for a subset of longitudes defined by their absolute value, in order to add-up symmetric regions with respect to the Galactic Center. Affected region by the lack of objects due to observational difficulties goes from 90°$<|l$-180°$|<$180°.

In Figure 6.12, the number of objects in the GLADE catalog within 200 Mpc, with respect to the Galactic Plane latitude profile from -50° $< b <$ 50° for a subset of longitudes defined by their absolute value, is plotted. It can be observed that the regions affected by the lack of objects go from 90°$<|l$-180°$|<$180°. Hence, the *avoidance zone*, defined by the white contour in Figure 6.10, to be parameterized as:

$$f(l,b) = \begin{cases} \text{if } (l \leq 130) \cup (0 \leq b \leq 10) \cup (|b - \frac{1}{13}l| \leq 10) & \rightarrow \text{2D-algorithm} \\ \text{if } (l \geq 240) \cup (0 \leq b \leq 10) \cup (|b - \frac{1}{12}l| \leq 10) & \rightarrow \text{2D-algorithm} \\ \text{if } (l \leq 130) \cup (0 \geq b \geq -10) \cup (|b + \frac{1}{13}l| \leq 10) & \rightarrow \text{2D-algorithm} \\ \text{if } (l \geq 240) \cup (0 \geq b \geq -10) \cup (|b + \frac{1}{12}l| \leq 10) & \rightarrow \text{2D-algorithm} \\ \text{else} & \rightarrow \text{ 3D-algorithm} \end{cases}$$

These conditions define a region which, even though at first sight seems quite extended, it only represents a ∼4% of the sky. In the scheduling algorithms, GW

events whose maximum value of probability for the localization confidence regions falls inside the avoidance zone are not correlated with the local distribution of galaxies. Instead, a 2D approach is used in those cases.

An additional consideration has to be made regarding the luminosity distance of the objects included in the catalog. The fiducial BNS horizon for the detections made by LIGO-Virgo do not currently go beyond 200 Mpc, although in the catalog there are objects at a distance greater by an order of magnitude. Moreover, the blue luminosity completeness of the catalog sets a limit on the number of objects which should be included through their distance. For these two reasons, a loose cut on the galaxy catalog at 400 Mpc is performed, reducing the catalog entries to a quarter of the initial number. In Figure 6.11, we see the distribution of galaxies used in the developed H.E.S.S. tools.

6.4.4 Comparison of 3D scheduling algorithm performances

In order to asses the advantages of using either of the two 3D scheduling algorithms, `One-galaxy` algorithm or `Galaxies-in-FoV` algorithm, simulations of the gravitational wave follow-up have been performed. The goal is to compare the achieved localization uncertainty coverage, so larger coverage means higher probability to cover the remnant and thus a higher chance to detect an EM counterpart. To this aim, the entire process is simulated: alert reception at a random time, calculation of the visibility constrains and the observation scheduling. Results of these simulations give us the uncertainty region coverage depending on the employed algorithm, and other parameters related to the gravitational wave signals (e.g. the number of interferometers involved or the uncertainty on the localization in the three spatial axes). The simulations have been performed using the following configuration:

- Random arrival times throughout the year.
- H.E.S.S. site location and effective telescope FoV of a radius $r = 2.5$ deg.
- A maximum of 20 observations of 30 minutes each, within 3 days, is allowed. This corresponds to a total of 10 hours of scheduled observations.
- Use of a total of 250 gravitational wave localization maps derived from simulated NS-NS merger events provided by the LIGO-Virgo collaboration before O2 (Singer et al., 2016a). Due to the specifications of a prompt response, the sky localizations reconstructed with the BAYESTAR algorithm have been chosen.
- GLADE galaxy catalog (version 2.2) by Dálya et al., 2018.

Results of these simulations are shown in Figure 6.13. An important difference on the density regions of these 2D histograms is observed, showing the dependency with respect to the number of observations and P_{GWxGAL} probability covered. The distributions in the `Galaxies-in-FoV` approach case is concentrated in small number of pointings, showing a *pseudo*-linear behaviour with further stagnation. In comparison, in the `One-galaxy` results, we observed that the algorithm is not efficient when it comes to a number of observations closer to mid-values, no giving any added value

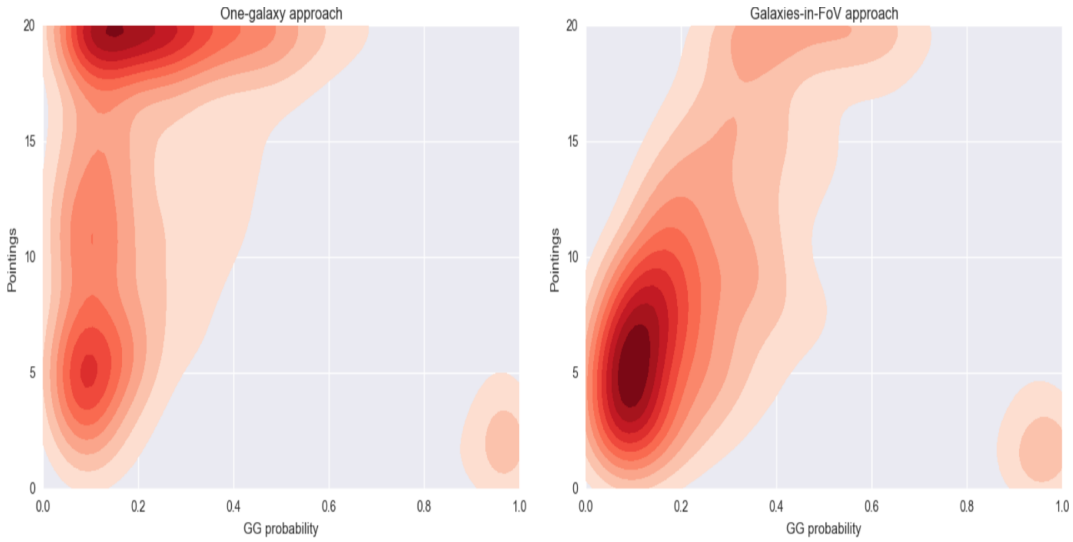

FIGURE 6.13: (Left) Density histogram showing the correlation between the number of observations and the convolved probability covered using the `One-galaxy` algorithm and (Right) the `Galaxies-in-FoV` approach which result from the coverage simulations described in the text.

to the observations and thus, not being able to adequately cover important fractions of the total convolved probability.

One has to note that the absolute numbers shown in Figure 6.13 are heavily influenced by the characteristics of the underlying simulated GW events. They contain for example a significant number of poorly localized events for which the localization regions span to both, northern and southern sky. This translates into a stagnation of the covered probability around $\sim 50\%$, which illustrates the impossibility to achieve higher probability coverage as some parts of the sky are simply not reachable for a single, ground-based experiment. Similarly, the concentration of events observed, where a high probability is covered with a low number of observations is due to several NS-NS input maps that present a very accurate localization in a convenient part of the sky for the H.E.S.S. experiment, so that they will be almost fully covered in few observations. These localization sky maps corresponds to the mergers that have been observed by all three interferometers of the network.

These simulations prove the performance of the developed algorithms and the advantages brought by the use of algorithms that optimize in integrated probabilities regions, as done in `PGW-in-FoV` and `Galaxies-in-FoV`. These two algorithms are indeed the result of the study and improvements of the most simple scheduling algorithms `Pix-in-FoV` and `One-galaxy`. These simulations have been helpful to assess the interest of developing more sophisticated algorithms, which can schedule observations that cover larger sky region in a more efficient way.

6.5 Discussion

The scheduling algorithms presented in this Chapter have been developed to be used in the context of gravitational wave follow-ups of IACTs like H.E.S.S and CTA.

Within the H.E.S.S. collaboration, the described algorithms have been used to follow-up gravitational waves since the beginning of O2. Not only they are accessible offline, where a human is responsible to run the code, but also they have been implemented within the automatic alert reception system of the H.E.S.S. collaboration. In Chapter 7, more details about the gravitational wave follow-ups with H.E.S.S. using the introduced codes is given.

The modular structure of the software allows to easily adapt it to other instruments with different characteristics like a different FoV, different total observation time, length of individual observing runs or visibility constrains. In the case of the future CTA, these codes have been adapted and used in order exploit the sensitivity and the capabilities of the future CTA. These points are discussed in Chapter 8, where the science case of gravitational waves follow-up by CTA is presented in detail.

Chapter 7

GW counterpart searches with H.E.S.S.

Contents

7.1 The H.E.S.S Transient Follow-up Program

7.1.1 H.E.S.S. sensitivity to transients

In time-domain astrophysics, transient phenomena, which are typically cataclysmic and short-lived, can have durations of the order of seconds to hours. The H.E.S.S. experiment is a well suited, performant instrument to effectively study the transient sky. Among its capabilities, the H.E.S.S. telescopes are able to perform fast-response follow-ups, it presents high sensitivity at VHE and a mid-size FoV which allows to explore relatively large regions in the sky.

The H.E.S.S. telescope, in particular in its phase II, is able to provide a rapid reaction to incoming alerts hardware-wise thanks to the installation of CT5, whose design is conceived to allow extremely rapid slewing. As shown in Figure 7.2, any sky coordinate accessible to H.E.S.S. is reached in less than a minute (Hofverberg et al., 2013).

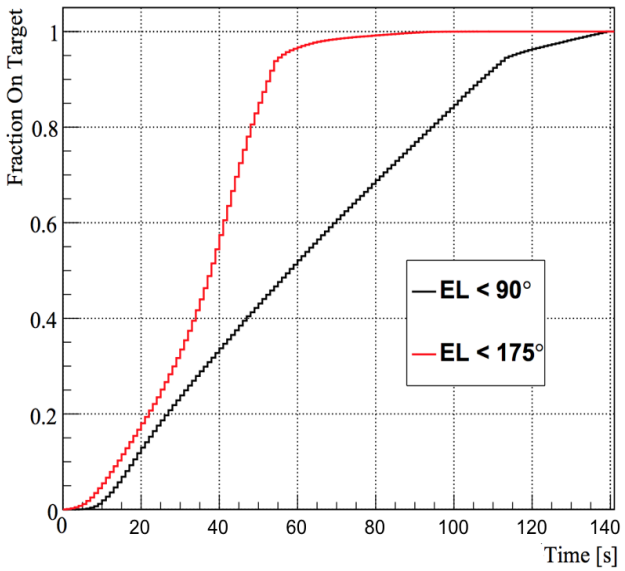

FIGURE 7.1: The fraction of times the CT5 telescope is on target to a random position on the sky versus the time since the start of the repositioning. Figure extracted Hofverberg et al., 2013

The effective area of the gamma-ray satellites like *Fermi*-LAT in the GeV range significantly smaller than the effective area of IACTs, so that to reach similar sensitivities, the gamma-ray satellites need to observe the source for longer periods of time. For this reason, at GeV-TeV energies, IACTs are such powerful instruments observing the variable sky. This is illustrated in Figure 7.2 (Holler et al., 2015), where the sensitivity as a function of the observing time has been plotted. However, *Fermi*-LAT observations are typically used as input of deeper IACT follow-ups since its significant larger FoV allows to monitor large portions of the sky and which enables serendipitous observations of flaring sources and transients.

In transient physics, the reaction time and the evaluation of the information provided by survey instruments play a key role. For this reason, transient follow-up observations need of strategies to successfully respond all the possible physical scenarios. On one side, hardware improvements, as the installation of CT5 in the H.E.S.S. II phase, are key in achieving fast, performant responses. On the other hand, software-wise, a significant effort has been done in the H.E.S.S. experiment to optimize the alert reception and the reaction to different type of astrophysical events.

The implemented multi-purpose alert system, known as VoAlerter (Hoischen, 2018), connects a large number of observatories from the entire multi-wavelength

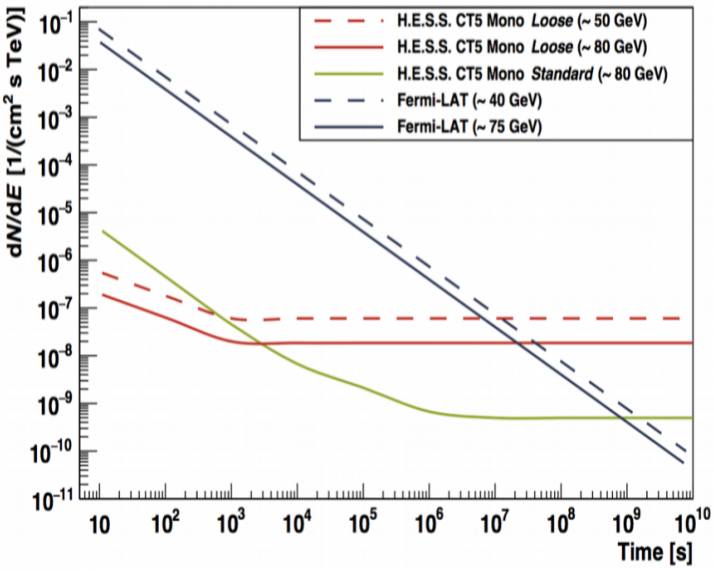

FIGURE 7.2: Differential flux sensitivity of the big telescope, CT5, of the H.E.S.S. experiment for different analysis cuts, at different energies as a function of observing time, compared to a gamma-ray satellite at energies around several tens of GeV. From Holler et al., 2015

and multi-messenger domain and from around the word to the H.E.S.S. experiment (Schüssler et al., 2015). As example, science cases that require a rapid response and repointing are neutrino alerts, gamma-ray burst alerts, fast radio bursts and gravitational wave triggers. Among all these follow-up programs, in this chapter we focus on the implementation of the gravitational waves follow-up observation scheduler into the H.E.S.S. alert system.

7.1.2 The gravitational-wave follow-up program

The observation scheduler to follow-up gravitational wave detections with instruments from mid to small FoV discussed in Chapter 6, has been developed, not only for an offline use but also it has been implemented in H.E.S.S. online alert system, VoAlerter in the following. All features of the gravitational wave follow-up observation scheduler are included as part as the automatized system in the H.E.S.S. experiment.

In order to study the number of times when the VoAlerter and the online codes will be fully in charge of the follow-up, I simulated the time delay between the injection of a set of point sources at a random time during the year, and the time when the first observation of each point source is possible. The effects causing the delay are the lack of darkness condition, which vary throughout the year. Note that point sources are preselected to be in the southern sky. Results are plotted in Figure 7.3 for zenith angles limits $\theta_{\rm ZENITH} < 45°$ and $\theta_{\rm ZENITH} < 60°$. Note that night zero translates in no scheduled observations were possible in any of the following 7 days.

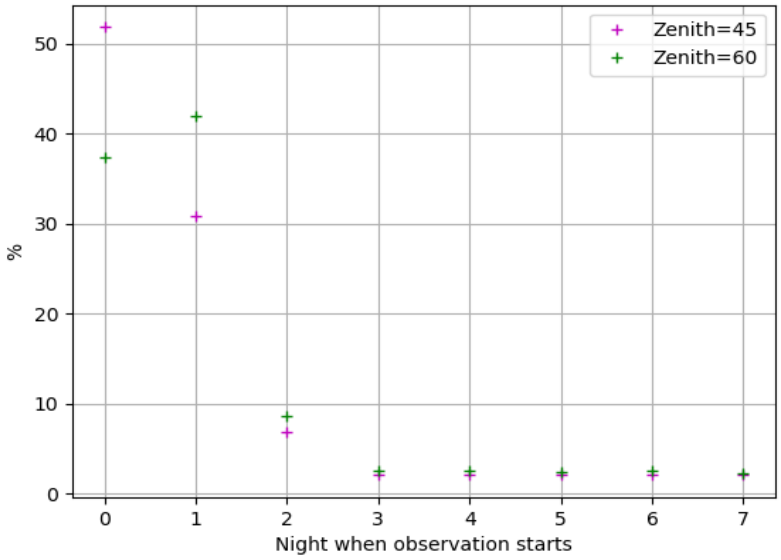

FIGURE 7.3: Night number in percentage when observations on a point source starts, obtained from the simulations explained in the text. Results are shown for two different values of the zenith angle, $\theta_{\mathrm{ZENITH}} = 45°$ and $\theta_{\mathrm{ZENITH}} = 60°$. Night zero translates in no scheduled observations where possible in any of the 7 days.

The first conclusion is that the variation of the allowed zenith angle range (defined by θ_{ZENITH}) translates to an important increase of followed-up observations, going from 31% for $\theta_{\mathrm{ZENITH}} < 45°$ to 42 % when $\theta_{\mathrm{ZENITH}} < 60°$. In addition, due to the zenith angle cut, there is an increase on the number of non-observable sources of about 15% of source at $\theta_{\mathrm{ZENITH}} < 45°$. This study motivates the use of $\theta_{\mathrm{ZENITH}} < 60°$ for the zenith angle cut, although it translates to a higher energy threshold of observation.

Besides the improvement due to the selection of the zenith angle cut, from Figure 7.3 we conclude that, considering that observations are possible at some point in the first 7 days, they will be scheduled starting from the first night after GW detection in 65%($\theta_{\mathrm{ZENITH}} < 45°$) and in 67% ($\theta_{\mathrm{ZENITH}} < 60°$) of the times. Although a subset of these alerts will be issued during daytime, there is a non negligible number of times when the alert will be issued and received during night time. However, no human intervention is granted during night time and there is an obvious benefit to be gain by automatizing as much as possible the chain of decisions, related to fast response purposes and minimization of number of errors. For these reasons, this study encourages the automatization of the algorithms in the VoAlerter, avoiding human intervention. Hence, online codes integrated in the VoAlerter will be fully in charge of the follow-up.

The automatic workflow of the VoAlerter mimics the decision tree that is done in an offline follow-up by a human. In Figure 7.5 , a summary of the main decisions is presented. The main steps can be summed up as:

- **Event identification**. In a first step, the gravitational wave event is identified as such and then analyzed in detail, depending on the probabilities included in the alert (see Section 4.5 for further details). A large terrestrial probability value, larger than 50% results do not trigger follow-up observations. Then, depending on the parameter `HAS_NS` and the BH-BH probability, a classification is made as either mergers *likely* to produce a EM counterpart (including GW events falling into the *Mass Gap*, BH-NS and NS-NS class) or *not likely*, i.e. the BH-BH case.

- **Algorithm selection**. Information included in the event alert is parsed and considered as input criteria to select the follow-up strategy in the VoAlerter. The main points of the decision tree to asses the use of galaxy catalogs, which are based on the provided localization reconstruction of the gravitational wave are: the availability of distance estimates, the distance estimate itself and the overlap of the GW localization uncertainty region with the Galactic plane. These conditions are illustrated in Figure 7.4.

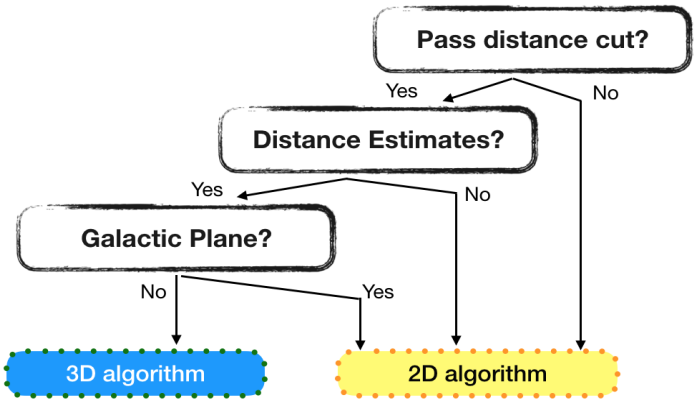

FIGURE 7.4: Workflow followed by the VoAlerter in order to select a scheduling algorithm, depending on the usefulness of including the local distribution of galaxies.

- **Response latency**. The arrival time of the gravitational wave alert to the H.E.S.S. alert system (which corresponds to the time when the alert is distributed by LIGO-Virgo) with respect to the compact binary merger time is used to select the scheduling *mode* of the follow-up observations. Two different scheduling modes are defined depending on this quantity: *prompt* response mode or *full-schedule* response mode. These have been defined in order to provide the fastest response possible from the alert system and the physics motivation underlying being to catch the prompt VHE emission of the source. The VoAlerter alert system is configured to schedule the first observation and start the data acquisition as soon as possible. The rest of the follow-up observation is obtained at later times, when the data acquisition is ongoing. The maximum observation delay for the prompt response mode of an observation scheduling is

set to 2 hours after the merger. The maximum observation delay time for the full schedule mode is 24 hours for BBH mergers and 24 hours for BNS mergers. The workflow for both response modes can be observed in Figure 7.5.

- **Scheduling**. Once the characteristics of a specific event have been successfully parsed and identified, the observation scheduling strategy is selected. The scheduling of observation starts by computing the visibility window for the H.E.S.S. telescopes at the time of the alert reception. The total visibility window is then divided in single observation windows, by considering a minimum and maximum time duration for each of the H.E.S.S. observation window.

  After the observation window of the H.E.S.S. telescopes are defined, the probability selection algorithms explained in Section 6.4 are applied in order to select the observation coordinates that maximizes the probability of covering the source. The other features of the scheduling algorithms, i.e zenith angle optimization and second round, which have been explained in Chapter 6 , are also part of the decision chain. If the potentially covered uncertainty region passes some predefined cuts, observation are effectively scheduled.

  The current values for the parameters on which the H.E.S.S. observation scheduling depends, can be found in Table 7.1.

Probability cut single pointing	5 %
Probability cut *prompt* schedule	5 %
Probability cut *full* schedule	10 % (if NS) / 50 % (if BH-BH)
H.E.S.S. observation window	Max: 28 min / Min: 10 min

TABLE 7.1: Current parameters used as criteria to scheduled H.E.S.S. follow-up observations

The H.E.S.S. experiment participated in multi-messenger follow-up of events during the O2 observation run, which started November 2016 until August 2017. These algorithms were developed during the last months of 2016 and beginning of 2017, in parallel to the first months of data acquisition of the O2 observation run. They were presented for the first time in Seglar-Arroyo and Schüssler, 2017 and were off-line commissioned and further developed during the rest of the O2 observation run. They were proven to be a successful approach for the H.E.S.S. experiment to overcome the challenges that gravitational wave observation scheduling pose, as it will be shown in the following sections.

They were fully included in the VoAlerter in the scope of the O3 observation run and they are running online, ready to react to gravitational wave alerts. The reaction of the H.E.S.S. experiment to the gravitational wave event alerts issued during O3, is discuss in detail in Section 7.3.

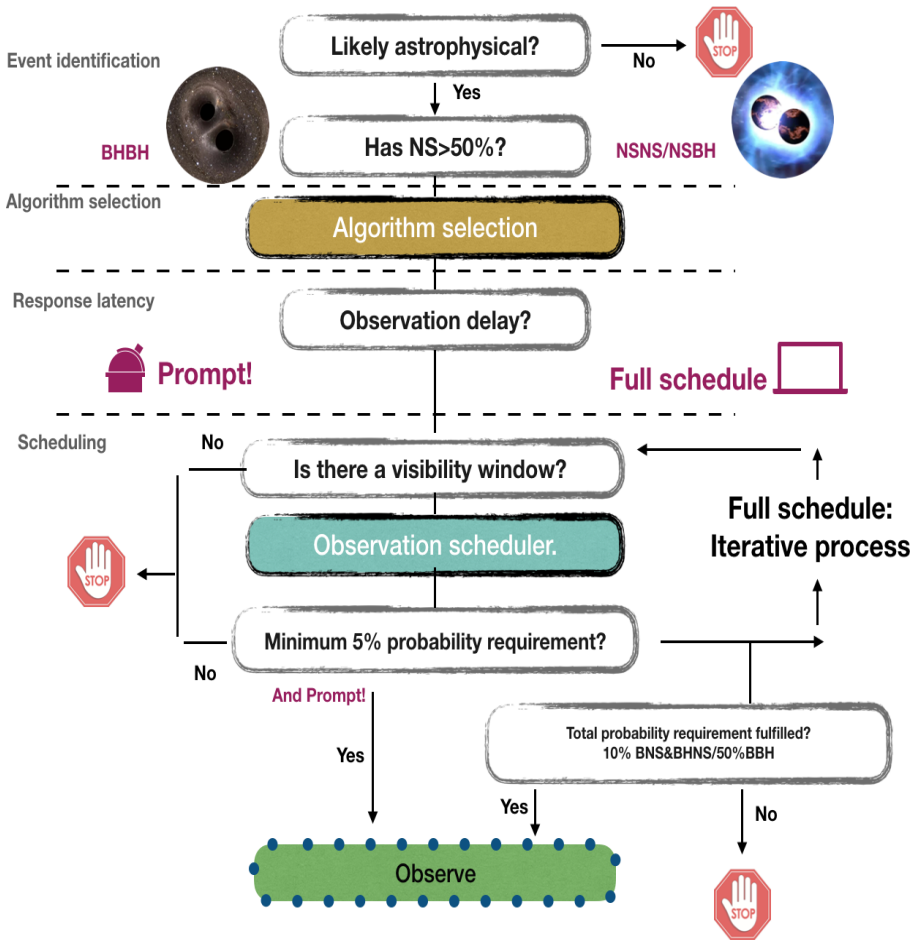

FIGURE 7.5: Schematic workflow of the response of the VoAlerter to a gravitational wave alert. It follows the same decision tree as offline scheduled observations

7.2 GW follow-up observations with H.E.S.S. during O2

In this section, the three follow-up observation of gravitational wave triggers, G284239, GW170814 and GW170817, performed by H.E.S.S. during O2 observation run, are discussed in detail.

7.2.1 G284239: commissioning of the follow-up Observation Scheduler

In May 2, 2017 at 22:26 UTC, the gravitational wave trigger G284239 was identified by LIGO *Hanford* and LIGO *Livingston* as a binary back hole, with a FAR $<$ 4/ year. The 90% localization uncertainty region spanned over 3600 deg^2 and the gravitational wave sky map only included the ρ_i two dimensional probability sky map.

The derived scheduled observations were obtained by using a 2-dimensional approach, due to the absence of 3D reconstruction in the skymap. In addition, the

selection of a 2-dimensional approach could also have come from the fact that the highest probability region of the total localization uncertainty region visible for the H.E.S.S. experiments crossed the Galactic Plane, as can be observed in Figure 7.6.

The derived schedule using `One-pix` algorithm consisted on 9 observations covering the central part of the uncertainty region, which are shown in Figure 7.6. H.E.S.S. observations were requested to start the night of May 3, at 23:30 UTC, but due to bad weather conditions at the beginning of the night, the star of observation was shifted to 02:01 UTC, and only 4 runs could be taken (in green in Figure 7.6).

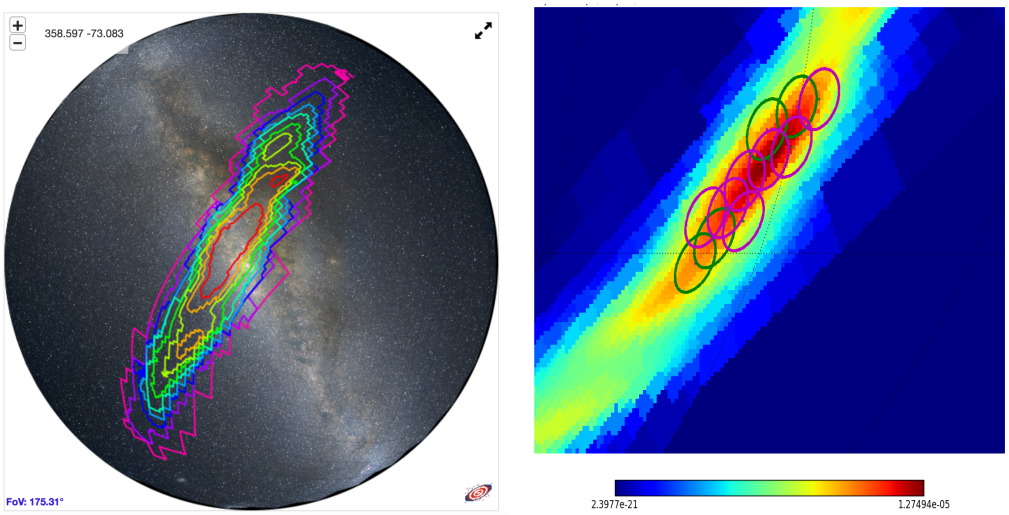

FIGURE 7.6: (Left) Contours corresponding to the uncertainty region of the localization of the gravitational wave, from 10% to 90%, in steps of 10°, where an image of the galactic plane in optical wavelengths has been included (Right) H.E.S.S. follow-up scheduled observations of the gravitational wave trigger G284239 where green circles correspond to those which were eventually performed

The H.E.S.S. follow-up observations were shared with the astrophysics community through a GCN Circular (H.E.S.S. collaboration, 2017). The RTA preliminary analysis did not reveal significant gamma-ray emission from any of the observed regions, and the gravitational wave trigger was later classified as noise. Nevertheless, this example helped to improve the set up chain of decisions, underlying the importance of commissioning periods.

7.2.2 GW170814: a Binary Black Hole merger follow-up

In August 14 2017, LIGO *Livingston*, LIGO *Handford* and Virgo performed the first joint detection of a binary black hole coalescence G297595, renamed afterwards as GW170814 (Abbott et al., 2017b). The merger of these two stellar masses black holes of $30.5^{+5.7}_{-3.0}$ $M_\odot$ and $25.3^{+2.8}_{-4.2}$ $M_\odot$ happened at a redshift $0.11^{+0.03}_{-0.04}$, which corresponds to a luminosity distance of 540^{+130}_{-210} Mpc.

The H.E.S.S. follow-up of the event got delayed due to visibility constraints on that region of the sky. For this reason the observation scheduling used the updated LALInference map, which was published on August 15, at 20h17m51s UTC. The 90% credible region for the event localisation for this reconstruction spans for 190 deg^2. Due to the redshift of the event, observations were scheduled using the `One-pix` 2D-algorithm approach, including the various optimisations explained in previous sections.

Observations were scheduled throughout the next three nights after the start of observations, which happened in August 17 at 00:10 UTC. A total of 11 pointings were obtained with CT5 and three of the CT1-4 small telescopes. Each of the observations reached a sensitivity of about 20% of the flux from the Crab nebula at 5 σ. The sky coordinates and times of the pointing observations are summarized in Table 7.2.

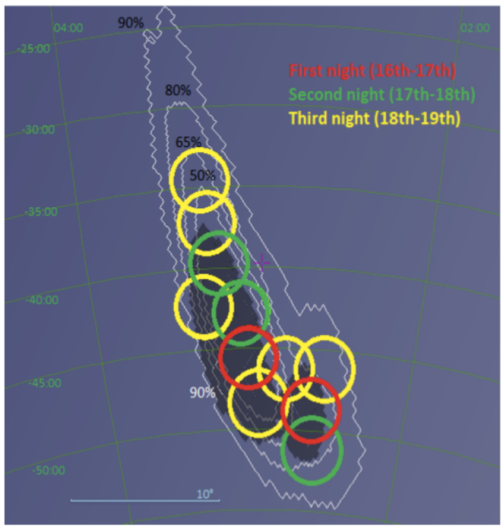

FIGURE 7.7: (Left) Observation directions of FoV 1.5° scheduled for the first night of H.E.S.S. follow-up of GW170814 (Ashkar, Schüssler, and Seglar-Arroyo, 2019)

The obtained H.E.S.S. observations cover about 80% of the LALInference localization uncertainty, as can be seen in Figure 7.7. However, an updated sky localization was distributed, which is the final reconstruction (Abbott et al., 2017b) shift with respect to the LALInference map used to scheduled observations. The H.E.S.S. observations cover around 90% of the localization of the final region.

The analysis of the obtained data was performed using *Model Analysis* in Stereo mode, which used the data from all available telescopes and `Loose` event selection was applied. The significance sky map which results from this analysis is shown in Figure 7.8. No significant gamma-ray emission is observed. Integral upper limits constraining gamma-ray emission from the remnant of the binary coalescence have been derived assuming a power-law spectrum of E^{-2} for energies between 250 GeV

Time (UTC)	RA	Dec
2017-08-17 00:10	2h38m19s	-48d43m12s
2017-08-17 00:40	3h03m07s	-45d35m24s
2017-08-18 00:10	2h36m58s	-51d15m59s
2017-08-18 00:40	3h05m57s	-42d45m49s
2017-08-18 01:10	3h13m53s	-39d46m14s
2017-08-18 23:55	2h34m20s	-46d11m42s
2017-08-19 00:25	2h59m24s	-48d23m28s
2017-08-19 00:55	3h16m57s	-37d07m49s
2017-08-19 01:25	2h49m10s	-46d15m52s
2017-08-19 01:55	3h18m53s	-34d30m06s
2017-08-19 02:25	3h19m28s	-42d22m29s

TABLE 7.2: H.E.S.S. scheduled follow-up observations of the binary black hole merger GW170814.

$< E <$ 10 TeV (Ashkar, Schüssler, and Seglar-Arroyo, 2019). Results are shown in Figure 7.8.

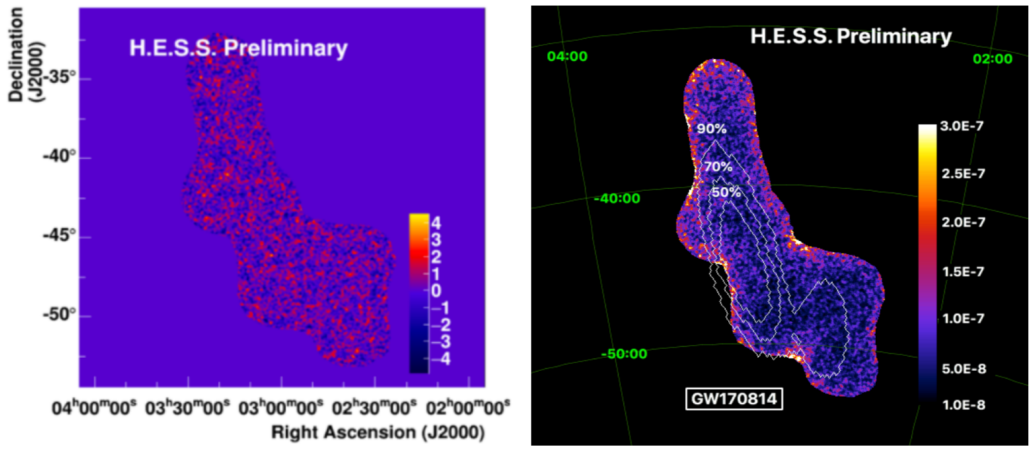

FIGURE 7.8: (Left) Map of significances of the gamma-ray emission obtained from the three nights of observations by H.E.S.S. of GW170814. (Right) Integral upper limits in units of erg cm^{-2} s^{-1} between energies 250 GeV $< E <$ 20 TeV. The uncertainty region of the reconstruction with LALInference of the sky localization of the GW170814 is overlaid in white (Ashkar, Schüssler, and Seglar-Arroyo, 2019).

7.2.3 GW170817: a Binary Neutron Star merger follow-up

The first ever detected gravitational wave coming from the coalescence of a neutron star binary was recorded on August 17, 2017, at 12:41:04 UTC by the Advanced LIGO and Advanced Virgo interferometers. Details on the broad multi-wavelength campaign have been discussed in 4.5.2. Here I present the very high energy observations during the prompt follow-up performed by the H.E.S.S. experiment (Abdalla

et al., 2017).

An initial notice was issued by the LVC on August 17, 2017 at 13h8m16s UTC. It included a first reconstruction with the BAYESTAR algorithm of the localization of the merger using data only from LIGO-Hanford, due to a glitch in LIGO-Livingston data, which we refer as `BAYESTAR` skymap. As only data from a single interferometer was used in this initial reconstruction, the sky location of the event expanded over 8061deg^2 (50% containment) and 24200 deg^2 (90% containment). This represent 37% of the whole sky and basically corresponds to the antenna pattern of the interferometer.

An update on the gravitational wave reconstructed skymap, to which we refer in the following as `BAYESTAR_LHV`, still using BAYESTAR algorithm, was provided at 17:54:51 UTC by the LIGO-Virgo collaboration and included cleaned data from LIGO-Livingston and Virgo data. The result of this joint analysis reduced the 90% localization uncertainty of the GW event to $\sim$ 31 deg^2. A further update using LALInference localization reconstruction algorithm was distributed 9 hours after the merger, to which we refer as *final* or `LALInference` in the following. In Figure 7.9, the three mentioned updates on the gravitational wave localization reconstruction are plotted.

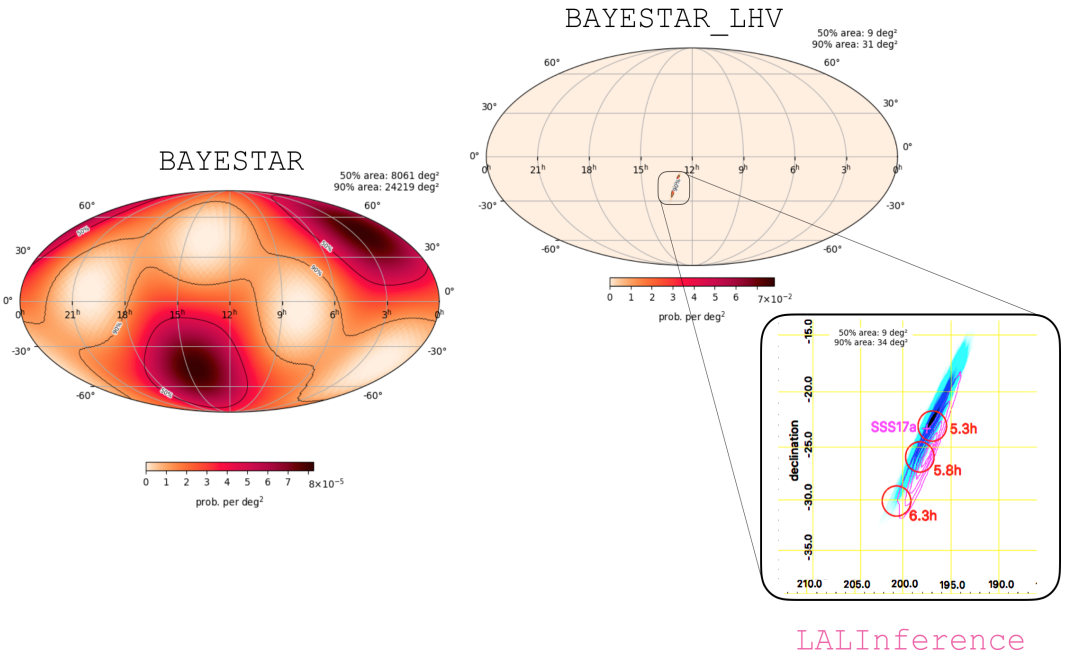

FIGURE 7.9: Updates on the gravitational wave localization reconstruction of the neutron star merger GW170817 (`BAYESTAR` ,`BAYESTAR_LHV` and `LALinference`) during the first day after the merger.

Thanks to the preparation and commissioning of the scheduling tools, I was able to react rapidly to the incoming information regarding GW170817. For this event,

there was no automatic reaction of the VoAlerter as the notices arrived outside dark-time. Hence, once the `BAYESTAR_LHV` sky map was received, I manually ran the scheduling algorithms. The obtained observation scheduling was sent by email to the shift-crew with the pointing coordinates and the corresponding observation times. All this steps were performed in a short period of time between the reception of the updated skymap at 17:54:51 UTC and the beginning of dark time in the H.E.S.S. site in Namibia, several minutes later.

Observations started at 17:59 UTC, five minutes after the reception of the new localization of the neutron star merger, and continued until 19:30 UTC, time at which the last part of the localization region moved outside the FoV. The algorithm chosen to schedule observations is the so-called `One-Galaxy` 3D algorithm. This selection was based in the short time available compared to what the `Galaxies-in-FoV` used to take in previous simulated follow-ups, due to the large load of galaxies, the probability integration and the iterative process. A total of 3 runs were scheduled, which directions can be found in Table 7.3 and Figure 7.11. The observations were performed by the CT5 telescope, which represents an effective FoV $\sim$1.5°. The scheduled pointings covered about a 56% of the LALInference uncertainty region. However, if we consider the probability derived when convolving the localization with galaxy catalogs, the total probability $P_{GW\times GAL}$ covered by H.E.S.S. observations is 86%.

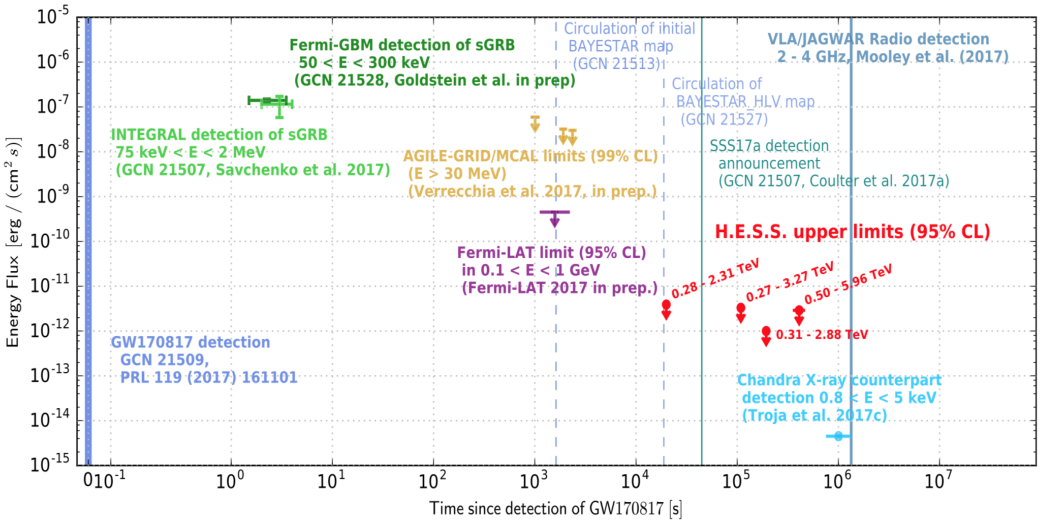

FIGURE 7.10: Simplified timeline of the performed observations after the detection of the BNS merger, focusing on the high-energy, non-thermal emission, with the H.E.S.S. observation in red. It can be observed that the first H.E.S.S. observation, which include the remnant, where performed previous to the SSS17a detection announcement. For a complete picture, see Abbott et al., 2017c

By the time the first three H.E.S.S. observations were performed, the remnant had not yet been localized. Yet, the first pointing performed by H.E.S.S. covered the remnant hosted in the galaxy NGC4993. The H.E.S.S. observations are therefore the first obtained by a ground-based pointing instrument in the follow-up campaign

ID	Observation time (UTC)	Pointing coordinates [deg]	<zenith angle> [deg]
1a	2017-08-17 17:59	196.88, -23.17	59
1b	2017-08-17 18:27	198.19, -25.98	58
1c	2017-08-17 18:56	200.57, -30.15	62
2a	2017-08-18 17:55	197.75, -23.31	53
2b	2017-08-18 18:24	197.23, -23.79	60
3a	2017-08-19 17:56	197.21, -23.20	55
3b	2017-08-19 18:24	197.71, -23.71	60
5a	2017-08-21 18:15	197.24, -24.07	60
6a	2017-08-22 18:10	197.70, -24.38	60

TABLE 7.3: H.E.S.S. scheduled follow-up observations of the binary neutron star merger GW170817

covering the remnant location, and we are thus able to provide stringent, timely constrains of the VHE emission of the remnant.

After the remnant was pinpointed by optical instruments, the H.E.S.S observation schedule was modify accordingly for the following nights. The remnant was monitored as long as the location was visible within a maximum zenith angle of $\sim 60°$ and darkness condition. In Table 7.3, further observation coordinates are given. They are plotted in Figure 7.12, together with the time delay with respect to the merger.

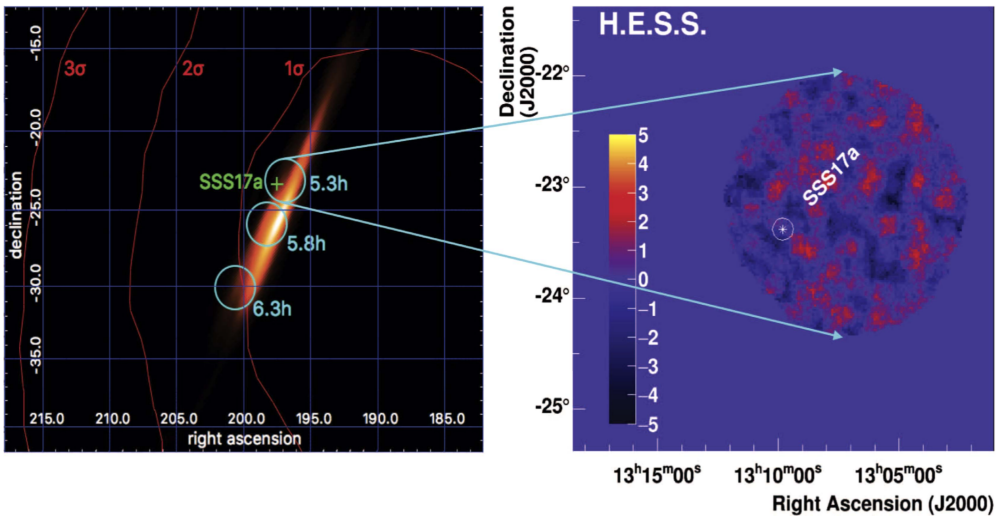

FIGURE 7.11: (Left) Observation directions of FoV 1.5° scheduled for the first night of H.E.S.S. follow-up of GW170817, starting August 17 2017 at 17:59 UTC, the time of delay respect to the merger is quoted. (Right) Map of significances of the gamma-ray emission for the pointing scheduled during the first night, which includes the counterpart SSS17a / AT 2017gfo. The white circle corresponds to the H.E.S.S. point spread function which is used for the oversampling of the map.

The obtained data were analyzed using the *Model Analysis* using only data from the 28 m telescope in the center of the H.E.S.S. array in order to achieve a low energy threshold, using `Loose` cuts. Due to the large zenith angle of the observations, with a value of 50° for the first observation, the analysis results in an energy threshold of 280 GeV. For the combined dataset on SSS17a, the $\theta \sim 60°$, giving an energy threshold of 270 GeV. Additional details can be found in Table 7.4. Note that due to the redshift of the remnant z=0.0097, no EBL correction has been applied.

The analysis of the H.E.S.S. observations shows no significant excess. The map of significances resulting of the analysis of the observed sky regions during the first observations, covering the source, is shown in Figure 7.11 and in Figure 7.12 for the combined dataset on the source.

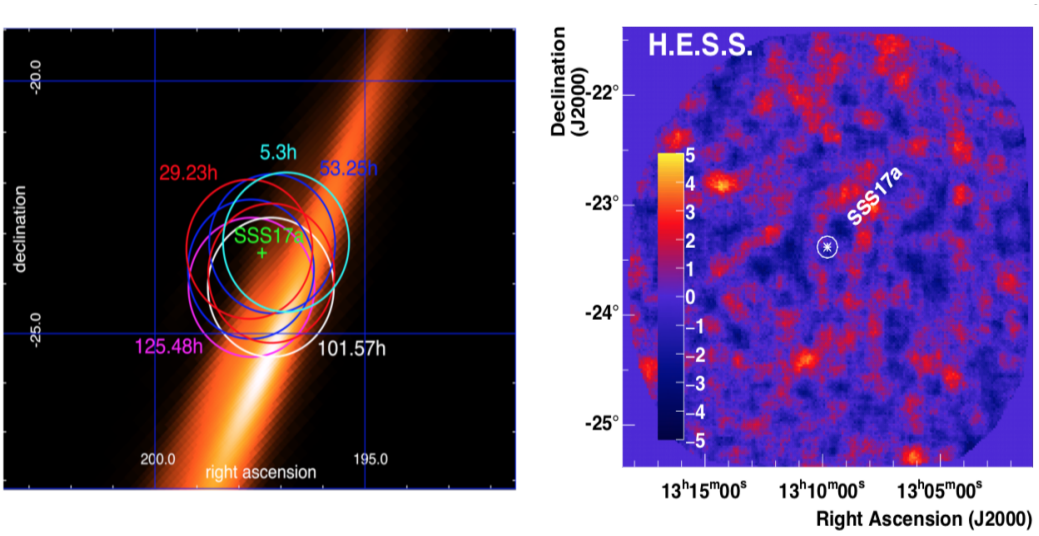

FIGURE 7.12: (Left) Pointings of FoV 1.5° performed by H.E.S.S. during the follow-up campaign on GW170817, where numbers indicated the time when the observation was performed with respect to the merger GW170817 (Right) Significance map of the gamma-ray emission, combining all the observations obtained during the follow-up campaign, where no significant detection at high energies is observed at the remnant position

Due to the non-detection, 95% C.L. upper limits have been derived on the gamma-ray flux following Feldman and Cousins, 1998. The flux limits have been assuming a generic E^{-2} energy spectrum for the potential emission of the remnant, and can be found in Figure 7.13 and in Table 7.4, where the energy ranges are quoted.

A search for fainter but temporally extended emission from SSS17a was performed, where the entire data set except from 1b and 1c, has been combined. In Figure 7.13, the resulting significance map of the analysis is shown. Again, no gamma-ray emission is detected. H.E.S.S. results are fully compatible with the background-only hypothesis, so upper limits on the flux of the source have been derived for the emission. In the energy range from $0.27 < E$ [TeV] < 8.55, the gamma-ray flux limit is set to

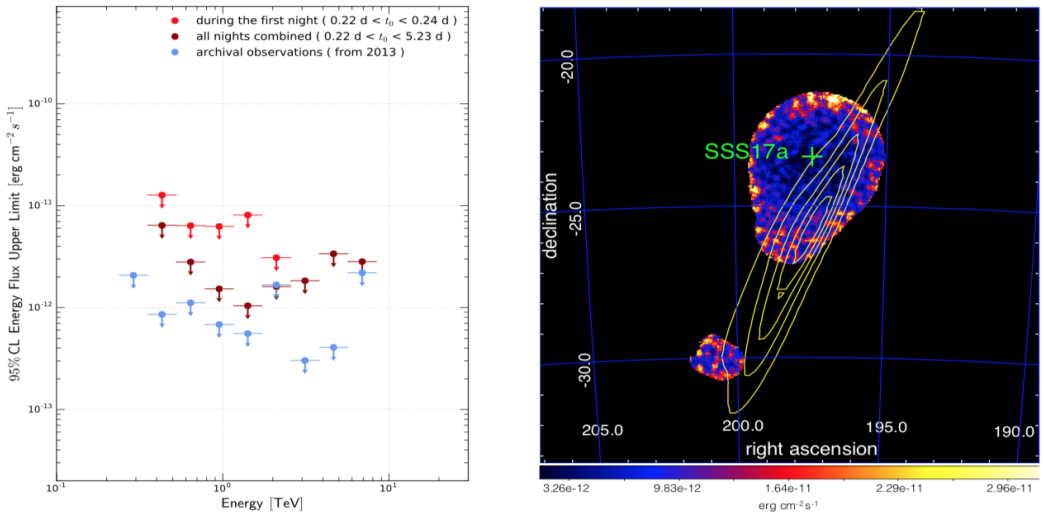

FIGURE 7.13: (Left) Differential upper limits on the gamma-ray flux emitted by SSS17a which result from the H.E.S.S monitoring campaign and archival observations of the region. (Right) Sky map of the integral upper limits in the 270 GeV to 8.55 TeV energy range, obtained by assuming an E^{-2} energy spectrum, derived from the H.E.S.S. follow-up observations of GW170817. The yellow contours correspond to the localization of the GW event reconstructed by the LALInference algorithm, distributed by the LIGO-Virgo Collaboration.

$\phi_\gamma < 1.5 \cdot 10^{-12}$ erg cm^{-2} s^{-1}. In order to compute the limits on the VHE gamma-ray luminosity of SSS17a at a distance of 42.5 Mpc, a radially symmetric emission has been assumed, which gives a value of $L_\gamma < 3.2 \cdot 10^{31}$ erg s^{-1}.

The observing upper limits of the analysis are given in two ways, as a integral upper limit skymap but also as differential upper limits as a function on energy for different periods, which are shown in Figure 7.13 for the first observation on SSS17a, the combined data set (which includes the remnant) and archival H.E.S.S. observations obtained in 2013 on the same region. Deep observations centered on SSS17a result on constraining integral upper limits from 270 GeV to 8.55 TeV, which are shown as a skymap in Figure 7.13 for all observations obtained with H.E.S.S. during

Pointings	Time since GW trigger (days)	f_γ (erg cm^{-2} s^{-1})	Energy band (TeV)
1a	0.22	$< 3.9 \cdot 10^{-12}$	0.28-2.31
2a+2b	1.22	$< 3.3 \cdot 10^{-12}$	0.27-3.27
3a+3b	2.22	$< 1.0 \cdot 10^{-12}$	0.31-2.88
5a+6a	4.23, 5.23	$< 2.9 \cdot 10^{-12}$	0.50-5.96
all	0.22 - 5.23	$< 1.5 \cdot 10^{-12}$	0.27-8.55

TABLE 7.4: Limits on the high-energy gamma-ray emitted flux at 95% C.L., assuming a E^{-2} energy spectra, in the corresponding energy band, of the remnant of the BNS merger observed by H.E.S.S.

the follow-up campaign of GW170817. Expected features as the radially decreasing acceptance of the telescope, which result on less constraining limits when approaching the border of the FoV, can be observed.

In order to asses the robustness of these results, a cross-check analysis was performed using the fully independent data calibration chain and the analysis, using IMPACT. The results of the IMPACT analysis are consistent with the ones shown here. The approval of the analysis, which is based on the agreement of the two main calibration and analysis chains, was done in less than a month. The publication of the results of the H.E.S.S. follow-up observation of GW170817 is the fastest paper that has ever been published by the H.E.S.S. collaboration. The paper was published in a total time of 10 weeks of work between data acquisition and publication, passing by the data transfer to Europe, calibration and reconstruction, validation and unblinding approval, high level analysis and paper drafting.

Moreover, the experience gained with this event had a strong impact in the data transfer from Namibia to Europe, which was used to be done through hard disks, with important consequences on the delays of beginning of data analysis. This update is crucial in the time-domain astrophysics.

Model constrains from H.E.S.S. observation of GW170817

Theoretical studies have addressed the question of the high-energy emission production from the long-lasting central engine after the coalescence. In the work by Murase et al., 2018, they investigate the GeV-TeV gamma-ray emission that involves a short GRB-like jet, for both on-axis and off-axis observers, under certain assumptions, as a simple top-hat jet model hypothesis.

Inverse Compton radiation processes in afterglow shocks with external photons from the long-lasting jet can produce high energy gamma-rays (Mészáros and Rees, 1993). They consider that in the presence of late prompt emission (extended emission, plateau emission or X-rays) both synchrotron self-Compton and external inverse Compton processes by forward external shock electrons could contribute strongly to the emission. They computed the contribution from the external inverse Compton radiation to the emission, due to the up-scattering of X-ray photons by the relativistic electron in the jet, for different viewing angles and jet opening angles, using a simple top-hat jet model.

In Figure 7.14 and 7.15, we present the results of the simulations obtained by Murase et al., 2018, which have been adapted to include the H.E.S.S. results from GW170817 observations. The derived H.E.S.S. upper limits on the gamma-ray emission are consistent with the off-axis interpretation of a canonical jet observed at a viewing angle which is larger that 15°.

To conclude, their results show that the inverse Compton radiation for a jet seen

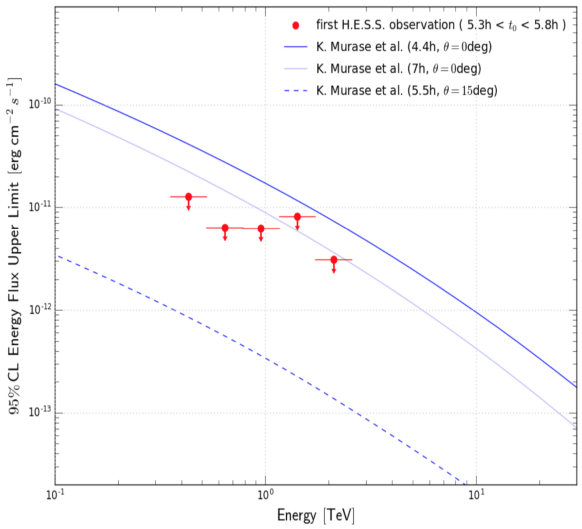

FIGURE 7.14: Gamma-ray spectra generated by external inverse Compton radiation for emission at different times and with the assumption of viewing angle 0° and 15°. The H.E.S.S. upper limits derived for the first observations of SSS17a at 5.3 h< t_0<5.8 h. The distance is set to d = 40 Mpc. Adapted from Murase et al., 2018

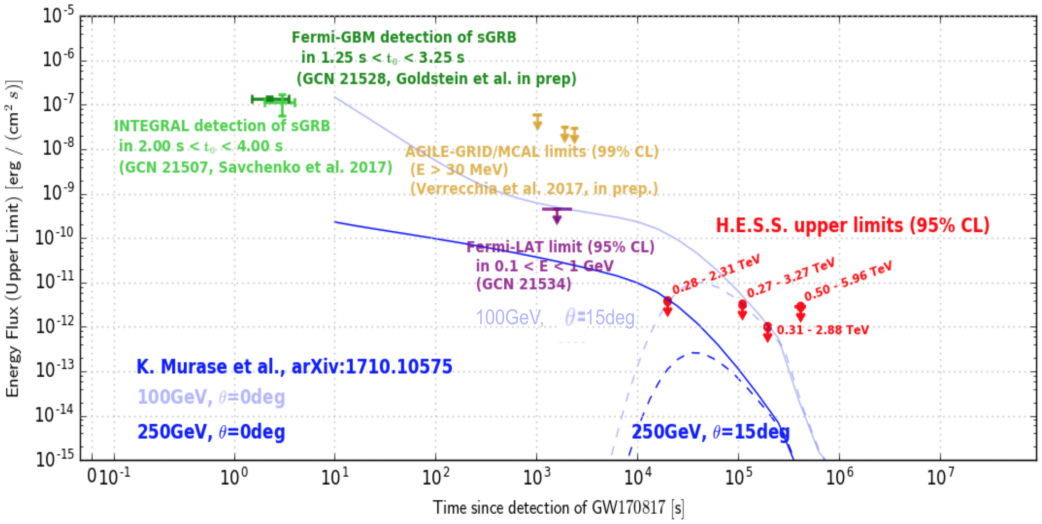

FIGURE 7.15: Light curves of high-energy gamma rays generated by external inverse Compton radiation, for E=100 GeV and E=250 GeV and a distance of d = 40 Mpc. Two viewing angles measured from the jet axis are considered, and a plateau emission (with T_a=10^4s) is assumed as seed photons. Adapted from Murase et al., 2018

on-axis is bright enough to be detectable up to 300 Mpc by current IACTs, Fermi-LAT and HAWC. Also, they conclude that in the case of an off-axis observer at $\theta \sim 10° - 30°$, the duration of the emission is significantly longer, of the order of $t \sim$ 1-10 days. Nevertheless, the study underlines that the expected gamma-ray flux decreases significantly for observing angles larger than the opening angle of the jet.

7.3 GW follow-up observations with H.E.S.S. during O3

The observation run O3 started in April 1, 2019. Several binary black holes have been detected so far, at a rate which matches well the BH-BH expectations of one/week.

The H.E.S.S. experiment has attentively considered all the sent alerts since the beginning of O3. The characteristics of each gravitational wave have been studied and decisions have been taken about starting follow-up observations. A summary of the H.E.S.S. reactions to the detected binary merger coalescences can be found in Table 7.5, where a compilation of some of the key parameters which are considered when considering to do a follow-up are included.

The three main features that were considered when making the decision of triggering a follow-up observation are summed up in the following. First, for the events with large 90% C.R. values, as it is the case for S190425 (NS-NS) or S190426 (BH-NS), the H.E.S.S. FoV coverage do not reach in any case a 5% of the GW confidence regions, so no observation is scheduled in this case, as too many observations will be required to cover a reasonable region of the GW localization. The second most common reason is the delay to find a visibility window for observations being larger than a day, and some times being infinite, for events in the northern sky, as it is the case for S190408. Then, a third reason explaining the choice of no triggering follow-up observations, which only apply to the case of BH-BH, is the *goal* of the observations. A clear example is S190701, for which a nice visibility window was available and a good coverage could be achieved, although there was a delay of $\sim$ hours with respect to merger. The underlying reason is that only a finite number of triggers are granted, and the choice to keep triggers to test a prompt response of the VoAlerter was made. This tests of the VoAlerter serve as a *commisioning* of the alert system to alerts that arrive during the night, and could be crucial to react to NS-NS, BH-NS alerts, in future GW alerts.

7.3.1 BBH follow-up observations during O3

The first gravitational wave event followed-up by the H.E.S.S. collaboration during O3 is a coalescence of binary black holes at a distance of 1331 ± 341 Mpc. The BBH S190512at, which happen on May 12, 2019, was detected by the three interferometers of the GW network, LHV. It presented a FAR of 1 per 16.6 years, and it was relatively well localized, as the 50% containment region expanded over *only* 79 deg^2 (90% C.R.: 399 deg^2), in the prompt reconstruction using BAYESTAR algorithm.

The goal of this type of observations is technical since although no VHE emission is *a priori* expected from BBH mergers, we do trigger on some of these events in order to test the entire alert system. Due to the distance of this event and its nature, the `PGW-in-FoV` algorithm was use to schedule observations. In the night of the May 12, starting at 23h41 UTC, i.e. $\sim$ 5 hours after the merger, eight observations were schedule under very favorable zenith angles, e.g the first scheduled observation presented $\theta_{\mathrm{ZENITH}} < 10^{\circ}$. Nevertheless, technical problems delayed the data acquisition

ID	Time (UTC)	Type	90% C.R.	Δ_t	N_p	P_{GW}	Follow-up
S190408	19-04-08 18:18	BH-BH	387 deg^2	-	-	-	No
S190412	19-04-12 05:31	BH-BH	156 deg^2	$\sim$ 13h	6	66%	No
S190425	19-04-25 08:18	NS-NS	7461deg^2	-	-	-	No
S190426	19-04-26 15:22	NS-NS	1262 deg^2	$\sim$ 6h	9	4 %	No
S190503	19-05-03 18:54	BH-BH	443 deg^2	-	-	-	No
S190512	19-05-12 18:07	BH-BH	339 deg^2	5h30m	9	34%	Yes
S190513	19-05-13 20:54	BH-BH	691deg^2	4h20m	1	9%	No
S190519	19-05-19 15:36	BH-BH	967 deg^2	$>$ days	-	-	No
S190521	19-05-21 03:03	BH-BH	1163 deg^2	$>$ days	-	-	No
S190521-II	19-05-21 07:44	BH-BH	488 deg^2	$>$ days	-	-	No
S190602	19-06-02 18:00	BH-BH	1172 deg^2	$>$ days	-	-	No
S190630	19-06-30 18:52	BH-BH	8493 deg^2	-	-	-	No
S190701	19-07-01 20:33	BH-BH	67 deg^2	6h	3	51%	No
S190706	19-07-06 22:26	BH-BH	1100 deg^2	$>$ days	-	-	No
S190707	19-07-07 09:33	BH-BH	1375 deg^2	15h	-	-	No
S190718	19-07-18 14:35	Terrestrial	7246 deg^2	-	-	-	No
S190720	19-07-20 00:09	BH-BH	1599 deg^2	$>$ days	-	-	No
S190727	19-07-27 06:03	BH-BH	841 deg^2	$>$ days	-	-	No
S190728	19-07-28 06:45	BH-BH	104 deg^2	13h	4	50%	Yes

TABLE 7.5: Summary of the H.E.S.S. reaction to gravitational wave triggers during O3, from April 2019 to July 2019. $\Delta_t \equiv t_{window} - t_{merge}$ refers to the time between the coalescence and the first possible observation, which sometimes is never possible due to the localization in the northern sky (this is represented by -). The `Type` refers to the event classification type which has the highest probability value, although note that sometimes the probability is shared between different type of events. N_p refers to the number of pointings potentially scheduled, the covered probabilities by these *potential* H.E.S.S. observations, P_{GW}, as well as the final decision on scheduling follow-up observation.

by a total of 2 hours, so only four complete observations were finally obtain. These are shown in Figure 7.16.

7.4 Discussion

As seen in this chapter, the codes developed in Chapter 6 have been implemented in the H.E.S.S. VoAlerter system. They are also used offline in order to schedule observations and study the characteristics of each event.

The developed codes have been used to performed follow-up observations during Observation runs O2, where two successful follow-ups were performed. The codes are currently used in O3 observation run by the H.E.S.S. experiment, and the first follow-ups have been performed. Although the first BBH followed up during O3 was meant as *commissioning* observations, H.E.S.S. data is being analyzed and results

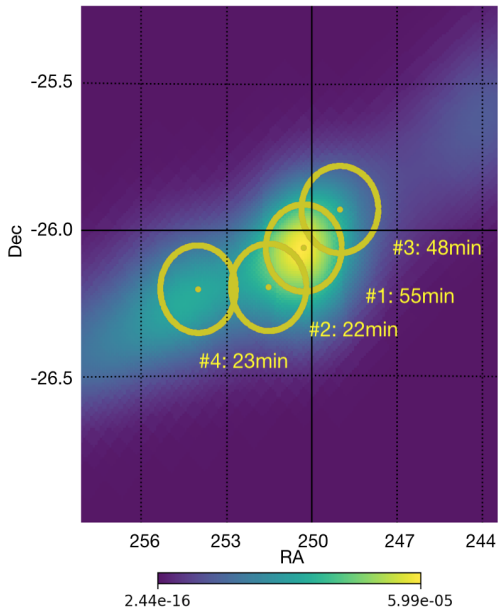

FIGURE 7.16: H.E.S.S. follow-up scheduled observations of the BBH merger S190512, which include four observations of a total time of 148 minutes. The quoted values represent the observation number and the acquisition time per observation.

constraining the nature of the remnant in the observed region at very high energies will be obtain soon.

Chapter 8

GW counterparts searches with the future CTA

Contents

8.1 Science with CTA: Key Science Projects

The scientific focus of the Cherenkov Telescope Array has been addressed and carefully prepared during more than a decade and the product of such effort is summed up in the Key Science Projects (KSPs)(CTA Consortium et al., 2017). These have been established to ensure that the main open science questions in the energies CTA has access to are studied, following a well defined, up-to-date strategy.

Although various different topics are included in the KSPs, they are grouped under three big blocks which are associated to open questions in fundamental physics, astrophysics and particle physics, that they aim to answer. One of this questions is *Understanding the origin and role of Relativistic Cosmic Particles*, where topics related to the study of the sites of high-energy particle acceleration, the mechanisms in place and the role accelerated particles play in feedback on star formation and evolution are tackled. A second big question is about *Probing Extreme Environments* which aims to unveil the physical processes ongoing close to neutron stars and black

holes and the characteristics of relativistic jets, winds and explosions. The third question addressed in the KSPs is related to *Exploring Frontiers of Physics* which includes fundamental questions on the nature of dark matter and its distribution, the quantum gravitational effects that a photon may suffer through its propagation, and the search for axion-like particles.

The study of these questions is planned and proposed in the context of the CTA Consortium, where a Core Program of highly motivated observations have guaranteed time of observations of about 40% to 50% in the first ten years (CTA Consortium et al., 2017). In general the KSPs have been conceived to provide a wide legacy of data for the entire astrophysics and astroparticle community.

A total number of nine KSPs have been defined to address these questions, which are subdivided into galactic and extragalactic physics, shown in Figure 8.1.

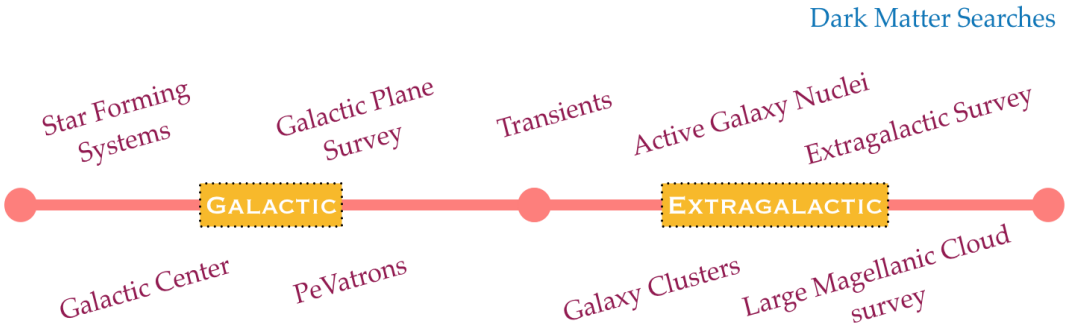

FIGURE 8.1: Illustration of the KSPs (bordeau) divided between galactic and extragalactic. The dark matter program (cyan) is included as it is considered to be part of the science with CTA, but will in principle use data obtained for other KSPs, e.g the LMC survey or the Galactic Center.

The extragalactic KSPs include four different topics, which we briefly discuss in the following:

- **Active Galactic Nuclei**. It includes long-term monitoring of AGNs in order to complement the biased dataset obtained after triggering observations based on MWL data. In addition, deep observations will provide high resolution spectra in a broader energy range and AGN flare programs will react to external triggers. AGN observations aim to answer questions on the very-high-energy emission of AGNs, cosmology using gamma rays, ultra high cosmic rays physics and fundamental physics with Lorentz Invariance Violation (LIV studies).
- **Extragalactic survey**. An unbiased survey of 1/4 of the sky is planned to be performed by CTA, which will enable the discovery of new source in VHE, like the discovery of extreme blazars peaking between hundreds of GeV and TeV energies, and population studies like the construction of an unbiased BL Lac sample in the nearby universe.

- **Galaxy clusters**. Clusters of galaxies are interesting astrophysical objects as they are in the latest and most intense phase of structure formation. Deep observations of these massive gravitationally bound systems aim to detect for the first time the expected diffuse gamma-ray emission, to prove cosmic rays acceleration, propagation and confinement, as well as the magnetic field distribution in clusters.

- **Transients**. The Transients KSP includes the studies of transients of galactic and extragalactic origin. The extragalactic follow-up program includes gamma-ray bursts, gravitational wave counterparts and neutrino counterparts. This KSP will be described in detail in the following section.

For more details on the different Key Science Projects set by CTA, the reader is invited to check CTA Consortium et al., 2017.

8.1.1 Transients KSP in CTA

The Transient KSP includes six classes of targets, all of them associated to cataclysmic events which involve relativistic compact objets at the most extreme physical condition of the Universe, and a seventh case dedicated to an unbiased survey for transients using a divergent pointing of the CTA telescopes.

The aim of the Transient KSP is to answer a plethora of questions including the mechanisms that drive jets and winds around extremely dense objects, or the connection between different messenger which are detected from those sources, e.g. GW-EM connection, the origin of fast radio bursts (FRB) or the discovery of other unknown types of explosive phenomena.

The observations can be triggered by *external* facilities, as it is the case for multi-wavelength and multi-messenger topics. These include GRBs and galactic transients, both triggers based on monitoring facilities, X-ray, optical and radio transients, whose alerts come from *transient factories* with a high rate of detections, high energy neutrino transients, triggered by neutrino telescopes and GW transients, which are based on GW observatories. The later will be discussed and explained in detailed in the next section.

Nevertheless, the transient trigger can also be *internal*. This is the case for serendipitous VHE transients observed via Real-Time Analysis (RTA) during scheduled observations and for the VHE transient surveys, which together with the Extragalactic survey will cover large regions in the sky in order to search for potential discoveries in VHE, non-biased by external facilities.

A preliminary estimate of the time allocated for the different Transient KSPs can be found in Figure 8.1. The quoted values could be subject of significant adjustments due to the latest results on multi-messenger astrophysics and the expected rapid evolution to come in the next years.

		Observation times (h yr^{-1} $site^{-1}$)			
Priority	Target class	Early phase	Years 1–2	Years 3–10	Years 1–10
1	GW transients	20	5	5	
2	HE neutrino transients	20	5	5	
3	Serendipitous VHE transients	100	25	25	
4	GRBs	50	50	50	
5	X-ray/optical/radio transients	50	10	10	
6	Galactic transients	150	30	0(?)	
	Total per site (h yr^{-1} $site^{-1}$)	390	125	95	
	Total both sites (h yr^{-1})	780	250	190	
	Total in different CTA phases (h)	1560	500	1520	2020

TABLE 8.1: Summary of the proposed observation time dedicated to follow-up targets in the context of the Transient KSP. The early phase refers to the period of time prior to array completion, which is expected to last for two years. From CTA Consortium et al., 2017

In the scheme of Key Science Projects of CTA on transients, gravitational wave transients are ranked as one of the highest priority to be studied (Table 8.1). GW follow-up strategies are been discussed in order to put in place a competitive, rapid response to alerts which considers the instrument capabilities and optimizes the source detection probability. In the next Section, an update of the GW follow-up program of CTA will be introduced and discussed in detail.

8.2 A new approach for GW follow-up program with CTA

The capabilities and strategies of CTA to follow-up gravitational waves have been discussed through the last years. Connected to the KSPs, the details of future operation and observation strategies with CTA, which depend of the target of observations, have been defined as *use cases*. Different *use cases* have been produced at all levels of the observatory and have been combined in a high-level layer known as *Top Level Use Cases* (Bulgarelli et al., 2016). These prescriptions, which are based on the experience with current IACTs, discuss in detail the sequence from the reception of the alerts, the reaction of the CTA infrastructure, the data taking and the final physics analyses. Nevertheless, these represent a first approach to the different science cases that can be refined in a case-to-case basis where further decision should be made and some cases require extra feedback from different CTA groups, e.g. Real-Time Analysis (RTA).

GW follow-up strategies previously presented in different works, take into account various considerations. In Bartos et al., 2014 and more recently in Patricelli et al., 2018b, fast, tiling strategies have been proposed based on the LST capabilities. They typically consider that the most efficient way to detect an EM-counterpart is to obtain a grid of pointings with an important overlap, covering the entire GW. Patricelli et al., 2018b includes the proposal to adapt the observation window in case source parameters are *a priori* known. For GRBs these can be the total isotropic prompt

emission energy E_{iso}, defined as the released energy during the prompt phase of the GRB, assuming that the emission is isotropic in all directions, the distance or/and the spectral behaviour.

Connecting previous works with the experience with current IACTs, further updates on the follow-up scheduling can be proposed. Regarding response latency, a low-latency response to GW alerts can be critical which clearly motivates the automation of the reception and scheduling in order to decrease as much as possible the interval between the observation time of the merger by GW detectors and the beginning of observations with CTA. In principle, the number of follow-up candidates will depend on the rate of detection but as a first approach, most of the GW candidates will be followed up, with a focus on BNS. The allocated time per event will be however limited to $T \sim 1000$ seconds per event in the prompt phase. Further constraints on the GW False-Alarm Rate (FAR) will be imposed in the future but depend on the allocated time per observation. Note that multi-messenger detections (GRBs, neutrinos) as well as RTA results would be a reason to modify the schedule and refine the pointing. In that case, deeper observations are envisaged. The strategy to follow-up gravitational wave events with CTA developed in this work, includes the feedback between the Observation Scheduler and the RTA, as illustrated in Figure 8.2.

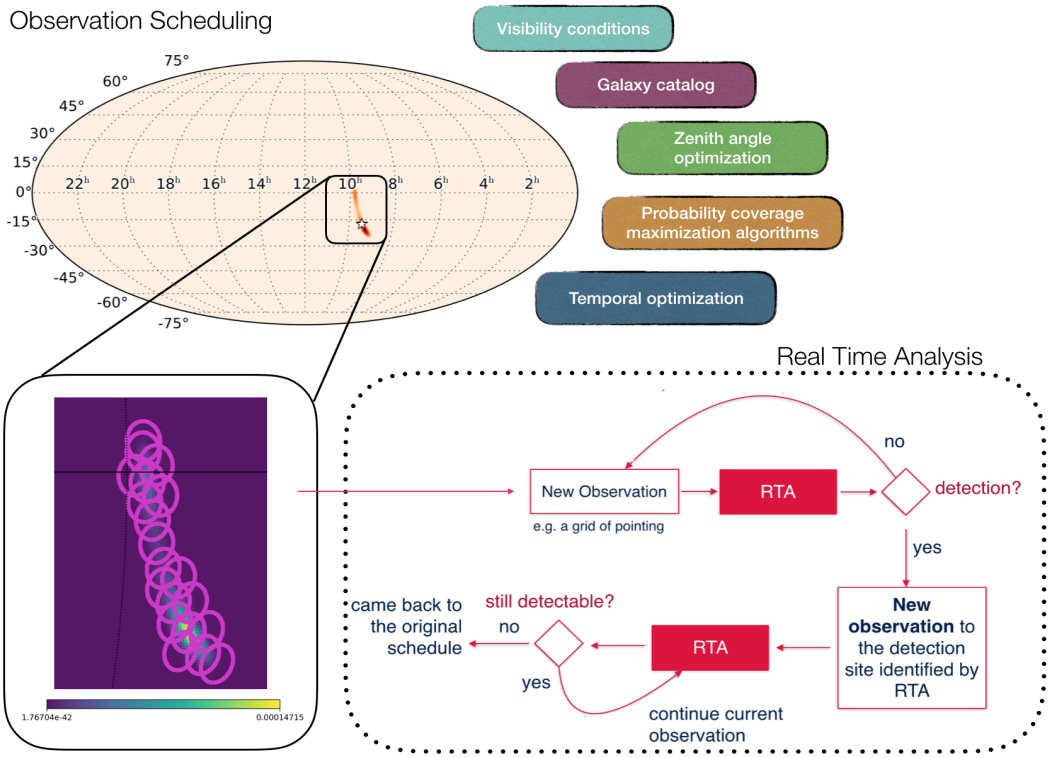

FIGURE 8.2: Illustration of the gravitational waves follow-up program of CTA proposed in this work.

8.2.1 Observation scheduler

The GW alert is received by the alert system, which includes a GW sky localization, which is used to derived the CTA observation scheduling of the event. To this aim, the observation scheduler calculates the visibility window for each of the CTA sites and has the goal of determining the most favorable sky coordinates for the observation.

The GW follow-up algorithms which are considered as a first step for the CTA follow-up strategy are explained in detail in Chapter 6. These algorithms include zenith angle optimization, maximization of the probability coverage, consider visibility conditions and the use of galaxy catalogs in case it is possible. They have been adapted to CTA characteristics by including the two sites and the dynamic time windows, following the scheme proposed in Patricelli et al., 2018b. In this way, the observation scheduling optimizes the observation in three axes: energy, probability coverage and time.

The motivation of the temporal optimization is to look for a good compromise between the minimum time needed to detect a transient, evolving source and the need to scan the largest possible GW localization region. In particular, the sensitivity of the LSTs, where a source detection can be made in much smaller time window than current instruments like H.E.S.S. (see Chapter 2), allow to scan the extended region much faster than what it is possible with today's IACTs capabilities.

For this reason, a temporal optimization is included in our algorithms, which is based on the prior knowledge of the evolving transient parameters: the source emits an isotropic energy E_{iso}, presents certain spectral behavior, and the flux in a given band can be expressed as $F(t_0, t)$. The source would be detected if the observation time is larger than the time required to obtain a 5 σ *post-trials* detection at the sensitivity that has been quoted for certain observation conditions and a flux. This means that we chose T_{obs} so that the following condition is fulfilled:

$$\int_{t_0}^{t_0+T_{obs}} \frac{dF(t)}{dt} dt \geq F_{5\sigma}^{int}(t_0, t_0 + T_{obs}) \tag{8.1}$$

This gives us a set of observing times T_{obs} which become larger as the $t - t_{merger}$ becomes larger, since the lightcurve evolution of the source decays with time, until the moment when $T_{obs} \rightarrow$ inf and a 5 σ detection is no longer possible. In order to derive these observation windows, the IRF for the observation site and zenith angle observation are used. Moreover, a total number of 10 background gamma-rays need to be detected as a minimum requirement to be able to analyze the acquired data.

The resulting algorithms used in Section 8.4.1 are optimized to cover large probability regions, where the exposure per observation is optimized, and where lower energy thresholds are prioritized. They have been used to derive pointing schedule for gravitational wave follow-up of the simulated events.

8.2.2 Real-Time Analysis

The Real Time Analysis science alert system, explained in Chapter 2 is a crucial part of the gravitational wave follow-up program. Each observation is analyzed in real-time by the RTA pipeline, which is able to detect sub-minute emission, trigger deeper observations on the region to asses the detection of the potential EM counterpart and issue science alerts at low latencies below 30 seconds to external observatories (Fioretti et al., 2015).

Coupling the RTA to the Observations Scheduling will enable the processing of the acquired data in real time and the modification of the follow-up strategy on the fly. In this way, the observation of an *interesting* excess compatible with the detection of the EM counterpart will be a reason to modify the schedule, and perform deeper observation. Nevertheless, if these deeper observations proves that the potential detection is indeed a background fluctuation, observations will continue following the GW observation scheduler.

In order to asses the proposed strategy for the GW-follow up program with CTA and with the goal of deriving GW-EM detection rates with CTA at VHE following this approach, a set of simulated GW-EM events have been obtained which will be used as an input of the simulation chain. They are described in the following.

8.3 Ingredients to simulate GW follow-ups with CTA

8.3.1 Simulation of a Neutron Star Merger and GRB emission

For this study, simulation of neutron star merger and the associated electromagnetic emission are considered. They reproduce the whole evolution of the two neutron stars: from the inspiral phase to the GRB VHE emission. The gravitational wave and electromagnetic counterparts properties are linked: distances, opening angles, viewing angles, which impact detection by the GW interferometers and the VHE instruments. This connection has been considered to produce a coherent sample of GW-EM simulations.

`GWCOSMoS`: Gravitational wave simulation bank

For the simulated merging compact binary systems and the associated gravitational wave detection and sky localisation with the Advanced LIGO-Advanced Virgo interferometers, a public simulation database known as the Gravitational Wave COmpact binary SysteM Simulations (GW COSMoS,Patricelli et al., 2018a) has been chosen. These have been produced by a dedicated Monte Carlo. To obtain the neutron star mergers, distribution of galaxies have been simulated for distances smaller that 500 Mpc, consistent with the expectations for Advanced Virgo and Advanced LIGO in their final configuration. This database consists of a realistic ensemble of BNS merging systems evenly distributed in the local universe accordingly to a merger rate of

830 $\mathrm{Gpc}^{-3}\mathrm{yr}^{-1}$, that is within the range estimated after the detection of GW170817 (Abbott et al., 2017a). The galaxies are populated by binary neutron star mergers randomly, following phenomenological BNS population rates. Then, the inspiral phase, the BNS merger, the emission of gravitational waves and the detection by gravitational wave interferometers are simulated.

Different interferometer configuration have been considered for the detection, based on duty cycle expectations, set to 80% for each independent interferometer. The gravitational signals from the merger are simulated using `TaylorT4` waveforms (Buonanno et al., 2009) which is a post-Newtonian template family that includes approximations of waveforms in time-domain. They are later convolved with the GW detector response functions. These simulations have been then analyzed using matched filtering technique as it is commonly done in GW interferometers (see Chapter 4). The output parameters of this detection pipeline are then used to compute the source localization using the rapid position reconstruction algorithm BAYESTAR (Singer and Price, 2016). The sky localization reconstruction yields to a 2D posterior probability distribution in the sky, given in FITS format.

In the `GWCOSMoS` template bank, each neutron star merger is linked to a simulated galaxy distribution. These galaxy distributions can be used to derive a follow-up of gravitational wave events by considering a 3D-approach. Nevertheless, the localization for the neutron star merger events does not include estimates on the distance of the event but instead only the posterior probability distribution p_{GW} is available. Also, the galaxies have been distributed uniformly in the considered volume, thus reducing the effectiveness of the galaxy targeting approach which is benefitting from the inhomogeneities in the cosmological matter distribution. For this reason, a different approach is taken here in order to obtain a convoluted probability using galaxy catalogs.

In order to use the galaxy catalogs associated to the `GWCOSMoS` simulations, the distance estimated in the gravitational wave source localization is to set as a constraint in order to select galaxies within a range. Then, one associates to each of the remaining galaxies the value ρ_i corresponding to the galaxy coordinates, following:

$$f_d(\mathrm{RA},\mathrm{Dec}) = \begin{cases} \frac{\mathrm{prob(RA,Dec)}}{\int \mathrm{prob(RA}_i,\mathrm{Dec}_i)} & if \quad d_{min} < d < d_{max} \\ 0 & else \end{cases} \tag{8.2}$$

8.3.2 Quantifying systematics of the `GWCOSMoS` bank of simulations

Location systematics of the `GWCOSMoS` bank of simulations

In an initial analysis of the GW `GWCOSMoS` simulations, I studied the correspondence between the location of the injected merger and the 2D GW localization map reconstructed by BAYESTAR. We use the *cumulative density function* (CDF) defined as the probability that X takes a value less than or equal to x. In the case of the case of a continuous variable X, the CDF is expressed as the integral of its probability

density function f_X, as:

$$\mathrm{CDF_X}(x) = P(X \leq x) = \int_{-\infty}^{x} f_\mathrm{X}(t)dt \tag{8.3}$$

The statistic is applied to the posterior probability distribution of the localization of the gravitational wave. For each pixel, we compute the value $1-CDF(\rho_{pix})$, which represents the probability that ρ takes higher values than ρ_{pix}. If one computes this quantity for the pixel corresponding to the coordinates of the NS-NS merger injection, the $1-CDF(\rho_{pix})$ value of the NS-NS injection coordinates gives an idea of the *ranking* of the source location with respect to the distribution of the ρ. By definition of the localization probability regions of a gravitational wave localization, the output distribution of the $1-CDF(\rho_{source})$ for a set of sky localizations should follow a straight line with slope equal to 1.

We compare the distributions obtained for `GWCOSMoS` and a set of sky localizations which have been shared by LIGO-Virgo previous to the O2 run, in the context of the article *Going the Distance* (GtD) (Singer et al., 2016a). Results are shown in Figure 8.3, where in the left figure, the values for a single GW event are shown. The cross marker correspond to the $1-CDF(\rho_{source})$ value in the $1-CDF(\rho_{pix})$ distribution.

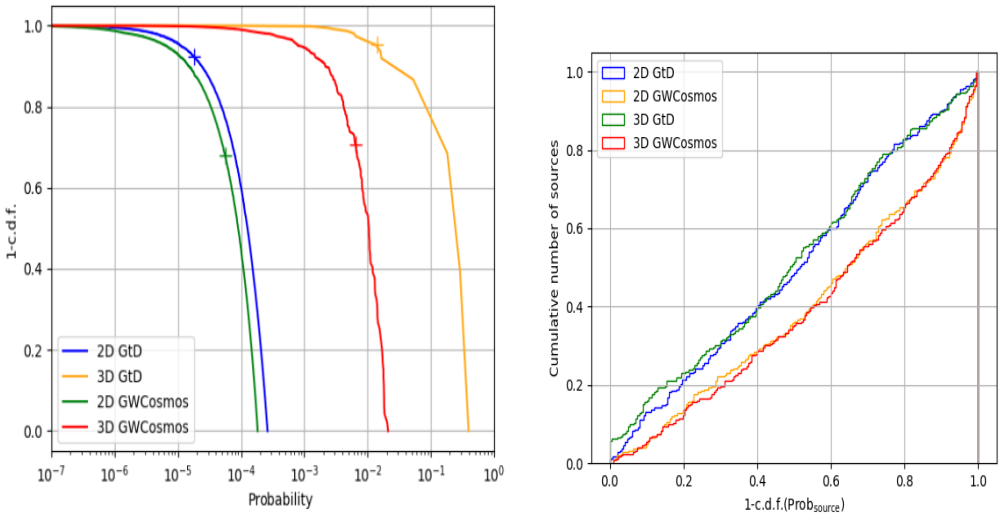

FIGURE 8.3: (Left)1-CDF function for a given set of probabilities for the gravitational wave localization region and for the galaxy catalog convolved probability distribution, for the GtD dataset and the `GWCOSMoS`. The crosses represent the value for the source linked to the sky localization given as input.(Right) Distribution of $1-CDF(\rho_{pix})$ values for a subset of $\sim$ 250 GW sky localizations for the GtD and `GWCOSMoS` dataset, for the 2D and 3D probabilities

It can be observed that for the `GWCOSMoS` bank of templates, the distribution does not completely follow the behaviour expected for events reconstructed by the BAYESTAR algorithm. A shift is observed to higher values, which means that the reconstructed localization area is shifted with respect to the injected position of the

source to regions with lower probabilities. This may bias our performance results when searching for the source in simulated follow-ups. In particular, this systematic error which appears in the GWCOSMoS simulation bank will impact the rate of joint GW-EM, causing the number to be extremely conservative. Note that in the case of the *Going the Distance* bank template, the $1 - CDF(\rho_{pix})$ distribution follows our expectations.

Comparison of NS-NS location and highest posterior probability pixel

Further studies using the GWCOSMoS simulations have been performed on the true location of the neutron star merger injected compared to the highest probability pixel of the reconstructed GW sky map. The angular distance between these two coordinates has been quantified for ∼10.000 reconstructed gravitational wave skymaps.

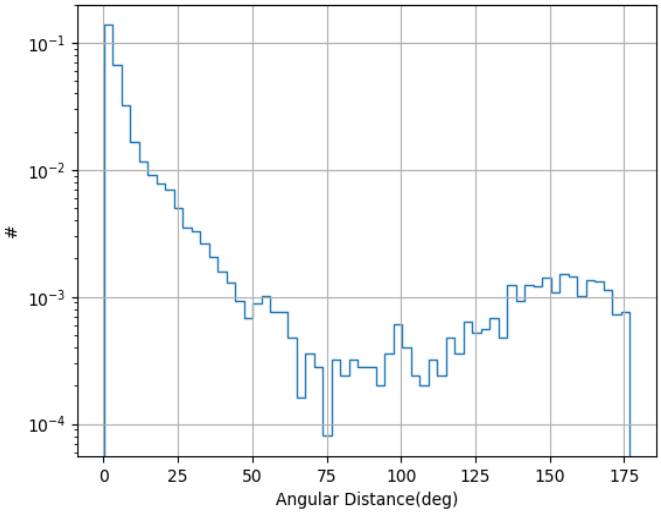

FIGURE 8.4: Angular distance between the highest probability pixel of the sky localization region and the real position of the injected source for the GWCOSMoS simulation bank

The angular distance results obtained are shown in Figure 8.4, where two different populations can be identify. In the right side, the case corresponds to sources that have been reconstructed in a way that there are two opposite probability localization *lobes*, with the source and the highest probability coordinates being opposed. This accounts for the the high values of the angular distance, reaching 175°. In contrast, in the left side of the distribution towards lower values of the angular distance, we observe the cases where the highest probability coordinates of the reconstructed GW area is slightly shifted, but still in the same region than the NS-NS injection location.

This means that there is a non-negligible number of times where follow-up observers are limited by the effects from the gravitational wave reconstruction. This situation clearly encourages interaction and complementary approaches between northern and southern observatories, which could be driven by a network as it is the case in VHE-instruments by CTA North and CTA South, or HAWC and SGSO.

Study of the impact of galaxy catalog convolution in the classification of candidate locations

In order to study the power of galaxy catalogs to guide follow-up observations, one needs to study how the NS-NS merger localization is improved. Nevertheless, since only one GW event has been detected so far from a NS-NS mergers events, a complementary study has been performed. In this section, we show the effect of isotropic distribution of galaxies in 3D follow-up observations as well as the use of galaxy catalogs in the case where the NS-NS is not spatially connected to any of the galaxies.

In order to quantify the effect of including galaxy catalogs, the procedure explained in the previous section is followed, and 1-CDF values are obtained for each of the events in the `GWCOSMoS` template bank, with and without using using the corresponding galaxy catalog. Results are shown in right part of Figure 8.3. The observed behaviour indicates that, as expected, using isotropic galaxy catalogs does not improve the ranking of the source with respect at the cumulative density function level.

For the sake of completeness, the Going the Distance NSM bank template has been convolved with the Glade catalog to see how using a non-isotropic, incomplete galaxy catalog affects the ranking of the source at the CDF level. Due to the isotropic, random localization of the NSM events of the GtD database, which are non associated with any galaxy, again no major effect is observed. This means that even if a BNS source can not be associated with any galaxy included in a galaxy catalog, which can be linked to the incompleteness of some galaxy catalogs, we can say that, in average this will not have a major influence at the 1-CDF level, and thus, ranking with respect to other possible locations included in the reconstructed sky map.

8.3.3 EM counterpart of the BNS merger in `GWCOSMoS`

The simulated BNS in the `GWCOSMoS` database are associated with a short GRB. In previous work (Patricelli et al., 2018b), the source has been described by an isotropic energy E_{iso} and the spectral behaviour is assumed to follow a power-law with an exponential cut-off $E^{-\alpha}\exp(-E/E_c)$. The GRB 090510 detected by *Fermi*-LAT (Ackermann et al., 2010) was used as a template, due to the high energy up to 30 GeVs and extended emission, up to 200 s. The extrapolation to higher energies is done through a power-law with exponential cut-off, which comes from the consideration that if the emission is synchrotron in origin, a cut-off is expected for those energies (Patricelli et al., 2018b).

A purely phenomenological approach based on observations of GRBs at GeV energies is considered here, mainly based on Fermi-LAT observations. The distance and angle with respect to the line of sight are known for each event in the mock catalog of BNS mergers `GWCOSMoS`. To model the very high-energy emission, an association is made for each event with an isotropic energy E_{iso}. This association consists on randomly extracting values from the intrinsic distribution inferred for short GRBs in Ghirlanda et al., 2016.

The 0.1-10 GeV luminosity as a function of time is derived based on the typical properties of LAT GRBs, and in particular of the short event GRB 090510. During the initial phase of the afterglow emission (before deceleration) the flux is assumed to be proportional to t^2 (as expected for homogeneous medium); the afterglow onset is fixed at $t_{peak} = 3$ s; during the deceleration phase the luminosity decreases as $t^{-1.4}$. The lightcurve is normalized following the correlation found in Nava et al., 2014 between E_{iso} and $L_{\rm LAT}^{\rm t=60s}$. For the spectral shape we consider a simple power-law with photon index -2.1 ($\mathrm{d}N_E/\mathrm{d}E \propto E^{-2.1}$) matching the *Fermi*-LAT measurement of GRB 090510 and normalization derived from the integrated luminosity 0.1-10 GeV. The spectrum is extrapolated up to 10 TeV.

The lightcurves and spectra generated using this method refer to emission detected on-axis. Based on these results, we consider the viewing angle θ_{view} and apply a correction assuming a homogeneous jet, with jet opening angle of 5 degrees. Following the prescription given in Granot et al., 2002, two overall regimes are defined: on-axis emission and off-axis emission.

The simulated spectrum of the remnant is corrected in order to take into account EBL attenuation with redshift, even though the effect is small at the expected distances at design sensitivity that were used for the `GWCOSMoS` simulations (< 500 Mpc).

8.3.4 Simulating GRBs and their detection with `Gammapy`

If the GW uncertainty region is visible and observable from either (or both) CTA sites, we proceed with the simulation of the observations which would be performed by CTA. In this work, the open access `Gammapy` tools, introduced in Chapter 2, are used to simulate and analyze the corresponding CTA observations.

In order to simulate the CTA observations, we use the `gammapy.maps` module which allows to store images cubes with an arbitrary number of non-spatial dimensions. Whereas the first two dimensions are spatial and correspond to the source model, the selected non-spatial dimensions for the cubes are time and energy. A full observation will be represented by several 4D hypercube of simulated data, including counts, background and exposure.

The performance of the CTA instrument is described by the Instrument Response Functions (IRFs) obtained from detailed Monte Carlo simulations as explained in Chapter 2. The IRFs include information about the effective area, the point spread

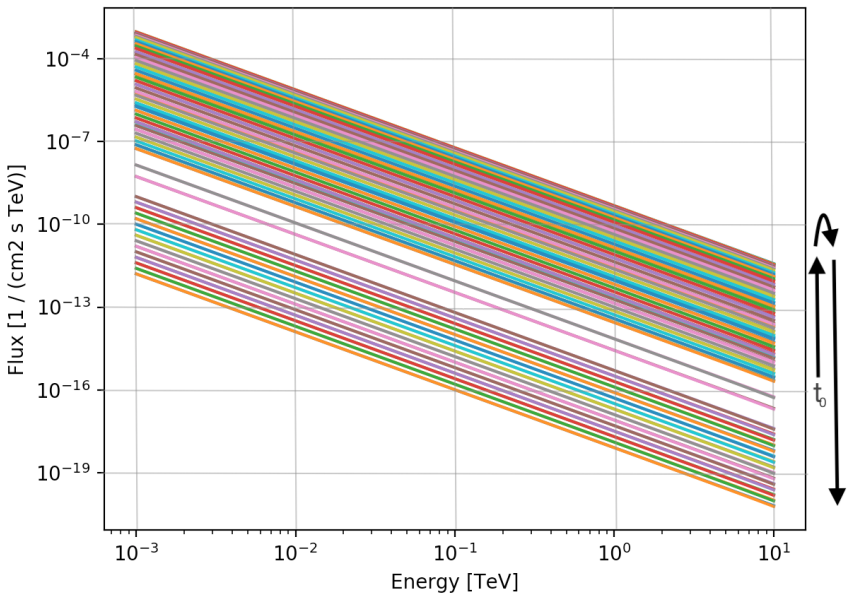

FIGURE 8.5: Simulated on-axis emission of a GRB associated with a BNS merger obtained as detailed in the text, which includes 71 different epochs of the source evolution. As it can be appreciated, the simulations consider no spectral change as function of time

function, the energy dispersion and the background, and are quoted for a given site, zenith angle, night sky background and observation time. The IRFs are used in order to extract the background and exposure maps for a given lifetime and pointing coordinates. Then, the point spread function is obtained for a given field of view offset and the energy dispersion is derived from a given offset and energies.

The source is defined by a *spatial* model and a *spectral* model, which together build the *sky* model for the given source. For each observation we integrate the flux for each epoch of the GRB emission in order to obtain the total flux observed. Then, the 3D skymodel for a source is evaluated and convolved with the IRFs, returning a map with the predicted number of counts. In order to reproduce the Poisson regime expected for background counts, the final number of counts is obtained by drawing samples from a Poisson distribution, where a minimum requirement of 10 background photons in order to be able to properly analyze the observations is considered. The resulting counts from the simulation of one of the GRBs, for an observation of T_{obs}=2 s in a given GW follow-up observation can be found in the left side of Figure 8.6

Analysis of simulated GW follow-up observations

The chosen method to analyze the data is the Test-Statistic (TS) analysis. The TS map is computed by a single parameter amplitude fit, which finds the roots of the

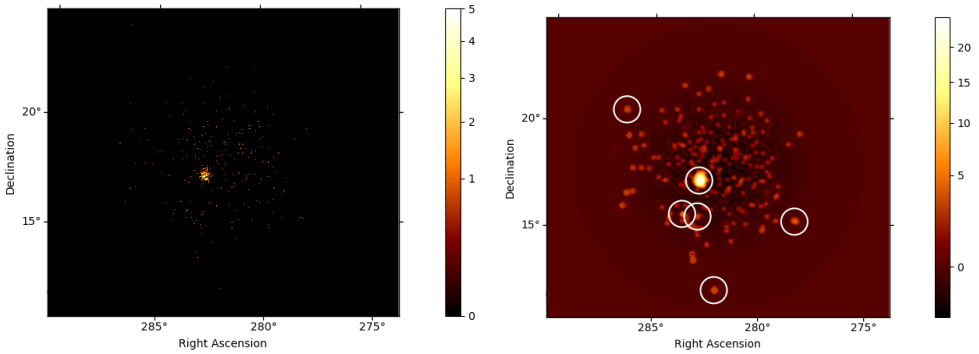

FIGURE 8.6: (Left) Simulated counts for a GW follow-up observation which contains the associated simulated GRB source with T_{obs}=2 s (Right) Test-Statistic analysis of the simulated follow-up observation containing the GRB source. White circles represent the hotspots found above $3\,\sigma$, and the GRB is detected at $20\,\sigma$. Both Figures have been obtained using `Gammapy`.

derivatives of the fit statistics, following Stewart, 2009.

The possibility to derive TS maps in various time bins have been considered. In this scenario, `Gammapy` allows to create 5D hypercubes, where the non-spatial axis are Time, Energy, and Test-Statistics. This option has been considered although it requires some further development of the `Gammapy` analysis framework.

In Figure 8.6, one of the GRBs of the template of simulations has been simulated for an observation time of 2 seconds, and analysed using the TS analysis. The TS analysis has been performed using the `TSMapEstimator` function, considering a 2D-Gaussian kernel of 1.5°. The excess is observed at more than $20\,\sigma$. Further *hot spots* are observed at $\sim 3\,\sigma$, which correspond to expected fluctuations of the background due to the small lifetimes of the simulation.

8.4 Simulating electromagnetic counterpart detection of GW follow-up with CTA

The simulation steps needed to study the performance of GW follow-ups with CTA are:

1. **Alert injection and GW follow-up observation scheduling**. The gravitational wave is injected in the follow-up pipeline at a random time. The choice of the CTA site which will follow-up the event is done based on the declination of the BNS associated to the GW uncertainty region. The set of observation windows are obtained by taking into account the latency time for the alert reception T_{alert} which is set to $\sim$ 3 minutes, the initial slewing time of the telescopes T_{slew}, estimated to be $T_{slew} \simeq 30$ seconds and the observation times derived as explained in previous sections. Hence, each observation window T_j is given by:

$$T_j = T_{alert} + T_{slew} + \sum_{1}^{j-1} T^j_{obs}. \tag{8.4}$$

The maximum observation time is set to $T_{\rm MAX}$=10^4 seconds and whenever the detection is not possible for a $T_j > T_{\rm MAX}$, no observation is scheduled. For the computation of T^j_{obs}, the CTA-site which has been chosen to follow-up the gravitational wave event and the mean zenith angle of the observations are considered in order to select the corresponding IRFs.

2. **CTA observation: searching for an EM counterpart**. The evolution of GRB emission which is linked to the injected gravitational wave, is considered and integrated for each of the derived observational windows. The obtained simulated gamma-ray dataset is subsequently analyzed.

3. **Analysis of the CTA scheduled observations** The observations are analyzed in a run-by-run basis, in order to mimic a real-time response. A TS analysis example on a CTA observation considering a Field of View (FoV), FoV=2.5°, corresponding to the LST FoV in the CTA array design when acceptance is at 50% is shown in Figure 8.7. Note that this consideration is conservative as larger FoV telescopes, i.e. MSTs, are expected to be part of the observations.

4. **Sensitivity of CTA to gravitational wave follow-ups** As a final result of the simulations, rates for detections of very high energy gamma-rays in GW follow-ups with CTA, are given, as well as the dependency of those rates with the characteristics of the input parameters of the GW-EM simulations, e.g. the 90% containment region (CR) of the GW localization uncertainty or the GRB luminosity,

In order to illustrate the results of a follow-up simulation of an injected gravitational wave, in Figure 8.7 the resulting six scheduled observations obtained with the Observation Scheduler developed within this work and the simulated gamma-ray counts. In the second observation in descending order the source has been covered. Due to the large luminosity of the GRB, the event can be observed by eye in the counts map in Figure 8.7.

8.4.1 Studies on detectability of on-axis emission from neutron star mergers with CTA

A first study of the sensitivity of CTA to GW counterpart searches and the detectability of an EM counterpart in VHE gamma rays has been performed by considering a subpopulation of events defined by selecting *on-axis* BNS mergers of the `GWCOSMoS` dataset. Then, a further selection is applied on the injection time of the merger based on the visibility conditions, so that the injected time is convenient for CTA observatories.

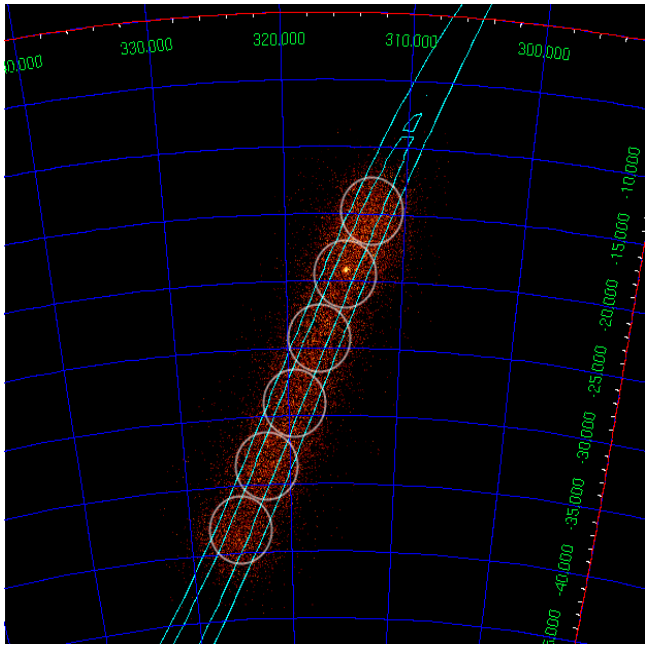

FIGURE 8.7: Simulated counts for a gravitational wave follow-up where 6 observations of 15 seconds have been taken assuming a conservative FoV=2.5 °(white) which corresponds to the $\mathrm{FoV_{LST}}$ in the CTA array design. Cyan contours illustrate the localization uncertainty of the injected gravitational wave.

Selection of on-axis NS-NS/GRB events

The procedure used in order to obtain a sub-dataset which fulfills the two mentioned conditions is the following:

1. The selection of on-axis events, which is based on the consideration of events whose viewing angle is smaller than the opening angle of the jet, set to $\theta < 5°$, results on a reduction of the number of events in the `GWCOSMoS` sample to around $\sim$1.3%.

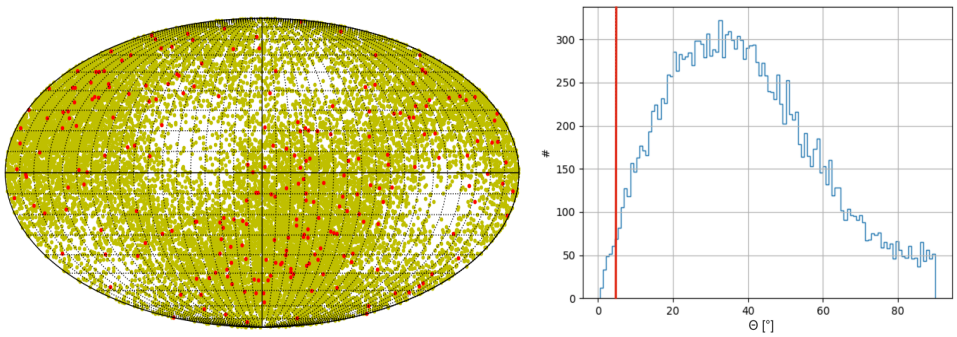

FIGURE 8.8: (Left) Location of the simulated neutron start mergers in the `GWCOSMoS` dataset whose emission is observed *on-axis* from Earth. (Right) Inclination angle of the BNS in the `GWCOSMoS` dataset, where the red line represents the *on-axis* set to $\theta < 5°$.

2. Random injection times are obtained with *good* visibility conditions. These times are found by first selecting the CTA-site which will follow-up the event, which depends on which hemisphere the most of the GW localization uncertainty is localized. Afterwards, a set of times through an entire year are produced. Constraints on darkness and a minimum value to the altitudes of the GW are applied to the set of times, and one of the times with *good* visibility conditions is randomly selected.

3. Once the injection time is obtained, zenith angle is binned into two values, 20° or 40°, in order to select the IRFs in later steps of the simulation. The bins are defined as 20° IRFs for angles up to 30°, and for the range 30°-50° the 40° IRFs.

First detectability studies of EM counterparts in GW follow-ups of on-axis NS-NS/GRB events

A search for observation windows is performed, considering a temporal optimization where the maximum time is set to the time when a 5 σ (post-trials) detection is achieved. This search has been performed for each of the selected on-axis events. As a result, we obtain the number of the scheduled observation windows and the duration of each of them, with a maximum observation time set to $T_{\rm MAX}$=10^4 s. Note that in several cases, no observation window has been found where the GRB signal is detected at the mentioned threshold. From the simulations presented here, we quantify this scenario to occur in ∼15% of the GW follow-up whose GRB emission is observed on-axis, and corresponds to values for the isotropic energy below $E_{iso} \sim 8 \cdot 10^{48}$ ergs.

In Figure 8.9 we can observe the dependency of the number of scheduled observations with the luminosity of the GRB. Note that we have only included the events for which observation windows are found.

We observe that there is a linear dependency between these parameters, which saturates around $E_{iso} \sim 10^{51-52}$ ergs where the number of scheduled windows reaches it maximum $N_{PotWind} = 10^4$ as the minimum duration of an observation is T_{obs} =1 second for $T_{\rm MAX}$=10^4 seconds. The upper and lower value for a given luminosity range are explained by the fact that these values have been computed for different observation conditions, including different sites and zenith angles.

Using the obtained observations times, the coordinates of the follow-up observations are computed, as described in Section 8.2.1, using the `PGW-in-FoV` algorithm and `PGal-in-FoV` algorithm, presented in Chapter 5. The first thing that was noticed is that no significant improvement can be determined when using `PGal-in-FoV` algorithm, due to the low number of events of the dataset but also due to the sensitivity of LST which enables a large uncertainty region coverage in general, which in some cases reached $N_{windows} \sim 10^4$. In this sense, any preference for either of the algorithms is considered a *fluctuation* rather than an *evidence*. For this reason, only the results obtained using the `PGW-in-FoV` algorithm to schedule observations will be discussed in the following.

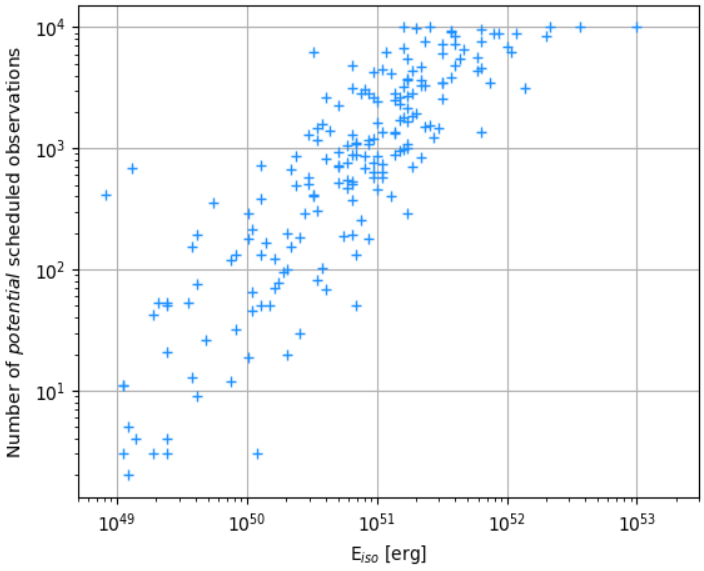

FIGURE 8.9: Number of *potential* observation windows with respect to the E_{iso} obtained from the temporal optimization explained in the text with a maximum value for the entire observation window of $T_{\rm MAX}$=10^4.

Once the GW follow-up scheduled observations are obtained, we check whether the source has been covered by the observations. For this set of simulations, the BNS-GRB source is covered in 75 % of the cases (including the cases where no observations have been scheduled, which represent 15%). For those events, we obtained the number of observation when the source is covered and study the dependency on the 90% confidence region of the GW localization. The number of pointing when the source is found, as well as the median value and standard deviation for the 90% C.R. in decade bins, are shown in Figure 8.10.

The crucial impact that the size of the GW localization region has when scheduling GW follow-up observations is observed. We find that due to the fact that the FoV$_{LST}$ $\sim 2.5°$ (quoted for acceptance value at 50%), the covered area per observations is $A_{obs} \sim 20$ deg^2, so the source is covered in few observations below 90% C.R ~ 100 deg^2. Nevertheless, the decadal bin centered in 90% C.R ~ 1000 deg^2 shows a large standard deviation. This means that there are important variations of the number of observations needed to cover the source from case to case in this bin and although the median value is rather low, ~ 10 observations, in extreme cases this quantity can be up to ~ 4 times the median value.

The aim of this first study on the detectability of EM counterparts from GW follow-ups on a subset of *on-axis* events for which a *good* visibility window has been obtained *a priori* is not to derive *overall* detection rates of joint GW-EM detections using CTA, which would need to broaden the set of injected GW and times, and further considerations regarding the complementary between CTA sites. However,

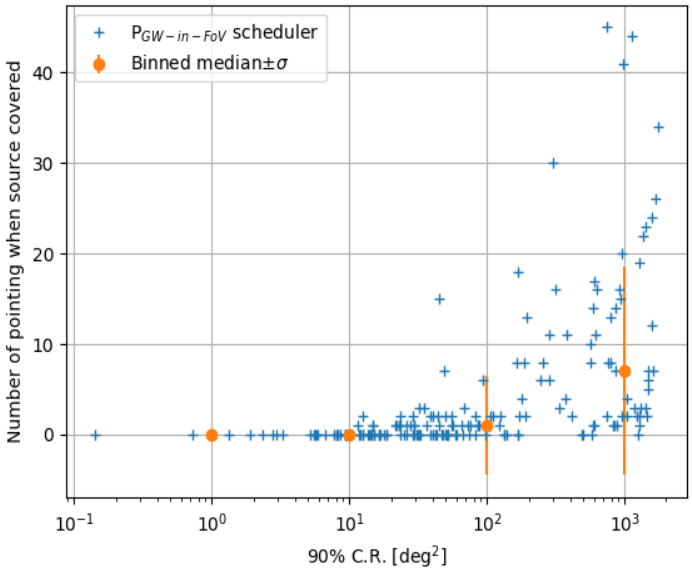

FIGURE 8.10: Number of CTA pointing/observation when the NS-NS/EM source is covered with respect to the 90% confidence region of the GW localization for each of the GWCOSMoS events (blue). The median value and standard deviation of the number of CTA pointing/observation when the NS-NS/EM source is covered, in decade bins of 90% C.R. (orange)

conclusions from these first results can be already derived.

Due to the method used to compute observation times, we consider that the percentage of *covered* NS-NS/GRB events also represent the percentage of *detections* of EM-counterparts. The percentage of expected joint NS-NS/GRB *detections* in decade bins in isotropic energy E_{iso} obtained in this study is shown in Figure 8.11.

It can be observed that the GW-EM detectability rises with E_{iso} and above a certain value of $E_{iso} \sim 10^{50}$ ergs, the detection rate is above 80% and grows smoothly until it reaches a value of 100% for the highest E_{iso} of the GRB sample. Nevertheless, for low values of E_{iso}, the fraction of joint detections is null, which is already seen at the level of the time duration computation of each window, which is larger that the total time allocated for each GW follow-up.

The study of on-axis GW-EM simulations correspond to a $\sim 1\%$ of the entire GW-EM GWCOSMoS database, and the *good* visibility conditions correspond in IACTs to $\sim$ 15% of the time for each observation site, which is the typical duty cycle of IACTs, if neither twilight nor moonlight observation are considered. Hence, the results of this first study, which serves as a proof-of-concept study for the future *complete* results of the entire dataset of EM-GW simulations, should be scaled by those two factors.

Another result that can be derived from this study is related to the strategy

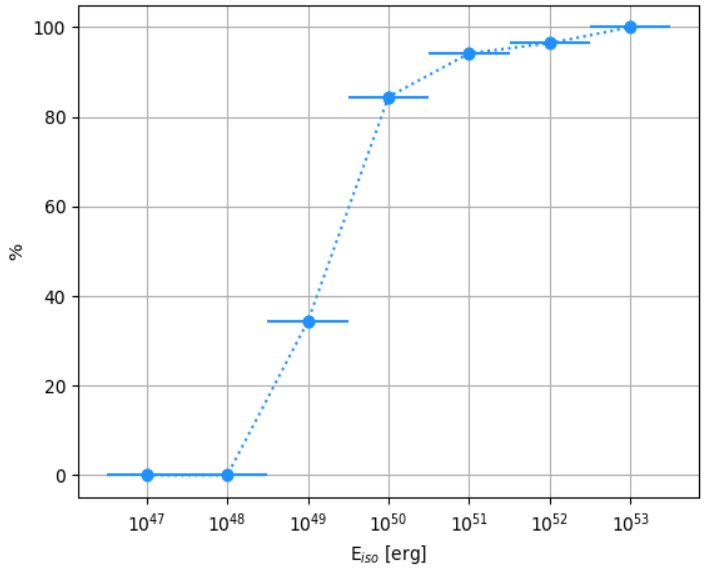

FIGURE 8.11: Number of joint GW-EM detections of the subset of on-axis GRBs for which a *good* visibility window has been obtained, in percentage units, with respect to the isotropic energy E_{iso} of the GRB, in decade bins.

that is in preparation for the CTA follow-up observations. In the case that during a GW follow-up observation scheduling where none of these parameters are known, the computation of the optimum observation time per window for such GRB will not be possible.

A *plausible* solution would be to derive an *a priori* optimum observation time in which a good compromise between the risk of *failures* and *detections* rates is found. The value that maximizes our chances would be found in the parameter space between allocated time per pointing/number of allocated pointings and rate of detections. One can study the distribution of the observation times in each of the considered windows, independently of the luminosity of the GRB, and derive conclusions from it. One can obtain the maximum, medium and mean values of the window, and based on this information, perform the selection of an optimum window that maximize the chances to detect the EM signal. The interpretations of the results derived for the entire dataset of *on-axis* GRBs give us hints on the timescales we should consider *in average*.

Note that once we have understood the deviations that appear from considering isotropic luminosities in the range $E_{iso} \sim 10^{47} - 10^{53}$ ergs, another possible, more straightforward approach to the computation of time windows would be to consider an average GRB of the sample and derive the time windows.

In Figure 8.12, we present the relationship between the number of *potential* observation and the maximum, the mean and the median time duration of each of the observations.

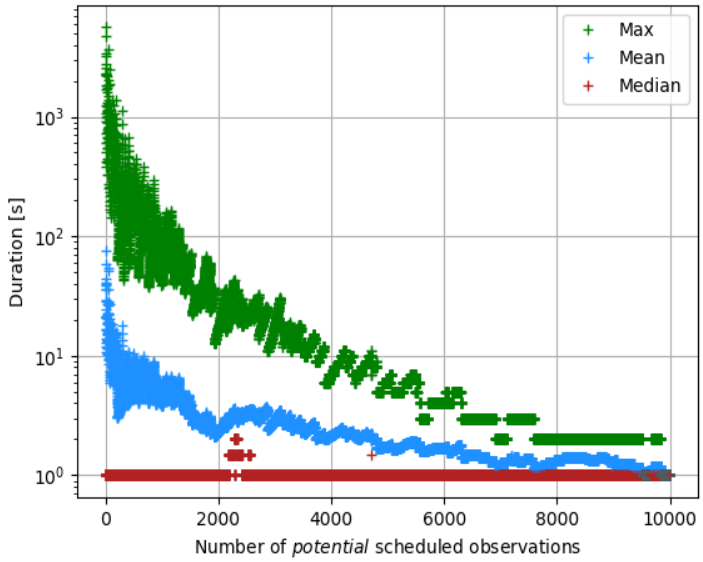

FIGURE 8.12: Mean (blue) and median (red) values of the duration of the *potential* observation windows with respect to the observation.

While the maximum-value distribution shows large values of observation time in the first scheduled pointings, the median value of each observation window shows that the distribution of the observation window duration is dominated by low values of T_{obs} ∼1 second. Moreover, the median distribution also shows that the scheduling of observations for such short values will be dominated by T_{slew} from one position to the next one, as it will be larger than the median value for each observations that has been found, which is T_{median} ≃1 second in average for all windows, neglecting the outliers of the distribution which corresponds to fluctuations due to low statistics in those bins.

These first results are a first hint on the need of reconsideration of the GW follow-up strategy with CTA, and a further update from the concept of pointing observations to a new concept of *slow scan* of the GW localization uncertainty region. Nevertheless, the validity of this statement will be only confirmed when the presented study will be expanded to the entire set of simulations, expected to be performed in the near future.

8.5 Discussion and outlook

In this chapter, the study of the capabilities of CTA on gravitational wave follow-ups and the detectability of *on-axis* events under good visibility condition has been addressed. The presented work provides an overview of the complex pipeline of GW-EM detectability simulations which is ongoing in the GW group of the CTA Transients science group. The results of the study are optimistic on the number of joint GW-EM

detections for this set of conditions, where we have seen that for larger values of the isotropic energy than $E_{iso} \sim 10^{50}$ ergs, the detection rate is above 80%.

In the near future, the study will be expanded to the entire set of `GWCOSMoS` simulations, which will enable the derivation of the sensibility of CTA to gravitational wave follow-ups.

Moreover, this type of studies are needed in order to understand the challenges of the science case, and be able to adapt the strategy of the facility to react smartly to such transient events, in this case gravitational waves. Regarding follow-up observations of event where no information about the GRB emission is in hand, the distribution of the duration of the scheduled observation shows that a good compromise can be obtained between the detection rate and the time allocated per observation, in order to maximize the chances to detect the very-high-energy gamma-ray counterpart. In addition, we have identified that the size of the GW localization region could also be considered as an extra input to put in place a case-to-case follow-up strategy.

Further points which are under discussion are the mentioned *scanning* of the GW localization uncertainty region and the best strategy to handle sharing the information during the GW follow-up between the CTA-North and CTA-South observatories (Figure 8.13).

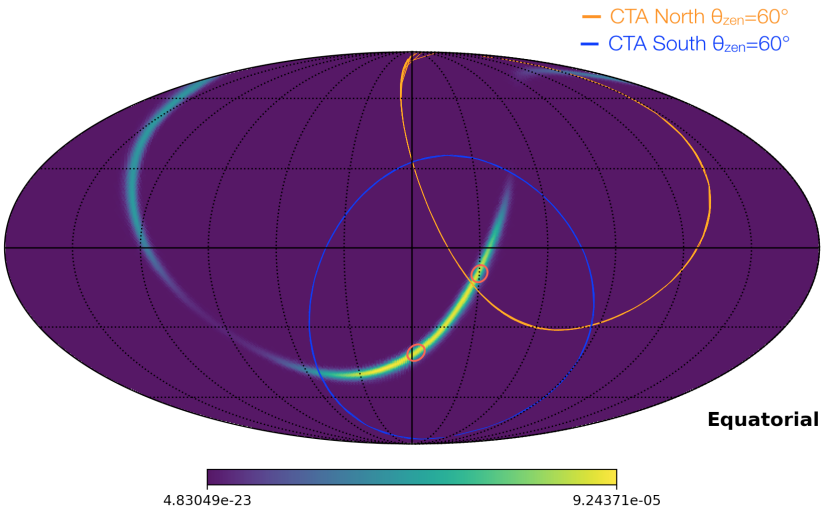

FIGURE 8.13: Illustration of the CTA two-sites GW follow-up observations, showing the *potential* of complementary follow-up with CTA-North and CTA-South observatories.

By the time CTA will be able to produce science results, the sensitivity of gravitational wave interferometers will reach design expectations and further detectors may have successfully join the network, as it is the case for KAGRA, and LIGO-India (Abbott et al., 2018). Expectations from gravitational wave reconstruction in the incoming years, considering 4-5 interferometers being part of the GW network, include

important improvements on the GW localization regions which, as it could be seen in this study, represent the main challenge to perform follow-up observations.

In this scenario and considering the sensitivity of CTA to very-high-energy gamma rays and the set-up of a real-time analysis, able to adapt in real-time the observation scheduler, the future of EM-GW joint observations seems bright, as it does the use of multi-messenger astrophysics to provide answer the open questions on the processed ongoing in extreme environments as the merger of compact binary objects and subsequent particle acceleration.

Summary and perspectives

During my research work, I have focused on studying the Universe through very-high-energy gamma rays and the link to multi-messenger and multi-wavelength astrophysics. The particular research work that I have performed during my PhD is summarized in the following points.

- My main research topic is the study of the link between gamma-ray bursts (GRBs) and compact binary coalescences (CBCs), and the emission at very-high-energy gamma-rays. In particular I focused in the search of electromagnetic counterparts from compact binary coalescences producing gravitational waves with IACTs. I developed novel, optimized GW follow-up observation strategies, able to perform a competitive, rapid response to alerts, taking into account the characteristics of the GW event and maximizing the chances to detect the electromagnetic counterpart. The algorithms that I developed not only consider the observation constraints of the H.E.S.S. site and the optimization on the selection of observation coordinates to reach low energy coverage, but also the distribution of galaxies that could potentially host the cataclysmic event. This work was presented for the first time at the Rencontres de Moriond and published as a Proceedings of Science (Seglar-Arroyo and Schüssler, 2017).

  I used the developed algorithms to perform the follow-up observation of GW170817. This led to successful follow-up observations of the neutron star merger by H.E.S.S., which was the first ground-based telescope covering the location of the lately identified electromagnetic counterpart (Abbott et al., 2017c). The analysis of this gravitational-wave follow-up observations set constraints on the emission of the remnant at very-high-energy gamma rays, which was published in Abdalla et al., 2017.

  This work, which started at the beginning of O2, enabled us to perform an efficient GW follow-up at very-high-energy gamma rays with the H.E.S.S. experiment, starting at the beginning of 2017 until today. Nowadays, the GW follow-up observation scheduler has been implemented in the H.E.S.S. alert system and it is able to perform follow-ups in an automatic way, whenever the prestablished criteria are fulfilled. Nevertheless, the CEA-Saclay team and myself attentively study the characteristics of every gravitational wave alert detected by LIGO-Virgo and take the decision on triggering follow-up observations, in the cases where the alert comes during daytime. The GW follow-up program of the H.E.S.S. collaboration has been presented at the 36th International Cosmic Rays Conference and it is described in the corresponding Proceedings of Science (Seglar-Arroyo et al., 2019).

- Within the HE.S.S. Collaboration, I have been during these last three years an *expert on call* for the GW follow-up. I have also been *expert on call* of the GRB follow-up program as well as member of the flaring AGN group. I presented the status of the Target-of-Opportunity program of the AGN group at the 35th International Cosmic Rays Conference (Seglar-Arroyo et al., 2017). This type of follow-up and target of opportunity programs are key to time-domain astronomy.

- As a result of these activities, I am currently leading the analysis of the first detection of VHE emission from the AGN OT081. This source, classified as low-synchrotron peak BL Lac, present a broadband emission which has been challenging to model with one-zone SSC models, similar to other sources (as AP Lib) with intermediate behavior between FSRQs and BL Lacs. The obtained MWL observations from radio to gamma-rays energies, have enabled a deeper understanding source and the flaring state. This work led to a cross-collaboration, multi-wavelength analysis involving H.E.S.S., MAGIC and Fermi-LAT, which will be published soon.

- I worked on the search of electromagnetic counterparts in GW follow-ups in a different, yet complementary, wide field-of-view VHE observatory: the HAWC experiment. In the context of the study of the GRB-CBC connection, I joined the AMON network, which focusses on the exploitation of sub-threshold events by performing correlation studies which can potentially lead to the identification of astrophysical events. I developed a novel multi-messenger analysis which combines gravitational wave events with HAWC data, by first performing spatial and temporal selection, and then an estimation of the likelihood on the origin of the event. I used this technique in pre-analysed sub-threshold LIGO/Virgo data and HAWC sub-threshold data obtained during the period of the first observation run of LIGO-Virgo (O1) although, unfortunately, no coincident GW+γ event has been identified. The discussion of the current status of AMON network by colleagues and myself has been recently published (Solares et al., 2020).

- I studied the perspectives of the next generation IACT telescope, CTA, on gravitational wave follow-up observations and the potential detection of electromagnetic counterpart in very-high-energy gamma rays. I focused on the adaptation and further development of the gravitational wave follow-up algorithms and strategy to the CTA gravitational wave program, with the aim to connect observations with the real-time analysis. In this context, I lead the complex simulation effort for the preparation of CTA to gravitational wave triggers. This detailed study starts from simulations of NS-NS mergers and the simulation of the GRB counterpart emission at very-high-energy gamma-rays, which has been done using `Gammapy`. Then, I developed a dedicated `Gammapy` analysis pipeline for the obtained dataset, where observations cover large regions in the sky and the source can be located anywhere in the FoV. In addition, due to the fading nature of the transient, first studies have been performed on the optimisation of the observation scheduling as well as the temporal windows by using GRB simulation based on phenomenological models. The knowledge gained

with this work includes the launch of the discussions on GW follow-up future strategies of CTA and the derivation of joint GW-EM detection rates. I have presented the main lines and steps of these simulations at the 36th International Cosmic Rays Conference (Seglar-Arroyo et al., 2019). A CTA consortium paper including the details of these simulations and the prospects of CTA to detected gamma-rays in GW follow-up observations is in preparation.

Bibliography

Aab, A et al. (2017a). "Combined fit of spectrum and composition data as measured by the Pierre Auger Observatory". In: *Journal of Cosmology and Astroparticle Physics* 2017.04, p. 038.

Aab, Alexander et al. (2017b). "Observation of a large-scale anisotropy in the arrival directions of cosmic rays above 8×10^{18} eV". In: *Science* 357.6357, pp. 1266–1270.

Aasi, J et al. (2014). "First searches for optical counterparts to gravitational-wave candidate events". In: *The Astrophysical Journal Supplement Series* 211.1, p. 7.

Abadie, J et al. (2012). "Implementation and testing of the first prompt search for gravitational wave transients with electromagnetic counterparts". In: *Astronomy & Astrophysics* 539, A124.

Abbott, Benjamin P et al. (2016). "Observation of gravitational waves from a binary black hole merger". In: *Physical review letters* 116.6, p. 061102.

Abbott, Benjamin P et al. (2017a). "Gravitational waves and gamma-rays from a binary neutron star merger: GW170817 and GRB 170817A". In: *The Astrophysical Journal Letters* 848.2, p. L13.

Abbott, Benjamin P et al. (2017b). "GW170814: a three-detector observation of gravitational waves from a binary black hole coalescence". In: *Physical Review Letters* 119.14, p. 141101.

Abbott, Benjamin P et al. (2017c). "Multi-messenger observations of a binary neutron star merger". In: *Astrophys. J. Lett* 848.2, p. L12.

Abbott, Benjamin P et al. (2018). "Prospects for observing and localizing gravitational-wave transients with Advanced LIGO, Advanced Virgo and KAGRA". In: *Living Reviews in Relativity* 21, pp. 1–57.

Abbott, BP et al. (2019). "GWTC-1: A gravitational-wave transient catalog of compact binary mergers observed by LIGO and Virgo during the first and second observing runs". In: *Physical Review X* 9.3, p. 031040.

Abdalla, H et al. (2017). "TeV Gamma-Ray Observations of the Binary Neutron Star Merger GW170817 with HESS". In: *Astrophysical Journal, Letters* 850.2.

Abdo, AA et al. (2010). "The spectral energy distribution of Fermi bright blazars". In: *The Astrophysical Journal* 716.1, p. 30.

Abeysekara, AU et al. (2012). "On the sensitivity of the HAWC observatory to gamma-ray bursts". In: *Astroparticle Physics* 35.10, pp. 641–650.

Abeysekara, AU et al. (2017a). "Observation of the crab nebula with the HAWC gamma-ray observatory". In: *The Astrophysical Journal* 843.1, p. 39.

Abeysekara, AU et al. (2017b). "The 2HWC HAWC observatory gamma-ray catalog". In: *The Astrophysical Journal* 843.1, p. 40.

Abeysekara, AU et al. (2019). "Measurement of the Crab Nebula at the Highest Energies with HAWC". In: *arXiv:1905.12518*.

Abramovici, Alex et al. (1992). "LIGO: The laser interferometer gravitational-wave observatory". In: *science* 256.5055, pp. 325–333.

Abramowski, Attila et al. (2015). "The high-energy γ-ray emission of AP Librae". In: *Astronomy & Astrophysics* 573, A31.

Acero, Fabio et al. (2015). "Fermi large area telescope third source catalog". In: *The Astrophysical Journal Supplement Series* 218.2, p. 23.

Ackermann, M et al. (2014). "Fermi-LAT observations of the gamma-ray burst GRB 130427A". In: *Science* 343.6166, pp. 42–47.

Ackermann, Markus et al. (2010). "Fermi observations of GRB 090510: A short-hard gamma-ray burst with an additional, hard power-law component from 10 keV to GeV energies". In: *The Astrophysical Journal* 716.2, p. 1178.

Adams, T et al. (2016). "Low-latency analysis pipeline for compact binary coalescences in the advanced gravitational wave detector era". In: *Classical and Quantum Gravity* 33.17, p. 175012.

Aharonian, F et al. (2007). "An exceptional very high energy Gamma-Ray flare of PKS 2155-304". In: *The Astrophysical Journal Letters* 664.2, p. L71.

Aharonian, F et al. (2008). "High energy astrophysics with ground-based gamma ray detectors". In: *Reports on Progress in Physics* 71.9, p. 096901.

Aharonian, Felix et al. (2006). "Observations of the Crab nebula with HESS". In: *Astronomy & Astrophysics* 457.3, pp. 899–915.

Ajello, M et al. (2017). "3FHL: The Third Catalog of Hard Fermi-LAT Sources". In: *The Astrophysical Journal Supplement Series* 232.2, p. 18.

Albert, A et al. (2019). "Science Case for a Wide Field-of-View Very-High-Energy Gamma-Ray Observatory in the Southern Hemisphere". In: *arXiv:1902.08429*.

Albert, Arnauld et al. (2017). "Search for high-energy neutrinos from binary neutron star merger GW170817 with ANTARES, IceCube, and the Pierre Auger Observatory". In: *The astrophysical journal. Letters* 850.2.

Albert, Jordi et al. (2007). "Variable very high energy γ-ray emission from Markarian 501". In: *The Astrophysical Journal* 669.2, p. 862.

Alexander, KD et al. (2017). "The electromagnetic counterpart of the binary neutron star merger LIGO/VIRGO GW170817. VI. Radio constraints on a relativistic jet and predictions for late-time emission from the kilonova ejecta". In: *The Astrophysical Journal Letters* 848.2, p. L21.

Alexander, KD et al. (2018). "A decline in the X-ray through radio emission from GW170817 continues to support an off-axis structured jet". In: *The Astrophysical Journal Letters* 863.2, p. L18.

Alexandreas, DE et al. (1992). "The CYGNUS extensive air-shower experiment". In: *Nuclear Instruments and Methods in Physics Research Section A: Accelerators, Spectrometers, Detectors and Associated Equipment* 311.1-2, pp. 350–367.

Alexeyev, EN et al. (1988). "Detection of the neutrino signal from SN 1987A in the LMC using the INR Baksan underground scintillation telescope". In: *Physics Letters B* 205.2-3, pp. 209–214.

Alfaro, R et al. (2017). "Search for Very-high-energy Emission from Gamma-Ray Bursts Using the First 18 Months of Data from the HAWC Gamma-Ray Observatory". In: *The Astrophysical Journal* 843.2, p. 88.

Allen, Bruce et al. (2012). "FINDCHIRP: An algorithm for detection of gravitational waves from inspiraling compact binaries". In: *Physical Review D* 85.12, p. 122006.

Amaldi, E et al. (1989). "Coincidences among the Maryland and Rome gravitational wave detector data and the Mont Blanc and KAMIOKA neutrino detector data in the period of SN1987A". In: *Annals of the New York Academy of Sciences* 571.1, pp. 561–576.

Antoni, T et al. (2002). "Muon density measurements with the KASCADE central detector". In: *Astroparticle Physics* 16.4, pp. 373–386.

Arrieta Lobo, Maialen (Dec. 2017). "A study of the emission processes of two different types of gamma-emitting Active Galactic Nuclei". PhD thesis. PSL Research University. URL: `https://tel.archives-ouvertes.fr/tel-01851649`.

Ashkar, H., F Schüssler, and M Seglar-Arroyo (2019). "Searches for TeV gamma-ray counterparts to Gravitational Wave events with H.E.S.S". In: *arXiV:1906.10426*.

Ashton, Gregory et al. (2018). "Coincident detection significance in multimessenger astronomy". In: *The Astrophysical Journal* 860.1, p. 6.

Atkins, R et al. (2003). "Observation of tev gamma rays from the crab nebula with milagro using a new background rejection technique". In: *The Astrophysical Journal* 595.2, p. 803.

Atkins, R et al. (2004). "Tev gamma-ray survey of the northern hemisphere sky using the milagro observatory". In: *The Astrophysical Journal* 608.2, p. 680.

Axford, W. I., E. Leer, and G. Skadron (1977). "The acceleration of cosmic rays by shock waves". In: International Cosmic Ray Conference 11, pp. 132–137.

Baixeras, Carmen, Magic Collaboration, et al. (2003). "The MAGIC telescope". In: *Nuclear Physics B-Proceedings Supplements* 114, pp. 247–252.

Balonek, Thomas J et al. (2016). "Detection of optical outburst activity in the BL Lac object OT 081 (PKS 1749+ 096)". In: *The Astronomer's Telegram* 9259.

Band, D et al. (1993). "BATSE observations of gamma-ray burst spectra. I-Spectral diversity". In: *The Astrophysical Journal* 413, pp. 281–292.

Band, David L and Jonathan E Grindlay (1986). "The synchrotron self Compton process in spherical geometries. II Application to active galactic nuclei". In: *The Astrophysical Journal* 308, pp. 576–591.

Baret, Bruny et al. (2012). "Multimessenger science reach and analysis method for common sources of gravitational waves and high-energy neutrinos". In: *Physical Review D* 85.10, p. 103004.

Barthel, Peter D (1989). "Is every quasar beamed?" In: *The Astrophysical Journal* 336, pp. 606–611.

Barthelmy, SD et al. (1995). "BACODINE, the real-time BATSE gamma-ray burst coordinates distribution network". In: *Astrophysics and Space Science* 231.1-2, pp. 235–238.

Barthelmy, SD et al. (1998). "The GRB coordinates network (GCN): A status report". In: *AIP Conference Proceedings*. Vol. 428. 1. AIP, pp. 99–103.

Bartos, Imre, Patrick Brady, and Szabolcs Marka (2013). "How gravitational-wave observations can shape the gamma-ray burst paradigm". In: *Classical and Quantum Gravity* 30.12, p. 123001.

Bartos, Imre and Marek Kowalski (2017). "Multimessenger Astronomy". In: *Multimessenger Astronomy, by Bartos, Imre; Kowalski, Marek. ISBN: 978-0-7503-1369-8. IOP ebooks. Bristol, UK: IOP Publishing, 2017.*

Bartos, Imre et al. (2014). "Cherenkov Telescope Array is well suited to follow up gravitational-wave transients". In: *Monthly Notices of the Royal Astronomical Society* 443.1, pp. 738–749.

Batista, Rafael Alves et al. (2019). "Open questions in cosmic-ray research at ultrahigh energies". In: *Frontiers in Astronomy and Space Sciences* 6, p. 23.

Baum, S. A. and T. M. Heckman (1989). In: *The Astrophysical Journal* 336.702.

Becerra Gonzalez, J and D for the Fermi-LAT collaboration Thompson (ATeL 9231). "Fermi-LAT detection of a GeV gamma-ray flare from the BL Lac object OT 081". In: *11-Jul-2016.*

Begelman, Mitchell C, Andrew C Fabian, and Martin J Rees (2008). "Implications of very rapid TeV variability in blazars". In: *Monthly Notices of the Royal Astronomical Society: Letters* 384.1, pp. L19–L23.

Bell, AR (1978). "The acceleration of cosmic rays in shock fronts–I". In: *Monthly Notices of the Royal Astronomical Society* 182.2, pp. 147–156.

Bellido, Jose (2017). "Depth of maximum of air-shower profiles at the Pierre Auger Observatory: Measurements above $10^{17.2}$ eV and Composition Implications". In: *PoS*, p. 506.

Berge, David, S Funk, and J Hinton (2007a). "Background modelling in very-high-energy γ-ray astronomy". In: *Astronomy & Astrophysics* 466.3, pp. 1219–1229.

— (2007b). "Background modelling in very-high-energy γ-ray astronomy". In: *Astronomy & Astrophysics* 466.3, pp. 1219–1229.

Bernlöhr, K et al. (2003). "The optical system of the HESS imaging atmospheric Cherenkov telescopes. Part I: layout and components of the system". In: *Astroparticle Physics* 20.2, pp. 111–128.

Bernlöhr, Konrad (2008). "Simulation of imaging atmospheric Cherenkov telescopes with CORSIKA and sim_telarray". In: *Astroparticle Physics* 30.3, pp. 149–158.

Blandford, Roger D and James P Ostriker (1978). "Particle acceleration by astrophysical shocks". In: *The Astrophysical Journal* 221, pp. L29–L32.

Blandford, Roger D and Martin J Rees (1978). "Extended and compact extragalactic radio sources: interpretation and theory". In: *Physica Scripta* 17.3, p. 265.

Blinnikov, SI et al. (1984). "Pis' ma Astron". In: *Zh* 10, p. 422.

— (2018). "Exploding neutron stars in close binaries". In: *arXiv:1808.05287.*

Blumenthal, George R and Robert J Gould (1970). "Bremsstrahlung, synchrotron radiation, and compton scattering of high-energy electrons traversing dilute gases". In: *Reviews of Modern Physics* 42.2, p. 237.

Böttcher, Markus (2007). "Modeling the emission processes in blazars". In: *The Multi-Messenger Approach to High-Energy Gamma-Ray Sources*. Springer, pp. 95–104.

Brindle, C et al. (1986). "Simultaneous optical and infrared polarization measurements of blazars". In: *Monthly Notices of the Royal Astronomical Society* 221, pp. 739–768.

Brown, AM (2005). "Atmospheric monitoring for the HESS Cherenkov telescope array by transmissometer and LIDAR". In:

Bulgarelli, A et al. (2016). "The Cherenkov Telescope Array Observatory: top level use cases". In: *Software and Cyberinfrastructure for Astronomy IV*. Vol. 9913. International Society for Optics and Photonics, p. 991331.

Bulgarelli, Andrea et al. (2015). "The On-Site Analysis of the Cherenkov Telescope Array". In: *arXiv:1509.01963*.

Buonanno, Alessandra et al. (2009). "Comparison of post-Newtonian templates for compact binary inspiral signals in gravitational-wave detectors". In: *Physical Review D* 80.8, p. 084043.

Cannon, Kipp et al. (2012). "Toward early-warning detection of gravitational waves from compact binary coalescence". In: *The Astrophysical Journal* 748.2, p. 136.

Cerruti, M et al. (2018). "Leptohadronic single-zone models for the electromagnetic and neutrino emission of TXS 0506+ 056". In: *Monthly Notices of the Royal Astronomical Society: Letters* 483.1, pp. L12–L16.

Cherenkov, PA (1937). "Visible radiation produced by electrons moving in a medium with velocities exceeding that of light". In: *Physical Review* 52.4, p. 378.

Ciprini, S et al. (July 2016). "Fermi and Swift observations of correlated outburst activity from the BL Lac object OT 081". In: *The Astronomers Telegram* 9260.

Clements, Sandra Denise et al. (1995). "Correlation Analysis of Optical and Radio Light Curves for a Large Sample of Active Galactic Nuclei". In: *The Astronomical Journal* 110, p. 529.

Cohen, AS et al. (2007). "The VLA low-frequency sky survey". In: *The Astronomical Journal* 134.3, p. 1245.

Collaboration, Auger et al. (1997). "The Pierre Auger observatory project: an overview". In: *International Cosmic Ray Conference*. Vol. 5, p. 205.

Cook, David O et al. (2017). "Census of the Local Universe (CLU) I: Characterization of Galaxy Catalogs from Preliminary Fields". In: *arXiv:1710.05016*.

CTA Consortium, The Cherenkov Telescope Array et al. (2017). "Science with the Cherenkov Telescope Array". In: *arXiv:1709.07997*.

Curtis, H.D. (1917). In: *Publi. A. S. P* 29.180.

Dal Canton, Tito et al. (2014). "Implementing a search for aligned-spin neutron star-black hole systems with advanced ground based gravitational wave detectors". In: *Physical Review D* 90.8, p. 082004.

Dálya, Gergely et al. (2018). "GLADE: A galaxy catalogue for multimessenger searches in the advanced gravitational-wave detector era". In: *Monthly Notices of the Royal Astronomical Society* 479.2, pp. 2374–2381.

De Lotto, Barbara et al. (2016). "MAGIC electromagnetic follow-up of gravitational wave alerts". In: *Proceedings of the International Astronomical Union* 12.S324, pp. 287–290.

De Naurois, Mathieu (May 2000). "L'expérience CELESTE: Reconversion d'une centrale solaire pour l'astronomie gamma. Première observation de la Nébuleuse du Crabe et du Blazar Markarian 421 entre 30 et 300 GeV." Theses. Université Pierre et Marie Curie - Paris VI. URL: `https://tel.archives-ouvertes.fr/tel-00004261`.

— (Mar. 2012). "Very High Energy astronomy from H.E.S.S. to CTA. Opening of a new astronomical window on the non-thermal Universe". Habilitation à diriger

des recherches. Université Pierre et Marie Curie - Paris VI. URL: https://tel.archives-ouvertes.fr/tel-00687872.

De Naurois, Mathieu and Loïc Rolland (2009). "A high performance likelihood reconstruction of gamma-rays for imaging atmospheric Cherenkov telescopes". In: *Astroparticle Physics* 32.5, pp. 231–252.

DeYoung, Tyce, HAWC Collaboration, et al. (2012). "The HAWC observatory". In: *Nuclear Instruments and Methods in Physics Research Section A: Accelerators, Spectrometers, Detectors and Associated Equipment* 692, pp. 72–76.

Di Sciascio, G, LHAASO Collaboration, et al. (2016). "The LHAASO experiment: from gamma-ray astronomy to cosmic rays". In: *Nuclear and particle physics proceedings* 279, pp. 166–173.

Dole, Herve (Sept. 2010). "The night is not dark: the extragalactic background light and the evolution of infrared galaxies". Habilitation à diriger des recherches. Université Paris Sud - Paris XI. URL: https://tel.archives-ouvertes.fr/tel-00529539.

Dominguez, Alberto et al. (2011). "Extragalactic background light inferred from AEGIS galaxy-SED-type fractions". In: *Monthly Notices of the Royal Astronomical Society* 410.4, pp. 2556–2578.

Donath, Axel et al. (2015). "Gammapy-A Python package for {\gamma}-ray astronomy". In: *arXiv:1509.07408*.

Dubois, F, G Lamanna, and A Jacholkowska (2009). "A multivariate analysis approach for the imaging atmospheric Cherenkov telescopes system HESS". In: *Astroparticle Physics* 32.2, pp. 73–88.

Duncan, Robert C and Christopher Thompson (1992). "Formation of very strongly magnetized neutron stars-Implications for gamma-ray bursts". In: *The Astrophysical Journal* 392, pp. L9–L13.

Einstein, Albert (1916). "Zur allgemeinen Relativitaetstheorie". In: *Sitzungsberichte der Preussischen Akademie der Wissenschaften zu Berlin*.

— (1918). "Ueber Gravitationswellen". In: *Sitzungsberichte der Preussischen Akademie der Wissenschaften zu Berlin*.

Evans, PA et al. (2012). "Swift follow-up observations of candidate gravitational-wave transient events". In: *The Astrophysical Journal Supplement Series* 203.2, p. 28.

Evans, PA et al. (2017). "Swift and NuSTAR observations of GW170817: detection of a blue kilonova". In: *Science* 358.6370, pp. 1565–1570.

Feldman, Gary J and Robert D Cousins (1998). "Unified approach to the classical statistical analysis of small signals". In: *Physical Review D* 57.7, p. 3873.

Fermi, Enrico (1949). "On the origin of the cosmic radiation". In: *Physical Review* 75.8, p. 1169.

Fermi-LAT Collaboration, The scientific et al. (2013). "The First Fermi LAT Gamma-Ray Burst Catalog". In: *arXiv:1303.2908*.

Finke, Justin D (2016). "External compton scattering in blazar jets and the location of the gamma-ray emitting region". In: *The Astrophysical Journal* 830.2, p. 94.

Finlay, Christopher Charles et al. (2010). "International geomagnetic reference field: the eleventh generation". In: *Geophysical Journal International* 183.3, pp. 1216–1230.

Fioretti, Valentina et al. (2015). "Real-Time Analysis sensitivity evaluation of the Cherenkov Telescope Array". In: *arXiv:1509.01943*.

Fisher, R et al. (1934). "Statistical methods for research workers." In: *Statistical methods for research workers.* 5th Ed.

Fishman, Gerald J (1995). "Gamma-ray bursts: An overview". In: *Publications of the Astronomical Society of the Pacific* 107.718, p. 1145.

Fleury, Patrick and Giuseppe Vacanti (1992). *Towards a Major Atmospheric Cerenkov Detector for TeV Astro/particle Physics.* Atlantica Séguier Frontières.

Fossati, G al et al. (1998). "A unifying view of the spectral energy distributions of blazars". In: *Monthly Notices of the Royal Astronomical Society* 299.2, pp. 433–448.

Freiburghaus, C, S Rosswog, and F-K Thielemann (1999). "R-process in neutron star mergers". In: *The Astrophysical Journal Letters* 525.2, p. L121.

Funk, Stefan et al. (2004). "The trigger system of the HESS telescope array". In: *Astroparticle Physics* 22.3-4, pp. 285–296.

Galbraith, W and JV Jelley (1953). "Light pulses from the night sky associated with cosmic rays". In: *Nature* 171.4347, p. 349.

GCNs, AGILE (2019). `http://agile.rm.iasf.cnr.it/gnc/gcn.html`.

Gehrels, Neil et al. (2016). "Galaxy strategy for LIGO-Virgo gravitational wave counterpart searches". In: *The Astrophysical Journal* 820.2, p. 136.

Gerstenshtein, ME and VI Pustovoit (1963). "On the detection of low frequency gravitational waves". In: *Journal of Experimental and Theoretical Physics* 16.2, pp. 433–435.

Ghirlanda, G et al. (2016). "Short gamma-ray bursts at the dawn of the gravitational wave era". In: *Astronomy & Astrophysics* 594, A84.

Ghirlanda, G et al. (2018). "Bulk Lorentz factors of gamma-ray bursts". In: *Astronomy & Astrophysics* 609, A112.

Ghirlanda, G et al. (2019). "Compact radio emission indicates a structured jet was produced by a binary neutron star merger". In: *Science* 363.6430, pp. 968–971.

Ghisellini, G et al. (2017). "The Fermi blazar sequence". In: *Monthly Notices of the Royal Astronomical Society* 469.1, pp. 255–266.

Gillessen, S (2004). In: *PhD thesis*.

Gilmore, Rudy C et al. (2013). "IACT observations of gamma-ray bursts: prospects for the Cherenkov Telescope Array". In: *Experimental Astronomy* 35.3, pp. 413–457.

González, MM et al. (2003). "A γ-ray burst with a high-energy spectral component inconsistent with the synchrotron shock model". In: *Nature* 424.6950, p. 749.

Granot, Jonathan et al. (2002). "Off-axis afterglow emission from jetted gamma-ray bursts". In: *The Astrophysical Journal Letters* 570.2, p. L61.

Greisen, Kenneth (1960). "Cosmic ray showers". In: *Annual Review of Nuclear Science* 10.1, pp. 63–108.

Grieder, Peter KF (2010). *Extensive Air Showers: High Energy Phenomena and Astrophysical Aspects-A Tutorial, Reference Manual and Data Book.* Springer Science & Business Media.

Guilbert, PW, AC Fabian, and MJ Rees (1983). "Spectral and variability constraints on compact sources". In: *Monthly Notices of the Royal Astronomical Society* 205.3, pp. 593–603.

Haggard, Daryl et al. (2017). "A deep Chandra X-ray study of neutron star coalescence GW170817". In: *The Astrophysical Journal Letters* 848.2, p. L25.

Haines, Todd et al. (1988). "Neutrinos from SN1987a in the IMB detector". In: *Nuclear Instruments and Methods in Physics Research Section A: Accelerators, Spectrometers, Detectors and Associated Equipment* 264.1, pp. 28–31.

Hassan, Tarek et al. (2017). "Monte Carlo performance studies for the site selection of the Cherenkov Telescope Array". In: *Astroparticle Physics* 93, pp. 76–85.

Haungs, A (2014). "The heavy knee and the light ankle observed with KASCADE-Grande". In: *Frascati Phys. Ser.* 58, p. 238.

Hauser, M et al. (2004). "ATOM an Automatic Telescope for Optical Monitoring". In: *Astronomische Nachrichten: Astronomical Notes* 325.6-8, pp. 659–659.

Heck, Dieter et al. (1998). "CORSIKA: a Monte Carlo code to simulate extensive air showers". In: *No. FZKA-6019*.

Heger, Alexander et al. (2003). "How massive single stars end their life". In: *The Astrophysical Journal* 591.1, p. 288.

Hervet, O, C Boisson, and H Sol (2015). "Linking radio and gamma-ray emission in Ap Librae". In: *Astronomy & Astrophysics* 578, A69.

H.E.S.S. collaboration, H.E.S.S. (2018). "Morphology study of a radio galaxies". In: *TeVPA presentation*.

H.E.S.S. Collaboration, H.E.S.S. (2019). "H.E.S.S. observations of VHE emission from GRBs". In: *1st CTA Symposium*.

H.E.S.S Collaboration, H.E.S.S (in preparation). "HESS-II performance paper". In:

H.E.S.S. collaboration, The scientific (2017). *GCN Circular 21084*. `https://gcn.gsfc.nasa.gov/gcn3/21084.gcn3`.

Hillas, A Michael (1985). "Cerenkov light images of EAS produced by primary gamma". In:

Hillas, AM et al. (1985). "19th International Cosmic Ray Conference". In: *La Jolla* 3, p. 445.

Hillas, Anthony M (1984). "The origin of ultra-high-energy cosmic rays". In: *Annual review of astronomy and astrophysics* 22.1, pp. 425–444.

— (2006). "Cosmic rays: Recent progress and some current questions". In: *arXiv: astro-ph/0607109*.

Hirata, Kazuto et al. (1987). "Observation of a neutrino burst from the supernova SN1987A". In: *Physical Review Letters* 58.14, p. 1490.

Hirata, KS et al. (1988). "Observation in the Kamiokande-II detector of the neutrino burst from supernova SN1987A". In: *Physical Review D* 38.2, p. 448.

Hofmann, Werner and Hess Collaboration (2000). "The high energy stereoscopic system (HESS) project". In: *AIP Conference Proceedings*. Vol. 515. 1. AIP, pp. 500–509.

Hofverberg, P et al. (2013). "Commissioning and initial performance of the HESS II drive system". In: *arXiv:1307.4550*.

Hoischen, Clemens (2018). "Multi-Messenger Astronomy with H.E.S.S: the Starburst Galaxy NGC253 and the Search for Short Time-Scale Transients". doctoralthesis. Universität Potsdam, p. 135. DOI: 10.25932/publishup-42452.

Holder, Jamie et al. (2006). "The first VERITAS telescope". In: *Astroparticle Physics* 25.6, pp. 391–401.

Holler, Markus et al. (2015). "Observations of the Crab Nebula with HESS phase II". In: *arXiv:1509.02902*.

Homan, Daniel C (2012). "Physical properties of jets in AGN". In: *International Journal of Modern Physics: Conference Series*. Vol. 8. World Scientific, pp. 163–171.

Hulse, Russell A and Joseph H Taylor (1975). "Discovery of a pulsar in a binary system". In: *The Astrophysical Journal* 195, pp. L51–L53.

Hurley, K et al. (1994). "Detection of a γ-ray burst of very long duration and very high energy". In: *Nature* 372.6507, p. 652.

IceCube, Collaboration et al. (2018). "Multimessenger observations of a flaring blazar coincident with high-energy neutrino IceCube-170922A". In: *Science* 361.6398, eaat1378.

IceCube Collaboration, IceCube et al. (2018). "Neutrino emission from the direction of the blazar TXS 0506+ 056 prior to the IceCube-170922A alert". In: *Science* 361.6398, pp. 147–151.

Jaffe, Walter et al. (1993). "A large nuclear accretion disk in the active galaxy NGC4261". In: *Nature* 364.6434, p. 213.

Joshi, Vikas and Armelle Jardin-Blicq (2017). "HAWC High Energy Upgrade with a Sparse Outrigger Array". In: *arXiv:1708.04032*.

Kampert, Karl-Heinz and Alan A Watson (2012). "Extensive air showers and ultra high-energy cosmic rays: a historical review". In: *The European Physical Journal H* 37.3, pp. 359–412.

Kaneko, Yuki et al. (2006). "The complete spectral catalog of bright BATSE gamma-ray bursts". In: *The Astrophysical Journal Supplement Series* 166.1, p. 298.

Kellermann, KI et al. (1989). "VLA observations of objects in the Palomar Bright Quasar Survey". In: *The Astronomical Journal* 98, pp. 1195–1207.

Klebesadel, Ray W, Ian B Strong, and Roy A Olson (1973). "Observations of gamma-ray bursts of cosmic origin". In: *The Astrophysical Journal* 182, p. L85.

Klein, Oskar and Yoshio Nishina (1929). "Über die Streuung von Strahlung durch freie Elektronen nach der neuen relativistischen Quantendynamik von Dirac". In: *Zeitschrift für Physik* 52.11-12, pp. 853–868.

Knödlseder, J et al. (2016). "GammaLib and ctools-A software framework for the analysis of astronomical gamma-ray data". In: *Astronomy & Astrophysics* 593, A1.

Kostelecký, V Alan and Stuart Samuel (1989). "Spontaneous breaking of Lorentz symmetry in string theory". In: *Physical Review D* 39.2, p. 683.

Kotera, Kumiko and Angela V Olinto (2011). "The astrophysics of ultrahigh-energy cosmic rays". In: *Annual Review of Astronomy and Astrophysics* 49, pp. 119–153.

Kouveliotou, Chryssa et al. (1993). "Identification of two classes of gamma-ray bursts". In: *The Astrophysical Journal* 413, pp. L101–L104.

Kovalev, Yu Yu et al. (1999). "Survey of instantaneous 1-22 GHz spectra of 550 compact extragalactic objects with declinations from to". In: *Astronomy and Astrophysics Supplement Series* 139.3, pp. 545–554.

Krymskii, GF (1977). "A regular mechanism for the acceleration of charged particles on the front of a shock wave". In: *Akademiia Nauk SSSR Doklady*. Vol. 234, pp. 1306–1308.

Lanyi, GE et al. (2010). "The celestial reference frame at 24 and 43 GHz. I. Astrometry". In: *The Astronomical Journal* 139.5, p. 1695.

Le Bohec, Stéphane et al. (1998). "A new analysis method for very high definition Imaging Atmospheric Cherenkov Telescopes as applied to the CAT telescope". In: *Nuclear Instruments and Methods in Physics Research Section A: Accelerators, Spectrometers, Detectors and Associated Equipment* 416.2-3, pp. 425–437.

Lemoine-Goumard, M, B Degrange, and M Tluczykont (2006). "Selection and 3D-reconstruction of gamma-ray-induced air showers with a stereoscopic system of atmospheric Cherenkov telescopes". In: *Astroparticle Physics* 25.3, pp. 195–211.

Lenain, J-P (2018). "FLaapLUC: A pipeline for the generation of prompt alerts on transient Fermi-LAT γ-ray sources". In: *Astronomy and computing* 22, pp. 9–15.

Lennarz, D et al. (2017). "The HAWC GRB programme". In: *AIP Conference Proceedings*. Vol. 1792. 1. AIP Publishing, p. 050033.

Li, T-P and Y-Q Ma (1983). "Analysis methods for results in gamma-ray astronomy". In: *The Astrophysical Journal* 272, pp. 317–324.

LIGO Collaboration, The scientific and the Virgo Collaboration (2019). *GCN Circular 24503*. `https://gcn.gsfc.nasa.gov/gcn3/24503.gcn3`.

LIGO Collaboration, The scientific et al. (2017). "A gravitational-wave standard siren measurement of the Hubble constant". In: *Nature* 551.7678, pp. 85–88.

LIGO Scientific Collaboration, LIGO et al. (2009). "The path to the enhanced and advanced LIGO gravitational-wave detectors". In: *Classical and Quantum Gravity* 26.11, p. 114013.

Loeb, Abraham (2016). "Electromagnetic counterparts to black hole mergers detected by LIGO". In: *The Astrophysical Journal Letters* 819.2, p. L21.

Longair, Malcolm S (2011). *High energy astrophysics*. Cambridge university press.

Lu, R-S et al. (2012). "The parsec-scale jet of PKS 1749+ 096". In: *Astronomy & Astrophysics* 544, A89.

Lynch, Ryan et al. (2018). "Observational implications of lowering the LIGO-Virgo alert threshold". In: *The Astrophysical Journal Letters* 861.2, p. L24.

Magee, Ryan et al. (2019). "Sub-threshold Binary Neutron Star Search in Advanced LIGO's First Observing Run". In: *The Astrophysical Journal Letters* 878.1, p. L17.

Malkov, MA (1997). "Analytic solution for nonlinear shock acceleration in the Bohm limit". In: *The Astrophysical Journal* 485.2, p. 638.

Margutti, Raffaella et al. (2018). "The Binary Neutron Star event LIGO/VIRGO GW170817 a hundred and sixty days after merger: synchrotron emission across the electromagnetic spectrum". In: *arXiv:1801.03531*.

Martinez-Castellanos, Israel et al. (2018). "HAWC observations of EM conterparts of GW events". In: URL: `https://indico.scc.kit.edu/event/390/contributions/4452/attachments/2245/3111/2018-09-10-LIGOfollowups-MonitoringCochem.pdf`.

Mészáros, P and Martin J Rees (1993). "Gamma-ray bursts: multiwaveband spectral predictions for blast wave models". In: *arXiv: astro-ph/9309011*.

Metzger, Brian D and Edo Berger (2012). "What is the most promising electromagnetic counterpart of a neutron star binary merger?" In: *The Astrophysical Journal* 746.1, p. 48.

Mickaelian, Areg M (2015). "AGN Zoo and Classifications of Active Galaxies". In: *Iranian Journal of Astronomy and Astrophysics* 2.1.

Mirzoyan, R., K. Noda, and E. et al. Moretti (2019). In: *GRB Coordinates Network, Circular Service, No. 23701*.

Mirzoyan, Razmik (2016). "MAGIC detects very high energy gamma-ray emission from the blazar OT 081 (PKS 1749+ 096, 4C+ 09.57)". In: *The Astronomer's Telegram* 9267.

Murase, Kohta et al. (2018). "Double Neutron Star Mergers and Short Gamma-ray Bursts: Long-lasting High-energy Signatures and Remnant Dichotomy". In: *The Astrophysical Journal* 854.1, p. 60.

Nakar, Ehud (2007). "Short-hard gamma-ray bursts". In: *Physics Reports* 442.1-6, pp. 166–236.

Nambu, Yoichiro (1968). "Quantum electrodynamics in nonlinear gauge". In: *Prog. Theor. Phys. Suppl.* 68, pp. 190–195.

Naurois, Mathieu de and Daniel Mazin (2015). "Ground-based detectors in very-high-energy gamma-ray astronomy". In: *Comptes Rendus Physique* 16.6-7, pp. 610–627.

Nava, Lara (2018). "High-energy emission from gamma-ray bursts". In: *International Journal of Modern Physics D* 27.13, p. 1842003.

Nava, Lara et al. (2014). "Clustering of LAT light curves: a clue to the origin of high-energy emission in gamma-ray bursts". In: *Monthly Notices of the Royal Astronomical Society* 443.4, pp. 3578–3585.

Nishizawa, Atsushi et al. (2009). "Probing nontensorial polarizations of stochastic gravitational-wave backgrounds with ground-based laser interferometers". In: *Physical Review D* 79.8, p. 082002.

Oechslin, Roland, H-T Janka, and A Marek (2007). "Relativistic neutron star merger simulations with non-zero temperature equations of state-I. Variation of binary parameters and equation of state". In: *Astronomy & Astrophysics* 467.2, pp. 395–409.

Paggi, A et al. (2009). "SSC radiation in BL Lacertae sources, the end of the tether". In: *Astronomy & Astrophysics* 504.3, pp. 821–828.

Parsons, RD and JA Hinton (2014a). "A Monte Carlo template based analysis for air-Cherenkov arrays". In: *Astroparticle Physics* 56, pp. 26–34.

— (2014b). "A Monte Carlo template based analysis for air-Cherenkov arrays". In: *Astroparticle physics* 56, pp. 26–34.

Patricelli, Barbara et al. (2018a). *GW COSMoS: Gravitational Wave COmpact binary SysteM Simulations*. DOI: 10.6084/m9.figshare.c.4243595.v1. URL: https://figshare.com/collections/GW_COSMoS_Gravitational_Wave_COmpact_binary_SysteM_Simulations/4243595/1.

Patricelli, Barbara et al. (2018b). "Searching for Gamma-Ray counterparts to Gravitational Waves from merging binary neutron stars with the Cherenkov telescope array". In: *Journal of Cosmology and Astroparticle Physics* 2018.05, p. 056.

Patrignani, CPDG et al. (2016). "Review of particle physics". In: *Chin. Phys.* 40, p. 100001.

Petropoulou, Maria, Georgios Vasilopoulos, and Dimitrios Giannios (2016). "The TeV emission of Ap Librae: a hadronic interpretation and prospects for CTA". In: *Monthly Notices of the Royal Astronomical Society* 464.2, pp. 2213–2222.

Piran, Tsvi (1999). "Gamma-ray bursts and the fireball model". In: *Physics Reports* 314.6, pp. 575–667.

Piron, Frédéric (2016). "Gamma-ray bursts at high and very high energies". In: *Comptes Rendus Physique* 17.6, pp. 617–631.

Piron, Frédéric et al. (2001). "Temporal and spectral gamma-ray properties of Mkn 421 above 250 GeV from CAT observations between 1996 and 2000". In: *Astronomy & Astrophysics* 374.3, pp. 895–906.

Potter, William J and Garret Cotter (2013a). "Synchrotron and inverse-Compton emission from blazar jets–III. Compton-dominant blazars". In: *Monthly Notices of the Royal Astronomical Society* 431.2, pp. 1840–1852.

— (2013b). "Synchrotron and inverse-Compton emission from blazar jets–IV. BL Lac type blazars and the physical basis for the blazar sequence". In: *Monthly Notices of the Royal Astronomical Society* 436.1, pp. 304–314.

Primack, Joel R et al. (2011). "Extragalactic Background Light and Gamma-Ray Attenuation". In: *AIP Conference Proceedings*. Vol. 1381. 1. AIP, pp. 72–83.

Rachen, Jorg P and Peter L Biermann (1993). "Extragalactic ultra-high energy cosmic-rays-part one-contribution from hot spots in Fr-II radio galaxies". In: *Astronomy and Astrophysics* 272, p. 161.

Ravasio, ME et al. (2019). "GRB 190114C: from prompt to afterglow?" In: *arXiv:1902.01861*.

Rees, MJ (1978). "Emission from the Nuclei of Nearby Galaxies: Evidence for Massive Black Holes?" In: *Symposium-International Astronomical Union*. Vol. 77. Cambridge University Press, pp. 237–244.

Reuter, H-P et al. (1997). "Millimetre continuum measurements of extragalactic radio sources-IV. Data from 1993–1994". In: *Astronomy and Astrophysics Supplement Series* 122.2, pp. 271–276.

Reynolds, Stephen P (1998). "Models of synchrotron X-rays from shell supernova remnants". In: *The Astrophysical Journal* 493.1, p. 375.

Righi, C, F Tavecchio, and L Pacciani (2018). "A multiwavelength view of BL Lac neutrino candidates". In: *Monthly Notices of the Royal Astronomical Society* 484.2, pp. 2067–2077.

Rodrigues, Xavier et al. (2019). "Binary neutron star merger remnants as sources of cosmic rays below the "Ankle"". In: *Astroparticle Physics* 106, pp. 10–17.

Ros, Eduardo (2008). "Kinematics of AGN jets". In: *Journal of Physics: Conference Series*. Vol. 131. 1. IOP Publishing, p. 012061.

Rutledge, Robert E (1998). "The Astronomer's Telegram: A Web-based Short-Notice Publication System for the Professional Astronomical Community". In: *Publications of the Astronomical Society of the Pacific* 110.748, p. 754.

Sanchez, D et al. (2015). "From radio to TeV: the surprising spectral energy distribution of AP Librae". In: *Monthly Notices of the Royal Astronomical Society* 454.3, pp. 3229–3239.

Sathyaprakash, Bangalore Suryanarayana and SV Dhurandhar (1991). "Choice of filters for the detection of gravitational waves from coalescing binaries". In: *Physical Review D* 44.12, p. 3819.

Scargle, Jeffrey D (1998). "Studies in astronomical time series analysis. V. Bayesian blocks, a new method to analyze structure in photon counting data". In: *The Astrophysical Journal* 504.1, p. 405.

Scargle, Jeffrey D et al. (2013). "Studies in astronomical time series analysis. VI. Bayesian block representations". In: *The Astrophysical Journal* 764.2, p. 167.

Schüssler, Fabian et al. (2015). "The HESS multi-messenger program". In: *arXiv:1509.03035*.

Seglar-Arroyo, M, F Schüssler, et al. (2017). "Gravitational wave alert follow-up strategy in the HESS multi-messenger framework". In: *arXiv:1705.10138*.

Seglar-Arroyo, M et al. (2017). "Target of Opportunity Observations of Blazars with HESS". In: *arXiv:1708.01083*.

Seglar-Arroyo, M. et al. (July 2019). "Searches for counterparts of gravitational waves at very high energies with H.E.S.S." In: *36th International Cosmic Ray Conference (ICRC2019)*. Vol. 36. International Cosmic Ray Conference, p. 789. arXiv: 1908.06705 [astro-ph.HE].

Seglar-Arroyo, M et al. (2019). "The gravitational wave follow-up program of the Cherenkov Telescope Array". In: *36th International Cosmic Ray Conference (ICRC2019)*. Vol. 36.

Share, GH et al. (1986). "SMM observation of a cosmic gamma-ray burst from 20 keV to 100 MeV". In: *Advances in Space Research* 6.4, pp. 15–18.

Shibata, Masaru and Koji Uryū (2006). "Merger of black hole-neutron star binaries: Nonspinning black hole case". In: *Physical Review D* 74.12, p. 121503.

Shibata, Masaru et al. (2006). "Magnetized hypermassive neutron-star collapse: a central engine for short gamma-ray bursts". In: *Physical review letters* 96.3, p. 031102.

Singer, Leo P and Larry R Price (2016). "Rapid Bayesian position reconstruction for gravitational-wave transients". In: *Physical Review D* 93.2, p. 024013.

Singer, Leo P et al. (2016a). "Going the distance: mapping host galaxies of LIGO and Virgo sources in three dimensions using local cosmography and targeted follow-up". In: *The Astrophysical Journal Letters* 829.1, p. L15.

— (2016b). "Supplement:"Going the Distance: Mapping Host Galaxies of LIGO and Virgo Sources in Three Dimensions Using Local Cosmography and Targeted Follow-up"(2016, ApJL, 829, L15)". In: *The Astrophysical Journal Supplement Series* 226.1, p. 10.

Solares, Hugo A. Ayala et al. (2020). "The Astrophysical Multimessenger Observatory Network (AMON): Performance and science program". In: *Astroparticle Physics* 114, pp. 68 –76. ISSN: 0927-6505. DOI: https://doi.org/10.1016/j.astropartphys.2019.06.007. URL: http://www.sciencedirect.com/science/article/pii/S0927650519301227.

Sommer, M et al. (1994). "High-energy gamma rays from the intense 1993 January 31 gamma-ray burst". In: *The Astrophysical Journal* 422, pp. L63–L66.

Stewart, IM (2009). "Maximum-likelihood detection of sources among Poissonian noise". In: *Astronomy & Astrophysics* 495.3, pp. 989–1003.

Stickel, M, JW Fried, and H Kuehr (1988). "The redshifts of the BL Lac objects 1749+ 096 and 2254+ 074". In: *Astronomy and Astrophysics* 191, pp. L16–L18.

Stickel, M et al. (1991). "The complete sample of 1 Jansky BL Lacertae objects. I-Summary properties". In: *The Astrophysical Journal* 374, pp. 431–439.

Strittmatter, PA et al. (1972). "Compact extragalactic nonthermal sources". In: *The Astrophysical Journal* 175, p. L7.

Taboada, Ignacio and Rudy C Gilmore (2014). "Prospects for the detection of GRBs with HAWC". In: *Nuclear Instruments and Methods in Physics Research Section A: Accelerators, Spectrometers, Detectors and Associated Equipment* 742, pp. 276–277.

Tanaka, Masaomi (2016). "Kilonova/macronova emission from compact binary mergers". In: *Advances in Astronomy* 2016.

Tavecchio, F and G Ghisellini (2014). "On the spine-layer scenario for the very high-energy emission of NGC 1275". In: *Monthly Notices of the Royal Astronomical Society* 443.2, pp. 1224–1230.

Tavecchio, F. et al. (Apr. 2017). "The Fermi blazar sequence". In: *Monthly Notices of the Royal Astronomical Society* 469.1, pp. 255–266. ISSN: 0035-8711. DOI: 10.1093/mnras/stx806. eprint: http://oup.prod.sis.lan/mnras/article-pdf/469/1/255/17503062/stx806.pdf. URL: https://dx.doi.org/10.1093/mnras/stx806.

Tavecchio, Fabrizio, Laura Maraschi, and Gabriele Ghisellini (1998). "Constraints on the physical parameters of TeV blazars". In: *The Astrophysical Journal* 509.2, p. 608.

Torniainen, I et al. (2005). "Long term variability of gigahertz-peaked spectrum sources and candidates". In: *Astronomy & Astrophysics* 435.3, pp. 839–856.

Troja, E et al. (2018). "The outflow structure of GW170817 from late-time broad-band observations". In: *Monthly Notices of the Royal Astronomical Society: Letters* 478.1, pp. L18–L23.

Urban, Alexander L (2016). "Monsters in the Dark: High Energy Signatures of Black Hole Formation with Multimessenger Astronomy". In:

Urry, C Megan and Paolo Padovani (1995). "Unified schemes for radio-loud active galactic nuclei". In: *Publications of the Astronomical Society of the Pacific* 107.715, p. 803.

Urry, C Megan et al. (1996). "Soft X-ray properties of a complete sample of radio-selected BL lacertae objects". In: *The Astrophysical Journal* 463, p. 424.

Veitch, John et al. (2015). "Parameter estimation for compact binaries with ground-based gravitational-wave observations using the LALInference software library". In: *Physical Review D* 91.4, p. 042003.

VERITAS collaboration, The scientific (2017). *GCN Circular 21153*. https://gcn.gsfc.nasa.gov/gcn3/21153.gcn3.

Vianello, Giacomo et al. (2017). "Searching for high-energy gamma-ray counterparts to gravitational-wave sources with Fermi-LAT: A needle in a haystack". In: *The Astrophysical Journal Letters* 841.1, p. L16.

Waxman, Eli (2004). "Gamma-ray bursts: Potential sources of ultra high energy cosmic-rays". In: *arXiv: astro-ph/0412554*.

Weekes, Trevor C et al. (1989). "Observation of TeV gamma rays from the Crab nebula using the atmospheric Cerenkov imaging technique". In: *The Astrophysical Journal* 342, pp. 379–395.

Weinberg, Steven (2008). *Cosmology*. Oxford university press.

Wills, RD and B Battrick (1977). "Recent advances in gamma-ray astronomy". In: *Recent Advances in Gamma-Ray Astronomy*. Vol. 124.

Wood, Joshua (2018). "An all-sky search for bursts of very high energy gamma rays with HAWC". In: *arXiv:1801.01550*.

Woosley, SE (1993). "Gamma-ray bursts from stellar mass accretion disks around black holes". In: *The Astrophysical Journal* 405, pp. 273–277.

Younk, Patrick W et al. (2015). "A high-level analysis framework for HAWC". In: *arXiv:1508.07479*.

Zhang, Bing (2019). "Charged Compact Binary Coalescence Signal and Electromagnetic Counterpart of Plunging BH-NS mergers". In: *arXiv:1901.11177*.

université PARIS-SACLAY | ÉCOLE DOCTORALE PHENIICS

Titre : A la recherche des origines du rayonnement cosmique : études multi-messagers avec des instruments en rayons gamma de très haute énergie

Mots clés : rayons gamma, études multi-messagers, ondes gravitationnelles, sursaut gamma, H.E.S.S., rayons cosmiques

Résumé : Les phénomènes explosifs qui se produisent dans l'Univers à haute énergie sont capables d'accélérer les particules jusqu'aux énergies les plus élevées. Ces processus produisent des particules secondaires de nature différente, comme des photons et des neutrinos. Dans certains cas particuliers, ces événements induisent des perturbations sur l'espace-temps : des ondes gravitationnelles détectables par des interféromètres sur Terre. La combinaison des informations complémentaires fournies par ces messagers cosmiques peuvent potentiellement répondre à des questions ouvertes en astrophysique. Parmi les événements les plus violents qui produisent de tels signaux figurent la fusion des deux objets les plus denses, comme les étoiles à neutrons et les trous noirs ou l'activité accréatrice dans les galaxies sur un trou noir supermassif. Dans ce travail, nous nous concentrons sur les photons à très haute énergie que produisent ces événements extrêmes, et sur la connexion avec les autres contreparties, afin de fournir une image globale multi-messagers qui permet l'étude des mécanismes physiques en place. Les défis inhérents à l'astronomie multi-messager dans le domaine temporel, ce qui implique un effort mondial coordonné et simultané entre les installations et les disciplines astronomiques, sont discutés et abordés. Une nouvelle stratégie d'observation optimisée du suivie des ondes gravitationnels pour les observatoires avec un petit/moyen champ de vue comme l'experience H.E.S.S. et le futur CTA, capables d'apporter une réponse rapide aux alertes, qui prend en compte les risques caractéristiques de l'événement GW et maximise les chances de détecter la contrepartie électromagnétique, sera présentée. Cette stratégie s'est avérée fructueuse lors d'observations de suivi avec les télescopes H.E.S.S., et en particulier dans le cas de la première detection de la fusion d'une binaire d'étoiles à neutrons, GW170817. Dans le cadre du réseau AMON, une analyse multi-messagers qui combine des événements d'ondes gravitationnelles LIGO/Virgo avec des données HAWC a été développée dans le but d'identifier les coïncidences astrophysiques à partir d'événements sous-seuil indépendants. De plus, la découverte par H.E.S.S. en très hautes énergies du noyau galactique actif OT 081, lors d'un état de flux élevé en juillet 2016, sera présentée.

Title : Searching for the origin of extragalactic cosmic rays : Multi-messenger studies with VHE gamma-ray instruments

Keywords : gamma rays, multi-messenger studies, gravitational waves, gamma-ray burst, H.E.S.S., cosmic rays

Abstract : The explosive phenomena occurring in the high-energy Universe are able to accelerate particles up to the highest energies. These processes produce secondary particles of different nature, i.e. photons and neutrinos. In special cases, these events induce perturbations on the space-time, i.e. gravitational waves detectable by interferometers on Earth. The combination and the complementary information provided by these cosmic messengers may allow to answer open questions in astrophysics, as the origin of cosmic rays. Amongst the most violent events producing such signals are the merge of the two densest objects, as neutron stars and black holes or the accretion activity in galaxies onto a supermassive black hole. In this work, we focus on the very-high energy photons that these extreme events produce, and the connection with the other counterparts, in order to provide a broad multi-messenger picture which enables the study of the physical mechanisms in place. The challenges inherent to time-domain multi-messenger astronomy are discussed and tackled, which involves simultaneous coordinated worldwide effort across facilities and astronomical disciplines. A novel, optimized GW follow-up observation strategy for small/mid-FoV instruments as H.E.S.S. and the future CTA, able to perform a rapid response to alerts, which considers the characteristics of the GW event and maximizes the chances to detect the electromagnetic counterpart will be presented. This strategy was proven successful in follow-up observations with the H.E.S.S. telescopes and in particular in the case of the first ever detected binary neutron star merger, GW170817. In the context of the AMON network, a multi-messenger analysis that combines gravitational wave LIGO/Virgo events with HAWC data, with the aim to identify astrophysical coincidences out of independent sub-threshold events, has been developed. In addition, the discovery by H.E.S.S. in very-high energies of the active galactic nucleus OT 081, during a flaring episode in July 2016, will be presented.

Université Paris-Saclay
Espace Technologique / Immeuble Discovery
Route de l'Orme aux Merisiers RD 128 / 91190 Saint-Aubin, France